



Gilroy, Cameron (2021) *The application of chiral metamaterials for sensing and active plasmonics*. PhD thesis.

<http://theses.gla.ac.uk/82336/>

Copyright and moral rights for this work are retained by the author

A copy can be downloaded for personal non-commercial research or study, without prior permission or charge

This work cannot be reproduced or quoted extensively from without first obtaining permission in writing from the author

The content must not be changed in any way or sold commercially in any format or medium without the formal permission of the author

When referring to this work, full bibliographic details including the author, title, awarding institution and date of the thesis must be given

Enlighten: Theses

<https://theses.gla.ac.uk/>
research-enlighten@glasgow.ac.uk



University
of Glasgow

ISM 

The application of chiral metamaterials for sensing and active plasmonics

Cameron Gilroy

Submitted in fulfilment of the requirements for the Degree of Doctor of Philosophy

School of Chemistry
College of Science and Engineering
University of Glasgow

Abstract

Chirality, the property of asymmetry, is ubiquitous in nature, observed in the handednesses of molecules to the twist of galaxies. This work concerns artificial chiral metamaterials, periodic arrays of chiral metal nanostructures. The extraordinary properties that they exhibit are determined not only by the materials from which they are constructed, as in traditional materials, but by the size, shape and spacing of nanostructures which constitute them. The chirality of the structures means that they strongly interact with the chiral manifestation of light, circularly polarised light. It is this interaction that is the theme that runs through this work.

Two applications of chiral metamaterials are investigated here. The first is their use for the detection of chiral biological material. Arrays of gammadion nanostructures are created using state of the art electron beam lithography fabrication techniques in the James Watt Nanofabrication Centre. The effect of deformations to the nanostructure geometry and morphology on their interaction with circularly polarised light is investigated. In particular focus is the effect on the circular dichroism (CD) spectra and levels of enhanced optical chirality, a parameter which has been related to the enhancement of the interaction of light with chiral molecules. It is shown here that whilst geometric changes do not have a significant effect on CD spectra, surface roughness on the surface of the nanostructure can support optical chirality ‘hotspots’. These enhancements are, however, not as large as those observed for electric field enhancements commonly exploited for surface enhanced Raman spectroscopy. It is subsequently shown through numerical simulation that the sensing capabilities of the gammadion nanostructure is correlated to its thickness. This is reconciled within a framework of an interference mechanism for the “dissipation” of optical chirality into chiral material currents. The presence of a chiral dielectric can cause an asymmetric change to the phase difference between two spatially separated chiral modes resulting in asymmetric changes to their chiral optical properties.

The second application is in the field of active plasmonics, which allows for the properties of metamaterials to be tuned post-fabrication by changing their size and shape using an external stimulus. Current approaches can require complex fabrication techniques which are inherently high cost. Here, a simple and novel approach is described which allows the chiral optical properties, namely the optical rotatory dispersion spectra, to be controlled electrically through a flexoelectric effect. The flexoelectric element, a lead zirconate titanate film, does not require high temperature processing and so can be integrated with polymer-based material.

Table of contents

0	FRONT MATTER	1
1	INTRODUCTION AND STRUCTURE	13
2	BACKGROUND AND THEORY	20
2.1	MAXWELL'S EQUATIONS	21
2.1.1	Microscopic Maxwell's equations	21
2.1.2	Macroscopic Maxwell's Equations	24
2.2	LIGHT POLARISATION	25
2.3	CHIROPTICAL EFFECTS	27
2.3.1	Optical rotatory dispersion	27
2.3.2	Circular dichroism	28
2.4	PLASMONICS	30
2.4.1	Dielectric function of metals	30
2.4.2	Localised surface plasmon resonance	32
2.5	CHIRAL PLASMONICS	35
2.5.1	Chiroptical effects in chiral plasmonics	36
2.6	CHIRAL METAMATERIALS	39
3	FABRICATION OF CHIRAL METAMATERIALS	41
3.1	GAMMADION STRUCTURE FABRICATION	42
3.1.1	Sample preparation	43
3.1.2	Resist spin coating	44
3.1.3	Electron beam writing	46
3.1.4	Development	47
3.1.5	Metallisation and lift-off	47
3.1.6	Process summary	48
3.2	SHURIKEN STRUCTURE FABRICATION	48
3.2.1	Shim fabrication	49
3.2.2	Substrate fabrication	49
4	METHODS	51
4.1	NANOSCALE CHARACTERISATION	52
4.1.1	Atomic force microscopy	52
4.1.2	Scanning electron microscopy	54
4.2	SPECTROSCOPIC MEASUREMENTS	56
4.2.1	Polarisation microscope	56
4.2.2	Circular dichroism spectroscopy	58
4.3	SIMULATION METHODS	59
4.3.1	Finite element method	59
4.3.2	COMSOL simulation strategy	60
5	AN INTRODUCTION TO CHIRAL METAMATERIALS FOR BIOLOGICAL SENSING	64
5.1	OPTICAL CHIRALITY AND CONSERVATION	65
5.1.1	Optical chirality	66
5.1.2	Optical chirality flux	68
5.2	SENSING WITH GAMMADION NANOSTRUCTURES	71

6	MORPHOLOGY AND GEOMETRY EFFECTS IN CHIRAL PLASMONIC NANOSTRUCTURES	73
6.1	EXPERIMENTAL GEOMETRY AND FABRICATION	74
6.2	MODELLING PROCEDURE	77
6.2.1	Nanostructure design	77
6.2.2	Calculated parameters	79
6.3	RESULTS	80
6.3.1	Circular dichroism spectra	80
6.3.2	Cleaning Effects	83
6.3.3	Simulated transmission plots	85
6.3.4	Electric field plots	87
6.3.5	Optical chirality	92
6.4	DISCUSSION	96
7	SUPERCHIRALITY AND INTERFERENCE FOR CHIRAL PLASMONIC BIODETECTION	101
7.1	MODELLING PROCEDURE	102
7.1.1	Nanostructure design	102
7.1.2	Modelling the unit cell	103
7.1.3	Calculated parameters	104
7.2	METAMATERIAL FABRICATION & MODEL VALIDATION	106
7.3	RESULTS	108
7.3.1	Structures in achiral media	108
7.3.2	Structures in chiral media	117
8	THE FLEXOELECTRIC EFFECT FOR ACTIVE CHIRAL METAMATERIALS	125
8.1	INTRODUCTION TO ACTIVE METAMATERIALS	126
8.1.1	Chemically active metamaterials	126
8.1.2	Thermomechanical active metamaterials	129
8.1.3	Electromechanical active metamaterials	131
8.1.4	Electromechanical coupling and the flexoelectric effect	133
8.2	DEVICE COMPOSITION AND FABRICATION	136
8.3	RESULTS	138
8.3.1	Spectroscopic measurements	138
8.3.2	Electric field simulations	144
8.3.3	Spectroscopic simulations	146
8.4	DISCUSSION	150
9	SUMMARY AND OUTLOOK	155
10	REFERENCES	157

List of Figures

Figure 1.1: The statue of Lord Kelvin which sits by the River Kelvin near Glasgow University.	16
Figure 1.2: The (<i>R</i>) and (<i>S</i>)-enantiomers of carvone. The (<i>R</i>) enantiomer smells minty and the (<i>S</i>) enantiomer smells like caraway seeds.	17
Figure 2.1: Schematic diagram of the components of linearly polarised light. E_{TOTAL} is the vector sum of E_x and E_y .	28
Figure 2.2: Schematic diagram of circularly polarised light components.	28
Figure 2.3: Optical rotation. Propagation of linearly polarised light (a) in an achiral medium. There is no phase difference between left and right circular components. (b) In a chiral medium there is a phase difference between left and right circular components causing optical rotation.	29
Figure 2.4: Circular dichroism. Propagation of linearly polarised light (a) in an achiral medium. There is no absorption difference between left and right circular components. (b) in a chiral medium where is a difference in absorption between left and right circular components. (c) Optical rotation and circular dichroism happening simultaneously.	31
Figure 2.5: Optical rotation spectrum and the corresponding expected ellipticity spectrum. Reproduced from [20].	32
Figure 2.6: (a) Drude-Sommerfeld model showing the real and imaginary parts of the dielectric function of gold. (b) The Lorentz model showing the same. Reproduced from [30][29].	33
Figure 2.7: Schematic diagram showing localised surface plasmon resonance. The electric field displaces the electron cloud surrounding the metal. Reproduced from [31].	35
Figure 2.8: (a) Absorbance spectra for 22, 48 and 99 nm Au nanoparticles. The resonance position red shifts as the particles become larger. (b) Absorbance spectra for gold nanorods with increasing aspect ratio. The longitudinal surface plasmon resonance band red shifts as aspect ratio increases. The inset shows the position maxima of the longitudinal (circles) and transverse (square) modes. Reproduced from [35].	36
Figure 2.9: Some interesting nanoparticle geometries. Reproduced from [36]–[38]	36
Figure 2.10: SEM of a gammadion array taken from an oblique angle showing dissymmetry of the side profile. SEM taken by Kensaku Endo, Osaka Prefecture University.	38
Figure 2.11: (a) Linearly polarised light interacts with an achiral nanoparticle causing LSPR. (b) If the incident light is CPL, the surface plasmons follow a helical shape. (c) A chiral nanostructure geometry can accommodate the helical plasmon which yields a strong interaction. (d) Mismatch between the chiral nanostructure and the plasmonic helix causes a weak chiroptical interaction. Reproduced from [49].	39
Figure 2.12: Plasmonic Born-Kuhn Model. (a) Nanorods stacked at 90° to one another. The left and right stacks are enantiomorphs of another. (b) Interaction between RCP (red) and LCP (blue) with the stacked nanorods. (c) Energy diagram for the in phase and out of phase excitation of the stacked nanorods. Reproduced from [50].	40
Figure 2.13: Examples of chiral metamaterials. (a) Plasmonically active helices [56]. (b) Moire chiral metamaterials [57]. (c) Pseudo 2D chiral shurikens. (d) Pseudo 2D chiral heptamers [58].	41
Figure 3.1: The desired outcome from the fabrication of the gammadion array, an array of gold nanostructures on a quartz slide.	44
Figure 3.2: Schematic of the electron beam lithography process for the fabrication of gold nanostructures	45
Figure 3.3: Poly-methyl methacrylate (PMMA)	47
Figure 3.4: Using only a monolayer of resist results in ‘ears’ on the finished structure.	47
Figure 3.5: A bilayer process can improve the quality of fabrication by preventing the formation of ‘ears’.	48
Figure 3.6: SEM images comparing the monolayer and bilayer nanofabrication processes.	48
Figure 3.7: Dose test for a gammadion array.	49
Figure 3.8: The desired outcome from the fabrication of the shuriken templated plasmonic substrates.	51

- Figure 4.1: Schematic of the operation of an atomic force microscope. 54
- Figure 4.2: Force between the tip and the surface as a function of tip sample distance. Reproduced from [65]. 55
- Figure 4.3: Atomic force microscopy can generate topographical maps of the metamaterials. In this example, the vertical profile of a plane (identified in the 2D and 3D profile maps, top) on the surface is calculated (bottom plot) 56
- Figure 4.4: Schematic diagram of the edge effect. 57
- Figure 4.5: Schematic diagram of custom-built microscope. 58
- Figure 4.6: Top panel: ORD of left-handed (LH) and right-handed (RH) shuriken structures. They are mirror images of one-another. Bottom panel: Reflectance spectra of LH and RH structures are identical. 59
- Figure 4.7: 3D printed cell for CD measurements. 60
- Figure 4.8: The two most common finite element shapes (a) HEX 8 and (b) TET 4. (c) Three triangular elements with common boundaries. 62
- Figure 4.9: (a) Geometry of the simulation with PML, light ports and integration surfaces identified. (b) The geometry after generation of the mesh. 63
- Figure 5.1: The electric vector of superchiral light undergoes a greater sense of twist over shorter length scales than CPL. 69
- Figure 5.2: ‘Superchiral spectroscopy’ for the detection of protein composition (a) C.D. of left and right-handed gammadions surrounded by water. An electron micrograph shows the the gammadion structure and periodicity. (b) C.D. of left and right-handed gammadions immersed in haemoglobin, heat treated β -lactoglobulin and β -lactoglobulin. (c) $\Delta\Delta\lambda$ changes for a range of proteins. Reproduced from [81]. 73
- Figure 6.1: The gammadion arrays are arranged in a chessboard formation. Each square in the chessboard has dimension of 1 mm \times 1 mm. 76
- Figure 6.2: AFM images collected from the three gammadion structure arrays and their measured dimensions. (a) The narrow arm gammadion has thinner arms compared to that of the (b) broad arm gammadion. (c) The broad arm stretched gammadion is based upon the broad arm gammadion with its vertical dimensions stretched by 1.25% and its horizontal dimensions compressed by 1.25%. The measured dimensions for each of the structures calculated from AFM images are presented on the red idealised structure. Only the left-handed structures are shown here. 77
- Figure 6.3: A top and three-dimensional view of the LH models of the gammadion nanostructures. Structures (a)-(c) are idealised models of the narrow arm gammadion, broad arm gammadion and stretched gammadion. Structure (d) is called the ‘real’ structure as it is generated directly from an AFM image of the broad arm gammadion array. 79
- Figure 6.4: Cut slice profile of the ‘real’ structure 0, 50 and 100 nm above the glass substrate. The structure shows significant sloping. 80
- Figure 6.5: Three dimensional electric field plots. (a) Mapping the entire electric field range shows only the boundaries of the simulation. (b) Mapping electric fields greater than 10 V/m. 81
- Figure 6.6: Comparison of experimental (top panels, blue) and simulated (lower panels, red and green) CD spectra for the narrow arm, broad arm and stretched broad gammadion nanostructures. The idealised structure simulations are shown in red and the ‘real’ structure simulations are shown in green. For each panel, the spectrum from the LH structure is shown in the darker colour and the RH structure is shown lighter. Four positions (I-IV) corresponding to minima and maxima in the CD spectra are identified with a dotted red line on each panel. 83
- Figure 6.7: (Top three panels) Experimental CD spectra of the LH (dark spectra) and RH (light spectra) ‘narrow arm’ structure after multiple cleaning cycles. The resonances, identified with dotted lines, in all cases shift to the blue. (Bottom panels) The shifts of resonances I-IV are quantified for the LH (left panel) and RH (right panel) structures. 86
- Figure 6.8: Simulated transmission plots for RCP (red) and LCP (blue) for the LH of the four modelled structures. The LH CD spectrum is shown in black for reference. CD resonances I-IV are identified on each plot with red lines. 88

Figure 6.9: Three dimensional normalised electric field plots above 10 V/m generated for (a) the narrow arm gammadion structure (b) the broad arm structure. (c) stretched broad arm structure (d) 'real structure.	90
Figure 6.10: Three dimensional normalised electric field plots above 20 V/m generated for (a) the narrow arm gammadion structure (b) the broad arm structure. (c) stretched broad arm structure (d) 'real structure.	91
Figure 6.11: Z-component of the electric field for (a) the narrow arm gammadion structure (b) the broad arm structure. (c) stretched broad arm structure (d) 'real structure	92
Figure 6.12 (a-b): Time averaged normalised optical chirality plots above a threshold of 2.5 for (a) the narrow arm gammadion structure (b) the broad arm structure. The minimum and maximum values for each resonance and light handedness are included.	95
Figure 6.13: Volume integrated optical chirality for each of the structures illuminated with incident RCP (top panel) LCP (bottom panel) and the sum of these (middle panel).	97
Figure 7.1: Simulated cross (a) and gammadion (b) nanostructures. The gammadion structure studied had variable heights of $h = 5, 30$ and 100 nm.	104
Figure 7.2: Idealised gammadion with right (R) and left (L) faces identified.	105
Figure 7.3: (a) The 570×570 nm unit cell with a nanostructure in the centre. The 500 nm thick chiral layer is identified in blue.	105
Figure 7.4: The four combinations of the incident structure face and light handedness are, 1. LCP incident on the RH face. 2. RCP incident on the RH face. 3. LCP incident on the LH face. 4. RCP Incident on the LH face.	107
Figure 7.5: Time averaged optical chirality and surface charge density plots are taken at positions $z = 0$ and $z = h$ nm for each nanostructure.	108
Figure 7.6: Surface charge density plots are calculated looking down the y-axis.	108
Figure 7.7: SEM image of the right-handed nanofabricated gold gammadion array.	108
Figure 7.8: A comparison of experimentally derived CD spectra (top panel) and simulation (bottom panel) show good agreement.	109
Figure 7.9: CD spectra of a gold cross when light is incident on both of its planar faces (blue and red).	110
Figure 7.10: Simulated CD spectra for gammadions of $h = 5$ (top panel), 30 (middle panel) and 100 nm (bottom panel). Blue lines are spectra for light incident upon the right-handed face (visible in the diagrams to the right of the spectra). Red lines are spectra for light incident upon left-handed faces of the structure. The mean of the two configurations is shown in black is ~ 0 across the wavelengths studied.	111
Figure 7.11: Electric field plots at a plane which bisects the structure (top left) for the $h = 5, 30$ and 100 nm thick gammadion nanostructures.	112
Figure 7.12: Normalised optical chirality flux plots for the nanostructures suspended in achiral media for $h = 5$ nm (triangles) 30 nm (circles) and 100 nm (squares) for R face illumination (top panel) and L face illumination (bottom panel) by RCP (red plots) and LCP (blue plots).	112
Figure 7.13: Sum of \mathbf{F} for LCP and RCP for R face illumination and L face illumination for the three gammadions in achiral media. For opposite face illuminations, the sum is equal I magnitude but opposite in sign.	113
Figure 7.14: Optical chirality plots for the $h = 5, 30$ and 100 nm thick structures in achiral media. The integrated chirality value across the structure is shown in the centre of each plot.	114
Figure 7.15: Surface charge density plots on the R and L faces of the structure and side views for the $h = 5, 30$ and 100 nm gammadions suspended in achiral media.	115
Figure 7.16: Simulated CD spectra for the cross surrounded by chiral media for light incident in the forwards and backwards direction.	120
Figure 7.17: Simulated CD spectra for gammadions surrounded by chiral media of $h = 5$ (top panel), 30 (middle panel) and 100 nm (bottom panel). Blue lines are spectra for light incident upon the right-handed face (visible in the diagrams to the right of the spectra). Red lines are spectra for light incident upon left-handed faces of the structure. The mean of the two configurations is shown in black.	120

- Figure 7.18: Normalised optical chirality flux plots for the nanostructures suspended in chiral media for $h = 5$ nm (triangles) 30 nm (circles) and 100 nm (squares) for R face illumination (top panel) and L face illumination (bottom panel) by RCP (red plots) and LCP (blue plots). 121
- Figure 7.19: Sum of F for LCP and RCP for R face illumination and L face illumination for the three gammadians in chiral media. For opposite face illuminations of the same structure, the spectra are no longer mirror images of one another. 123
- Figure 7.20: Optical chirality plots for the $h = 5, 30$ and 100 nm thick structures in chiral media. The integrated chirality value across the structure is shown in the centre of each plot. 124
- Figure 8.1: Chemical active metamaterial (a) Control of the reflectance spectrum by oxidation and reduction of copper in an array of inverse copper nano-antennas. Reproduced from [112]. (b) A dynamic plasmonic colour display. The colour of each ‘pixel’ is controlled by the spacing between gold nano-squares. The pixels are arranged into the shape of Vincent van Gogh’s Flowers in a Blue Vase. Hydrogenation and dehydrogenation erases and restores the colour. Reproduced from [25]. (c) Four magnesium particles in a square arrangement are surrounded by four gold nanoparticles so that the arrangement is chiral. When hydrogenated from Mg to MgH_2 the central squares lose their plasmonic properties rendering the plasmonic element achiral. The CD spectrum of the metamaterial is ‘quenched’ by hydrogenation. Reproduced from [113]. 129
- Figure 8.2 Thermomechanical active metamaterials. (a) An array of split ring resonators suspended by cantilever legs is constructed of two materials with different thermal expansion coefficients. Increasing the temperature causes the rings to be lifted from the plane of the substrate [114]. (b) The tilt angle of an omega ring is changed by a similar effect; however, the heating is induced by applying a potential difference. The transmission spectrum is modulated by changing the driving current [115]. Corner stacked nanorods are separated by a 50 nm layer of GST-326. The phase change from amorphous to crystalline causes a change in refractive index which red shifts the resonance. Reproduced from [116]. 132
- Figure 8.3 (a) An active split ring resonator. In its initial state a cantilever arm bends upwards. When an intermediate voltage is applied, the arm bends towards the substrate. When the electrostatic force overcomes the cantilever restoring force, the arm lies flat. Reproduced from [117]. (b) A ‘meander near the wire’ pattern fabricated on dielectric strings (shown in brown). The application of voltage creates an attractive electrostatic force between neighbouring patterns. Increasing the voltage reduces the gap with a commensurate effect observed in the reflectivity spectrum. Reproduced from [122]. 134
- Figure 8.4: (a) A non-centrosymmetric crystal in its free state. (b) Under homogeneous distortion, the distance between the negative and positive charge centres changes increasing polarisation 135
- Figure 8.5: Schematic of the flexoelectric effect. (a) The free state of the crystal. (b) Under homogeneous deformation, the positive and negative charge centres are overlapping meaning there is no net polarisation. (c) Under inhomogeneous deformation, the centres of negative and positive charge are no longer coincident, thus polarisation is achieved. 136
- Figure 8.6: (a) Transmission electron microscopy image of the deposited PZT layer lacks the interference fringes which are characteristic of a crystalline material. (b) Electron diffraction pattern lacks sharp diffractive features. 139
- Figure 8.7: (a) Schematic diagram of a single nanoindentation with gold, PZT and platinum sandwich layer thicknesses identified. (b) A cross section view of the structure shows the distribution of each material. 140
- Figure 8.8: ORD spectrum of the $d_{PZT} = 50$ nm structure over 60 minutes without the application of voltage. It shows the stability of the device over time. 141
- Figure 8.9: ORD (top panels) and reflectance (bottom panels) of sample $d_{PZT} = 150$ nm maintained at the threshold voltage for (a) one (b) four and (c) eight cycles. [Collected by Katie McKay]. 142
- Figure 8.10: Relaxation of the $d_{PZT} = 150$ nm device after its 5th voltage cycle. After 180 minutes the ORD has returned to its original magnitude. [Collected by Katie McKay]. 143
- Figure 8.11: ORD spectra for LH (left panel) and RH (right panel) structures present on the same $d_{PZT} = 150$ nm device. They show a near-identical reduction in their ORD intensity. 143
- Figure 8.12: ORD spectra for a second $d_{PZT} = 150$ nm device. It shows a qualitatively similar reduction in ORD intensity after the application of voltage, albeit with a reduced threshold voltage. 144

- Figure 8.13: ORD (a) and reflectance (b) spectra for the $d_{PZT} = 50$ nm device before voltage has been applied (blue) and after the application of a voltage (red). The reduction in ORD and reflectance magnitude is less than that for the $d_{PZT} = 150$ nm device. SEM images have been collected pre- (c) and post- (d) application of voltage which show changes to the shuriken structures, most notably narrowing of the arms. 145
- Figure 8.14: Electromagnetic models of the $d_{PZT} = 50$ nm and 150 nm devices were developed. The positions of the top, side walls and base positions are shown relative to the top of the gold surface which has been assigned here as $z = 0$ nm. 147
- Figure 8.15: Electric field and electric field gradient plots of PZT material for the $d_{PZT} = 50$ nm (upper panels) and 150 nm (lower panels) devices. (a) Electric field and electric field gradients (both z-components) for a plane cutting the nanostructure at the point marked by the dashed line in (b). (b) Electric field and electric field gradient (z-component) at the base of the nanostructure. (c) Electric field and electric field gradient (y-component) surrounding the arms of the nanostructure, the slice is taken halfway between the top and bottom surfaces. (d) Electric field and electric field gradients (z-component) for the top surface of the PZT, 5 nm below the gold layer. 148
- Figure 8.16: The two geometric parameters changed in the spectroscopic models are the arm width (left) and the indentation depth (right) of the nanostructure. 149
- Figure 8.17: Simulated structures. (a) Reducing the arm width from 35 nm (blue line) to 23 nm (red line) nearly completely quenches the ORD signal. (b) ORD spectra for a 23 nm arm with shuriken with a progressively decreasing depth. As the depth decreases, the ORD bisignate peak to peak height decreases, as shown in the inset plot. 150
- Figure 8.18: (a) Simulation-derived spectra for the shuriken structure pre- and post-application of voltage for the $d_{PZT} = 50$ nm and the $d_{PZT} = 150$ nm structures. The modelling parameters which define the shuriken structures modelled is shown in (b). 151
- Figure 8.19: Stress strain curve for gold thin films. 153

Acknowledgements

It would not have been possible to complete this thesis without the help and support of the following people to whom I would like to give my thanks.

Malcolm Kadodwala, who first introduced me to plasmonics and nanoscience when I was an undergraduate student and encouraged me to pursue this work. Affar Karimullah, who patiently taught me most of the techniques described in this work and who I always look forwards to having a chat with. To all the members of the group, past and present, PhD and project students, who not only contributed to this work but did so with good humour. Hans Senn, Alastair Wark and Gordon Hedley who kindly agreed to conduct my viva.

The staff of the Joseph Black Building who kindly let me use their equipment. Sharon Kelly and June Southall who put up with me in their lab for many hours of the day for many months of the year. Stuart and Arlene solved many of my technological problems. Academics who took the time to read my work as part of my annual reviews. To my fellow PhD students in the chemistry department, especially Robert, Matt and Adam who have been good friends to me.

To the staff at the JWNC who were very patient with me as I navigated the depths of nanofabrication.

To my colleagues over the road in the Physics Department who were great fun at the conferences we attended together. Special thanks to Donald MacLaren for his advice and encouragement in the face of my occasional curmudgeonliness.

I was lucky to twice travel to Japan to complete projects under the supervision of Yoshihiko Togawa and it was a great highlight of my PhD work. To Francisco Goncalves and Kensaku Endo who looked after me there and with whom I shared many glasses of Sapporo.

To the CDT-ISM who supported this work and to my fellow PhD students on the programme with whom I started, especially Yuchen, Julia, Tomas and Laura. I always looked forward to conferences and weekends on Loch Tay with that cheerful lot.

And lastly to my friends and family whose support throughout this long haul has been unwavering. My friends outwith the Chemistry Building, Chris and Marsali. My granny, Margery, my Dad, Stuart and my Mum, Alison. My siblings, Jo-Anne, Stuart and Erin. And lastly, to my partner Mairi who I cannot thank enough for her good humour and welcome distractions from work.

Author's declaration

I declare that, except where explicit reference is made to the contribution of others, that this dissertation is the result of my own work and has not been submitted for any other degree at the University of Glasgow or any other institution.

Printed Name:

CAMERON GILROY

Signature:

Published work

The work described in Chapters 7 and 8 have been published in the journal articles listed below.

C. Gilroy *et al.*, “Roles of Superchirality and Interference in Chiral Plasmonic Biodetection,” *J. Phys. Chem. C*, vol. 123, no. 24, pp. 15195–15203, Jun. 2019, doi: 10.1021/acs.jpcc.9b02791.

C. Gilroy *et al.*, “Active Chiral Plasmonics: Flexoelectric Control of Nanoscale Chirality,” *Adv. Photonics Res.*, vol. 3, p. 2000062, 2020, doi: 10.1002/adpr.202000062.

Part A

Introduction & methods

Chapter 1

Introduction and structure

The word chiral is derived from the Greek for hand, ‘χειρ’, they are the archetypal objects which exhibit chirality. The term was introduced by William Thomson, 1st Baron Kelvin, a professor of Natural Philosophy at Glasgow University [1] whose titular name refers to the river that runs beside the campus [2] where his statue now sits, **Figure 1.1**. In his Baltimore Lectures published in 1904, he said [3]:

“I call any geometrical figure or group of points chiral and say it has chirality if its image in a plane mirror, ideally realised, cannot be brought to coincide with itself.”

Put plainly, a chiral object can never be made to be congruent with its mirror image merely by rotation or translation.

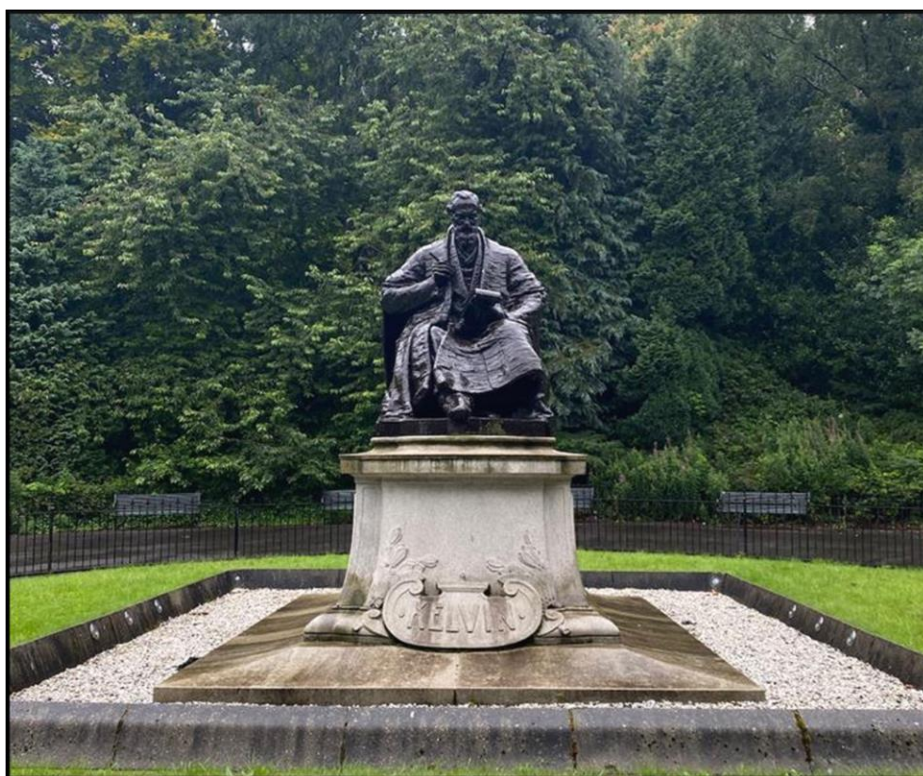


Figure 1.1: The statue of Lord Kelvin which sits by the River Kelvin near Glasgow University.

Chirality is a ubiquitous property observed in nature. Hands are the most obvious chiral objects to us, identical in almost all regards but mirror images of one another. Our hands are not only important in the field of chirality because they are the most immediate example we have of it: we often describe chiral objects as having a sense of right- or left-handedness. Some scientific fields use dextral and sinistral (from the Latin for left and right) to describe the different handednesses of objects that they study [4]. For example, snail shells have a

sense of twist and it has been found that 90 % of them are dextral: those in the chiral minority have difficulty finding a mate [5].

In chemistry, the mirror image forms of molecules are called enantiomers. The Cahn-Ingold-Prelog rules are applied to categorise a chiral centre as rectus (*R*) (another Latin translation for right) or sinister (*S*) [6]. In this work, the mirror image chiral structures produced will frequently be referred to as enantiomorphs, to distinguish them from molecular enantiomers and are characterised as either right- or left-handed (RH/LH respectively). This assignment is made arbitrarily, there is not a particular property which determines the structures' handedness other than the way that they look.

Chirality is an important property in nature, not only for the sinistral snail. All naturally occurring proteins which constitute living organisms are "left-handed", (except for glycine which is achiral) but all naturally occurring sugars are "right-handed". The prefixes L- and D- are commonly used to describe left and right handed biomolecules, respectively. Some bacteria absorb right-handed amino acids only to convert them into their left-handed form for use in their cell walls. [7]. The origin of this chiral imbalance in nature, termed homochirality, has not been precisely elucidated. Some have argued that asymmetric environmental factors such as a slight excess of either right or left circularly polarised light could be responsible for homochirality. Others claim that an initial imbalance of an enantiomer is amplified by promoting its own self-production and simultaneously acting to suppress the synthesis of its mirror image competitor [8].

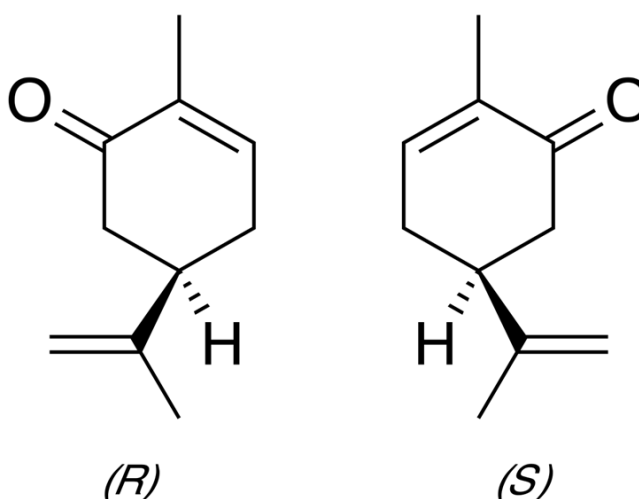


Figure 1.2: The (*R*) and (*S*)-enantiomers of carvone. The (*R*) enantiomer smells minty and the (*S*) enantiomer smells like caraway seeds.

No matter the origin of homochirality, the identification of chirality in molecular systems and the differentiation of enantiomers is of critical

importance. This is because a chiral object will interact with another chiral object differently depending upon its own handedness. Consider the previous example of a chiral object, the hand. If you shake your right hand with a friend's right hand, the two will fit together in a natural way. If you shake your right hand with a friend's left hand, the interaction is awkward and unwieldy. You could say one of these pairings is preferential.

Consider this now on the molecular scale. Different molecular enantiomers can display identical physical properties such as density and electronic and vibrational spectra. They can however exhibit profoundly different physiological effect. For example, the compound carvone, **Figure 1.2**: the (*4R*)-(-) enantiomer smells minty whereas its mirror image, the (*4S*)-(+) molecule smells like caraway seeds: evidence that our olfactory receptors contain chiral groups [9].

Although trivial to us, this difference in scent can be important for other organisms. Olean is a female produced sex pheromone of the olive fruit fly, however the (*R*)-enantiomer is only active on males and (*S*)-enantiomer is active only on females [10]. Medically, chirality is a critical consideration. The drug Naproxen found in the (*R*)-form is a non-steroidal anti-inflammatory used to treat the inflammation of joints caused by arthritis and gout. Its mirror image (*S*)-enantiomer causes liver damage and birth defects [11]. These examples illustrate a property which is unique to chiral objects: they interact identically with achiral objects but have a differential response to other chiral entities.

This work sits at the intersection of chirality and nanoscience. Plasmonic nanostructures can manipulate and confine light, giving rise to properties which are unique to their small length scales. An often-cited example is the use of metal nanoparticles to colour stained glass. Whilst the effect has been exploited for many centuries, it was not until Gustav Mie's application of Maxwell's equations that the effects first began to be understood [12].

In the foreword to Stefan A. Maier's book *Plasmonics: Fundamentals and Applications* [13], Bill Barnes writes that four elements underlie research in plasmonics today:

1. State of the art fabrication techniques.
2. High sensitivity optical characterisation techniques.
3. Advances in computing power which allow for numerical simulation.
4. A wide range of applications.

My hope is that this work touches upon each of these ideas. Here, chiral metamaterials, which are periodic arrays of chiral nanostructures, are fabricated with cutting edge processes and apparatus in one of the leading

centres for nanofabrication. Characterisation techniques like scanning electron microscopy, atomic force microscopy, circular dichroism and optical rotatory dispersion are used to characterise and better understand their properties. Powerful numerical methods are employed too which give even further insight into characteristics and processes that are difficult to obtain experimentally.

As for a wide range of applications, two themes related to chiral metamaterials are explored in this thesis. The first is the sensing of chiral materials using chiral nanostructures. This is of course particularly relevant in the field of biosensing due to the importance of chirality in nature. It is explored here with a particular focus on the role of a conserved quantity of electromagnetic fields which lay in relative mathematical obscurity for nearly half a century. Optical chirality was one of Lipkin's 'zilches', a mathematical quantity so called because it was initially thought to have no physical meaning. It was first described in 1964 [14] but shown by Tang and Cohen [15] to be directly related to the enhancement of the interaction of light with chiral molecules. Nanostructures have been shown to support optical chirality values which are much higher than the usual probe of chiral materials, circularly polarised light. The aim of the thesis in this area is to characterise the chiral optical (chiroptical) properties of chiral nanostructures and identify some guiding principles for their design as to maximise their sensing capabilities.

The second theme is that of active chiral metamaterials. Metamaterials can display novel and unexpected properties but, in most cases, these cannot be altered after their fabrication: active plasmonics is an area of research which seeks to remedy this. Creative approaches which allow for changes to the size and shape of plasmonic components by external stimuli have included chemical, thermomechanical and electromechanical mechanisms [16]. The potential applications of such devices are diverse. Imagine, for example, windows in a building which could control the amount of heat and light that they let in and out. Or a television display whose pixels are nanostructured elements which can change their shape [17]. This is the promise of active plasmonics. Here, an active chiral metamaterial is demonstrated where the shape of its constituent elements is controlled by electromechanical coupling via the flexoelectric effect. As a result, the material's chiroptical effects can be modulated.

This thesis is structured into four parts, (A-D). A summary of the chapters which comprise these parts is outlined next.

Part A: Introduction and structure

- Chapter 1** A brief introduction to chirality and its importance is given. Subsequently, the potential of plasmonics in its intersection with chirality is introduced.
- Chapter 2** Here, the general background and theory which is important throughout the thesis is given. First, Maxwell's equations are outlined along with polarisation of light, including circularly polarised light. Chiral optical effects are discussed in general. Subsequently, plasmonics and their incorporation in chiral metamaterials is introduced.
- Chapter 3** In this chapter, the chiral metamaterial geometries which are used throughout this thesis and their fabrication strategies are introduced. Two methods are outlined. The first is fabrication of gold gammadion arrays which extend from a quartz substrate. The second are shuriken nanostructure indentations in polycarbonate films.
- Chapter 4** Here, the methods which are used to characterise and better understand the nanostructure arrays are introduced. First, two microscopies are described which allow for images and models of the nanostructures to be generated. These are atomic force microscopy and scanning electron microscopy. Then, two spectroscopic techniques are discussed, namely optical rotatory dispersion and circular dichroism spectroscopy. Lastly, the simulation method 'finite element analysis' is introduced along with a description of its implementation by the software COMSOL Multiphysics.

Part B: Chiral metamaterials for biological sensing

- Chapter 5** Chapter 5 serves as an introduction to the application of chiral metamaterials for biological sensing. The quantity optical chirality and its relation to sensing of chirality is introduced. The concept of optical chirality flux is explained in terms of the conservation of optical chirality. Previous

examples of sensing with gammadion nanostructures are given.

Chapter 6 The first results chapter is a study of how geometric and morphological changes to the gammadion nanostructure can affect its chiroptical properties with a particular focus on circular dichroism spectra and optical chirality. A simulation technique which allows for the accurate modelling of nanostructure geometry based on atomic force micrographs is demonstrated.

Chapter 7 In Chapter 7, the sensing capabilities of the gammadion nanostructure is investigated through simulation. It is demonstrated that the thickness of the structure is a critical parameter for the sensing of chiral material. This is explained in terms an interference model for the dissipation of optical chirality.

Part C: Active chiral metamaterials

Chapter 8 Chapter 8 begins with a description of previous approaches for active control of chiral metamaterials. A layered metamaterial which incorporates a flexoelectric element is fabricated. It is then demonstrated that plasmonic elements which comprise the metamaterial array can have their shape changed post-fabrication via a flexoelectric effect mechanism. The chiroptical spectra of the metamaterial also exhibits changes and this is shown by simulation to be caused by the changes in geometry.

Part D: Summary and outlook

Chapter 9 A summary of the work contained in the thesis is given, along with recommendations for future work.

Chapter 10 The works cited in this thesis are listed.

Chapter 2

Background and theory

The purpose of this chapter is to introduce the theoretical concepts which are relevant throughout this thesis. After a brief introduction to Maxwell's equations and electromagnetic theory, plasmonic metamaterials and the chiroptical effect which can arise from their interaction with light is discussed.

2.1 Maxwell's equations

Maxwell's equations are arguably the most influential four equations in all of science, forming the basis of electromagnetic theory. They are:

1. Gauss's law for electric fields
2. Gauss's law for magnetic fields
3. Faraday's law
4. The Ampere-Maxwell law

Here, a brief introduction to the microscopic and macroscopic forms of Maxwell's equations are given.

2.1.1 Microscopic Maxwell's equations

The microscopic or general form of Maxwell's equations expresses the interaction of electric of magnetic and electric fields in terms of discrete charges and currents.

Gauss's law for electric fields in its integral form is given by the following equation:

$$\oint_S \mathbf{E} \cdot \hat{n} da = \frac{q_{enc}}{\epsilon_0} \quad \text{Equation 2.1}$$

where	\mathbf{E}	Electric field
	\hat{n}	Normal unit vector
	q_{enc}	Enclosed charge
	ϵ_0	Permittivity of free space

The integral form of Gauss's law for electric fields states that "electric charge produces an electric field and the flux of that field passing through any closed surface is proportional to the total charge contained within the surface" [18]. By application of divergence theorem, Gauss's law for electric fields can be expressed in its differential form like so:

$$\nabla \circ \mathbf{E} = \frac{\rho}{\epsilon_0} \quad \text{Equation 2.2}$$

where $\nabla \circ \mathbf{E}$ Divergence of the electric field
 ρ Electric charge density

The differential form of Gauss’s law for electric fields states that “the electric field produced by electric charge diverges from positive charge and converges upon negative charge” [18]. The key difference between the two forms is that the integral form describes the integral of the normal component of the electric field over a surface whilst the differential form concerns the divergence of the electric field and charge density at points in space.

Gauss’s law for magnetic fields in its integral form is written:

$$\oint_S \mathbf{B} \circ \hat{n} da = 0 \quad \text{Equation 2.3}$$

where \mathbf{B} Magnetic field

Gauss’s law for magnetic fields states that the magnetic flux which passes through a closed surface is zero. This arises because no magnetic monopoles exist [18], [19]. By application of divergence theorem, Gauss’s law for magnetic fields can be expressed in the differential form:

$$\nabla \circ \mathbf{B} = 0 \quad \text{Equation 2.4}$$

where $\nabla \circ \mathbf{B}$ Divergence of the magnetic field.

The differential form of Gauss’s law for magnetic fields states that the divergence of the magnetic field at all points is zero.

Faraday’s law can be expressed in the integral form using the following two equations:

$$emf = -\frac{d}{dt} \int_S \mathbf{B} \circ \hat{n} da \quad \text{Equation 2.5}$$

$$\oint_C \mathbf{E} \circ dl = - \int_S \frac{\partial \mathbf{B}}{\partial t} \circ \hat{n} da \quad \text{Equation 2.6}$$

where

emf electromagnetic force
 $\int_S \mathbf{B} \circ \hat{n} da$ Magnetic flux through a surface
 $\int_S \frac{\partial \mathbf{B}}{\partial t} \circ \hat{n} da$ Flux of the time rate of change of the magnetic field
 dl An incremental segment of a path

Equation 2.5 is the flux rule and **Equation 2.6** is the alternate form of Faraday’s law. It is also possible to write Faraday’s law with one expression. Faraday’s law states that, “changing magnetic flux through a surface induces an electromotive force in any boundary path of that surface and a changing magnetic field induces a circulating electric field” [18]. By application of Stokes’ Theorem, Faraday’s law can be expressed in its differential form:

$$\nabla \times \mathbf{E} = \frac{\partial \mathbf{B}}{\partial t} \quad \text{Equation 2.7}$$

where

$\nabla \times \mathbf{E}$	Curl of the electric field
$\frac{\partial \mathbf{B}}{\partial t}$	Rate of change of the magnetic field

In its differential form, Faraday’s law states that a circulating electric field is produced by a changing magnetic field.

Lastly, the Ampere-Maxwell is described in its integral form by:

$$\oint_C \mathbf{B} \circ d\mathbf{l} = \mu_0 \left(I_{enc} + \varepsilon_0 \frac{d}{dt} \int_S \mathbf{E} \circ \hat{\mathbf{n}} da \right) \quad \text{Equation 2.8}$$

where

μ_0	Permeability of free space
I_{enc}	Enclosed electric current
$\int_S \mathbf{E} \circ \hat{\mathbf{n}} da$	Electric flux through a surface bound by a closed path C

The integral form of the Ampere-Maxwell law states that, “an electric current or a changing electric flux through a surface produces a circulating magnetic field around any path that bounds that surface [18]. By application of Stokes’ theorem, the differential form of the Ampere-Maxwell law can be written as:

$$\nabla \times \mathbf{B} = \mu_0 \left(\mathbf{J} + \varepsilon_0 \frac{\partial \mathbf{E}}{\partial t} \right) \quad \text{Equation 2.9}$$

where

$\nabla \times \mathbf{B}$	Curl of the magnetic field
\mathbf{J}	Electric current density
$\frac{\partial \mathbf{E}}{\partial t}$	Rate of change of the electric field with time

In its differential form, the Ampere-Maxwell law describes how, “a circulating magnetic field is produced by an electric current and by an electric field that changes with time” [18].

2.1.2 Macroscopic Maxwell's Equations

In the previous section, Gauss's law considered all charges which are enclosed by the surface. In a dielectric material, positive and negative charges are slightly displaced in the presence of an electric field: this is polarisation and the charge which arises is called bound charge. The polarisation charge density induces a polarisation field whose vector is anti-parallel to the electric field. If the polarisation field is uniform throughout the material, then bound charge will only appear on the material surface. However, if it is non-uniform within the material, then charge will also accumulate within its volume. The permittivity of a material, ϵ is a measure of the polarizability of a dielectric: materials with a high permittivity polarise more in the presence of an electric field than those with lower values.

The volume density of the bound charge is given by:

$$\rho_b = -\nabla \cdot \mathbf{P} \quad \text{Equation 2.10}$$

where

ρ_b

Volume charge density

$\nabla \cdot \mathbf{P}$

Divergence of the electric polarisation

The differential form of Gauss's law for electric fields (**Equation 2.2**) can be expressed as the sum of both free charge density (ρ_f) and bound charge density (ρ_b):

$$\nabla \cdot \mathbf{E} = \frac{\rho}{\epsilon_0} = \frac{\rho_f + \rho_b}{\epsilon_0} \quad \text{Equation 2.11}$$

Which substituting with **Equation 2.10** becomes

$$\nabla \cdot (\epsilon_0 \mathbf{E} + \mathbf{P}) = \rho_f \quad \text{Equation 2.12}$$

The term in brackets is often written as the displacement vector, \mathbf{D} . And so, a differential form of Gauss's law that is only dependent on the density of free charge can be given:

$$\nabla \cdot \mathbf{D} = \rho_f \quad \text{Equation 2.13}$$

Which by application of divergence theorem can be written in integral form with reference to the flux of the displacement and free enclosed charge, $q_{free,enc}$:

$$\oint_S \mathbf{D} \cdot \hat{n} \, da = q_{free,enc} \quad \text{Equation 2.14}$$

With regards to the Ampere-Maxwell law in materials, a magnetic field can induce magnetisation within magnetic materials. Bound currents can act as

sources of additional magnetic fields. Furthermore, changes in polarisation over time can contribute to the current density. The differential form of the Ampere-Maxwell law in terms of magnetic field strength \mathbf{H} , displacement vector \mathbf{D} and free current density \vec{J}_{free} is given by:

$$\nabla \times \mathbf{H} = \left(\mathbf{J}_{free} + \frac{\partial \mathbf{E}}{\partial t} \right) \quad \text{Equation 2.15}$$

which by application of Stokes' theorem can be written in the integral form, with reference to the free enclosed electric current, $I_{free,enc}$:

$$\oint_C \mathbf{H} \circ d\mathbf{l} = I_{free,enc} \left(\frac{d}{dt} \int_S \mathbf{D} \circ \hat{\mathbf{n}} da \right) \quad \text{Equation 2.16}$$

Gauss's law in magnetic fields and Faraday's law do not concern electric charge or current and so no macroscopic equations are required [18]. Note that in all cases the microscopic equations can describe the macroscopic case by considering charge and current density as the sum of point charges [19].

2.2 Light polarisation

Propagating electromagnetic fields can be considered as a wave with electric and magnetic components orthogonal to one another. If the electric vector of light oscillates in a specific plane, then the wave can be described as plane polarised. The polarisation of light can be described algebraically. First consider two orthogonal electric fields, \mathbf{E}_x and \mathbf{E}_y which are travelling in the z direction and have the same frequency but different phases:

$$\mathbf{E}_x(z, t) = \hat{i}E_{0x}\cos(kz - \omega t) \quad \text{Equation 2.17}$$

$$\mathbf{E}_y(z, t) = \hat{j}E_{0y}\cos(kz - \omega t + \phi) \quad \text{Equation 2.18}$$

where

\mathbf{E}	electric field at a point x/y at a time t
E_0	wave amplitude
ω	angular frequency,
k	wave number and
ϕ	relative phase difference between the two waves.
\hat{i}	Unit vector in the x direction
\hat{j}	Unit vector in the y direction

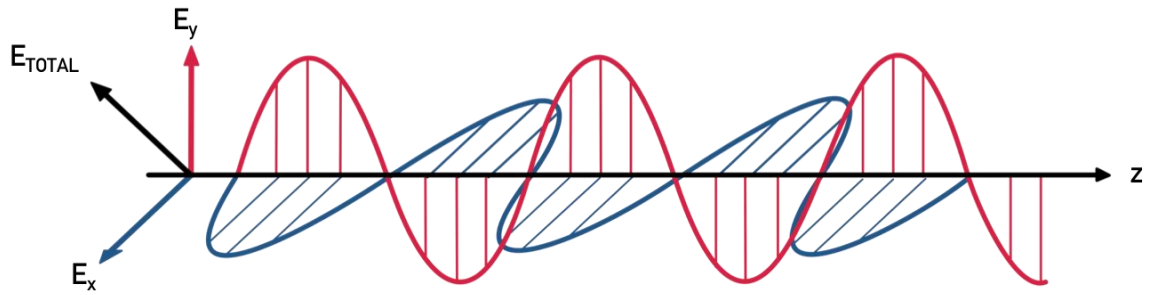


Figure 2.1: Schematic diagram of the components of linearly polarised light. E_{TOTAL} is the vector sum of E_x and E_y .

The resultant wave is given by the vector sum of the two components, E_{TOTAL} in **Figure 2.1**. If the phase difference, Φ is 0 or a multiple of $\pm 2\pi$ then the following equation describes a linearly polarised wave:

$$\mathbf{E} = (\hat{i}E_{0x} + \hat{j}E_{0y})\cos(kz - \omega t) \quad \text{Equation 2.19}$$

If the phase difference Φ is $2\pi + (-\pi/2)$ or a multiple thereof, as in **Figure 2.2**, then the resultant wave becomes:

$$\mathbf{E} = E_0[\hat{i}\cos(kz - \omega t) + \hat{j}\sin(kz - \omega t)] \quad \text{Equation 2.20}$$

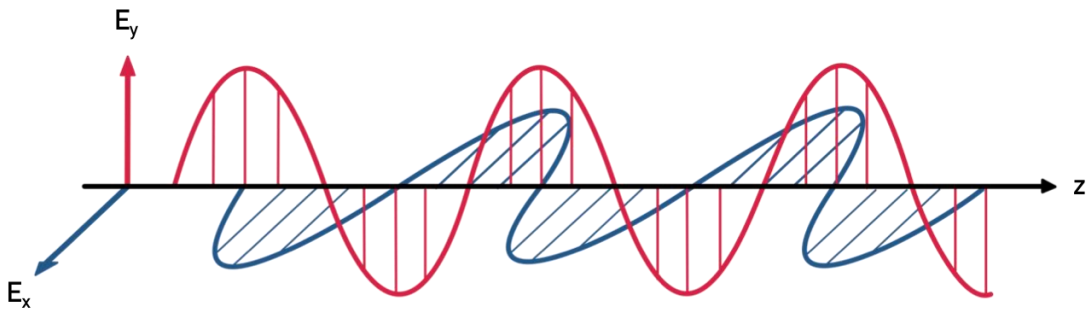


Figure 2.2: Schematic diagram of circularly polarised light components.

In this case the resultant electric vector traces out a circle as it propagates along the z axis. The light is described as being circularly polarised light (CPL) [20].

In this work, the chemistry convention is adopted whereby when viewed towards the source, the electric vector of right CPL rotates clockwise and left CPL rotates anticlockwise. The sum of left and right CPL is given by:

$$\mathbf{E} = 2E_0\hat{i}\cos(kz - \omega t) \quad \text{Equation 2.21}$$

Equation 2.21 describes linearly polarised light, hence linearly polarised light can be considered a superposition of left and right CPL.

2.3 Chiroptical effects

CPL is the optical manifestation of chirality and because it is a chiral entity it will interact differentially with other chiral objects. This makes CPL a good candidate for the probing of chiral molecules and structures. This work will primarily focus on two chiral optical (chiroptical) effects: optical rotatory dispersion and circular dichroism.

2.3.1 Optical rotatory dispersion

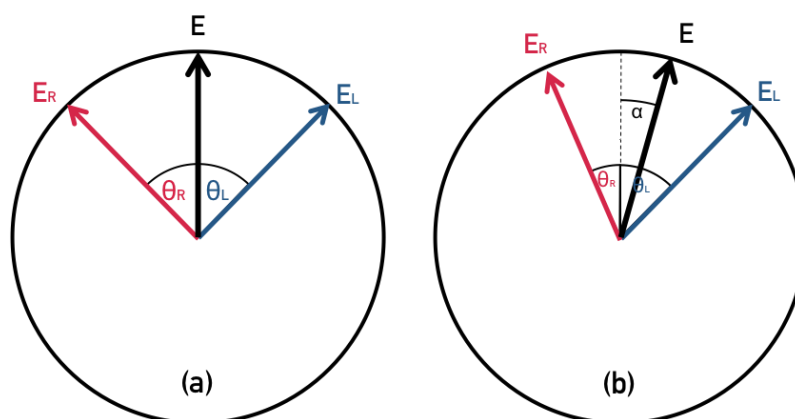


Figure 2.3: Optical rotation. Propagation of linearly polarised light (a) in an achiral medium. There is no phase difference between left and right circular components. (b) In a chiral medium there is a phase difference between left and right circular components causing optical rotation.

As previously noted, linearly polarised light can be considered the superposition of left and right CPL. If linearly polarised light travels through an achiral medium, then the left- and right-handed CPL components travel at the same velocities and there is no phase difference between the two components. At a given position within the material the electric vectors of CPL, E_R and E_L are oriented at the same angles θ_R and θ_L from the incident beam, as in **Figure 2.3 (a)**. Their recombination gives linearly polarised light whose electric vector has not rotated with respect to the incident beam polarisation.

If, however left and right CPL components propagate at different velocities within the material, v_L and v_R respectively, then a phase difference arises. E_R and E_L are oriented at angles θ_R and θ_L from the incident polarisation. Their recombination gives linearly polarised light whose electric vector has rotated with respect to the incident beam, as in **Figure 2.3 (b)**. The rotation, α , is given by:

$$\alpha = \frac{1}{2}(\theta_L + \theta_R) \quad \text{Equation 2.22}$$

The speed at which the light components travel through a material is determined by the real part of its complex refractive index which in optically active media is different for left circularly polarised light (LCP) and right circularly polarised light (RCP).

Chemists will describe enantiomers of a molecule which rotate the plane of polarisation clockwise when looking at the source dextrorotatory and those which rotate anti-clockwise laevorotatory [21]. This ability to differentiate between enantiomers has allowed optical rotation to be used as a molecular probe since the early 1800s. Biot discovered that solutions of sugar, camphor and tartaric acid could rotate the plane of linearly polarised light. The two enantiomers of a molecule are said to have opposite absolute configurations, and they will generate an optical rotation which is equal in magnitude but opposite in sign to one another. As previously stated, the Cahn-Ingold-Prelog priority rules can be used to assign chiral centres as R or S. It is also common to include the sign of the optical rotation associated with the absolute configuration in brackets: for example (*R*)-(+). This optical rotation is commonly measured at the sodium D-line at 589 nm. It is not possible to predict from the absolute configuration of a molecule whether it will have a positive or negative sign of optical rotation. When optical rotation is measured as a function of wavelength it is called optical rotatory dispersion (ORD) [21].

2.3.2 Circular dichroism

Circular dichroism (CD) is the different absorption of left and right CPL. Again, **Figure 2.4 (a)** shows the electric vectors of right and left components in an achiral medium. Differential absorption gives rise to left and right circularly polarised components having different amplitudes, as in **Figure 2.4 (b)** Their recombination gives a polarisation whose electric vector traces out an ellipse, hence the light is then described as being elliptically polarised. The extent of this ellipticity, θ , is used to measure the strength of CD and is measured by the minor and major axes of the ellipse:

$$\theta = \tan^{-1} \left(\frac{E_R - E_L}{E_R + E_L} \right) \quad \text{Equation 2.23}$$

Where E_R and E_L are the magnitudes of the electric field vectors of RCP and LCP respectively.

Light which is perfectly left and right circularly polarised have ellipticity values of $+45^\circ$ and -45° respectively [21], [22].

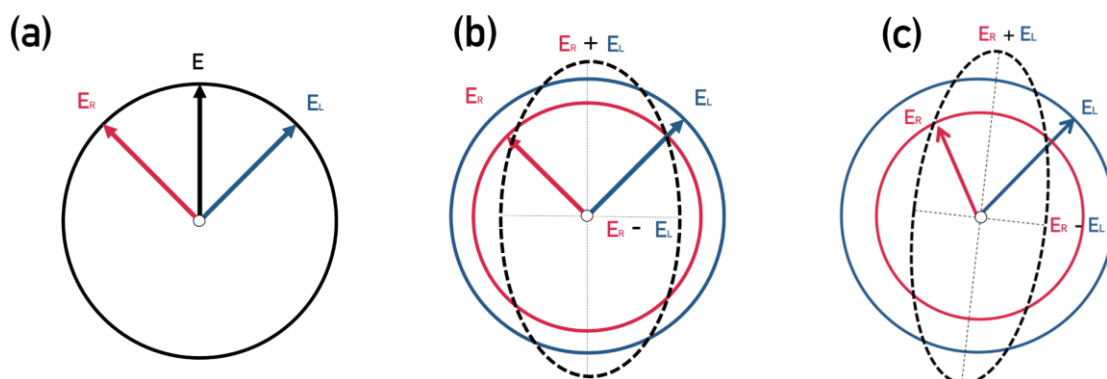


Figure 2.4: Circular dichroism. Propagation of linearly polarised light (a) in an achiral medium. There is no absorption difference between left and right circular components. (b) in a chiral medium where is a difference in absorption between left and right circular components. (c) Optical rotation and circular dichroism happening simultaneously.

Whilst ORD is determined by the real part of the refractive index of a material, CD relates to imaginary part, the extinction coefficient. In general, both the extinction coefficient and the real part of the refractive index is different for LCP and RCP which means that both optical rotation and circular dichroism occur simultaneously, as shown in **Figure 2.4 (c)**. Their relation to the real and imaginary parts of the complex refractive index mean that that ORD and CD spectra are related by the Kramers-Kronig relationship. A bisignate line shape in the optical rotation spectrum will appear as a peak in the ellipticity spectrum and vice versa, **Figure 2.5**. It is hence possible to calculate the ORD spectrum given the CD spectrum. [23].

The ORD spectrum in **Figure 2.5** shows a bisignate line shape, with a positive rotation peak shown near a negative rotation peak. The optical rotation is zero at the position of maximum ellipticity [21]. Collins and colleagues offer an intuitive explanation for this line shape by analogy with a harmonic oscillator. Consider a mass on a spring being driven. For a low energy driving force, oscillations will be in phase with the driving force. At higher energy driving forces, oscillation of the mass will be out of phase. At resonance, the amplitude of the oscillations will be large, and the phase will undergo a 180° transition. In this model, circular dichroism and optical rotation correspond to the amplitude and phase of the oscillator, respectively. This arises because CD relates to the absorption coefficients of CPL which causes differential absorption and ORD relates to the phase velocities of CPL.

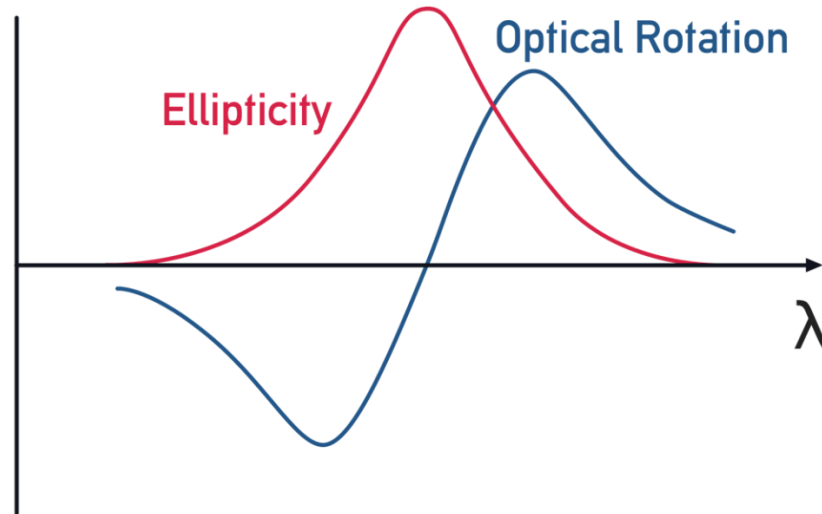


Figure 2.5: Optical rotation spectrum and the corresponding expected ellipticity spectrum. Reproduced from [21].

2.4 Plasmonics

Plasmonics has provided researchers with a great opportunity for the confinement and enhancement of light with metallic nanoparticles [24]. The applications of plasmonics are rich and varied and have included the photo-thermal ablation of cancer tumours in rats [25], the creation of dynamic plasmonic colour displays [26] and the development of sensors for the detection of TNT [27] amongst others. Here, a short introduction to plasmonic theory is given.

2.4.1 Dielectric function of metals

The optical properties of materials can be described by their dispersive (i.e. wavelength dependent) complex dielectric function at a given frequency (ω) which take the form:

$$\varepsilon(\omega) = \varepsilon_1(\omega) + i\varepsilon_2(\omega) \quad \text{Equation 2.24}$$

Here, the real part ε_1 corresponds to the permittivity of the material (its polarizability) and the imaginary part ε_2 describes the dissipation of energy by the material [24]. In some cases, the real part is expressed as ε_r and the imaginary part is expressed as ε_i [28].

The dielectric function of metals can be modelled by the Drude-Sommerfield model, which describes metals as positive ions fixed in a crystal lattice with freely mobile conduction electrons surrounding them. This model ignores any electron-electron interactions, treating conduction electrons as a gas which can be displaced from its rest position by an electric field. The dielectric function can be derived by solution of an oscillating electron's equation of motion with the appropriate conditions and yields the following expression:

$$\epsilon_{Drude} = 1 - \frac{\omega_{p,Drude}^2}{\omega^2 + \gamma^2} + i \frac{\gamma \omega_{p,Drude}^2}{\omega(\omega^2 + \gamma^2)} \quad \text{Equation 2.25}$$

where γ Damping constant
 ω Frequency

and where $\omega_{p,Drude}$ is the plasma frequency given by [29]:

$$\omega_{p,Drude} = \frac{ne^2}{\epsilon_0 m} \quad \text{Equation 2.26}$$

where n density of free electrons in the metal
 e electron charge
 ϵ_0 vacuum permittivity
 m mass of an electron

The modelled real and imaginary parts of the dielectric function of gold is shown in **Figure 2.6 (a)** calculated using the appropriate parameters [30].

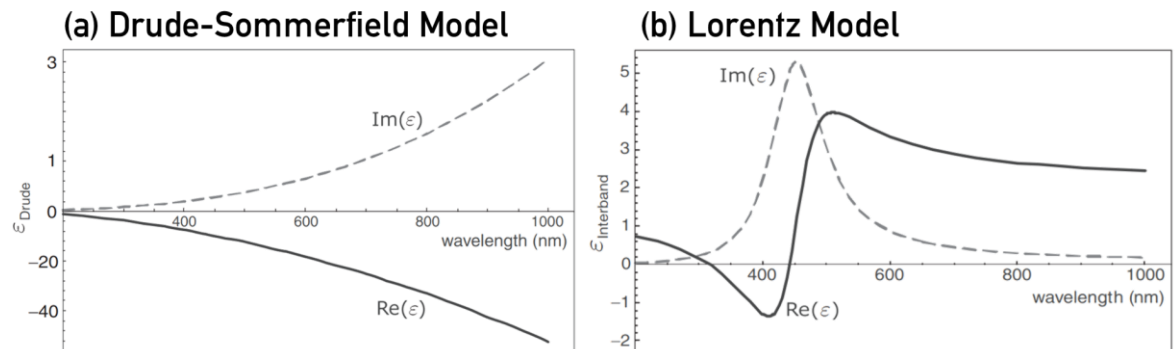


Figure 2.6: (a) Drude-Sommerfield model showing the real and imaginary parts of the dielectric function of gold. (b) The Lorentz model showing the same. Reproduced from [31][30].

The dielectric function described by the Drude-Sommerfield model is only adequate above the wavelength threshold where transitions between electronic bands occur, promoting bound electrons into the conduction band. For example, for gold, at ~550 nm the imaginary part of the dielectric increases much more

than is predicted by the Drude-Sommerfeld model due to promotion of electrons in low lying d-bands into the sp conduction band [30]. If this is accounted for, as in the Lorentz model, then the dielectric function becomes [19], [30]:

$$\varepsilon_{Lorentz} = 1 + \frac{\omega_{p,Lorentz}^2(\omega_0^2 - \omega^2)}{(\omega_0^2 - \omega^2)^2 + \gamma^2\omega^2} + i \frac{\gamma\omega_{p,Lorentz}^2\omega}{(\omega_0^2 - \omega^2)^2 + \gamma^2\omega^2} \quad \text{Equation 2.27}$$

$$\omega_0 = \sqrt{\frac{\alpha}{m}} \quad \text{Equation 2.28}$$

$$\omega_{p,Lorentz}^2 = \sqrt{\frac{\tilde{n}e^2}{(m\varepsilon_0)}} \quad \text{Equation 2.29}$$

where α Spring constant (which keeps electrons in place)

\tilde{n} Density of bound electrons

The modelled real and imaginary parts for the dielectric function of gold calculated by the Lorentz model is shown in **Figure 2.6 (b)**. Its real part shows resonance behaviour and is negative at its minimum values.

2.4.2 Localised surface plasmon resonance

Consider first a nanoparticle with dimensions that are much smaller than the wavelength of visible light. Simply, it can be considered a positively charged core surrounded by an electron gas. When a plane-polarised electromagnetic wave irradiates the nanoparticle, the oscillating electric field drives the electrons to deviate from their equilibrium position, as in **Figure 2.7**. The positive nucleus acts as a restoring force, attracting the electrons back to their equilibrium position. When the frequency of this oscillation matches the wavelength of the incident wave, it known as the localised surface plasmon resonance and is characterised by strong absorption and an enhancement of electric field around the nanostructure [32], [33].

For a nanosphere, the extinction cross section, which accounts for scattering and absorption is given by the following expression:

$$C_{ext} = \frac{24\pi^2 R^3 \varepsilon_m \left(\frac{3}{2}\right)}{\lambda} \left[\frac{\varepsilon_i}{(\varepsilon_r + 2\varepsilon_m)^2 + \varepsilon_i^2} \right] \quad \text{Equation 2.30}$$

where

C_{ext} Extinction cross section

R Radius of the sphere

ε_m	Relative dielectric constant of the surrounding medium
ε_r	Real part of the dielectric function
ε_i	Imaginary part of the dielectric function
λ	Wavelength

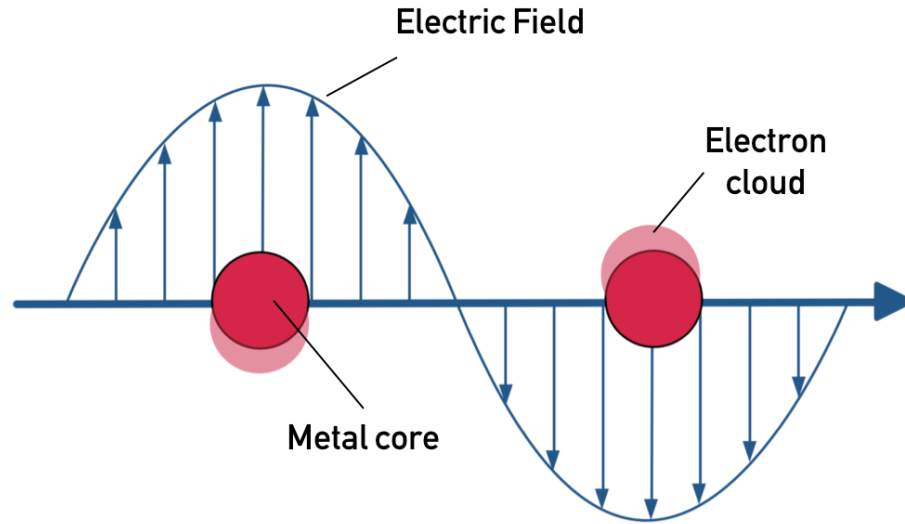


Figure 2.7: Schematic diagram showing localised surface plasmon resonance. The electric field displaces the electron cloud surrounding the metal. Reproduced from [32].

The implication of **Equation 2.30** is the extinction cross section of a metal nanoparticle is highly dependent upon its material properties, ε_r and ε_i . It reaches its maximum when the denominator of the bracketed term approaches zero. For this to occur, ε_r must be close to $-2\varepsilon_m$ [28]. This is the resonance condition for metal spheres, also called the Fröhlich condition [34]. There are different resonance conditions for different metal geometries [33].

The Fröhlich condition is not met for dielectrics and non-metals which typically have ε_r values between 1 and 50 in the optical regime [35]. **Equation 2.30** also implies that ε_i should be as close to zero as possible, with larger values resulting in weaker or lossier plasmons. For visible wavelengths gold, silver and copper are good candidates for supporting localised surface plasmon resonances. Practical considerations are also important. Based solely on its material properties, lithium should be as good as gold or copper for plasmonic applications, but it is not considered due to its high reactivity [28].

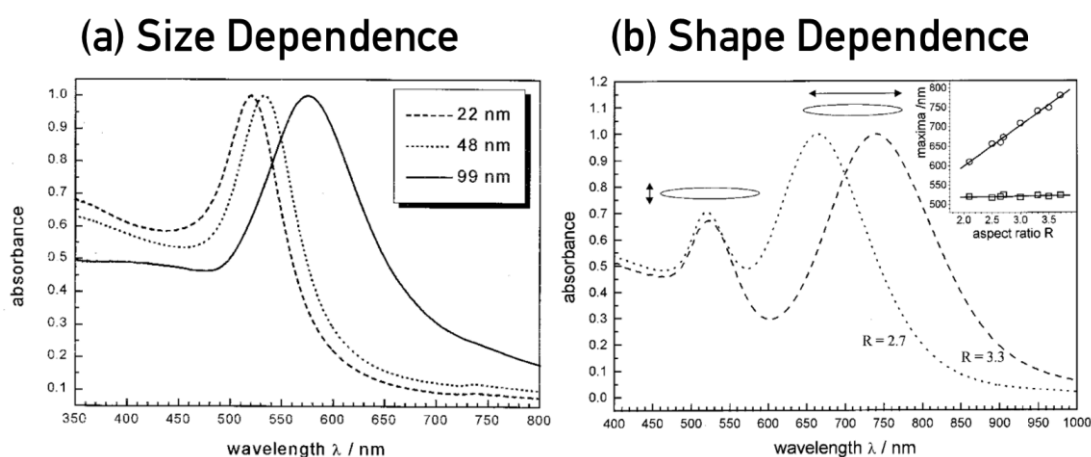


Figure 2.8: (a) Absorbance spectra for 22, 48 and 99 nm Au nanoparticles. The resonance position red shifts as the particles become larger. (b) Absorbance spectra for gold nanorods with increasing aspect ratio. The longitudinal surface plasmon resonance band red shifts as aspect ratio increases. The inset shows the position maxima of the longitudinal (circles) and transverse (square) modes. Reproduced from [36].

The position of the plasmonic resonance is sensitive to the size and shape of the nanoparticle. Link and El-Sayed demonstrated this simply by measuring the absorption spectrum of gold spherical nanoparticles with increasing diameters, observing a red shift as the particle size became larger, **Figure 2.8 (a)**. The absorbance spectra of ellipsoid nanoparticles with increasing aspect ratio (the length of the long axis divided by the short axis) was subsequently measured. In this case, as the aspect ratio increased, the mode associated with the longitudinal plasmon shifted to the red [36]. These simple examples illustrate the plasmonic size and shape dependence. There are of course now thousands of examples of interesting nanoparticle geometries not limited to the sphere or rod: some are presented in **Figure 2.9**.

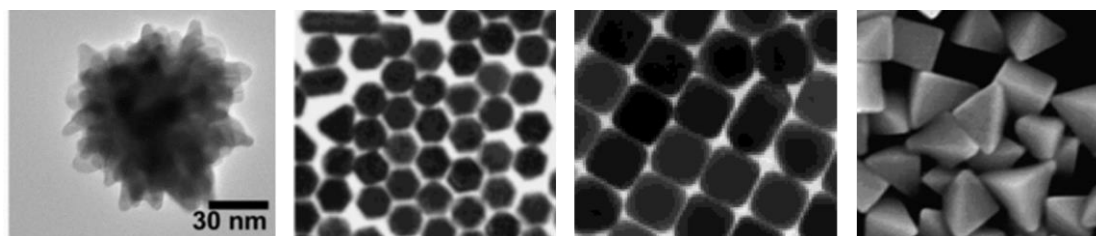


Figure 2.9: Some interesting nanoparticle geometries. Reproduced from [37]–[39]

As well as being sensitive to the size and shape of the nanoparticle, the LSPR position is particularly sensitive to the refractive index of the material which surrounds it. Increasing the refractive index results in a shift of the resonance to the red. Strategies which rely on this phenomenon have allowed

for the development of sensors for the detection of TNT [27], antibodies [40], conformational changes in proteins [41] amongst others.

The creation of intense near-fields by plasmons, so called ‘hotspots’ around the nanoparticle been shown to catalyse reactions [42] and increase photochemical yields [43]. Such hotspots are also responsible for the enhancement factors of $\sim 10^{10}$ reported for surface enhanced Raman scattering (SERS), allowing for the detection of single molecules on rough metal surfaces [44], [45].

2.5 Chiral plasmonics

There are now numerous examples of plasmonic systems which are chiral with many different design approaches employed to construct them [23]. We will limit this discussion to only two approaches.

The first approach is the assembly of achiral nanoparticles into a handed structure. Hentschel and colleagues describe two possibilities for this, by analogy with molecular systems. Configurational chirality is derived by arranging identical particles in a handed fashion. For nanoparticles which are identical in their size and shape, the minimum number of nanoparticles required to create a chiral system is four [23]. Compare this with constitutional chirality where differently sized particles are arranged in an unhanded geometry, such as a tetrahedron. Direct comparison can be made with the latter and the stereogenic centre that is often described in chemistry [46]. For non-spherical particles it is possible to create a chiral system using only two achiral components. The classic example of this is a pair of stacked nanorods, as shown in **Figure 2.12**.

The second approach is to use a single nanoparticle which has a chiral geometry. Even fabricated spherical nanoparticles to some extent can be described as chiral due to nonuniform defects on their surface, although their chiroptical effects are very weak [23]. Fan and colleagues studied chiral gold nanocrystals of varying geometries which exhibited large circular dichroism effects in the visible spectrum [47]. Advances in lithographic fabrication techniques has allowed for the creation of so-called 2D or planar chiral systems.

A low-symmetry planar nanoparticle still theoretically possesses planar symmetry and so is not considered a chiral object. It can be lifted from its substrate and rotated to become superimposable upon its own mirror image. In

practice however, there are two mechanisms by which the symmetry of the structure is broken.

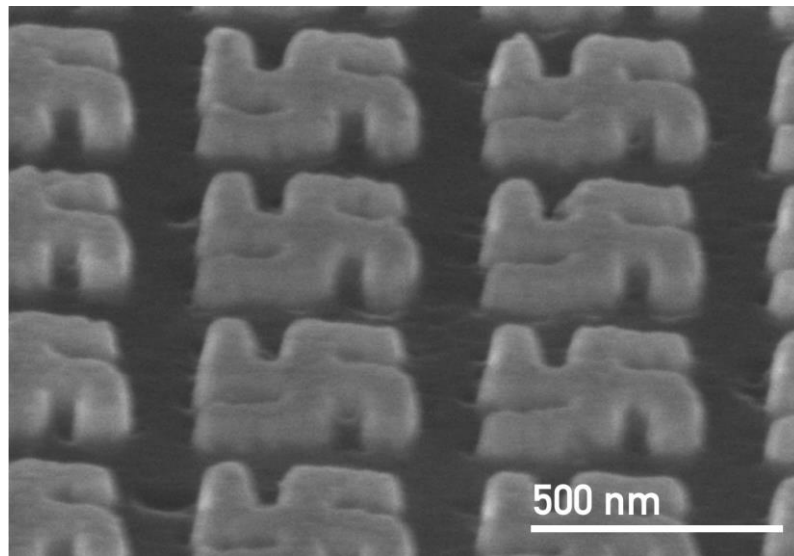


Figure 2.10: SEM of a gammadion array taken from an oblique angle showing dissymmetry of the side profile. SEM taken by Kensaku Endo, Osaka Prefecture University.

The first is that the fabrication of the nanoparticles does not produce perfectly planar structures. **Figure 2.10** shows an SEM image taken at an oblique angle of an array of right-handed ‘gammadion’ nanostructures. They show sloping of their side walls, a defect which has been shown to be sufficient to render the structure chiral [48]. Secondly, if the nanostructures are fabricated upon a glass substrate, the top surface of the nanostructure is a metal-air interface and the bottom surface is a metal-glass interface, a difference sufficient to break the symmetry of the system [49].

2.5.1 Chiroptical effects in chiral plasmonics

Valev [50] provides an intuitive picture of chiroptical effects in chiral nanostructures. Consider first an achiral nanoparticle interacting with linearly polarised light, as in **Figure 2.11 (a)**. A localised surface plasmon will arise, as described in previous sections. If, as in **Figure 2.11 (b)** the incident light is circularly polarised, the surface plasmon will follow a helical path. Now consider a nanoparticle helix. One hand of the enantiomorphs will accommodate the helical plasmon which is generated, whilst the other will be mismatched, **Figure 2.11 (c-d)**. This illustrates the basic premise of chiroptical effects in

chiral plasmonic nanostructures, a differential interaction with circularly polarised light.

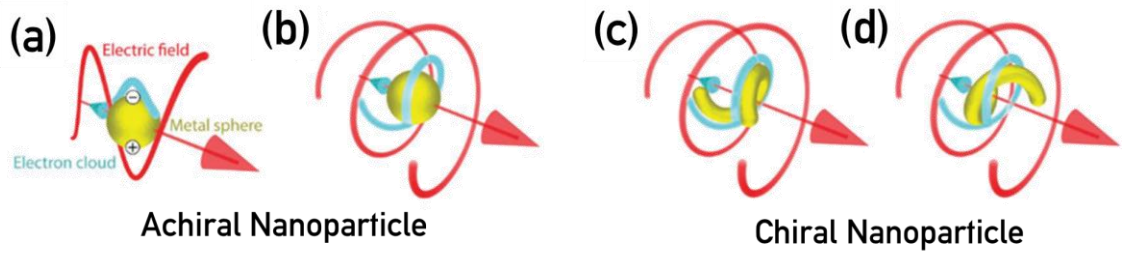


Figure 2.11: (a) Linearly polarised light interacts with an achiral nanoparticle causing LSPR. (b) If the incident light is CPL, the surface plasmons follow a helical shape. (c) A chiral nanostructure geometry can accommodate the helical plasmon which yields a strong interaction. (d) Mismatch between the chiral nanostructure and the plasmonic helix causes a weak chiroptical interaction. Reproduced from [50].

The plasmonic chiral structures described exhibit strong interactions with CPL and produce chiroptical effects which are much larger than in naturally occurring molecules. This is in part due to a much more comparable length scale between nanostructures and the wavelength of light than that of molecules which are orders of magnitude smaller [23].

Giessen and colleagues [51] have developed a chiral plasmonic analogue of the classical Born-Kuhn model of optical activity. They replace the coupled oscillator with the simple chiral system mentioned previously: two nanorods stacked vertically which have a 90° angle between them, **Figure 2.12 (a)**. The collective excitation of electrons can be approximated as a harmonic oscillator with coupling between the two resonators being mediated by near-fields. A vertical spacing d corresponds with a $\pi/2$ phase difference between the oscillators due to phase retardation effects. Incident y -polarised light can propagate along the $-z$ direction and excite the top nanorod. The bottom rod is excited due to its coupling to the top, causing the electric field which is associated with both the upper and lower oscillators to follow a helical path.

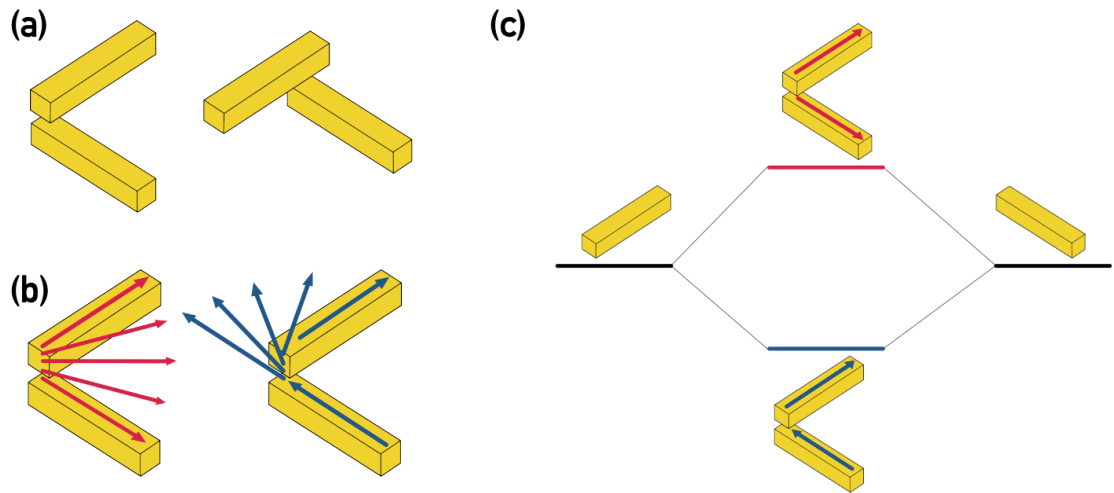


Figure 2.12: Plasmonic Born-Kuhn Model. (a) Nanorods stacked at 90° to one another. The left and right stacks are enantiomorphs of another. (b) Interaction between RCP (red) and LCP (blue) with the stacked nanorods. (c) Energy diagram for the in phase and out of phase excitation of the stacked nanorods. Reproduced from [51].

The same system can be used to probe the interaction of one enantiomorph of the chiral plasmonic systems with left and right CPL. It is assumed that the electric vector of the light is aligned with the top nanostructure when it is excited. If the light is right (left) handed, then the tip of the electric vector will trace out a clockwise (anticlockwise) helix as it propagates. The $\pi/2$ phase difference causes the electric vector to align with the bottom nanorod. Right-CPL excitation causes the electron oscillations at the nanorods to be in phase at all times, whereas excitation with left-CPL will cause charge of opposite sign to accumulate at the stacked corner **Figure 2.12 (b)**. The in-phase excitation is non-favoured and can be considered an anti-bonding mode which is higher in energy than the out of phase bonding mode, **Figure 2.12 (c)**. This explains why the transmission resonance positions of a chiral system are found at different positions for left and right CPL. The mirror image enantiomorph of the chiral nanorod system will give swapped bonding and anti-bonding modes. Practically, the Born-Kuhn system is a sub-system of more complex chiral geometries and can appear multiple times. The nanorods do not have to be stacked at their corners only to show asymmetric transmission and the angle between them is not constrained only to 90° . This model is suitable for simple structures, but can break down with increasing complexity and increasing number of coupled plasmonic modes [34].

It should be noted that experimentally, circular dichroism is usually measured by alternately illuminating the sample using oppositely handed CPL and calculating the difference in transmission. Arteaga and colleagues have contended that that it is only appropriate to describe a sample which generates

a signal using this method as ‘optically active’ if the chiral medium is isotropic. This is because in an isotropic medium, such as solution of molecules, the circular polarisation of the incident light is preserved. Nanostructures do cause depolarisation of the beam; thus it is more appropriate to discuss the effect as an asymmetric transmission of circularly polarised light. Arteaga describes suggests the use of Mueller matrix polarimetry in cases where more information about polarisation states of the beam is required [48], [52], [53]. For the applications discussed in this thesis, this is not required but is interesting to keep in mind.

2.6 Chiral metamaterials

Plasmonic metamaterials are an exciting new frontier in science at the intersection of physics, chemistry, engineering and material science. Their properties are not solely determined by the atoms and bonds which constitute the material, but by the size and spacing of periodic plasmonic metal nanostructures on their surface. The interaction of these sub-wavelength elements with light produces effects which are unseen in nature: negative refractive indices [54] and invisibility cloaking [55] amongst others. Advances in fabrication methods have given researchers the ability to produce novel designs, starting subareas of research within this field [56]. If the elements that constitute are made chiral, then the system can be described as a chiral metamaterial.

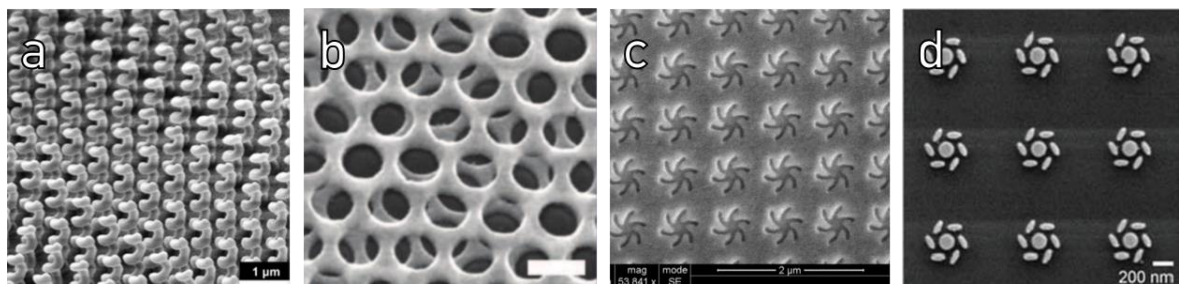


Figure 2.13: Examples of chiral metamaterials. (a) Plasmonically active helices [57]. (b) Moire chiral metamaterials [58]. (c) Pseudo 2D chiral shurikens. (d) Pseudo 2D chiral heptamers [59].

There are numerous ways to design a metamaterial whose constituent elements are chiral. The most conceptually simple chiral elements are three-dimension helices which extend from a substrate, as in **Figure 2.13 (a)**. They have a determined handedness depending upon whether they rotate clockwise or anti-clockwise when viewed from above but are among the most difficult to

fabricate. **Figure 2.13 (b)** shows a metamaterial whose fabrication is easier: it consists of two layers of nanohole arrays. When the two layers are rotated with respect to one-other, the arrangement becomes chiral. **Figure 2.13 (c)** and **(d)** are examples of aforementioned planar metamaterials. These designs can be more easily realised using conventional electron-beam lithography than three-dimensional systems and allow for the creation of nanostructures with interesting and unique morphologies.

In this next section, two metamaterial designs are outlined along with their fabrication strategies. In this thesis, the applications of chiral metamaterials for sensing of chiral materials and active plasmonics is explored.

Chapter 3

Fabrication of chiral metamaterials

In this work, there are two nanostructure arrays under consideration. These differ both in their geometry and method of fabrication. In this chapter, the respective fabrication processes for each of these arrays will be discussed.

3.1 Gammadion structure fabrication

The aim of the gammadion nanostructure fabrication is conceptually simple: to produce an array of gold nanostructures which extend out from a quartz slide substrate, as in **Figure 3.1**.

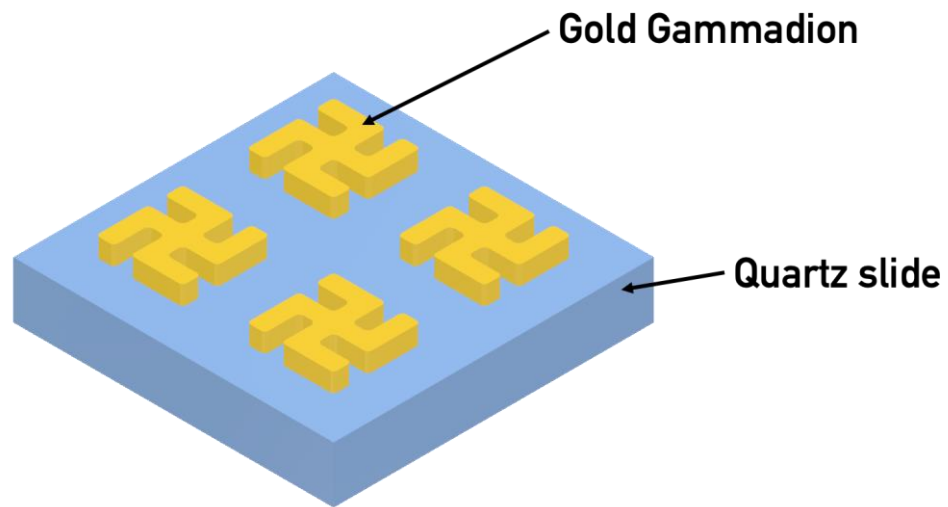


Figure 3.1: The desired outcome from the fabrication of the gammadion array, an array of gold nanostructures on a quartz slide.

The gammadion nanostructures are produced using electron beam (e-beam) lithography in the James Watt Nanofabrication Centre (JWNC) at the University of Glasgow. The JWNC contains a cleanroom within which nanofabrication of the nanostructures occurs. The ISO definition of a cleanroom is as follows [60]:

“A room in which the concentration of airborne particles is controlled, and which is constructed and used in a manner to minimize the introduction, generation and retention of particles inside the room, and in which other relevant parameters, e.g. temperature, humidity and pressure, are controlled as necessary”

A cleanroom is required to prevent contamination of the samples with undesired particles. This is achieved primarily by supplying the cleanroom with filtered air, which serves two purposes. The first is to dilute any particles which

personnel or equipment might shed. The second is to create positive pressure within the cleanroom to ensure that the flow of air only exits the cleanroom, not enters it.

Electron beam lithography is used to write the desired pattern because it confers several advantages over photon-based fabrication techniques including no requirement for expensive photomasks and, crucially, the ability to write high-resolution sub-10 nm lines due to the development of beam focusing optics. This comes at a cost of low throughput and high cost. The principle of e-beam lithography is, put simply, that a beam of high energy electrons changes the solubility of a ‘resist’ in a desired pattern which can then be removed by a developer and metallised. A schematic of this process is shown in **Figure 3.2**.

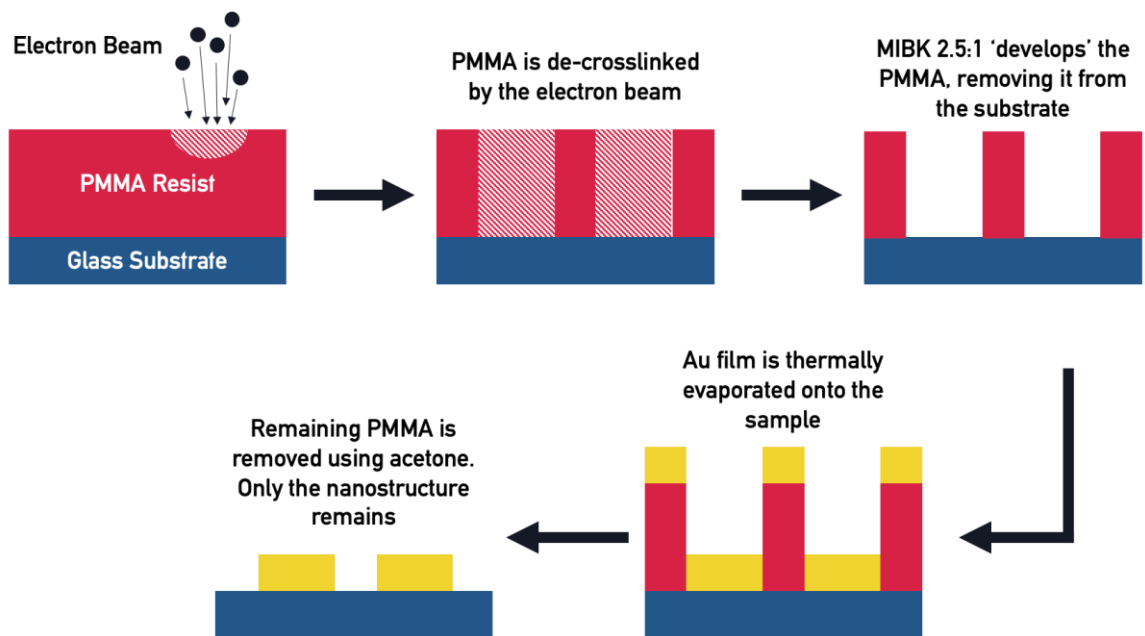


Figure 3.2: Schematic of the electron beam lithography process for the fabrication of gold nanostructures

The goal is to produce patterns with high resolution on a consistent basis; however, there are many parameters which can affect the process including choice of resist, beam dose and size, choice of developer, temperature and time of development and substrate. In this section, the optimised parameters to produce gammadion metamaterials are described.

3.1.1 Sample preparation

Quartz was selected as the substrate material due to its resistance to corrosion, high transmission in optical wavelengths and low cost. To prepare the

25 mm x 25 mm, 1mm thick substrate for subsequent processing, its surface must be thoroughly cleaned. The most common procedure is the acetone-methanol-isopropyl alcohol (AMI) process. The substrate is first submerged in acetone which dissolves most organic contaminants but will leave a layer on the glass surface upon drying. For this reason, the wet substrate is then transferred to methanol, which dissolves the acetone. Finally, IPA is used to rinse off the methanol and additionally, due to its high hygroscopicity, dehydrates the substrate surface. The substrate is dried under a high-speed stream of N₂. Each of the liquid chemical cleaning steps is performed in a megasonic bath for 5 minutes. In the bath, 1-2 MHz acoustic waves create areas of large compression and vacuum bubbles which can dislodge small (~100 nm) particles from the surface which would not ordinarily be removed. After chemical cleaning, any remaining organic contaminants are removed by plasma ashing. High energy metastable oxygen species like O²⁻, O²⁺, O₃, O⁻ and O⁺ are generated by exposing a stream of oxygen gas to high power radio waves. These reactive species bombard the substrate and combine with organic contaminants to generate CO₂ and H₂O which are subsequently removed under vacuum. Cleaning at 100 W for 5 minutes is sufficient at this stage [61].

3.1.2 Resist spin coating

Fundamentally, resists are solutions of molecules which undergo a change in their solubility when ‘exposed’ by electrons from the e-beam patterning tool. There are two classes. Those which undergo a change from high solubility to low solubility are known as negative resists, the most common of which is hydrogen silsesquioxane (HSQ). Here, inelastic collisions of electrons cause the cross linking of short-chain polymers into longer, less soluble molecules which cannot be removed during the development phase.

The second class, and the one which is used exclusively in this work, are positive resists which when exposed to electron beams will become more soluble. Poly-methyl methacrylate (PMMA), shown in **Figure 3.3**, is a popular positive resist which consists of long polymer chains with common masses of 496 and 950 kDa. Exposure to the electron beam causes de-crosslinking of these long chains, increasing their solubility which is exploited in the development stage. The chain lengths of exposed PMMA are dependent upon the beam dosage which is chosen by the user.

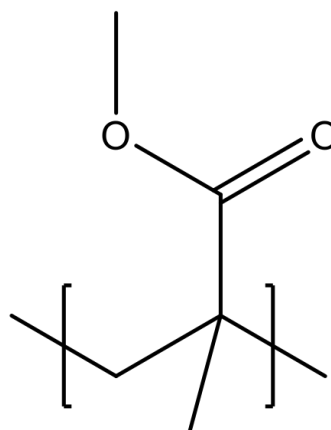


Figure 3.3: Poly-methyl methacrylate (PMMA)

The solvent suspended PMMA liquid resist is deposited upon the glass substrate by spin coating, which allows for control of the layer thickness by changing the speed of rotation and duration of the spin. Resists are spun such that they are three times the thickness of the desired nanostructures (i.e. for 100 nm thick nanostructures, a 300 nm resist layer is required). After being spun, the substrate is then baked in a 180 °C oven for 30 minutes to evaporate the solvent and harden the resist [62].



Figure 3.4: Using only a monolayer of resist results in 'ears' on the finished structure.

Initially in this project, samples were fabricated using a monolayer of resist. This can however lead to an excess of metal being deposited onto the substrate, called 'ears' as depicted in **Figure 3.4**. A bilayer process can improve the resolution of the fabrication and prevent these defects, as depicted in **Figure 3.5**. First, a 200 nm layer of a more sensitive, shorter chain resist solution, namely PMMA 2010, is spun onto the substrate. This is baked and then 100 nm of a less sensitive resist, PMMA 2041, is spun on top of it. After subsequent exposure and development, the resist will form an undercut structure which eliminates the defect-causing 'ears'.

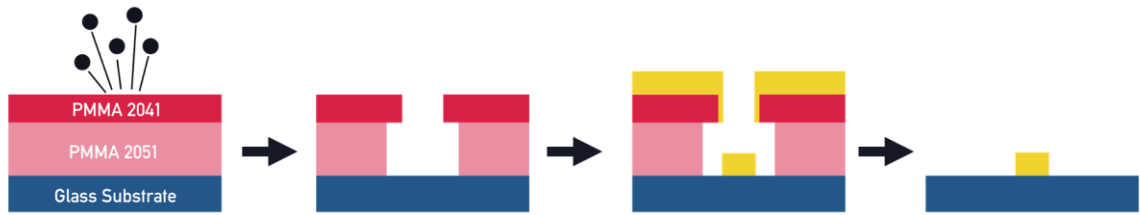


Figure 3.5: A bilayer process can improve the quality of fabrication by preventing the formation of 'ears'.

A comparison of arrays resulting from the monolayer and bilayer processes is shown in **Figure 3.6**. For future reference, it should be noted that the resists offered in the JWNC have now changed.

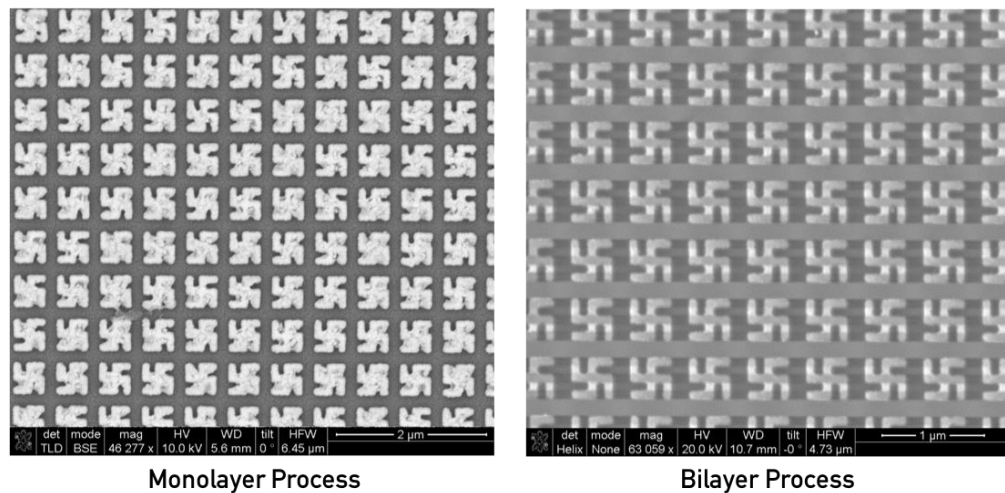


Figure 3.6: SEM images comparing the monolayer and bilayer nanofabrication processes.

If the substrate were a conducting material such as silicon, then the pattern could be written by the lithography tool at this point. A non-conducting quartz substrate will however accumulate charge, leading to overexposure of the pattern. For this reason, it is necessary at this stage to evaporate a 10 nm layer of conducting aluminium before the job is written by the e-beam.

3.1.3 Electron beam writing

The correct dose for the electron beam must be determined by fabricating a 'dose test' sample. These substrates contain ten small sections of the gammadion array, in our case a 100 μm² square which are written with sequentially increasing doses, **Figure 3.7**. This sample can then be imaged with the electron microscope to determine the most suitable process dose. The final

sample is written with this calculated dose. For the bilayer resist, the dose is usually around $800 \mu\text{C cm}^{-2}$.



Figure 3.7: The effect of electron beam dose on gammadion morphology

3.1.4 Development

After exposure of the resist by the e-beam in the shape of the desired pattern, the aluminium layer and de-crosslinked PMMA must be removed during development steps. First, the aluminium conducting layer is removed by a tetramethylammonium hydroxide (TMAH) containing developer, Microposit MF CD-26. This has no effect on the PMMA which must be developed by immersing the substrate in 23°C methyl isobutyl ketone (MIBK) in a 2.5:1 ratio with IPA for 60 seconds followed by a 5 second rinse in IPA.

Development of PMMA resists depends upon the interplay of many factors. Increasing the MIBK concentration will dissolve longer PMMA fragments and hence decrease the resolution of the resultant structures. Excessive time in the developer results in ‘overdevelopment’ which leads to broadening of the structures. It can further degrade the bonding between the substrate and resist in unexposed regions leading to its collapse. Too little time in the developer will not remove the resist, preventing the deposition of the metal. As the dissolving of the resist can be considered a kinetic diffusion process, temperature must be kept consistent for each substrate development [62]

3.1.5 Metallisation and lift-off

Gold is selected for the bulk nanostructure metal due to its chemical inertness in aqueous environments. It does however suffer from poor adhesion to silicate glasses creating the need for adhesion layers. Evaporation of 5 nm of a suitable adhesion layer (titanium, nickel, nichrome) followed by the required thickness of gold is sufficient for strong adhesion [63].

After metal evaporation, the undeveloped PMMA is dissolved by submerging the substrate in 50 °C acetone overnight. The hot acetone is then flowed over the substrate by a Beral pipette to dislodge the metal from the remaining pattern. If the lift-off is unsatisfactory at this stage, then the still submerged substrate can be returned to the megasonic bath. The substrate is then rinsed in IPA and dried under a stream of N₂.

3.1.6 Process summary

A summary of the above process for the fabrication of 100nm structures is shown below:

1. **Chemical clean.** Acetone, Methanol, IPA rinse for 5 mins each under sonication, dry under N₂.
2. **Plasma ash.** 100 W for 1 min.
3. **Spin resist and bake.** For monolayer, PMMA 2010 1 min 3000 rpm followed by 30 min bake. For bilayer, PMMA 8% 2010 1 min 5000 rpm followed by 20 min bake, PMMA 4% 2041 1 min 5000 rpm followed by 30 min bake.
4. **Metallise.** 10nm Al.
5. **Electron beam writing.**
6. **Develop.** CD26 for 1 min. MIBK 2.5:1 for 1 min at 23 °C followed by 20 secs IPA. Dry under N₂.
7. **Metallise.** 5nm Ti, 95nm Au.
8. **Liftoff.** Overnight in 50 °C acetone, perturb with pipette. Rinse with IPA then dry under N₂.

3.2 Shuriken structure fabrication

The shuriken structures have different geometries and fabrication methods to the gammadion nanostructures. The primary difference is that instead of gold structures being fabricated on top of a glass substrate, here the shuriken shapes are ‘indented’ into a polycarbonate substrate. They can be called ‘inverse’ structures because in effect they are the inverse of conventional lithography fabricated structures. The indented polycarbonate substrates can be coated with metal, commonly gold, to render the arrays plasmonic, **Figure 3.8**. The fabrication technique employs injection moulding; hence these samples have been called templated plasmonic substrates or TPSs. Injection moulding

confers several advantages over electron beam lithography including higher throughput and lower cost.

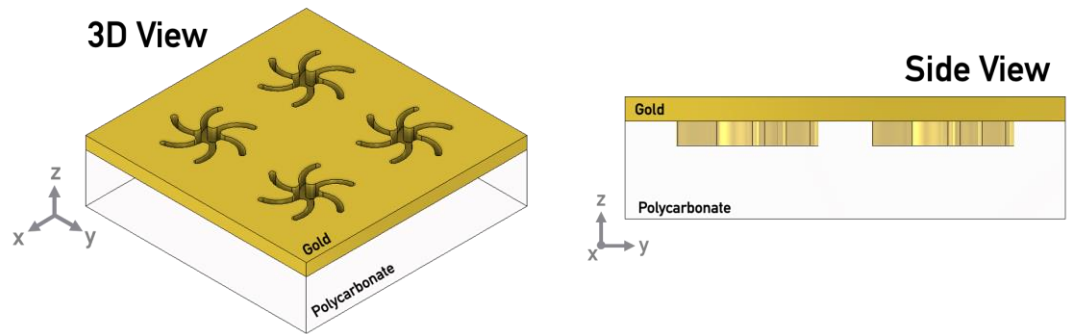


Figure 3.8: The desired outcome from the fabrication of the shuriken templated plasmonic substrates.

There are two primary steps in the fabrication of TPSs. First, the fabrication of the master pattern, known as the shim. Second, replication of the master pattern using injection moulding to produce the final substrate. These two steps will be outlined here.

3.2.1 Shim fabrication

The fabrication of the shim master is like that employed in the fabrication of the gammadion nanostructures. A silicon wafer is cleaned using the same protocol as previously described. A PMMA monolayer is spun onto the wafer with a thickness of 100 nm. The substrate is then baked allowing the PMMA to harden. The shuriken nanostructures are written via electron beam writer, then developed using an MIBK 3:1 solution. It is here where the process diverges with conventional fabrication.

A 1 mm thick layer of nickel is electroplated onto the silicon wafer. Nickel is chosen due to its low surface roughness and large thermal conductivity which allows for rapid cooling during the injection moulding process. Acetone is used as a lift off agent to separate the now patterned nickel shim from the silicon wafer. The nickel shim is now patterned with the nanostructures and is ready to be used for injection moulding of the TPSs [64], [65].

3.2.2 Substrate fabrication

The samples are fabricated onto polycarbonate as it can most reliably reproduce the desired features from the nickel shim. The shim is first fitted into

the injection moulder where heated liquid polycarbonate is subsequently floated over the nanopattern at high pressure. The polycarbonate cools and solidifies, after which the plate is retracted and the TPS is retrieved. Using this method, a substrate can be produced every 10 seconds [64], [65].

The newly fabricated substrates are then cleaned using methanol and IPA. Note here that acetone will dissolve the polycarbonate samples and should not be used. The samples are then ready to be coated with the metal of choice. In previous work, gold has been used as the metallisation layer, however in this work a tri-layer of platinum, lead zirconate titanate (PZT) and gold is used.

Chapter 4

Methods

4.1 Nanoscale characterisation

Tools which are used to measure and characterise nanoscale devices are as important as fabrication technologies themselves. Any improvement in fabrication performance must be met with a commensurate improvement in tools used to characterise them. The primary use of metrology technologies in this work is to determine whether fabricated structures match the designed patterns. They also allow for the production of accurate models for electromagnetic simulations. The next sections outline these characterisation techniques.

4.1.1 Atomic force microscopy

Atomic force microscopy (AFM) is a scanning probe microscopy. Its alternative name is scanning force microscopy (SFM) because the tool measures the force between a tip and a sample to calculate the morphology of its surface. This force is applied with a sharp triangular tip (2.5 μm in height with a tip radius of 2 nm) attached to a cantilever. The tool measures the vertical and horizontal deflections of the tip as it scans over a substrate by reflecting a laser beam off the cantilever. The position of the reflected beam is measured by a position sensitive photodetector, as in **Figure 4.1**.

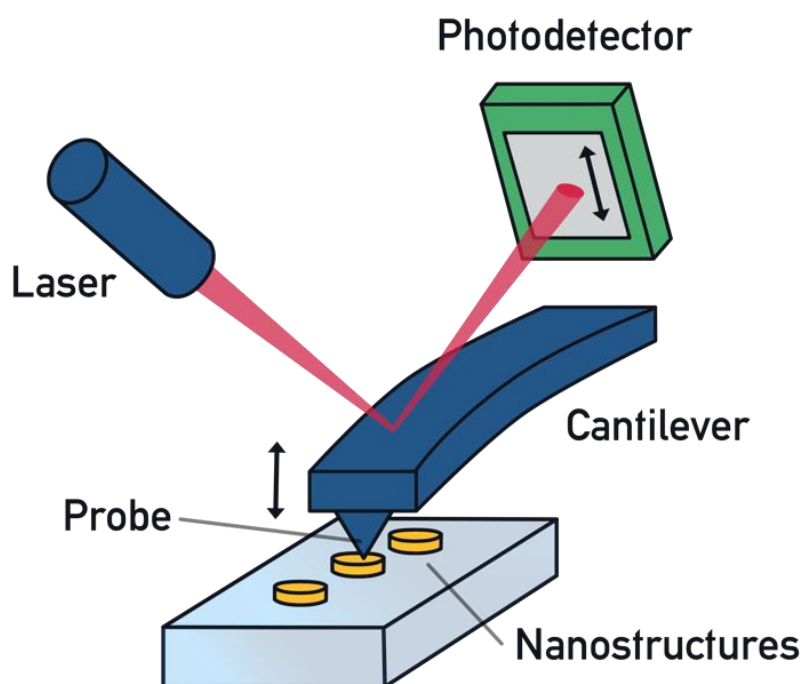


Figure 4.1: Schematic of the operation of an atomic force microscope.

The qualitative relationship between the force and the tip-sample distance is shown in **Figure 4.2**. There are three regimes identified. At large distances from the sample, the force is 0. As the tip gets closer to the sample there is an attractive force between the tip and the sample. At very short distances there is a repulsive force between the tip and the sample.

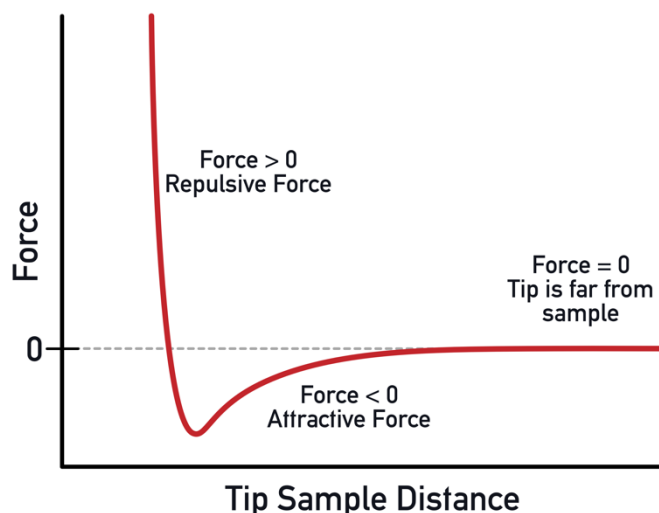


Figure 4.2: Force between the tip and the surface as a function of tip sample distance. Reproduced from [66].

The AFM can function in number of modes of operation. In static mode, the force, and hence the tip-sample distance, is kept constant. The tool changes the z-position of the tip commensurately. The z-position can then be mapped over an area containing the nanostructures under study to produce a topographical map. If the measurements are conducted in the repulsive regime, then this is called contact mode. Contact mode is unsuitable for biological or soft samples where the strong tip-sample interaction can cause damage. In these cases, non-contact mode is utilised. Here, measurements are conducted in the attractive regime of the force curve. The cantilever is excited to its free resonance, then the tip is brought close to the sample. The tool moves the cantilever in the z direction if there is any change to the resonance frequency. Thus, it is possible to measure surface topography without contacting the surface [66]. In this work the samples are sufficiently robust that contact mode can be utilised.

The primary use of AFM in this work is to measure deposited layer thicknesses and to generate topographical maps of the nanostructures which provide information for the generation of models for simulation. **Figure 4.3** shows an AFM micrograph of an array of left-handed gammadion nanostructures. From the raw AFM data, the vertical profile of a plane through the surface can be calculated.

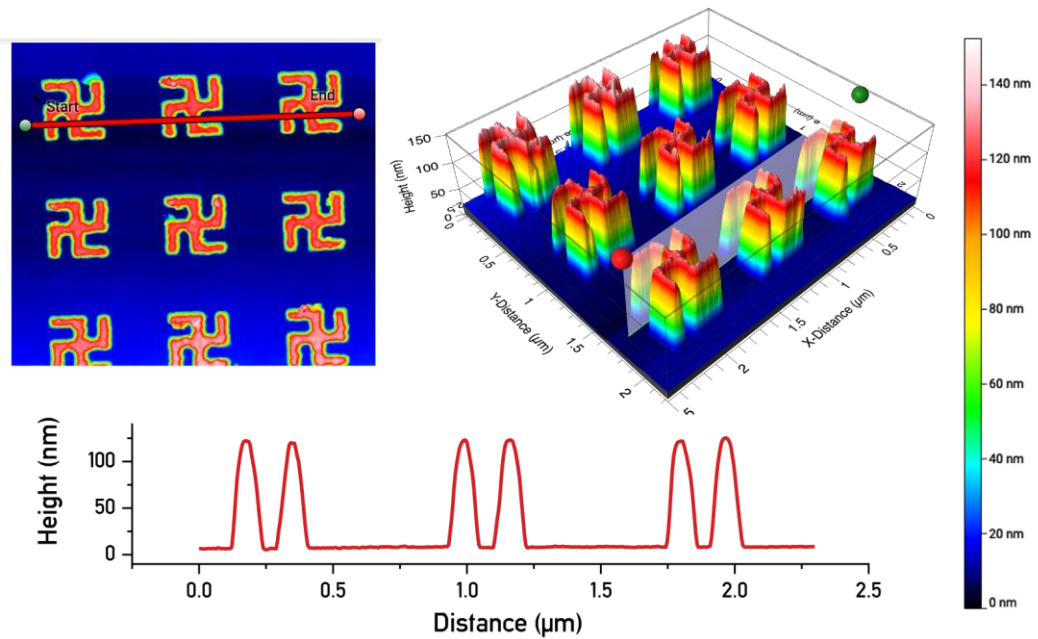


Figure 4.3: Atomic force microscopy can generate topographical maps of the metamaterials. In this example, the vertical profile of a plane (identified in the 2D and 3D profile maps, top) on the surface is calculated (bottom plot)

4.1.2 Scanning electron microscopy

The feature size of the patterns studied here is far smaller than that which can be resolved using optical microscopy and so scanning electron microscopy (SEM) must be utilised.

A scanning electron microscope has a similar configuration to the e-beam tool used to write patterns for nanolithography. A beam of electrons is generated and accelerated towards a sample under high vacuum. Along their path, they are focused using electron optics to a focal point which is 10 nm in diameter, a width one thousandth the original beam size. The beam raster scans over the sample in a rectangular pattern. This positional information is combined with signals detected from surface interactions to generate an image of the surface. There are two primary modes of SEM imaging which depend on two distinct but simultaneously occurring interactions between the electron beam and the sample: secondary electron generation and backscatter electron generation.

A secondary electron (SE) originates from the inelastic collision of the electron beam and the sample. SEs have energies less than 50 eV and upon their expulsion, a majority will be brought to rest within the interaction volume of the sample, typically within two nanometres. SEs which are generated close to the sample surface can escape into the vacuum where they can be detected. The

number of SE detected is combined with the positional information from the raster scan to construct an image of the surface. As the probability of SE escape is greatest near to surfaces, ridges will appear brighter in the image: this is known as the edge effect, as shown in **Figure 4.4**. SE mode is the most common mode for probing the surface of samples.

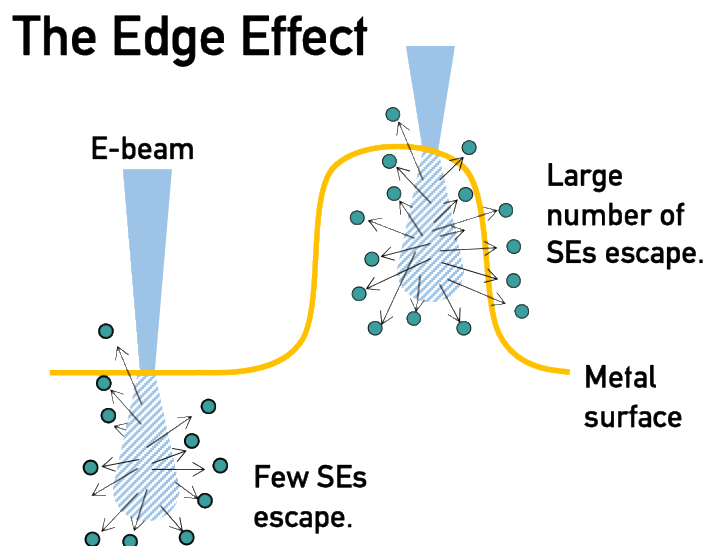


Figure 4.4. Schematic diagram of the edge effect.

Back-scattered electrons (BSE) are scattered elastically through an angle greater than 90 degrees. Elastic scattering only requires a small amount of energy transfer; hence BSEs possess energies very similar to that of the incident beam and can be easily differentiated from SEs. Because of their higher energies, escaped electrons can originate from further within the structure, from 10-100 nm. Furthermore, the extent of back-scattering is proportional to the atomic number of the material, allowing BSE mode to be used as an effective probe of sample composition [67].

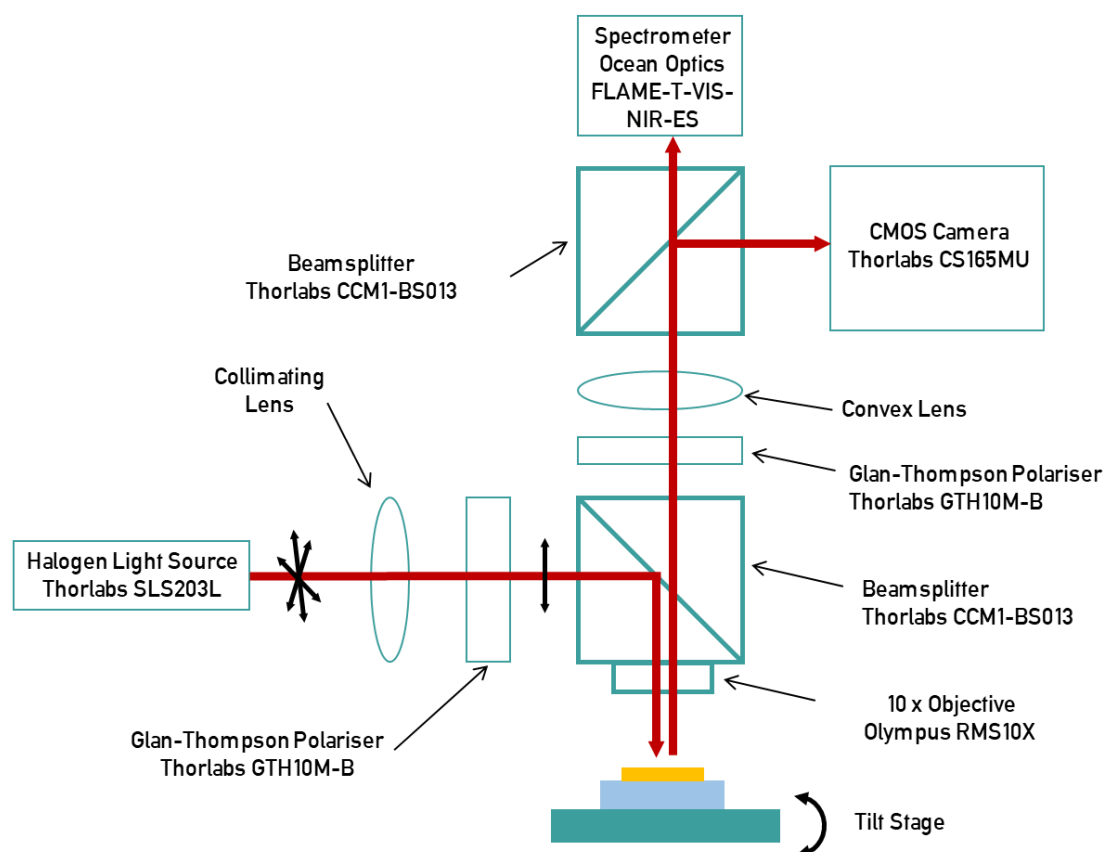
To provide high resolution imaging, it is necessary for the sample under interrogation to be electrically conducting. Insulating substrates accumulate surface charge causing artefacts and poor image quality. There are two approaches to resolve this issue. The first is sputter coating of the sample with a thin (10 nm) layer of an Au/Pd alloy. The alternative is to use the SEM in a lower vacuum mode which allows for the ionisation of gas within the chamber which prevents charging effects. This is used in conjunction with a commercially available 'helix detector' which amplifies the signal by increasing the SE path length (in the shape of a helix).

In this project, most of the SEM images are taken in SE mode using either a FEI Nova 630 NanoSEM or Hitachi S4700 microscope located in the JWNC.

4.2 Spectroscopic measurements

4.2.1 Polarisation microscope

ORD spectra in this work are collected using a custom polarisation microscope as shown in **Figure 4.5**.



Schematic diagram of custom-built reflectance microscope.

Figure 4.5: Schematic diagram of custom-built microscope.

The light source is a 50 W halogen lamp whose unpolarised broadband output then passes through a Glan-Thompson polariser. The now linearly polarised light then passes through a 50:50 beam splitter where the diverted beam passes through a 10 × objective lens with a numerical aperture of 0.3. Light is reflected from the sample and passes through a second polariser and beam splitter to a CCD camera and spectrometer. The field of view of the microscope is approximately 350 x 350 micrometres.

The angle of rotation cannot be directly measured, and so the Stokes method is used. Light intensity at four polarisation angles, (0° , 45° , 90° and 135°) are measured 5 times respectively and averaged. ORD is calculated using the following equation:

$$\text{ORD} = \frac{1}{2} \tan^{-1} \frac{I_{45} - I_{135}}{I_0 - I_{90}} \quad \text{Equation 4.1}$$

where I is the intensity at a given polarisation angles [68]. Arrays of oppositely handed nanostructures will show equal but opposite ORD spectra, as in **Figure 4.6 (top panel)**.

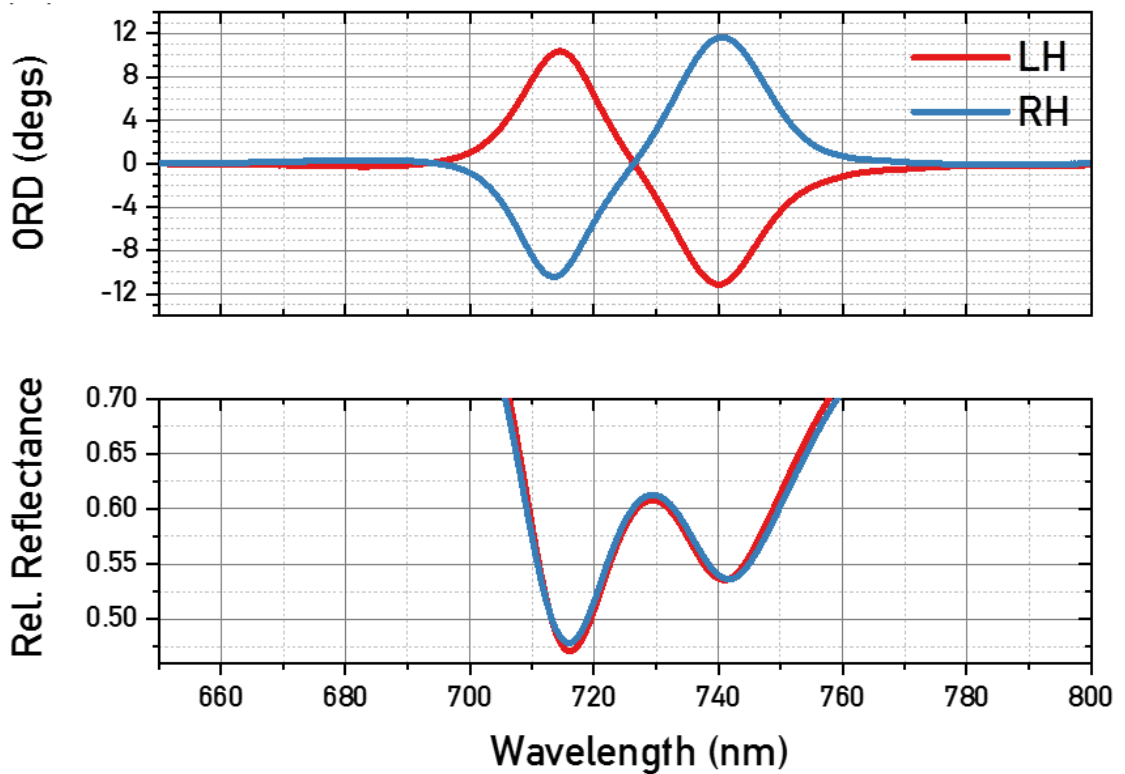


Figure 4.6: Top panel: ORD of left-handed (LH) and right-handed (RH) shuriken structures. They are mirror images of one-another. Bottom panel: Reflectance spectra of LH and RH structures are identical.

Relative reflectance spectra are generated using linearly polarised light and is given by the following calculation:

$$\text{Relative Reflectance} = \frac{\text{Reflectance from nanostructures}}{\text{Reflectance from substrate}} \quad \text{Equation 4.2}$$

A pair of nanostructure enantiomorphs will show identical reflectance spectra, as in **Figure 4.6 (bottom panel)**.

4.2.2 Circular dichroism spectroscopy

Commercial CD spectrometers do not typically measure the ellipticity of the beam directly. Instead they alternately illuminate the sample with left and right CPL and measure the differences in absorbance [48]. Where A_{LCP} and A_{RCP} are the absorbance of LCP and RCP respectively, ellipticity in millidegrees is given by the following expression:

$$CD_{mdeg} = (A_{LCP} - A_{RCP}) \times 32,980 \quad \text{Equation 4.3}$$

Ellipticity measurements for biomolecules are typically small, on the order of 10 millidegrees [22].

The experimental CD spectra in this work are collected using a JASCO J-810 spectropolarimeter. The path of the beam runs horizontally and so a custom-built cell is required to immerse the nanostructured array in liquids. A model of the 3D printed cell is shown in **Figure 4.7**. Liquid can be added to the cell by a needle and syringe through the rubber gasket.

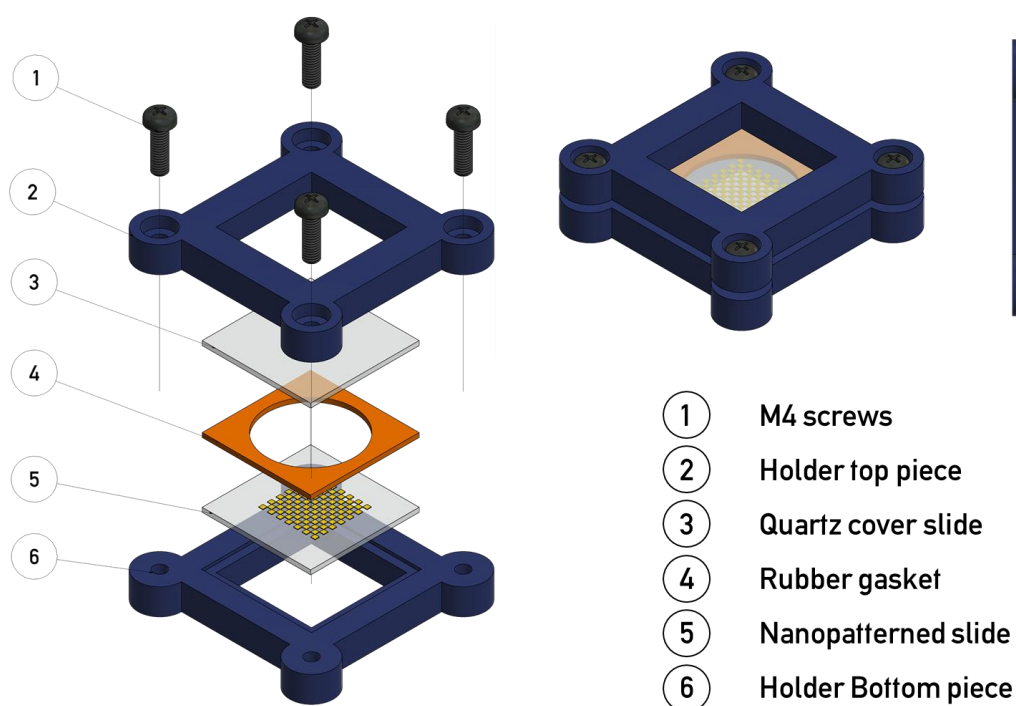


Figure 4.7: 3D printed cell for CD measurements.

4.3 Simulation methods

4.3.1 Finite element method

Increases in computational power and the development of commercially available software has popularised numerical simulation in the field of photonics. Numerical simulations are important because they can provide information which is either difficult or impossible to obtain experimentally. They also reduce the time and costs associated with the optimisation of physical parameters for photonic devices. Several different methods are routinely used including transfer matrix methods, finite-difference-based methods and the method which is utilised in this work, the finite element method (FEM). All solve Maxwell's equations, introduced in **Section 2.1** but it is the decision of the user which is most suitable for their applications [69]. Here, an introduction to the finite element method is given with a discussion of its advantages and disadvantages. Further to this, the general simulating method implemented by COMSOL is described.

The entire modelling domain is initially divided into simply shaped parts called finite elements. These elements can take many different forms, but the most common are the cuboid HEX 8 and the tetrahedral TET 4 elements, shown in **Figure 4.8 (a,b)**. The numbered suffix reflects the number of nodes that the element has, with nodes being coordinates where an approximate solution to the system of partial differential equations is calculated. Tetrahedral elements are commonly used because it is quicker and simpler to 'mesh' a structure (giving rise to the phrase "*TET it and forget it*"). A simulation which uses cuboid elements takes far longer to prepare, but the simulation can take less time to run. Nodes are shared by neighbouring elements, as in **Figure 4.8 (c)**. When two nodes are shared by neighbouring elements then the elements will have a common boundary: the calculated field will be continuous across this boundary [69]. The unknown field can then be expressed by an interpolation (commonly a polynomial function) of values which are calculated at the nodes for each of the elements. These element level equations are then assembled into a global system of equations and boundary conditions are introduced. The solution satisfies each of the local element requirements [69], [70].

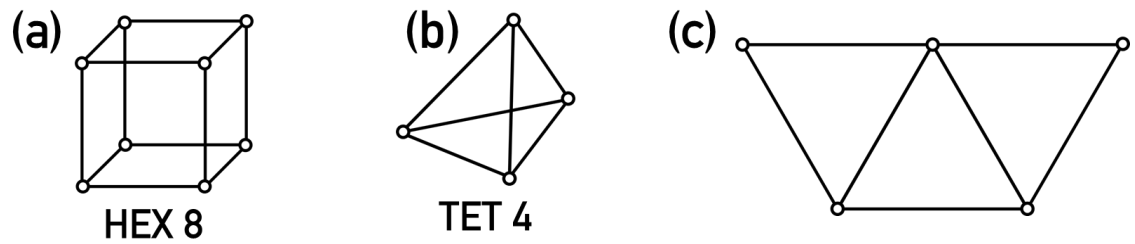


Figure 4.8: The two most common finite element shapes (a) HEX 8 and (b) TET 4. (c) Three triangular elements with common boundaries.

FEM confers several advantages over rival simulation methodologies. Crucially, the solved simulation produces solutions which exist everywhere in the domain. Other strategies, such as the finite difference approach, will only produce solutions at the nodal points, requiring post-processing to generate solutions at inter-nodal positions. The major advantage of FEM over other methods is how well suited it is towards the modelling of complex and irregular geometries. It cannot however provide a closed form solution: the response of the system to changing parameters cannot be assessed after the simulation has run. Additionally, FEM is considered a complex numerical method to implement with many opportunities for user error.

4.3.2 COMSOL simulation strategy

In this work, the software COMSOL Multiphysics is used to implement the finite element method. COMSOL is commonly used in the study of a range of engineering systems including electrodynamics, acoustic, electrochemistry, mechanical and fluid flow applications [71]. In this work, the COMSOL Wave Optics module is used to study the interaction of nanostructures with light. An outline of the COMSOL simulation process used in subsequent sections is outlined here.

The geometry of the nanostructures is constructed using two different methods. In most cases, the nanostructures are designed in a computer aided design (CAD) software, namely Autodesk Inventor. The dimensions of the nanostructures are taken directly from AFM and SEM images then imported into the COMSOL software. In one case in this thesis, the nanostructure geometry is generated directly from an AFM micrograph and imported into COMSOL directly.

The nanostructure is surrounded by a cuboid representing a unit cell with the x- and y- dimensions defining the periodicity of the metamaterial, as

calculated from micrographs. A schematic showing the simulation geometry is shown in **Figure 4.9 (a)**. The z - dimensions of the cell are sufficiently large that near-fields generated by the nanostructures do not extend to any integration surfaces above and below. Iteratively, it has been found that the nanostructure should be no less than $\lambda_{\max}/2$ away from integration surfaces above and below the gammadion. In our case, the total height of the cell is 1600 nm.

Generally, the unit cell is split up into layers of varying thickness. The top 200 nm is a perfectly matched layer (PML) which absorbs all reflections from the nanoparticle. The surface at 200 nm is the excitation port, from where light originates and its polarisation is specified. 100 nm below the excitation port is an integration surface where reflected power is measured. The gammadion is positioned in the centre of the cuboid. 300 nm from the bottom is another integration surface where transmitted power is calculated. 200 nm from the bottom is the radiation exiting port, followed by a 200 nm PML layer. To simulate an array of gammadions, Floquet periodic conditions are applied at the x - and y - boundaries.

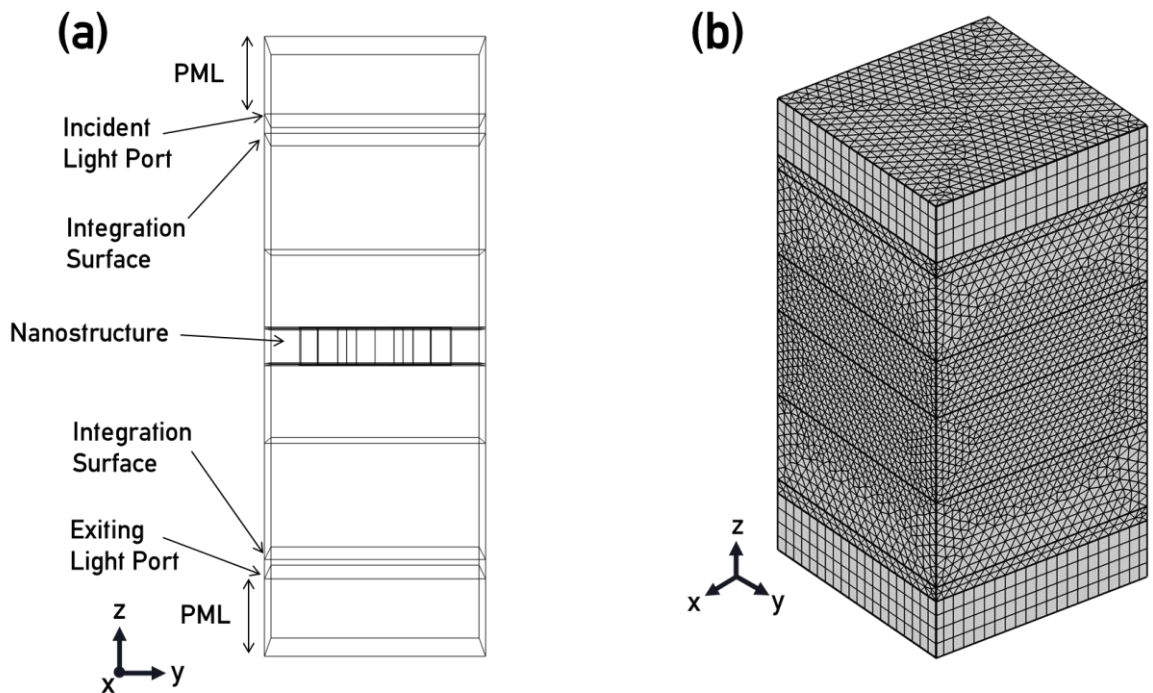


Figure 4.9: (a) Geometry of the simulation with PML, light ports and integration surfaces identified. (b) The geometry after generation of the mesh.

The number of mesh elements which can be used is limited by the computing power available. In this work, this limit is around 400,000 mesh elements per simulation. COMSOL allows for ‘adaptive’ meshing, meaning the size of the mesh does not have to be uniform across the entire geometry of the

simulation. In regions where large changes to the field are expected, the number of mesh elements can be increased. The wavelength and polarisation of incident light is determined by the user. If a wavelength-dependent property is to be calculated, then a wavelength sweep can be implemented across the desired range. If the resolution of this sweep is increased, so too is the time taken for the simulation to run.

Here, a brief outline of the simulation geometry and procedure has been described. In subsequent sections, the relevant simulation strategy and calculated parameters are more thoroughly explained.

Part B

Chiral metamaterials for biological
sensing

Chapter 5

**An introduction to chiral metamaterials for
biological sensing**

In previous chapters, some of the extraordinary properties of arrays of plasmonic elements have been outlined. The focus of the following two chapters is the application of chiral metamaterials, namely arrays of gammadion nanostructures, for biological sensing. **Chapter 6** discusses the CD of the gammadion nanostructure and the effects of geometric and morphological changes to their properties. In **Chapter 7**, the gammadion structure is discussed in terms of its properties as they relate to optical chirality. In this chapter an introduction to optical chirality and its conservation are discussed. This is followed by some examples of existing gammadion metamaterial sensing platforms.

5.1 Optical chirality and conservation

As stated previously, chiroptical effects in naturally occurring materials are weak, with optical rotations typically on the order of thousands of a degree. This occurs because the electric vector of CPL, with wavelengths of hundreds of nanometres in the visible region, undergoes a rotation which is near-imperceptible across the length scale of a molecule. A parameter widely used to quantify the differential absorbance of LCP over RCP light by a system is the dissymmetry factor (g) which measures absorbance of LCP and RCP at a given wavelength [72]:

$$g = \frac{A^{LCP} - A^{RCP}}{\frac{1}{2}(A^{LCP} + A^{RCP})} \quad \text{Equation 5.1}$$

where $A^{LCP/RCP}$ is the absorbance of left and right CPL (LCP and RCP respectively). **Equation 5.1** gives the ratio of CD relative to the conventional absorption of the molecule [21]. Generally, molecular CD signals of chiral molecules are found to be 10^{-6} to 10^{-2} that of conventional absorption [15], [73]. The consequence of this phenomenon is that making meaningful CD measurements requires large amounts of the material under investigation and very sensitive instrumentation. The goal of a good chiral sensor should therefore be to maximise this dissymmetry factor as much as possible. The strategy which is explored here is, put simply to match the helicity of the light to the length scale of the molecule [74].

5.1.1 Optical chirality

In 1964, Lipkin used Maxwell's equations to introduce ten new conservation equations. In his paper he stated [75]:

“This unexpected discovery of a complete set of ten new conservation equations is a source of mathematical embarrass de richesses because of the lack of any ready physical interpretation for the quantities that are found to be conserved.”

Unaware of any physical interpretation of these quantities, he called them zilches. It took until 2010 for Tang and Cohen [15] to identify the physical significance of one of Lipkin's zilches, Z^{000} as a descriptor of the chirality of an electromagnetic field. They called the quantity optical chirality and, in its time-dependent form, is defined as:

$$C = \frac{\epsilon_0}{2} \mathbf{E} \cdot \nabla \times \mathbf{E} + \frac{1}{2\mu_0} \mathbf{B} \cdot \nabla \times \mathbf{B} \quad \text{Equation 5.2}$$

where

- \mathbf{E} Complex time dependent electric field
- \mathbf{B} Time dependent magnetic field
- ϵ_0 permittivity of free space
- μ_0 permeability of free space

The time average form of optical chirality is given by the following expression:

$$\bar{C} = \frac{\epsilon_0 \omega}{2} \text{Im}(\mathcal{E}^* \cdot \mathcal{B}) \quad \text{Equation 5.3}$$

where

- ω Angular frequency
- \mathcal{E} Complex electric field amplitude
- \mathcal{B} Complex magnetic field amplitude

Tang and Cohen hypothesized the inherently weak CD response of chiral molecules could be enhanced by tailoring the optical chirality of the interacting fields. They found that if the optical chirality of the beam is included in the expression for the dissymmetry factor, it becomes [74]:

$$g = g_{CPL} \left(\frac{c\bar{C}}{2U_e\omega} \right) \quad \text{Equation 5.4}$$

where

- g_{CPL} dissymmetry factor under CPL
- c speed of light
- U_e time-averaged electric energy density

ω angular frequency.

The quantity g_{CPL} is purely molecular with the quantity in brackets being a property of the incident electromagnetic field [73]. The most important implication of **Equation 5.4** is that the dissymmetry factor can be enhanced by increasing the field chirality term relative to its value for CPL. If the value of the field chirality term $\left(\frac{c\bar{c}}{2U_e\omega}\right)$ is greater than the corresponding value for that of CPL, the fields are termed *superchiral*.

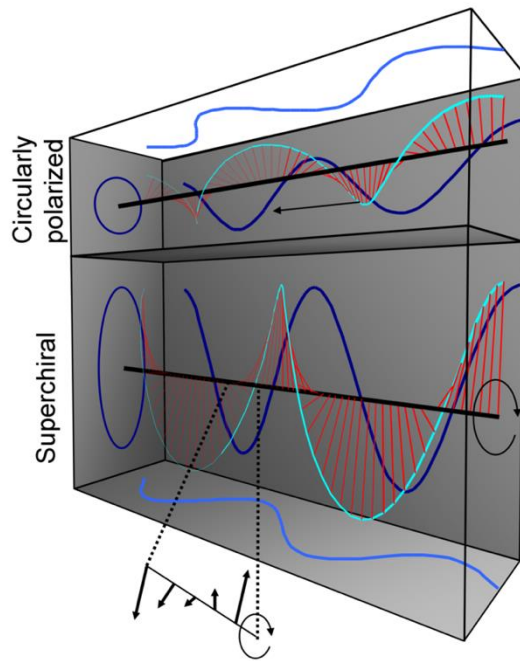


Figure 5.1: The electric vector of superchiral light undergoes a greater sense of twist over shorter length scales than CPL.

Optical chirality can be an intuitively difficult concept to understand. **Figure 5.1**, reproduced from [74] shows, in its top panel, CPL. The field has uniform optical chirality and energy density throughout space. The dark blue lines show projections of the field onto the xy , xz and yz planes at a single point in time and the field vectors rotate at a constant rate along the direction of propagation. By definition, they undergo one full rotation per wavelength. The superchiral field, shown in the bottom panel, rotates around the axis but it does not have a propagation direction because it does not propagate. The field vectors can rotate through 180° in a distance which is much shorter than half the wavelength. In effect, the electric vector of light undergoes a greater sense of twist over shorter wavelengths compared to CPL which is more comparable to the length scale of chiral molecules [74].

There are two general strategies for increasing $\left(\frac{c\bar{C}}{2U_e\omega}\right)$. The first is to decrease, U_e , the electric energy density. This method was favoured by Tang and Cohen who, in their original experiment, generated superchiral light by reflecting CPL off an imperfect mirror. The reflectance of the mirror was measured to be 0.72. The reflection reversed the handedness of the CPL (RCP became LCP and vice-versa), introduced a phase difference between incident light and reflected light and as well as decreasing its intensity. The interference of the two counterpropagating beams generates a standing wave with minimum values of U_e found at its nodes (the point where the wave is at its minimum amplitude). It is hence here where $\left(\frac{c\bar{C}}{2U_e\omega}\right)$ and the dissymmetry factor is at its maximum. They held chiral fluorescent molecules at these nodes and measured their differential emission. They found an approximately 10-fold increase in the dissymmetry factor compared with measurements taken without the superchiral light generation [74]. A more complete discussion of their technique can be found in their original paper [15].

The second strategy to increase $\left(\frac{c\bar{C}}{2U_e\omega}\right)$ is via the incorporation of plasmonic nanoparticles. The evanescent fields that are associated with localised surface plasmon resonances of nanostructures can possess enhanced optical chirality [76]. Initially it was thought that only chiral nanostructures could generate superchiral fields, but it has been shown that achiral nanostructures are also capable of generating fields with enhanced optical chirality [77]. Intuitively, one would assume that in order to maximise the sensing capability of the platform, it is sufficient to fabricate structures which can support the largest value of \bar{C} . This, however, is too simplistic an approach. Chiral nanostructures can exhibit large values of \bar{C} at one particular region or have areas of \bar{C} with opposite sign [78] and it has been shown that measurement of \bar{C} can vary with choice of integration volume or spatial coordinate [79]. Indeed, some structures which are predicted to have near fields with very high local values of \bar{C} can show very weak sensing capabilities [77].

5.1.2 Optical chirality flux

In their seminal paper, Tang and Cohen [15] derive the time dependent equations for optical chirality with respect to optical chirality flux, given by:

$$\frac{\partial C}{\partial t} + \frac{1}{\mu_0} \nabla \cdot \mathbf{F} = -\frac{1}{2} (\mathbf{j} \cdot \nabla \times \mathbf{E} + \mathbf{E} \cdot \nabla \times \mathbf{j}) \quad \text{Equation 5.5}$$

$$\mathbf{F} = \frac{1}{2}[\mathbf{E} \times (\nabla \times \mathbf{B}) - \mathbf{B} \times (\nabla \times \mathbf{E})] \quad \text{Equation 5.6}$$

where \mathbf{j} is the current density. These conservation equations have the same form as the Poynting theorem for the conservation of electromagnetic energy:

$$\frac{\partial U}{\partial t} + \frac{1}{\mu_0} \nabla \cdot \mathbf{S} = -\mathbf{j} \cdot \mathbf{E} \quad \text{Equation 5.7}$$

$$U = \frac{1}{2} \left[\epsilon_0 \mathbf{E} \cdot \mathbf{E} + \frac{1}{\mu_0} \mathbf{B} \cdot \mathbf{B} \right] \quad \text{Equation 5.8}$$

Where \mathbf{S} Poynting Vector
 U Electromagnetic energy density

The Poynting vector, which describes the direction of power flow, is given by the cross product of \mathbf{E} and \mathbf{B} . Put plainly, the Poynting theorem states that energy lost by electromagnetic fields is energy gained by particles and energy flow out of the system or vice versa. Currents within a material can therefore act as a sink or a source of energy [15], [79], [80].

And so, by analogy with the Poynting theorem, the continuity equations for optical chirality suggest that the optical chirality of electromagnetic fields and chiral currents within a material can be interconverted. This interconversion between the chirality of light and chiral surface charge distributions is referred to as the *dissipation* of optical chirality: it occurs through loss (i.e. absorption) and at the interfaces of different materials. [79], [81].

In this work, the time-averaged value of optical chirality flux is calculated and is important in the analyses, so a brief derivation is presented. For this model the terms $\mathcal{E}e^{i\omega t}$ and $\mathcal{B}e^{i\omega t}$ are introduced: the electric and magnetic complex time harmonic fields respectively. Their real parts of each expression are given by:

$$\text{Re}(\mathcal{E}e^{i\omega t}) = \frac{1}{2}(\mathcal{E}e^{i\omega t} + \mathcal{E}^*e^{-i\omega t}) \quad \text{Equation 5.9}$$

$$\text{Re}(\mathcal{B}e^{i\omega t}) = \frac{1}{2}(\mathcal{B}e^{i\omega t} + \mathcal{B}^*e^{-i\omega t}) \quad \text{Equation 5.10}$$

where ω is the angular frequency. Substituting **Equation 5.9** and **Equation 5.10** into the expression for optical chirality flux in free space, **Equation 5.6** yields the following expression for optical chirality flux:

$$\begin{aligned} \mathbf{F} = \frac{1}{2} & \left[\left(\frac{1}{2} (\boldsymbol{\mathcal{E}} e^{i\omega t} + \boldsymbol{\mathcal{E}}^* e^{-i\omega t}) \right) \times \left(\nabla \times \right. \right. \\ & \left. \left. \left(\frac{1}{2} (\boldsymbol{\mathcal{B}} e^{i\omega t} + \boldsymbol{\mathcal{B}}^* e^{-i\omega t}) \right) \right) - \left(\frac{1}{2} (\boldsymbol{\mathcal{B}} e^{i\omega t} + \right. \right. \\ & \left. \left. \boldsymbol{\mathcal{B}}^* e^{-i\omega t}) \right) \times \left(\nabla \times \left(\frac{1}{2} (\boldsymbol{\mathcal{E}} e^{i\omega t} + \boldsymbol{\mathcal{E}}^* e^{-i\omega t}) \right) \right) \right] \end{aligned} \quad \text{Equation 5.11}$$

which upon expansion becomes:

$$\begin{aligned} \mathbf{F} = \frac{1}{8} & \left[\boldsymbol{\mathcal{E}} \times (\nabla \times \boldsymbol{\mathcal{B}}) e^{i2\omega t} + \boldsymbol{\mathcal{E}} \times (\nabla \times \boldsymbol{\mathcal{B}}^*) \right. \\ & + \boldsymbol{\mathcal{E}}^* \times (\nabla \times \boldsymbol{\mathcal{B}}) \\ & + \boldsymbol{\mathcal{E}}^* \times (\nabla \times \boldsymbol{\mathcal{B}}^*) e^{-i2\omega t} \\ & - \boldsymbol{\mathcal{B}} \times (\nabla \times \boldsymbol{\mathcal{E}}) e^{i2\omega t} - \boldsymbol{\mathcal{B}} \times (\nabla \times \boldsymbol{\mathcal{E}}^*) \\ & - \boldsymbol{\mathcal{B}}^* \times (\nabla \times \boldsymbol{\mathcal{E}}) \\ & \left. - \boldsymbol{\mathcal{B}}^* \times (\nabla \times \boldsymbol{\mathcal{E}}^*) e^{-i2\omega t} \right] \end{aligned} \quad \text{Equation 5.12}$$

Given that $2\text{Re}(\mathbf{C} \times (\nabla \times \mathbf{D}^*)) = \mathbf{C} \times (\nabla \times \mathbf{D}^*) + \mathbf{C}^* \times (\nabla \times \mathbf{D})$, Equation 5.12 can be simplified to:

$$\begin{aligned} \mathbf{F} = \frac{1}{8} & \left[2\text{Re}(\boldsymbol{\mathcal{E}} \times (\nabla \times \boldsymbol{\mathcal{B}}) e^{i2\omega t}) + 2\text{Re}(\boldsymbol{\mathcal{E}} \times \right. \\ & (\nabla \times \boldsymbol{\mathcal{B}}^*)) - 2\text{Re}(\boldsymbol{\mathcal{B}} \times (\nabla \times \boldsymbol{\mathcal{E}}) e^{i2\omega t}) - 2\text{Re}(\boldsymbol{\mathcal{B}} \times \\ & \left. (\nabla \times \boldsymbol{\mathcal{E}}^*)) \right] \end{aligned} \quad \text{Equation 5.13}$$

The time averaged optical chirality flux $\bar{\mathbf{F}}$ is found by evaluating the integral:

$$\begin{aligned} \bar{\mathbf{F}} = \frac{1}{8} \frac{1}{T} \int_0^T dt & \left[2\text{Re}(\boldsymbol{\mathcal{E}} \times (\nabla \times \boldsymbol{\mathcal{B}}) e^{i2\omega t}) + \right. \\ & 2\text{Re}(\boldsymbol{\mathcal{E}} \times (\nabla \times \boldsymbol{\mathcal{B}}^*)) - 2\text{Re}(\boldsymbol{\mathcal{B}} \times (\nabla \times \boldsymbol{\mathcal{E}}) e^{i2\omega t}) - \\ & \left. 2\text{Re}(\boldsymbol{\mathcal{B}} \times (\nabla \times \boldsymbol{\mathcal{E}}^*)) \right] \end{aligned} \quad \text{Equation 5.14}$$

$$\bar{\mathbf{F}} = \frac{1}{4} \text{Re}(\boldsymbol{\mathcal{E}} \times (\nabla \times \boldsymbol{\mathcal{B}}^*) - \boldsymbol{\mathcal{B}} \times (\nabla \times \boldsymbol{\mathcal{E}}^*)) \quad \text{Equation 5.15}$$

Poulikakos and colleagues have argued that the flux of optical chirality measured in the far field is a more useful measurable physical quantity for the characterisation of chiral near fields [79], [80]. First, it is proportional to the third Stokes parameter: this is a measure of the polarisation of the beam. Thus, depending upon the calculation method, the optical chirality flux can serve as an indicator of polarisation or depolarisation of light. Furthermore, when the incident light is linearly polarised, maximum optical chirality dissipation occurs when the optical chirality flux is at its maximum. Thus, optical chirality flux in the far field is an indicator of optical chirality dissipation within a material. Poulikakos and colleagues showed that optical chirality flux could serve as a probe of the dominance of either left or right-handed local optical chirality

density in the near field of nanostructures whilst other far field measurements could not necessarily predict this information [15], [79], [80].

5.2 Sensing with gammadion nanostructures

Following Tang and Cohen's work on optical chirality, Hendry and colleagues demonstrated a novel use of chiral metamaterials for the characterisation of biological molecules. They fabricated arrays of left-handed (LH) and right-handed (RH) gammadions on quartz substrates. These arrays showed a strong CD response. When the structures are surrounded by an achiral solution, their CD spectra are mirror images of another: the RH is equal in intensity but opposite in its sign to the LH and vice versa, **Figure 5.2 (a)**. When chiral molecules are placed on top of the gammadion nanostructures, the shift to the CD spectrum is asymmetric, **Figure 5.2 (b)**. This asymmetry is parameterised by $\Delta\Delta\lambda = \Delta\lambda_{RH} - \Delta\lambda_{LH}$ where $\Delta\lambda_{RH/LH}$ is the shift of the CD resonances of the RH/LH array relative to an achiral reference. The technique was shown to be a sensitive measure of the secondary structure composition of protein macromolecules. Proteins which contained a high proportion of β -sheets (concanavalin A, β -lactoglobulin, and outer membrane protein A) exhibited a large and positive $\Delta\Delta\lambda$ whilst proteins which contained a high proportion of α -helices (BSA, myoglobin and haemoglobin) exhibited a much a smaller $\Delta\Delta\lambda$ value, **Figure 5.2 (c)** [82]. Work by the same group using 'shuriken' or star shaped nanoindentations also uses the principle of asymmetry in the chiroptical response for the characterisation of protein [83] and viruses [84].

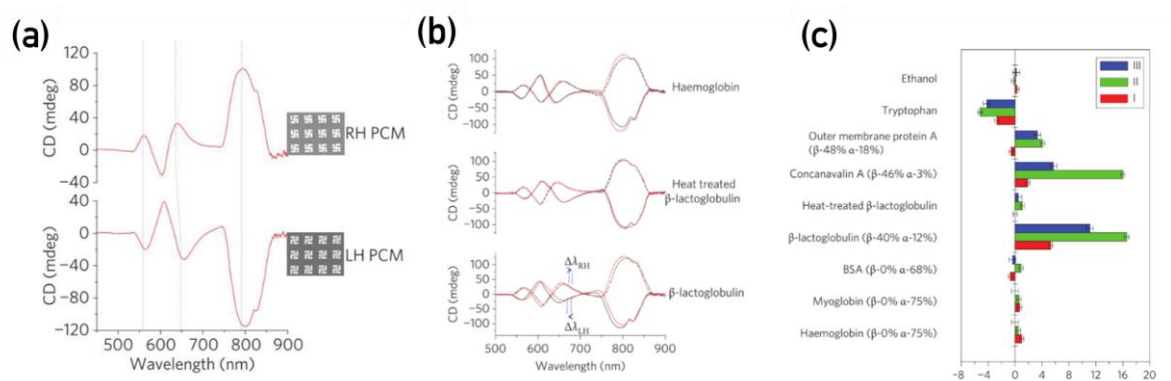


Figure 5.2: 'Superchiral spectroscopy' for the detection of protein composition (a) C.D. of left and right-handed gammadions surrounded by water. An electron micrograph shows the the gammadion structure and periodicity. (b) C.D. of left and right-handed gammadions immersed in haemoglobin, heat treated β -lactoglobulin and β - lactoglobulin. (c) $\Delta\Delta\lambda$ changes for a range of proteins. Reproduced from [82].

There is an argument to be made that the strong CD signals which are generated by the nanostructures can mask molecular signals which are much smaller. With this in mind, García-Guirado and colleagues developed a similar platform to the previous example, but instead of arrays of different handed gammadions, they produced an array which contained a ‘racemic’ mixture of structures. A given area on the sample contains an equal number of LH and RH structures. The result is that the measured CD spectrum is ~ 0 . They subsequently deposited L-phenylalanine (an essential amino acid) onto the substrate. The asymmetric interaction with the differently handed nanostructures was evident in the non-zero CD spectrum produced by the array. When the D-enantiomer of the protein was deposited, the CD signal of the array changed sign, indicating that the platform can be used for enantiomer differentiation [85].

Chapter 6

Morphology and geometry effects in chiral
plasmonic nanostructures

In this chapter, geometric and morphological variations to the gammadion structure which reflect common fabrication defects are investigated. The effect on their CD spectra is investigated experimentally with numerical modelling giving further insight into their local field properties.

6.1 Experimental geometry and fabrication

The nanostructures are fabricated on the face of a $25 \times 25 \times 1$ mm piece of polished quartz glass. Each piece of glass supports one handedness of the structure: (i.e. either LH or RH gammadion enantiomorphs). All of the fabricated structures are 100 nm in height, consisting of 95 nm of gold and 5 nm of nickel chrome (nichrome) to ensure adhesion of the gold to the quartz substrate [63]. The full method for the fabrication of the structures has been outlined previously in **Section 3.1: Gammadion Structure Fabrication**.

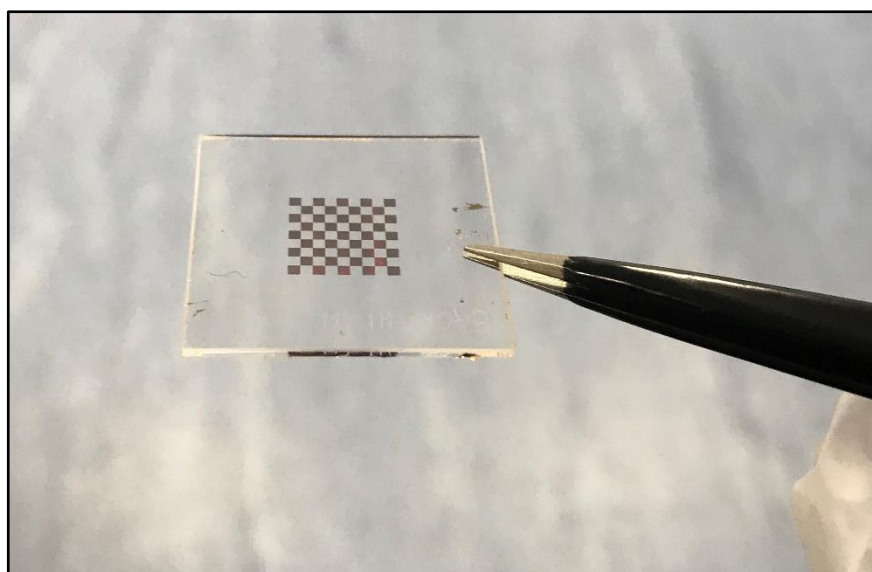


Figure 6.1: The gammadion arrays are arranged in a chessboard formation. Each square in the chessboard has dimension of $1 \text{ mm} \times 1 \text{ mm}$.

The gammadion arrays in all cases extend to a $1 \text{ mm} \times 1 \text{ mm}$ square (consisting of $1250 \times 1250 = 1,562,500$ individual nanostructures) which are arranged on the glass substrate in a ‘chessboard’ configuration so that an area of approximately $10 \text{ mm} \times 10 \text{ mm}$ is covered, as shown in **Figure 6.1**. This arrangement is chosen because it decreases the number of nanostructures by half, thus reducing the writing time for the electron beam lithography tool.

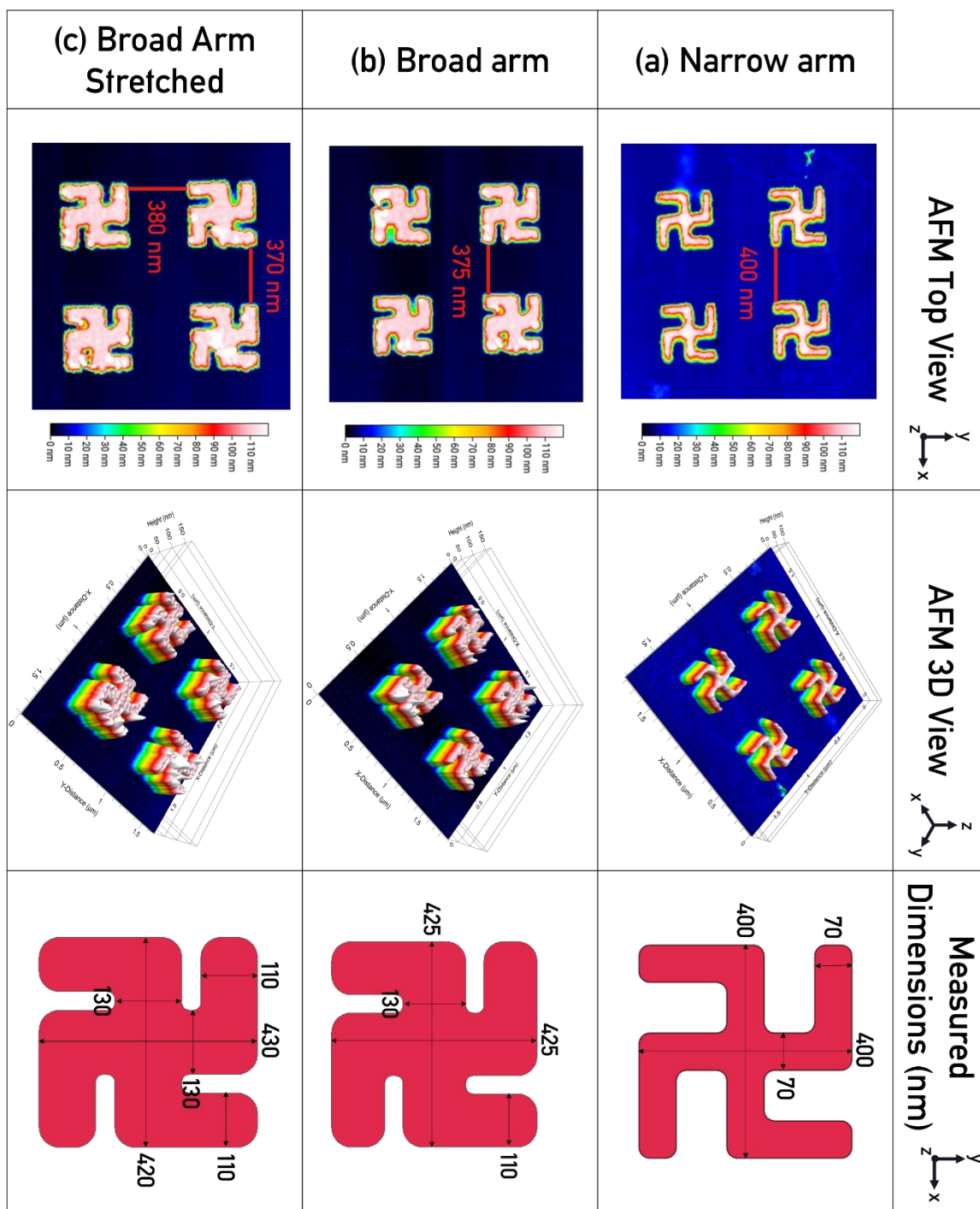


Figure 6.2: AFM images collected from the three gammadion structure arrays and their measured dimensions. (a) The narrow arm gammadion has thinner arms compared to that of the (b) broad arm gammadion. (c) The broad arm stretched gammadion is based upon the broad arm gammadion with its vertical dimensions stretched by 1.25% and its horizontal dimensions compressed by 1.25%. The measured dimensions for each of the structures calculated from AFM images are presented on the red idealised structure. Only the left-handed structures are shown here.

Three gammadion nanostructure variations have been fabricated. The first is the ‘narrow arm’ gammadion with AFM images of the array shown in

Figure 6.2 (a). The dimensions of the nanostructure are calculated by taking the mean of five measured values from the micrographs with the key parameters identified in the lower schematic. The narrow arm gammadion is constructed of arms which are approximately 70 nm in width at their widest. The central cross of the gammadion is 400 nm in length; hence the gammadion structure fits within a 400×400 nm square. The distance between equivalent positions on adjacent nanostructures (the periodicity) of the metamaterial is 800 nm. Thus, the spacing between each nanostructure at their closest point is approximately 400 nm.

The ‘broad arm’ gammadion replicates the effects of over development, which causes broadening of the nanostructure profile during the fabrication process. The AFM micrographs are shown in **Figure 6.2 (b)** with its calculated dimensions. The structure is constructed from a central cross whose arms are 130 nm in width and 425 nm in length and so the structure fits within a 425×425 nm square. The arms connected to the centre cross of the structure are thinner at 110 nm. The spacing between the nanostructures is 375 nm.

The third structure is the ‘broad arm stretched’ gammadion which replicates a defect which causes a dilation of the structure in one direction. This geometry is based on the broad arm gammadion; however, the planned dimensions measured in the x- and y- dimensions, as defined in **Figure 6.2 (b)** have been decreased and increased by approximately 1.25% respectively. Its micrographs and measured dimensions are presented in **Figure 6.2 (c)**. The measured arm widths are not changed significantly compared to the broad arm structure, likely because the changes do not exceed the step size of the electron beam lithography tool. The dimensions of the central cross of the gammadion is decreased by approximately 5 nm in the x-dimension and increased by 5 nm in y- dimension giving a 10 nm disparity. The result is that the structure is now contained within a 430×420 nm rectangle with a commensurate increase/decrease in the interparticle distance in the x- and y- directions respectively.

An ideal gammadion floating in a glass substrate belongs to the C_{4h} point group. When placed onto a substrate, the symmetry of the ideal gammadion is reduced to C_4 [49] and when the structure is stretched this symmetry is further reduced to C_2 . In practice, a non-uniform distribution of defects reduces the symmetry of all fabricated structure to C_1 [86].

6.2 Modelling procedure

Numerical simulations provide information about the interaction between nanostructures and light which cannot easily be measured experimentally. **Chapter 4.3: Simulation methods** gives a general description of the COMSOL software and the finite element method which is employed here.

6.2.1 Nanostructure design

Firstly, models of each of the structures are constructed based on the dimensions calculated from AFM micrographs in **Figure 6.2**. Three idealised structures which represent the ‘narrow gap’, ‘broad gap’ and ‘stretched’ gammadions are constructed and are shown in **Figure 6.3 (a-c)**. Note that only left-handed nanostructures are presented here, but models for right-handed structures have also been constructed. These models are described as ‘idealised’ as they include simplifications to the geometry and morphology of the structures. Most evident is that the faces and the vertical profiles of the gammadion are made planar: they do not account for surface roughness, sloping or other morphological defects which occur in the fabrication of the nanostructure arrays.

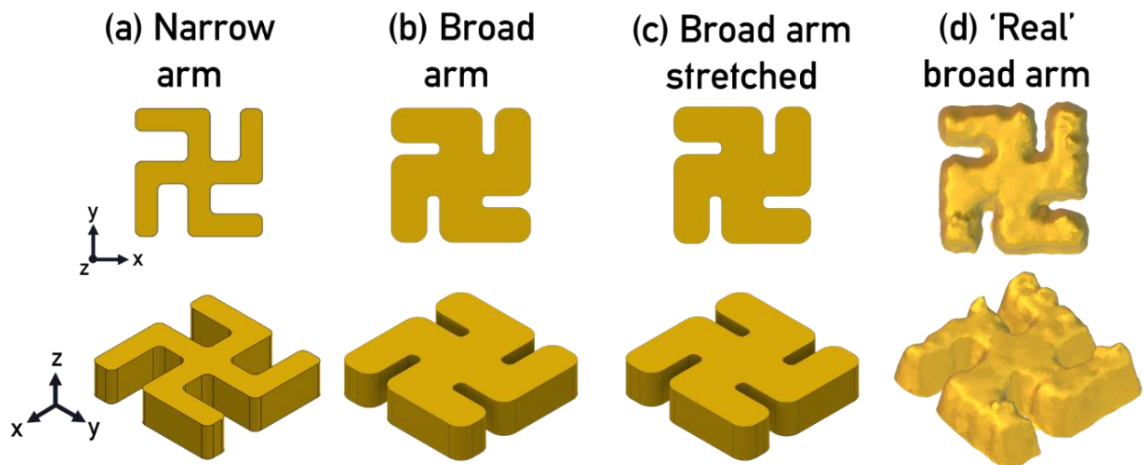


Figure 6.3: A top and three-dimensional view of the LH models of the gammadion nanostructures. Structures (a)-(c) are idealised models of the narrow arm gammadion, broad arm gammadion and stretched gammadion. Structure (d) is called the ‘real’ structure as it is generated directly from an AFM image of the broad arm gammadion array.

A fourth model, shown in **Figure 6.3 (d)** is constructed directly from an AFM micrograph of a single structure in the broad arm gammadion array. Starting with the micrograph of the entire array, it is cropped so it contains only one structure, selected arbitrarily, and the glass substrate is removed. The file is converted to a format that can be read by the numerical modelling software. This structure includes morphological defects and so it is described here as the ‘real’ structure.

Figure 6.4 shows the profile of the ‘real’ gammadion model at 0, 50 and 100 nm above the glass substrate. The structure shows significant sloping as the height of the structure increases. Tip convolution can overestimate the lateral dimensions of the nanostructures, making protrusions from the surface appear larger and making holes appear smaller [87] so it is likely that the micrograph most likely overestimates the extent of the sloping. Indeed, **Figure 2.10** presented previously shows an oblique SEM of a gammadion nanostructure in which the sloping of a similar nanostructure does not appear to be as extreme.

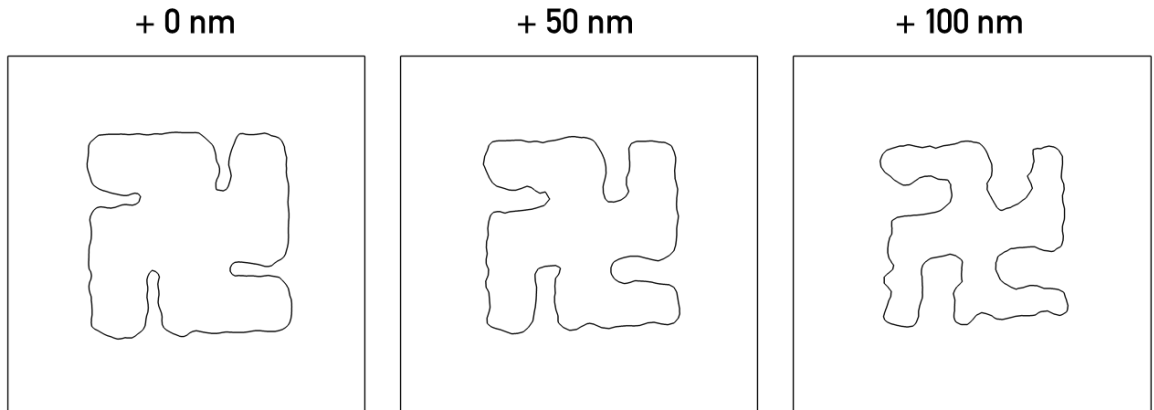


Figure 6.4: Cut slice profile of the ‘real’ structure 0, 50 and 100 nm above the glass substrate. The structure shows significant sloping.

The surface roughness, R_q of a given area is parameterised by the root-mean-square roughness. It is the root-mean-square average of height deviation from the mean plane and is expressed mathematically as:

$$R_q = \sqrt{\left(\frac{z_1^2 + z_2^2 + \dots + z_N^2}{N}\right)} \quad \text{Equation 6.1}$$

where	R_q	Root-mean-square roughness
	z_i	Deviation in height from the mean plane
	N	Number of points

N will correspond to the resolution of the scanning microscopy. For the idealised gammadion nanostructures the R_q will be 0 as the surfaces are planar [88]. For the real gammadion, the R_q calculated at its top face is approximately 3.40 nm. Compare this with the glass substrate with an R_q equal to approximately 0.45 nm.

The modelled structures are all constructed of solid gold, with refractive index values taken from Johnson and Christy [89]. To replicate the experimental conditions, the gammadion nanostructure is placed onto the glass substrate with a refractive index equal to 1.5 then covered with water with refractive index 1.33.

6.2.2 Calculated parameters

For each of these configurations, percentage transmission across the wavelength range is calculated using the ratio of incident power to time averaged power flow on the 'Integration Surface' beyond the nanostructure: this is identified previously in **Figure 4.9**. It is possible to calculate the CD spectrum for the nanostructure array using the differential transmission of RCP and LCP. Absorbance for incident LCP/RCP, A_{LCP} and A_{RCP} is given by the negative logarithm of the percentage transmission. CD in millidegrees is given previously by **Equation 4.3**.

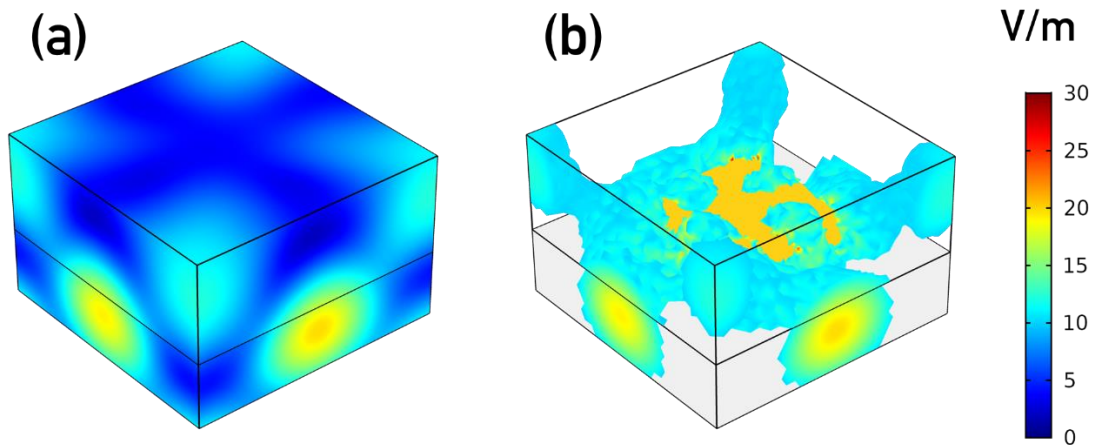


Figure 6.5: Three dimensional electric field plots. (a) Mapping the entire electric field range shows only the boundaries of the simulation. (b) Mapping electric fields greater than 10 V/m.

The interaction of the nanostructure with the incident electric field is probed here by calculation of the normalised electric field. This is given by the

root mean square of the x- y- and z- components of the electric field and so whilst it is a more comprehensive indicator of electric field distribution than calculating only one component, the sign is lost. Three dimensional plots of the electric field have been generated to aid interpretation. Mapping the entire electric field range is ineffective for three dimensional plots as then only the field at the boundaries of the simulation are visible, as in **Figure 6.5 (a)**. By limiting the mapped fields to only those above a certain threshold, 10 V/m in this example, a distribution which shows only the most intense fields is generated, as in **Figure 6.5 (b)**. The limitation of this technique is that only the ‘shell’ of the electric field is visible: the intensity of the electric field within this volume does not appear. It does nonetheless give a good indication of areas of most intense electric field. Further to this, the z-component of the electric field has been calculated at a cut plane 50 nm above the glass substrate.

6.3 Results

6.3.1 Circular dichroism spectra

The CD spectra of each of the structures is experimentally measured using the equipment and techniques introduced in **Chapter 4**. In each case, the LH and RH arrays of the three fabricated structures are immersed in water, giving a total of 6 configurations. For each configuration, two consecutive measurements are taken across the wavelength range and the mean calculated. These experimental CD collected after fabrication of the nanostructures are presented in the top panels of **Figure 6.6** in blue.

As expected, the LH and RH enantiomorphs of a given structure yield spectra that are equal in magnitude but opposite in sign: they are mirrored around the 0 millidegree line of the plot. On each spectrum, four wavelength positions which correspond to equivalent minima and maxima (i.e. CD resonances) between structures are identified with a red line. These are numbered I-IV with in order of increasing wavelength. A summary of these wavelength positions is presented in **Table 6.1** (top panel, in blue).

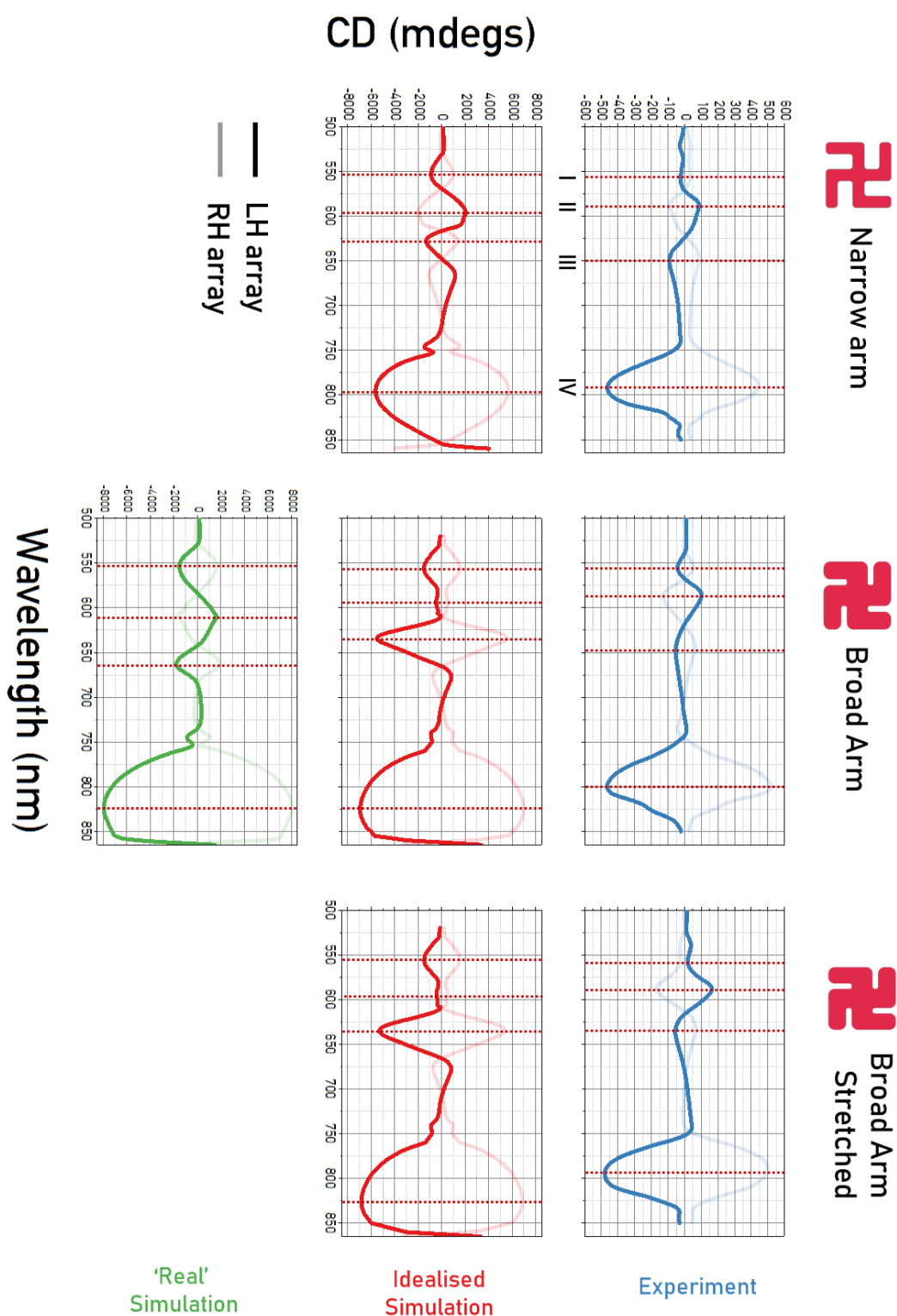


Figure 6.6: Comparison of experimental (top panels, blue) and simulated (lower panels, red and green) CD spectra for the narrow arm, broad arm and stretched broad gammadion nanostructures. The idealised structure simulations are shown in red and the 'real' structure simulations are shown in green. For each panel, the spectrum from the LH structure is shown in the darker colour and the RH structure is shown lighter. Four positions (I-IV) corresponding to minima and maxima in the CD spectra are identified with a dotted red line on each panel.

		Wavelength Position / nm				
		I	II	III	IV	
Narrow arm	RH	555.0	588.4	648.0	798.2	Experiment
	LH	558.4	588.0	650.8	791.6	
Broad arm	RH	555.0	587.8	643.8	800.8	
	LH	555.2	586.0	648.8	800.8	
Stretched broad arm	RH	555.0	588.0	633.6	788.4	
	LH	557.2	588.2	636.2	794.2	
Narrow arm	RH	554	596	629	794	Idealised Simulation
	LH	554	596	629	794	
Broad arm	RH	556.0	609.0	634.0	826.0	
	LH	556.0	609.0	634.0	826.0	
Stretched broad arm	RH	556.0	610.0	635.0	827.0	
	LH	556.0	610.0	635.0	827.0	
'Real' broad arm	RH	555.0	610.0	665.0	825.0	'Real' Simulation
	LH	555.0	610.0	665.0	825.0	

Table 6.1: The wavelength position of equivalent maxima/minima position calculated from spectra of the LH/RH enantiomorphs of the three structures. The positions are identified in the previous figure.

The experimentally derived CD spectra for the three structures are qualitatively similar. There are however some differences, with the most significant changes between structure occurring in the 500 – 700 nm range: this region encompasses resonances I, II and III. These resonances are smaller in intensity for the narrow gap structure than for broad or stretched gammadion structures. When spectra are compared between the ‘narrow arm’ and those based on the ‘broad arm’ structure, there are changes to the relative sizes of resonances II and III. In the narrow arm structure, these two resonances have approximately the same magnitude, whereas in the ‘broad arm’ structures, resonance III is smaller by a factor of approximately 0.75. For all the structures, the most intense resonance is found at position IV with an intensity up to four times larger than that of I, II and III. The position of resonance IV also undergoes the largest changes between structures with shifts of up to 12.4 nm measured between the ‘broad gap’ and ‘stretched’ gammadion structures.

The CD spectra calculated by numerical simulation are shown in **Figure 6.6** (bottom panels with red and green lines). As with the experimentally calculated spectra, the CD maxima/minima positions I – IV are identified with

a red line. The resonance positions are quantified in **Table 6.1** (bottom panels, in red and blue).

Qualitatively, the idealised structures can reproduce the experimentally derived spectra. There are however some differences between the spectra calculated for different structures. The positions of the resonances are reasonably well reproduced with position III showing the greatest discrepancy between experiment and simulation in all cases. Resonance IV, the largest found at approximately 825 nm does not appear to change shape much between different geometries. However, it shifts by 33 nm between the narrow arm and stretched broad arm.

There are some key inconsistencies. For the broad arm structures, the simulated spectra overestimate the intensity of resonance III, with it approaching the intensity of resonance IV. For the idealised broad arm structure, resonance II shows some distortion and has a magnitude of approximately 0. In effect, this means that there is not a difference between the transmission of LCP/RCP at this position, contrary to the experimentally derived spectra which gives a CD magnitude of ± 100 millidegrees. Lastly, in the simulated spectra the magnitude of the CD is approximately 10 times that of the those experimentally calculated. A reduction by a factor of 2 can be attributed to the ‘chessboard’ fabrication strategy. Further reductions must be attributed to fabrication defects such as missing nanostructures, or missing parts of the structure.

Predictably, the ‘real’ structure which is constructed directly from AFM topographic measurements can better replicate spectra derived from the broad arm structures than the idealised model. Resonance II in this ‘real’ simulation now has a non-zero magnitude as in the experimentally derived spectra. Resonances I, II and III in the ‘real’ simulated structures have approximately the same absolute magnitude, different to the experimental spectra where resonance II is largest. Resonance IV of the ‘real’ structure is found at nearly exactly the same position as for the idealised structure.

6.3.2 Cleaning Effects

To examine the effects of a cleaning procedure on the spectral properties of the nanostructure arrays, the ‘narrow arm’ structures were subject to multiple cleaning cycles. At fabrication, the structures were sequentially soaked in 2-propanol, methanol and acetone to dissolve inorganic contaminants and dehydrate the surface. Subsequently, the structures are plasma ashed,

bombarded with high energy metastable oxygen species which react with any remaining organic species and are removed by vacuum. The full cleaning procedure is described in **Section 3.1.1: Sample preparation**.

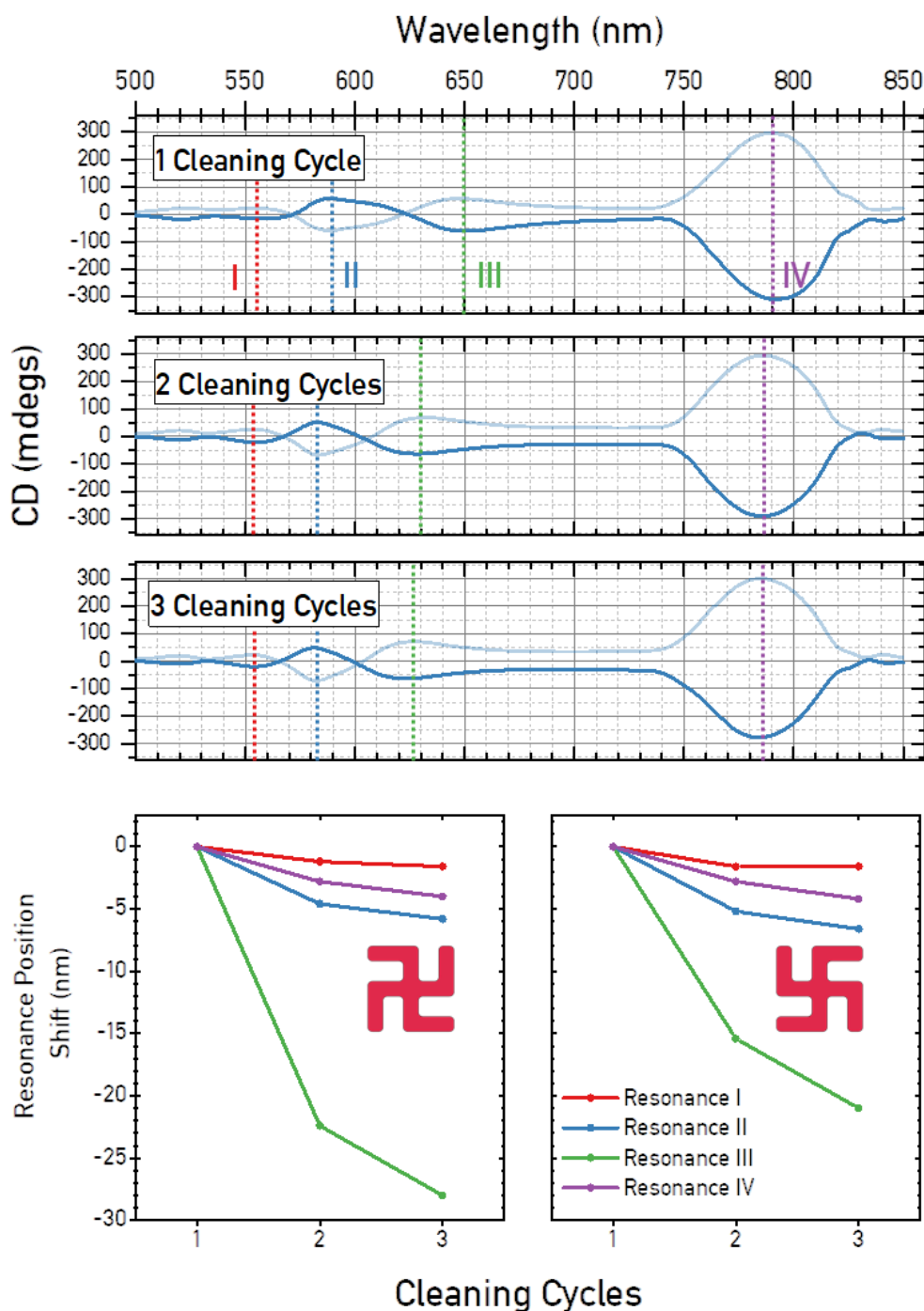


Figure 6.7: (Top three panels) Experimental CD spectra collected in air of the LH (dark spectra) and RH (light spectra) 'narrow arm' structure after multiple cleaning cycles. The resonances, identified with dotted lines, in all cases shift to the blue. (Bottom

panels) The shifts of resonances I-IV are quantified for the LH (left panel) and RH (right panel) structures.

Figure 6.7 (top panels) shows the experimental CD spectra of the ‘narrow arm’ structure after 1, 2 and 3 cleaning cycles for both the LH and RH structures. The effect of the cleaning procedure on the spectra causes changes both to the position of the CD resonances, previously labelled I-IV. The shift of these resonances is parameterised in **Figure 6.7 (bottom panels)** for the LH (left panel) and RH (right panel) enantiomorphs.

For all resonances, the wavelength position for both LH/RH enantiomorphs is shifted to shorter wavelengths. The largest change to the shape and position of the resonances occurs after the first cleaning cycle. Resonances I and IV undergo the smallest changes, under 5 nm. Resonance II is slightly larger, at approximately 5 nm for both enantiomorphs. All these resonances approximately retain their shape.

The largest change occurs in both LH and RH structures to resonance III, shifting 22 and 16 nm for LH/RH enantiomorphs, respectively. In addition to this shift, the shoulder which appears at approximately 610 nm at cleaning cycle 1 disappears in subsequent spectra. The changes to the shape of the spectra and shifts to the resonance position decrease after the second cleaning cycle. The resonance shifts are reduced by to approximately 20% of that observed after the first cleaning cycle.

6.3.3 Simulated transmission plots

The CD effect measured and simulated here can be described as an asymmetric transmission of left and right CPL. The generation of a CD spectrum requires the combination of two separate experiments, the transmission of LCP and RCP measured sequentially. A commercial spectrometer like the one used to calculate the experimental spectra in **Figure 6.6** does not provide separate transmission spectra for light handedness. Numerical simulation can however provide this insight.

Figure 6.8 shows the simulated transmission of RCP/LCP for the LH enantiomorph for the four structures modelled. The associated CD spectrum is provided to aid comparison. The positions I-IV have again been identified with a red line, as in previous figures. CD occurs when the difference between RCP and LCP transmission is at its largest and does not necessarily overlap with

resonances in the transmission spectra. Dips in transmission indicate areas of enhanced reflection or absorption.

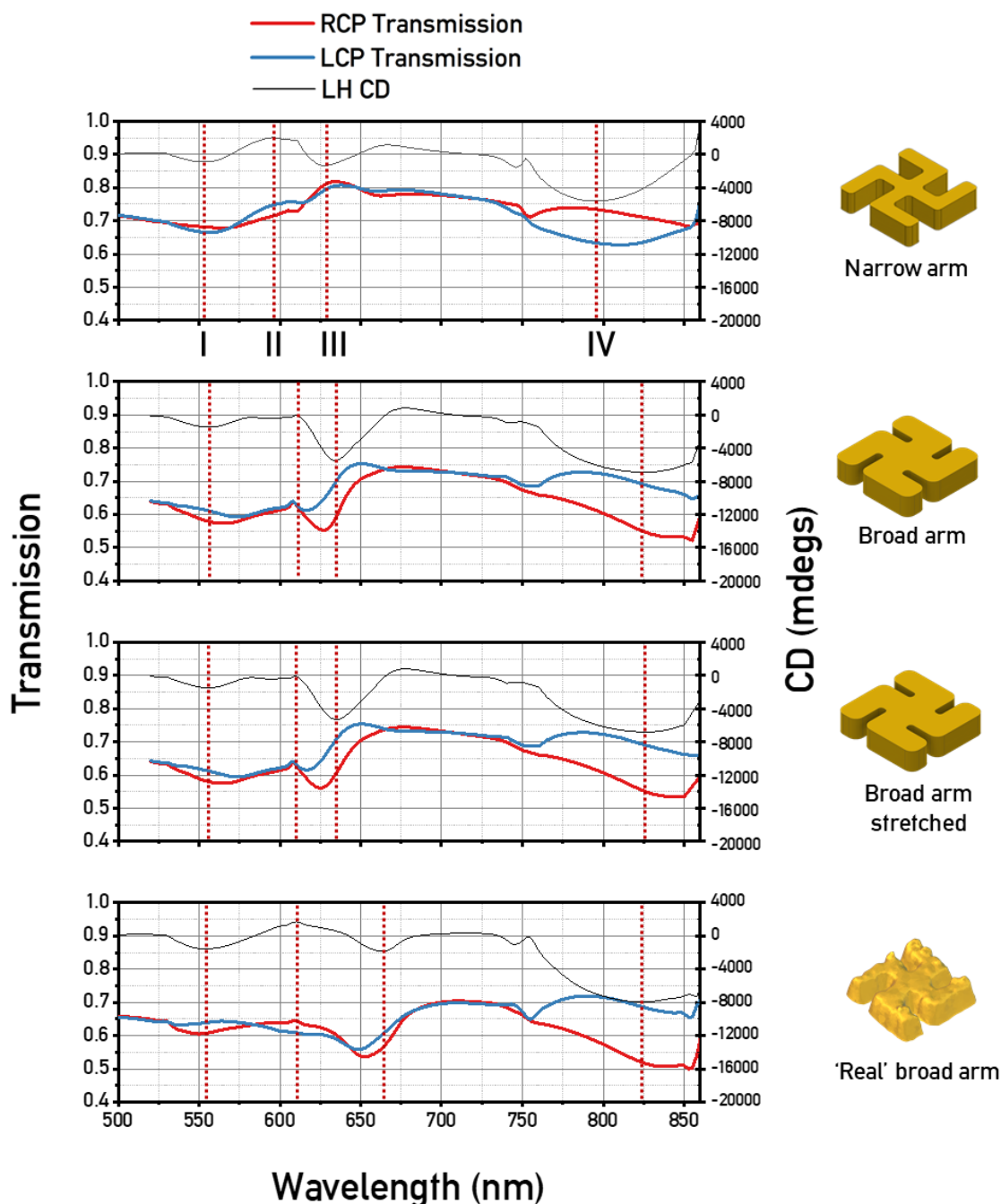


Figure 6.8: Simulated transmission plots for RCP (red) and LCP (blue) for the LH of the four modelled structures. The LH CD spectrum is shown in black for reference. CD resonances I-IV are identified on each plot with red lines.

The transmission spectra between idealised structures is qualitatively similar with the 'real' structures showing greatest similarity to the 'broad arm' spectrum, as would be expected. In all cases the largest difference between

LCP/RCP transmission occurs in the 750 - 850 nm region where resonance IV lies. LCP in this region is preferentially transmitted. For position II, the idealised broad arm structures show near-coincident transmission of LCP/RCP as expected as its CD at this position is ~ 0 millidegrees. For the real structure, the transmission of RCP at resonance I is approximately the same as that of LCP for resonance II and vice-versa.

6.3.4 Electric field plots

For each simulated structure, three-dimensional electric field plots have been generated at the CD resonance position absorption to provide insight into their origin. The strategy used is described in **Section 6.2.2: Calculated parameters**. The electric field plots for fields greater than 10 V/m are calculated for both the RCP and LCP components for each structure at resonances I-IV and are presented in **Figure 6.9 (a-d)**. Plots at identical positions for fields greater than 20 V/m are shown in **Figure 6.10 (a-d)**. Only the LH structure is presented in each case as the electric field distribution for RCP incident upon a RH structure is mirror symmetric to the distribution for LCP on a LH structure. A three-dimensional view and top-down view of the nanostructure is shown to aid understanding of the electric field distributions. For all the calculated distributions, areas of intense electric field exist predominantly in the plane of the nanostructure array rather than above the surface of the gammadion structures.

Most apparent is that at the position of the largest CD resonance, IV, there is a large distribution of intense fields for incident RCP. The strongest fields for incident RCP for this configuration are between nanostructures in all cases, including in the ‘real’ structure. This supports the findings of previous work concerning the origin of CD modes in gammadion nanostructures, where the origin of this large mode was attributed to interactions between adjacent structures [90]. For incident LCP, the intensity of fields between nanostructures is reduced. For the ‘real’ nanostructure they are reduced below the 10 V threshold and so do not appear.

Resonance III is well reproduced by both the idealised and ‘real’ structures. The electric field distributions are similar between structures: the largest field intensities are localised at the structures’ outer side walls and between arms in all cases for both structure handedness. For all structures, incident LCP produces fields which are more localised on the nanostructure than RCP, where fields are more delocalised between structures.

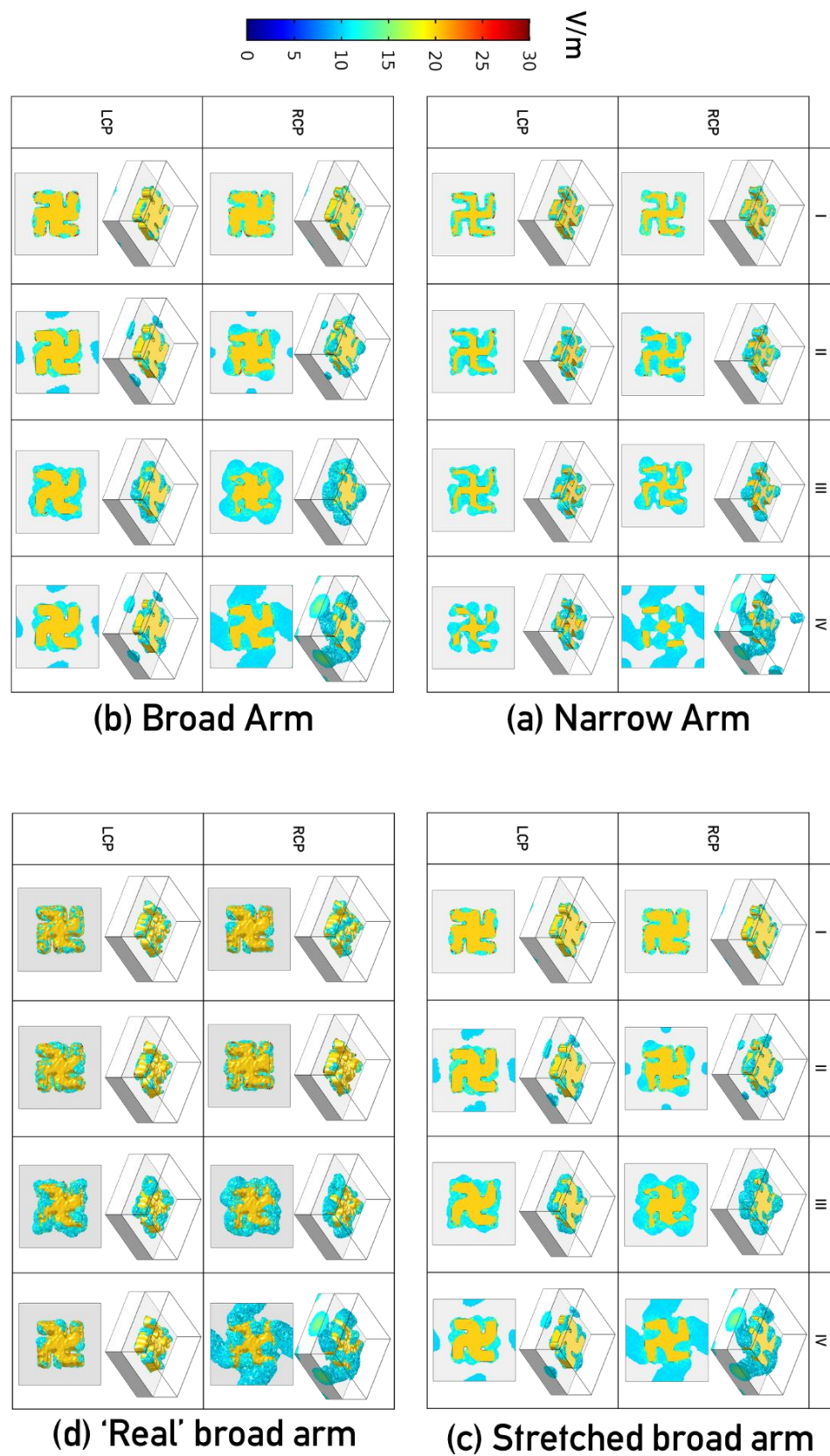


Figure 6.9: Three dimensional normalised electric field plots above 10 V/m generated for (a) the narrow arm gammadion structure (b) the broad arm structure. (c) stretched broad arm structure (d) 'real structure'.

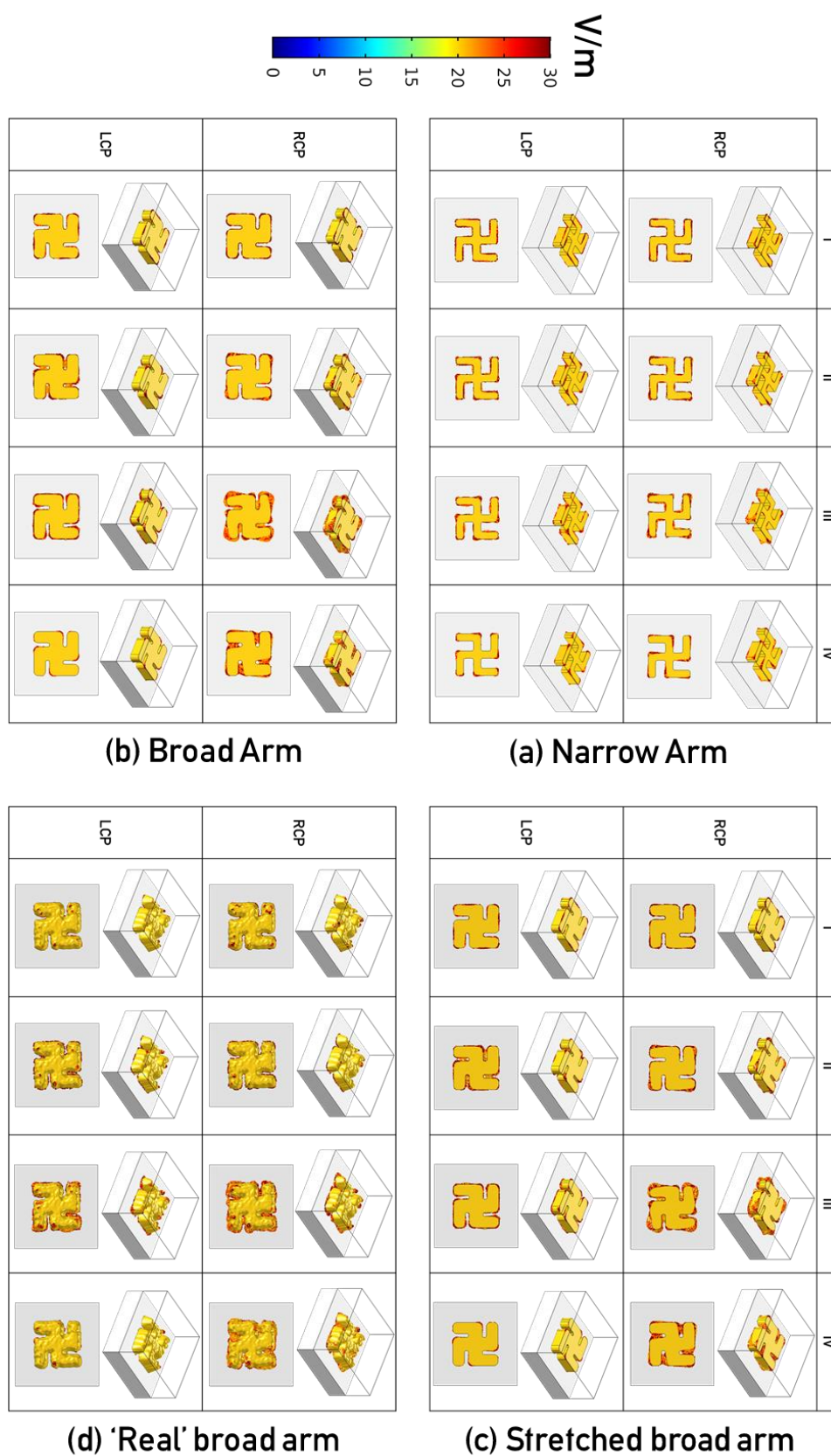


Figure 6.10: Three dimensional normalised electric field plots above 20 V/m generated for (a) the narrow arm gammadion structure (b) the broad arm structure. (c) stretched broad arm structure (d) 'real structure'.

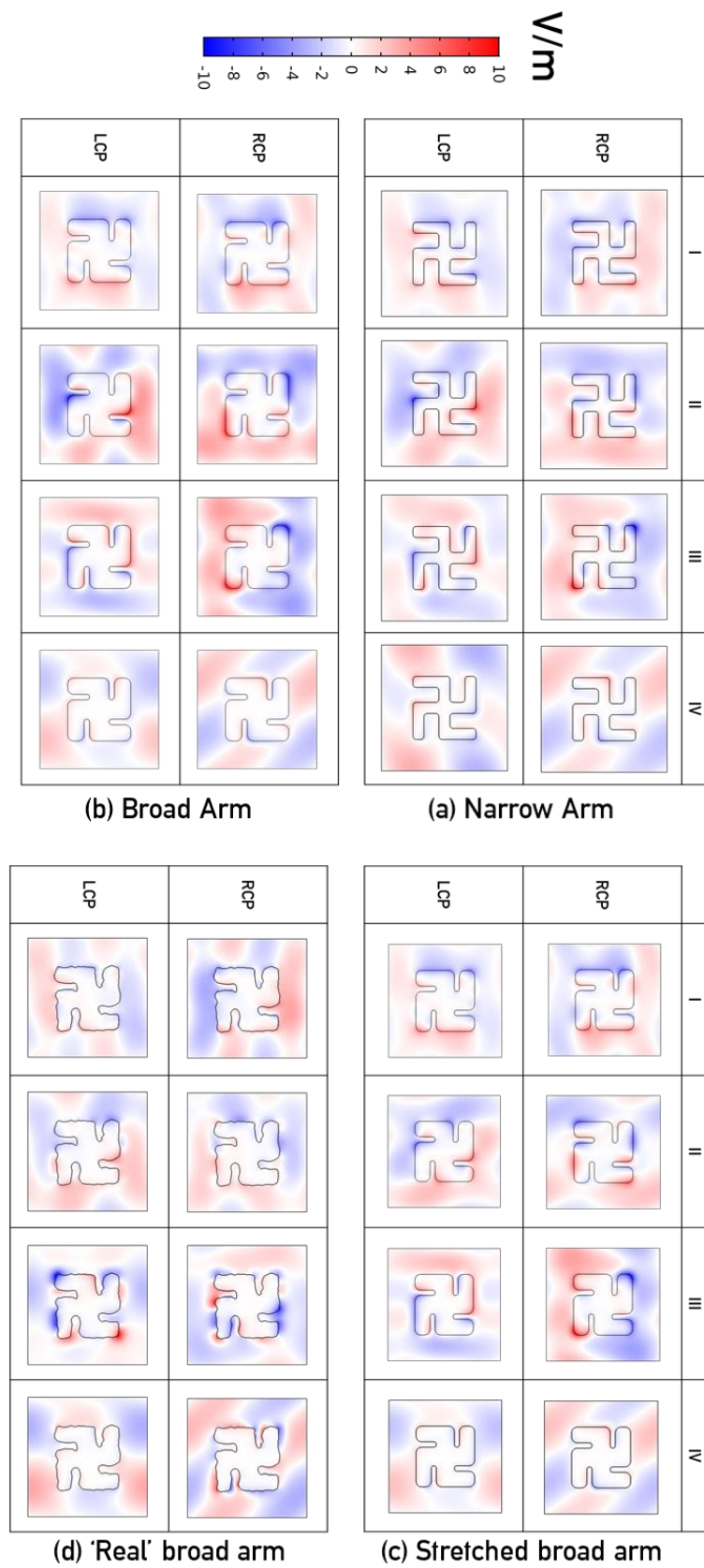


Figure 6.11: Z-component of the electric field for (a) the narrow arm gammadion structure (b) the broad arm structure (c) stretched broad arm structure (d) 'real' structure

The CD resonance II is only reproduced by the narrow arm and ‘real’ gammadions. For these structures, fields are again localised around the nanostructure. In the case of the ‘real’ structure, fields greater than the threshold extend far less than in resonance II. The idealised broad arm structures show an increase in field intensity between adjacent nanoparticles which is near identical between LCP and RCP. This is most likely the origin of the disappearing resonance in these structures.

Resonance I, which is well reproduced by the simulated CD spectrum in all cases, shows similar distributions for the different structures. In all cases, the electric fields are localised at the gold/glass interface. For the idealised structures, there is also high field intensities around the edges of the top face of the nanostructure. Interestingly, in the simulated ‘real’ structures, the distributions are very similar to those of resonance II but inversely: i.e. the distribution for LCP for resonance I resembles that for RCP for resonance II and vice versa.

To visualise the areas of most intense electric field, intensities only above 20 V/m are plotted in **Figure 6.10**. What is readily apparent is that in the idealised structures, there are no areas of intense electric field, ‘hotspots’, on the top face of the surface. In these idealised structures, hotspots are primarily found at the sharp edges where horizontal and vertical planes meet. For the broad arm structure, there are intense hotspots in the arm gaps, as is expected in plasmonic gap systems [12], [91], [92]. In contrast, the ‘real’ structure does support some hot spots on the face of the structure which are randomly distributed. These hot spots can be attributed to surface roughness. were small bumps and cavities can support large field intensities. These areas of localised, amplified electric fields are important as they can cause large enhancements for Raman spectroscopies and catalyse chemical reactions [93], [94].

The z-component of the electric field is calculated and shown in cut slices 50 nm from the substrate in **Figure 6.11**. Modes I-IV are all dipolar in character (i.e. their sign changes under inversion) with no higher order modes identified, such as quadrupolar which would be even under inversion.

Like the normalised electric field plots, fields here are localised to the surface of the nanostructures for resonances I-III. For resonance IV there is no such localisation around the nanostructure. For incident RCP, which showed strong enhancement between the nanostructures in the normalised field plots, there are areas of continuous field across the nanoparticle unit cell.

6.3.5 Optical chirality

For each of the nanostructures, three-dimensional time-averaged optical chirality, \bar{C} plots have been generated for both incident LCP and RCP for the four structures at the resonances I-IV, **Figure 6.12 (a-d)**. Again, these have been normalised to that of RCP light. Only enhancements larger than 2.5 are included in the plots so that the areas of greatest enhancement can be visualised. The minimum and maximum values have been included for each resonance and light handedness.

For the idealised structures, the largest distributions of enhanced \bar{C} occurs for resonance III (RCP) and resonance II (LCP). The broad-arm structures show maximal optical chirality enhancement values for resonance III (RCP). For the narrow arm structure, resonance II (LCP) shows a greater minimum despite showing a smaller distribution than resonance III. For the idealised structures, there are no areas of enhancement on the planar face of the structure, with most areas of most enhancement occurring at the edges and between the arms of the nanostructure. Interestingly, for resonance IV enhancement occurs predominantly at the corners of the nanostructure as opposed to between neighbouring structures, as in the electric field plots.

The ‘real’ gammadion nanostructure can support areas of enhanced optical chirality up to three times that of the equivalent idealised model. These areas of optical chirality hotspots are supported by the random protrusions of the nanostructure caused by the roughened surface. Like the idealised nanostructure models, resonance III supports both the highest maxima/minima of optical chirality and also shows the greatest spatial distribution.

In addition to the three-dimensional plots, the volume integrated time averaged optical chirality has been calculated at each resonance position for each of the nanostructure variations, **Figure 6.13**. For each structure, optical chirality values calculated from incident RCP/LCP are given as well as their sum. The sum is a useful parameter because it gives an indication of whether there is an excess of LH or RH chiral near fields in a CD experiment in which both handednesses are measured. This is most evident in the narrow structure: its LCP and RCP components show the largest values of $|\bar{C}|$ however their sum indicates there is not a large excess of handed fields.

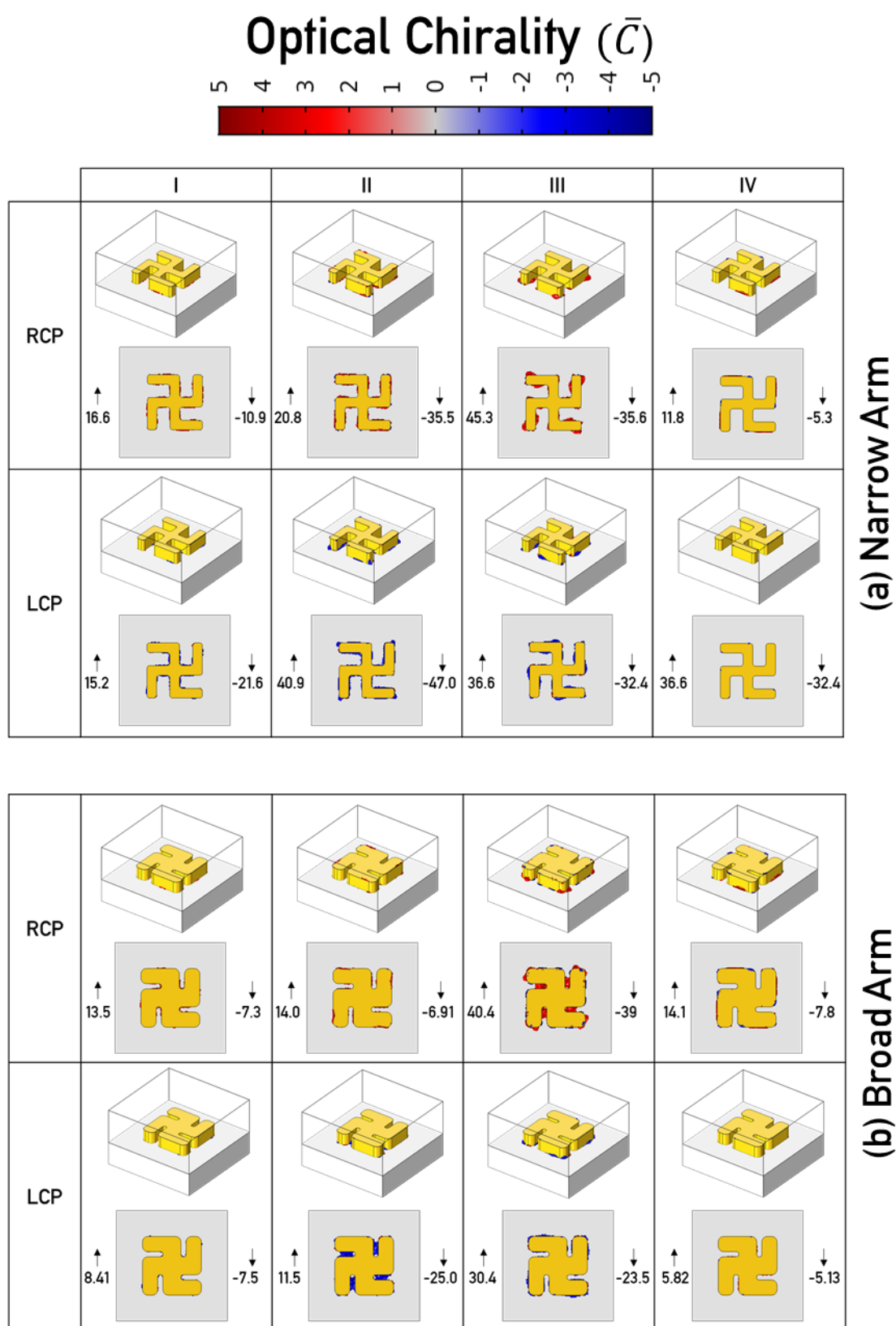


Figure 6.12 (a-b): Time averaged normalised optical chirality plots above a threshold of 2.5 for (a) the narrow arm gammadion structure (b) the broad arm structure. The minimum and maximum values for each resonance and light handedness are included.

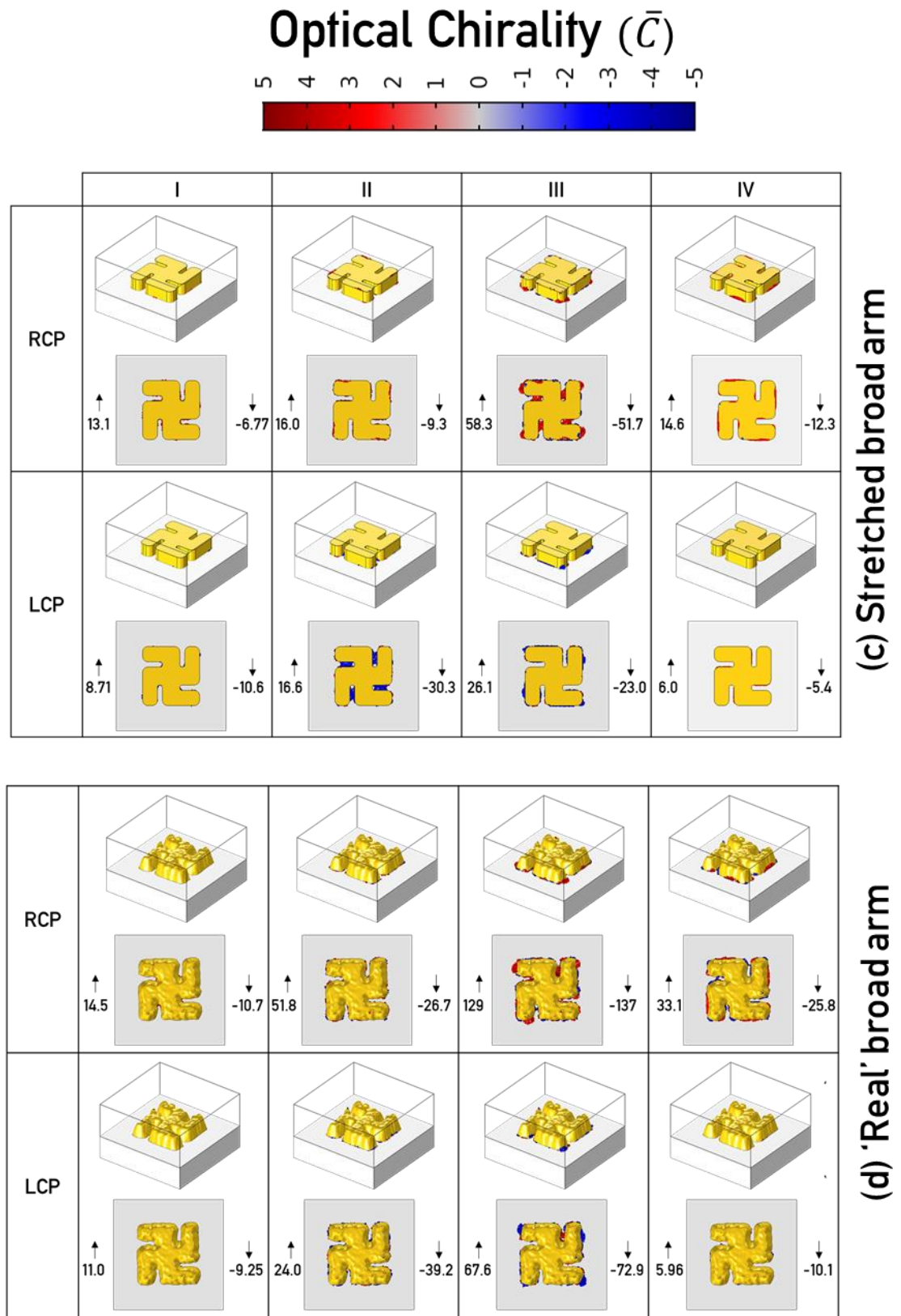


Figure 6.12 (c-d): Time averaged normalised optical chirality plots above a threshold of 2.5 for (c) the stretched broad arm structure and (d) the 'real' broad arm structure. The minimum and maximum values for each resonance and light handedness are included.

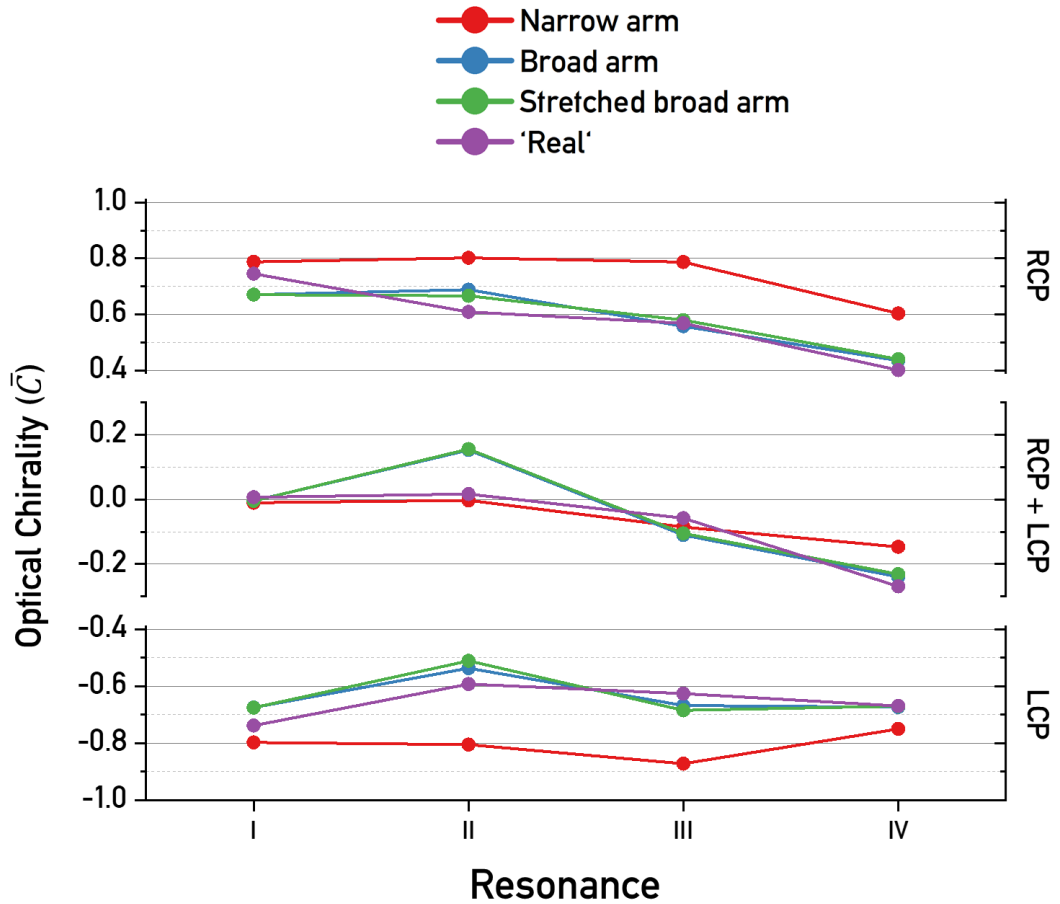


Figure 6.13: Volume integrated optical chirality for each of the structures illuminated with incident RCP (top panel) LCP (bottom panel) and the sum of these (middle panel).

For all the structures, the largest sum value is found at resonance IV. It is evident from both the optical chirality plots and the calculated integrated chirality values that the geometry of the nanostructure can greatly influence the enhancement of optical chirality and its distribution. Notably, despite the rough surface of the 'real' nanostructure supporting high maximum and minimum values of enhanced optical chirality, its volume integrated value is not significantly higher or lower than the idealised structures. It is also clear that the level of \bar{C} does not necessarily correlate with the magnitude of the CD resonance: at resonance II the broad arm structures show a large excess of RH fields despite this being one of the smallest CD resonances.

6.4 Discussion

The purpose of this chapter is to determine the effect of common fabrication defects on the properties of chiral nanostructures, namely the gammadion. Studying the geometrical and morphological origin of CD features allows for more rational design of the nanostructures to enhance their use for applications such as biological sensing.

With regards to the CD spectra, the dominant resonance derived both experimentally and by simulation, is resonance IV, found at around 800 nm. Previous work has described this resonance as a periodic mode [90], [95]. The electric field plots here support this assertion that the origin of this mode is coupling between adjacent nanostructures primarily mediated by a structure's interaction with RCP. In a RH gammadion structure, the opposite would be true, with strong absorption of LCP.

In their work, Phua and colleagues simulate an identical nanostructure and modulated the periodicity, the distance between equivalent point of adjacent nanostructures. They correlate a decrease in the periodicity of the array with a shift of resonance IV to shorter wavelengths [39]. Here, the periodicity is kept constant however the interparticle distance of the nanostructure is changed. The interparticle distance for the narrow arm and broad arm structure is 400 and 375 nm with resonance IV found at a shorter wavelength for the narrow arm structure both in the simulation and experiment. The transmission spectra for these structures show that LCP is nearly equally transmitted for both structures, but the RCP transmission is redshifted for the broad arm structure. This is consistent with previous observations that as the distance between adjacent nanoparticles decreases, the longitudinal eigenmode (in the plane of the pair) shifts to shorter wavelengths. [96]. Thus, this work suggests that both the periodicity and the interparticle distance must be considered to effectively tune the position of resonance IV.

With regards to the 'stretched broad arm' structure, the experimental CD shows that compared with the 'broad arm' structure, position IV falls at a shorter wavelength. The simulated spectra do not reflect this change, instead showing a very modest increase in the resonance wavelength position: in fact this is true of all the resonances in the simulated spectra of the stretched structure. One could expect that a different interparticle distance in the x- and y- directions would cause a splitting of this periodic resonance due to lifting of degeneracy. It is likely that the magnitude of the dilation measured here is

insufficient to cause these effects. A more exaggerated distortion is required to cause significant changes to the CD spectrum.

Resonances I – III can be described as localised structural modes, as the electric field plots show that for both LCP and RCP they are strongly localised around the nanostructure surface. Resonances I and III have previously been described as resulting from coupling between plasmonic modes in the arm of the nanostructure and the orthogonal mode which lies on the other side of the gap [90].

With regards to resonance II only appearing in the narrow arm and ‘real’ structure simulations, the suggestion is that the gaps in the simulated broad arm structures have been underestimated. The AFM micrographs show that this gap distance is 100 nm at the top of the nanostructure whereas the idealised models based their separation from measurements taken at the nanostructure base at 37.5 nm.

The near field optical chirality calculations show that resonance IV exhibits the largest asymmetry in the sum of the handedness of its near fields, with an excess of LH fields between -0.1 and -0.3. For the idealised broad arm and stretched broad arm structures, resonance II shows a large excess of RH fields. However as was previously alluded to, its geometry is likely not to be a true representation of the measured structure. Indeed, in the ‘real’ simulated structure, the value of this sum at resonance II falls nearly to zero.

The relative magnitude of these values appear to correlate with the asymmetry values measured in the original work [82], although resonance IV in this case exhibits slightly larger asymmetries than resonance III. As we have shown, the geometry and morphology of the nanostructures can influence its local optical chirality. For example, with the narrow arm structure shows the lowest excess of handedness for resonance IV, at nearly half the value of the other structures.

The optical chirality plots and calculation of the maximum and minimum values show that a roughened surface can support areas of optical chirality enhancement up to three times larger than an equivalent structure. This is however a modest increase when compared with electric field enhancements which can be several orders of magnitude [93] for roughened surfaces. Crucially, this enhancement of optical chirality does not occur across the entire nanostructure surface, with the idealised structures showing larger volume integrated values.

The effect of cleaning cycles has been shown to have an impact on the CD spectra of the structures. Plasmonic nanostructures have been shown to be

sensitive to changes in refractive index, as well as to changes in size and shape of the plasmonic elements. Beginning with changes in refractive index, contamination with organic molecules is unlikely. Given that the shift of a LSPR mode is given by [97]:

$$\Delta\lambda = m\Delta n[1 - e^{(-\frac{2d}{\lambda d})}] \quad \text{Equation 6.2}$$

where	$\Delta\lambda$	wavelength shift
	m	sensitivity factor of nanoparticle
	Δn	refractive index change
	d	effective thickness of the absorbed layer

A negative wavelength shift would require an absorbate with a refractive index less than that of water, which no common contaminants are. Besides, it is likely that plasma ashing for the long durations here would completely eliminate any organic contaminants. It has been suggested however that plasma ashing with reactive oxygen species can lead to the formation of gold oxides such as Au₂O₃ [98]. Calculations of the refractive index of gold oxide thin films reveal however they are significantly higher than unoxidized gold [99] and so would also result in a redshift.

The more likely origin of the observed effects is a change to the size or morphology of the nanostructure. Ha and colleagues have shown that deformations to the structure of gold nanorods can occur after only 180 seconds of oxygen plasma treatment. They showed that before the oxygen plasma treatment, the average diameter and length of the particles were 23.5 nm and 69.6 nm, respectively, giving an aspect ratio (AR) of 2.96. After treatment with oxygen plasma for 120 s, the diameter and length reduced to 22.5 nm and 64.3 nm (120 s), respectively, reducing the AR to 2.86 [100]. This caused a commensurate broadening and shift to the LSPR spectra of nanoparticles. The nanorods which comprise the gammadion nanostructure are larger than those described in this study, however the plasma ashing times used here are nearly twice as long. It is therefore possible that plasma ashing cleaning regime employed here could cause large deformations to the nanostructures which in turn cause large changes to the measured CD spectra. This would explain why structural modes would be most affected by the cleaning regime whilst the position of resonance IV, associated with the periodicity of the array, would be largely unchanged. The suggestion is therefore that the morphological change causes a broadening of the structure which causes a reduction in the gap

distance of the gammadion. Conservation of mass requires that there be a commensurate reduction in the height of the nanostructures.

With regards to the simulation strategy for this work, it has already been alluded to that AFM artefacts can distort the lateral dimensions of the nanostructure. For future work, it is suggested that careful consideration is given to the parameters used for the construction of the models. A practical example would be using the arm width measured at the top surface of the nanostructure, not the base where an overestimation of width is likely to occur. Additional nanostructure characterisation methods could also be employed, although SEM imaging with non-conductive samples generally results in a loss of resolution, as mentioned in previous sections.

With regards to the inclusion of surface roughness, there some pertinent points that should be made. The inclusion of surface roughness of the nanostructures allows for analysis of field enhancements (hot spots) and so in this regard it is a helpful addition. It is important to bear in mind however that over the array these morphological defects are effectively erased by averaging over many individual nanoparticles. Ciracì and colleagues have demonstrated that surface roughness in individual nanogap systems cause random shifts in their absorption spectra [91]. Over a large array these random shifts are averaged out, leading to a broadening of the resonance peak. So, both idealised and individual nanostructure can provide useful information to the researcher.

Here, four geometric variations of a gammadion have been investigated. A simulation method which incorporates surface roughness has been implemented, with suggestions made for its use in the future. The CD spectrum of the gammadion arrays appear similar despite the changes made to the geometry of the nanostructure. All retain four principal resonances whose origin are the same. The position of these resonances is dependent upon geometric parameters of the structure including arm separation and interparticle distance. The electric field distributions of the different structures are similar, even when the symmetry of the structures is reduced (as for the stretched and 'real' structure): the fields approximately retain their four-fold rotational symmetry. With regards to optical chirality, surface roughness can support 'hotspots', areas of enhanced optical chirality. However, this does not necessarily indicate that the structure will support areas of enhanced optical chirality across its entire surface. Further to this, the cleaning procedure of the nanostructures as it relates to plasma ashing requires further investigation to unambiguously link the spectral changes to the deformations suggested here.

In summary, the electric field and optical chirality properties of gammadion nanostructure arrays have been examined in response to

morphological and geometric changes. This will improve the understanding of the origin of CD modes in chiral metamaterials, allowing for a more rational design of their properties.

Chapter 6 Key Findings

- Circular dichroism modes associated with the gammadion array are dependent on interparticle spacing as well as periodicity.
- Surface roughness of the gammadion can support enhanced levels of optical chirality.
- Plasma ashing can cause distortions to nanostructure geometry which can change the position of circular dichroism modes associated with the nanostructure.

Chapter 7

**Superchirality and interference for chiral
plasmonic biodetection**

Nanostructures can support near fields whose chiral asymmetries are greater than that of CPL, a property which is referred to as superchirality. The ability of nanostructures to sense chiral molecules does not however scale with the magnitude of superchirality. In this section, it is shown that sensing capability does scale with the thickness of the nanostructure, a phenomenon which is discussed within the framework of optical chirality dissipation.

7.1 Modelling procedure

7.1.1 Nanostructure design

There are two nanostructure geometries under investigation in this section. They are chosen for their simplicity and because previous work has rendered them model systems for achiral and chiral nanostructures. The first is the gammadion, a cross formed from four Greek capital gammas (Γ) each rotated 90 degrees with respect to the previous. The structure therefore possesses 4-fold rotational symmetry. A cross structure with identical arm dimension to the gammadion was also constructed. The dimensions of these two nanostructures is shown in **Figure 7.1**.

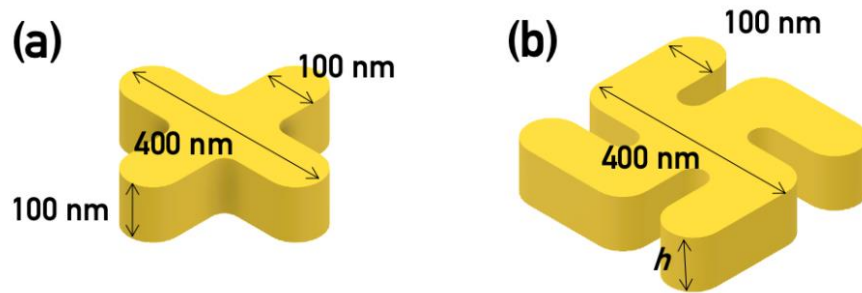


Figure 7.1: Simulated cross (a) and gammadion (b) nanostructures. The gammadion structure studied had variable heights of $h = 5, 30$ and 100 nm.

The cross structure is 100 nm thick with an arm width of 100 nm and an arm length of 400 nm. In free space, the cross is highly symmetric, belonging to the D_{4h} point group. The gammadion structure has a variable height, h equal to 5, 30 and 100 nm. Its arm width is 100 nm and the length of its central cross is 400 nm. The gammadion nanostructure in free space belongs to the C_{4h} point group. Although the gammadion structure is not chiral, its planar faces are intrinsically left or right handed and using a previous convention [82], [95], they will be referred to as the left (L) and right (R) faces (**Figure 7.2**).

The structures are constructed of solid gold, with refractive index values for the gold nanostructures taken from Johnson and Christy [89].

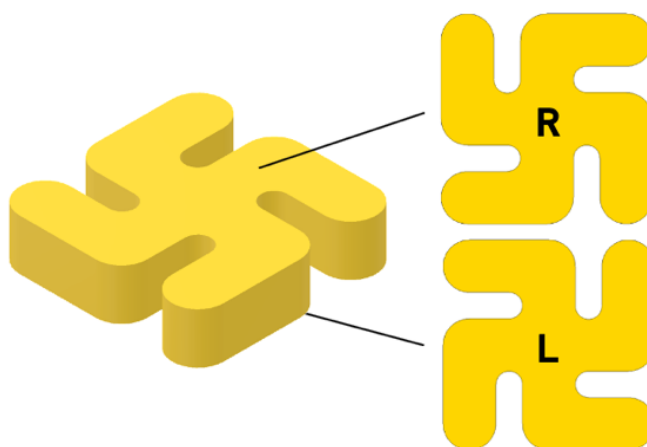


Figure 7.2: Idealised gammadion with right (R) and left (L) faces identified.

7.1.2 Modelling the unit cell

The modelling procedure in this section broadly replicates that which is outlined previously in **Chapter 6.2**. However, in this case the nanostructure is initially completely surrounded by a material with a constant refractive index, 1.5.

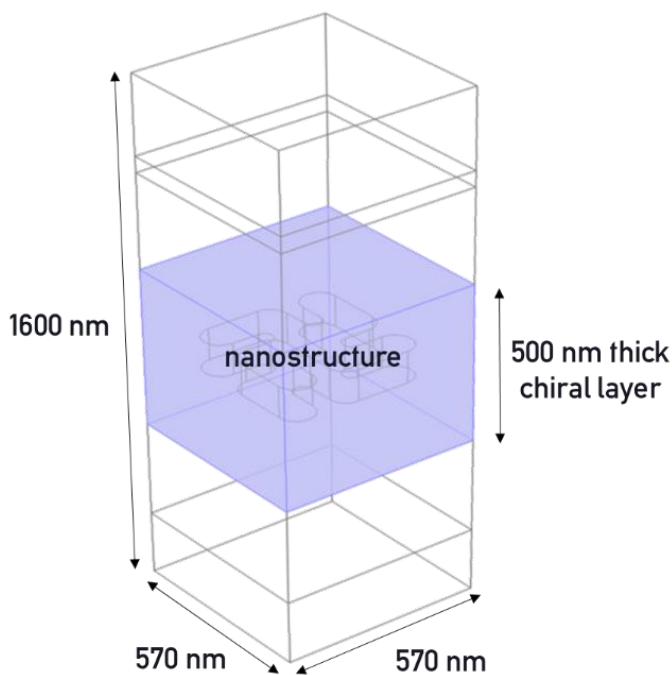


Figure 7.3: (a) 570×570 nm unit cell with a nanostructure in the centre. The 500 nm thick chiral layer is identified in blue.

The nanostructure was subsequently surrounded with a 500 nm thick isotropic non-absorbing chiral layer: its geometry with respect to the unit cell is shown in **Figure 7.3 (a)**. The simulation strategy implemented for modelling chiral dielectric layers has previously been used to replicate the experimental data of isotropic chiral layer adsorbed on chiral plasmonic metafilms [101]. The effect of a chiral dielectric on optical properties is modelled by modifying the constitutive equations for a chiral medium [102]:

$$\mathbf{D} = \varepsilon_0 \varepsilon_r \mathbf{E} + i \xi^{iso} \mathbf{B} \quad \text{Equation 7.1}$$

$$\mathbf{H} = \mathbf{B} / \mu_0 \mu_r + i \xi^{iso} \mathbf{E} \quad \text{Equation 7.2}$$

where

ε_r	relative permittivity
μ_r	relative permeability
\mathbf{D}	electric displacement field
\mathbf{H}	Magnetic field
ξ^{iso}	second rank tensor describing the chiral property of a molecular layer.

ξ^{iso} is only non-zero for a chiral dielectric. The sign of the pseudoscalar tensor elements ξ_{ij}^{iso} ($i, j = x, y \ \& \ z$) is defined by the handedness of the chiral dielectric. For an isotropic chiral medium only electric-dipole – magnetic dipole interactions contribute significantly to the asymmetry in optical responses [102]. In this case only the diagonal elements of the chirality tensor, ξ^{iso} are non-zero, with:

$$\xi^{iso} = \begin{bmatrix} \xi_{xx}^{iso} & 0 & 0 \\ 0 & \xi_{yy}^{iso} & 0 \\ 0 & 0 & \xi_{zz}^{iso} \end{bmatrix} \quad \text{Equation 7.3}$$

where

$$\xi_{xx}^{iso} = \xi_{yy}^{iso} = \xi_{zz}^{iso} \quad \text{Equation 7.4}$$

The nanostructures were simulated embedded in this isotropic chiral layer with a $\xi_{xx,yy,zz}^{iso} = 10^{-4}$ which is the value expected for isotropic chiral material which displays CD in the near UV [103]. Using a previous convention, [104] a positive value of the tensor elements models a right-handed material.

7.1.3 Calculated parameters

Simulations are performed with left CPL (LCP) and right CPL (RCP) which are incident on the L and R faces of the gammadion giving a total of four

combinations for each nanostructure (**Figure 7.4**). Simulations are also performed with LCP/RCP incident on the planar faces of the 100 nm thick cross structure giving a further two configurations.

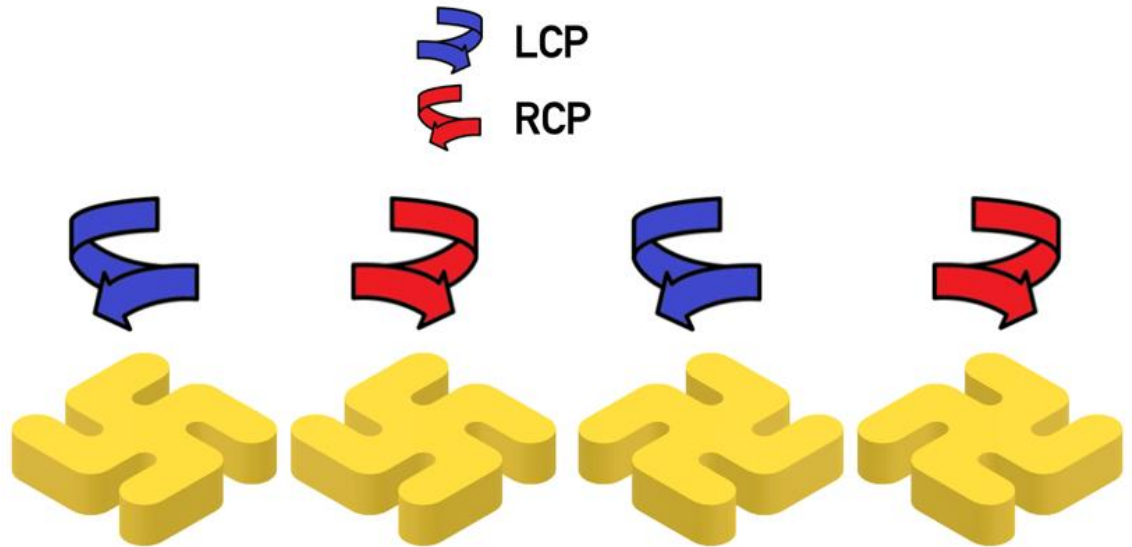


Figure 7.4: The four combinations of the incident structure face and light handedness are, 1. LCP incident on the RH face. 2. RCP incident on the RH face. 3. LCP incident on the LH face. 4. RCP Incident on the LH face.

CD spectra of each configuration is generated by separately calculating the transmission of RCP/LCP as outlined in previous sections.

Time averaged optical chirality flux, \bar{F} is calculated at a surface beyond the nanostructure and been normalised to the optical chirality flux and transmission of right CPL through glass. As previously stated, it has been shown the \bar{F} is proportional to the third Stokes parameter, S_3 [105] hence a reduction in the optical chirality flux corresponds to depolarisation of the incident beam and also to the dissipation of optical chirality. Time averaged optical chirality, \bar{C} has also been normalised to that of RCP, thus $\bar{C} = +1$ corresponds to RCP and $\bar{C} = -1$ corresponds to LCP. \bar{C} has been calculated at positions shown in **Figure 7.5**.

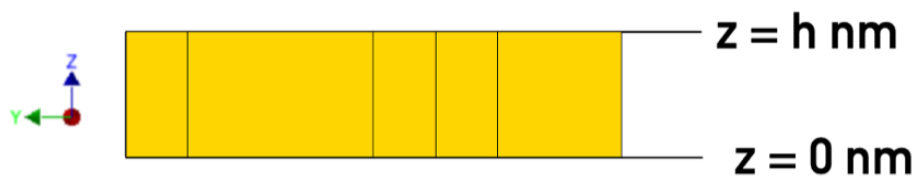


Figure 7.5: Time averaged optical chirality and surface charge density plots are taken at positions $z = 0$ and $z = h$ nm for each nanostructure.

Surface charge density plots are similarly calculated at positions identified in **Figure 7.5**. For surface charge density side plots, these were calculated looking down the y-axis for each nanostructure, as shown in **Figure 7.6**.

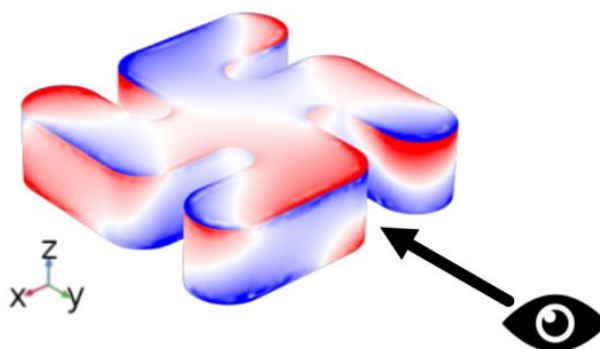


Figure 7.6: Surface charge density plots are calculated looking down the y-axis.

7.2 Metamaterial fabrication & model validation

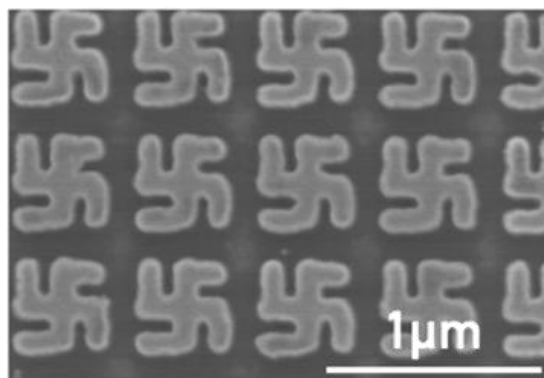


Figure 7.7: SEM image of the right-handed nanofabricated gold gammadion array.

To validate our modelling methodology, an array of right-handed gammadion structures was fabricated on a glass substrate. The CD spectra of this array was then compared with the simulated CD spectra of the structures. The sample for model validation was fabricated by Kensaku Endo, a collaborator from Osaka Prefecture University.

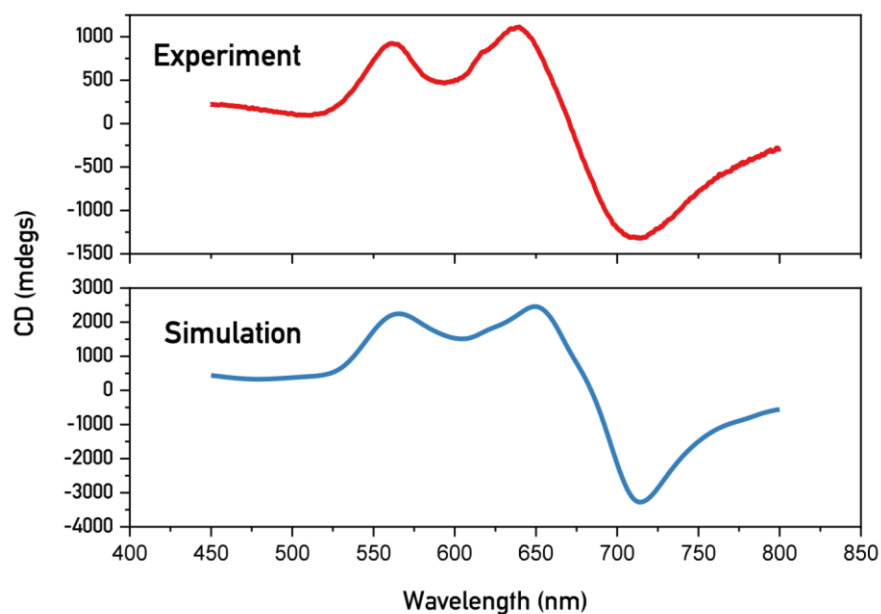


Figure 7.8: A comparison of experimentally derived CD spectra (top panel) and simulation (bottom panel) show good agreement.

In brief, the fabrication recipe was as follows. Borosilicate glass slides were cleaned using an acetone and Semiclean (a commercial wafer cleaner containing tetramethylammonium hydroxide) cleaning regime. Slides were spin coated with ZEP520A resist at baked for one hour at 180 °C. A charge conduction layer was spun. The pattern was subsequently written using an Elionix ELS-74000EXI electron beam lithography tool. The conduction layer was removed using water and the sample was developed in xylene before being metallised with 2 nm titanium and 100 nm of gold. The samples were soaked in butanone for lift off. An SEM image of the resulting array is shown in **Figure 7.7**. Using this SEM, with metallisation information, a model of the gammadion nanostructure was constructed.

The CD spectrum of the sample in air was measured and is compared with the simulation derived spectrum in **Figure 7.8**. The simulation replicates the CD spectrum of our experiment and that seen in previous work [82], [90], [95]. The magnitude of the simulated spectrum is approximately 2-3 times smaller than that of the experimental data. This can be rationalised by the fabrication strategy employed to reduce pattern writing time: 1 mm square arrays of the pattern are arranged in a checkerboard formation. Thus, only 50 % of the glass substrate is covered with gammadion structures, halving the CD signal intensity. Further intensity reduction is caused by structural defects caused by the fabrication process and missing nanostructures.

7.3 Results

7.3.1 Structures in achiral media

First, the CD spectrum of the cross is simulated surrounded in achiral media. As would be expected for an achiral and highly symmetric structure, the CD signal is approximately 0 across the wavelengths studied, **Figure 7.9**. The CD signal is independent of the planar face that light is incident upon which is expected as these two faces are identical.

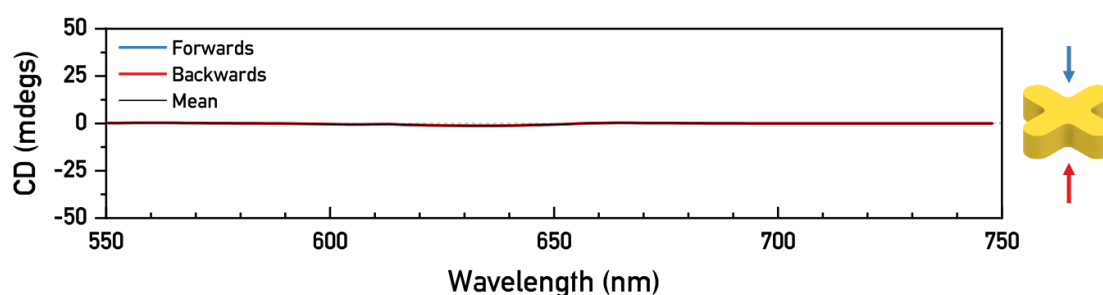


Figure 7.9: CD spectra of a gold cross when light is incident on both of its planar faces (blue and red).

The same CD calculations are subsequently performed on the two oppositely handed planar faces of the gammadion nanostructures of $h = 5, 30$ and 100 nm. Their CD spectra is shown in **Figure 7.10**. All structures exhibit a CD signal, however the sign changes depending upon the planar face that light is incident upon. The result is that the mean of these two spectra is ~ 0 across the wavelengths studied. This implies that if the nanostructures (both the gammadions and crosses) were freely floating in solution with an isotropic distribution of positions, they would exhibit no CD signal. The thinnest structure, $h = 5$ nm, shows the smallest CD signal, approximately an order of magnitude smaller than the $h = 30$ nm structure, which is in turn 5 times smaller than the $h = 100$ nm structure.

Because the CD signal is dependent upon the orientation of the nanoparticle the response can be described as non-reciprocal. This non-reciprocal response from achiral nanostructures can be rationalised by the non-uniform excitation of the structure due to its thickness. In a case where the gammadion nanostructure could be uniformly excited, no CD signal would be observed because L and R faces would display an equal but opposite interaction with CPL resulting in no net CD. This case can only occur where the attenuation length (λ_{Au} for gold) is much less than the thickness of the structure, h . At $550 -$

750 nm, $\lambda_{Au} = 17.7 - 13.3$ nm respectively, meaning this condition is not met for the h values and wavelengths studied.

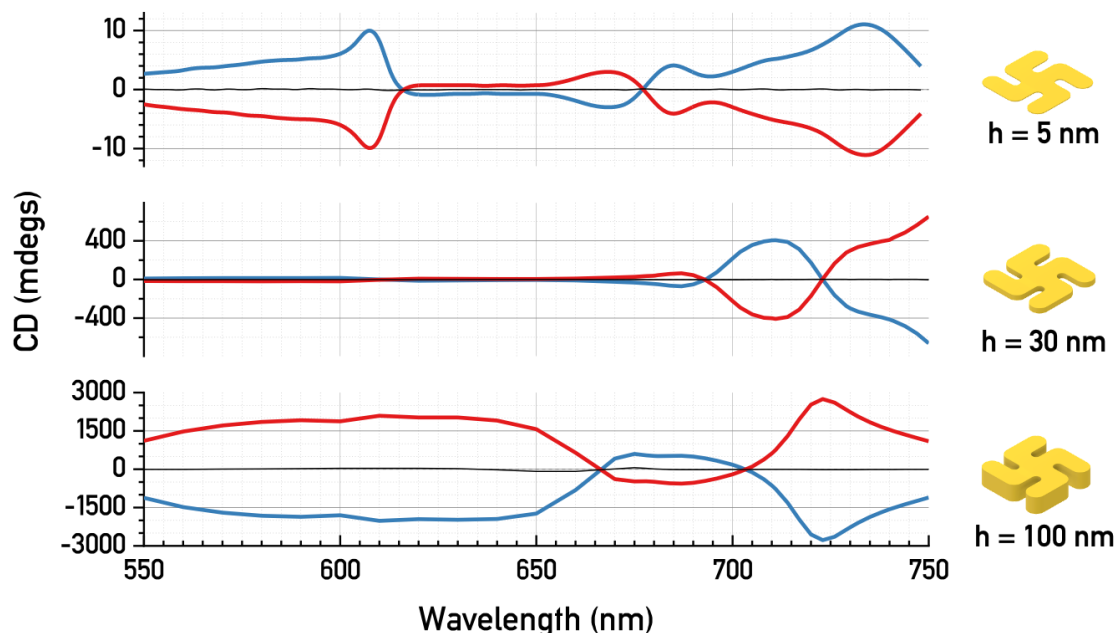


Figure 7.10: Simulated CD spectra for gammadions of $h = 5$ (top panel), 30 (middle panel) and 100 nm (bottom panel). Blue lines are spectra for light incident upon the right-handed face (visible in the diagrams to the right of the spectra). Red lines are spectra for light incident upon left-handed faces of the structure. The mean of the two configurations is shown in black is ~ 0 across the wavelengths studied.

It is possible to visualise the nanostructure absorption by generating electric field plots for each gammadion thickness at a plane which bisects the nanostructure, **Figure 7.11**. For comparative purposes, all plots have been generated for RCP light incident upon the R face of the gammadion nanostructure. In the 5 nm thick case, fields penetrate the gold bulk. In the 30 nm case, the fields are significantly weakened. In the 100 nm thick structure, the structure is sufficiently thick such that there is no penetration into the bulk of the metal.

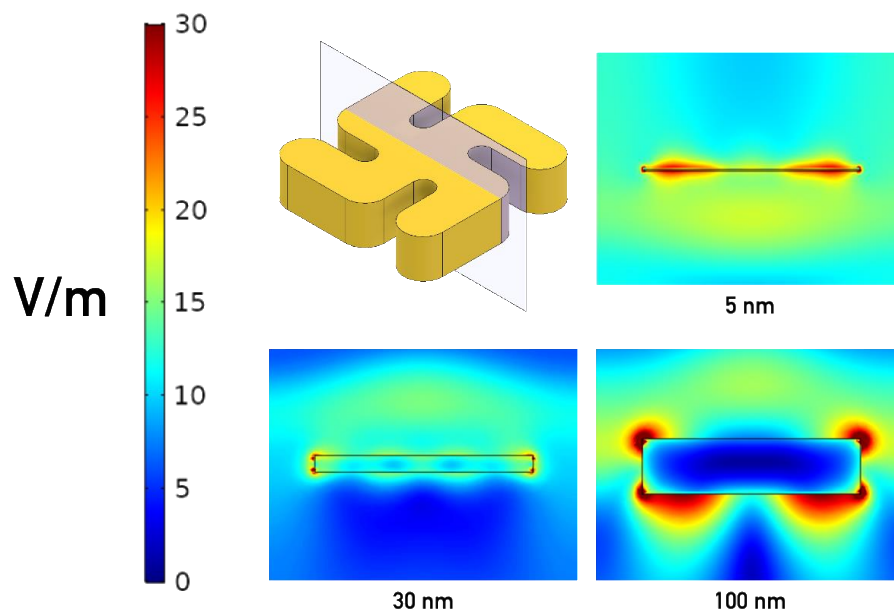


Figure 7.11: Electric field plots at a plane which bisects the structure (top left) for the $h = 5, 30$ and 100 nm thick gammadion nanostructures.

Optical chirality flux plots have been derived for each of the nanostructure face and light polarisation combinations (**Figure 7.12**). Transmitted time averaged optical chirality flux values have been normalised to that of RCP, giving \bar{F} . If $|\bar{F}|$ is less than unity it is an indication that optical chirality has been dissipated by the nanostructure.

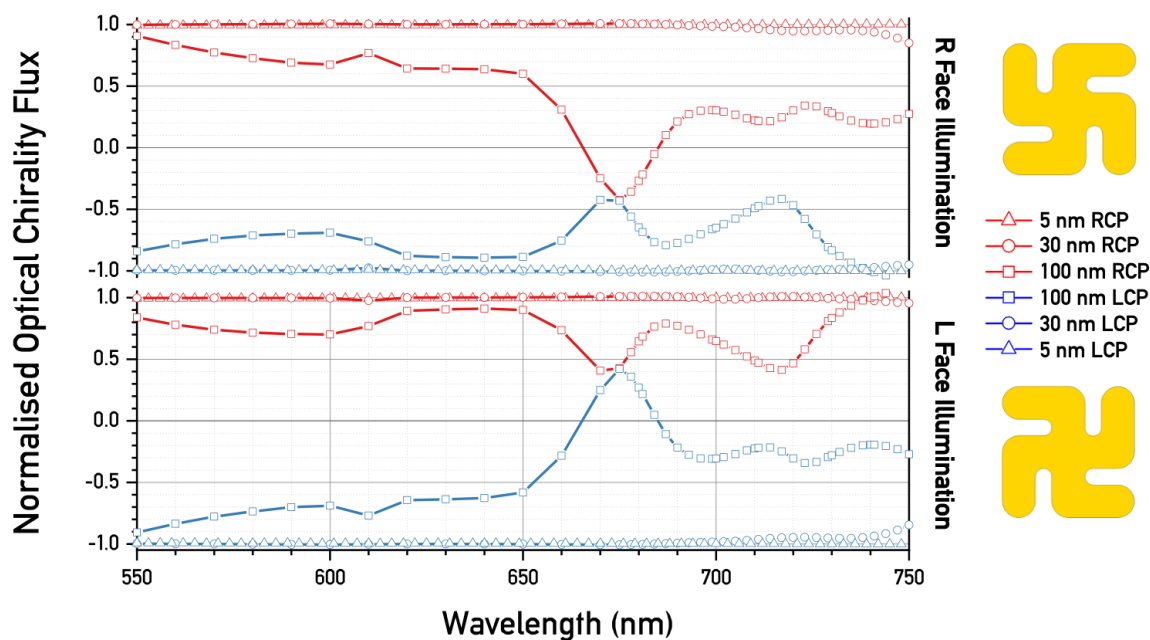


Figure 7.12: Normalised optical chirality flux plots for the nanostructures suspended in achiral media for $h = 5$ nm (triangles) 30 nm (circles) and 100 nm (squares) for R face illumination (top panel) and L face illumination (bottom panel) by RCP (red plots) and LCP (blue plots).

The plots in (Figure 7.12) show the optical chirality flux which exhibit the expected behaviour of a chiral system. That is, combinations of light polarisation and nanostructure face which are related by mirror symmetry display an equal yet opposite signal. Consider only the 100 nm case: the \bar{F} spectrum for RCP incident upon the R face is a mirror image of LCP incident upon the L face.

In the $h = 5$ nm and 30 nm case, there is very little dissipation of optical chirality. This too, as previously stated, means that there has been very little depolarisation of the beam. For the $h = 100$ nm thick structure however, there is a dramatic change to the optical chirality flux spectra. There is significant dissipation across the wavelength range studied with the greatest dissipation for the RCP (LCP), R (L) face combinations. In the 665-685 nm wavelength range, the sign for these combinations reverse.

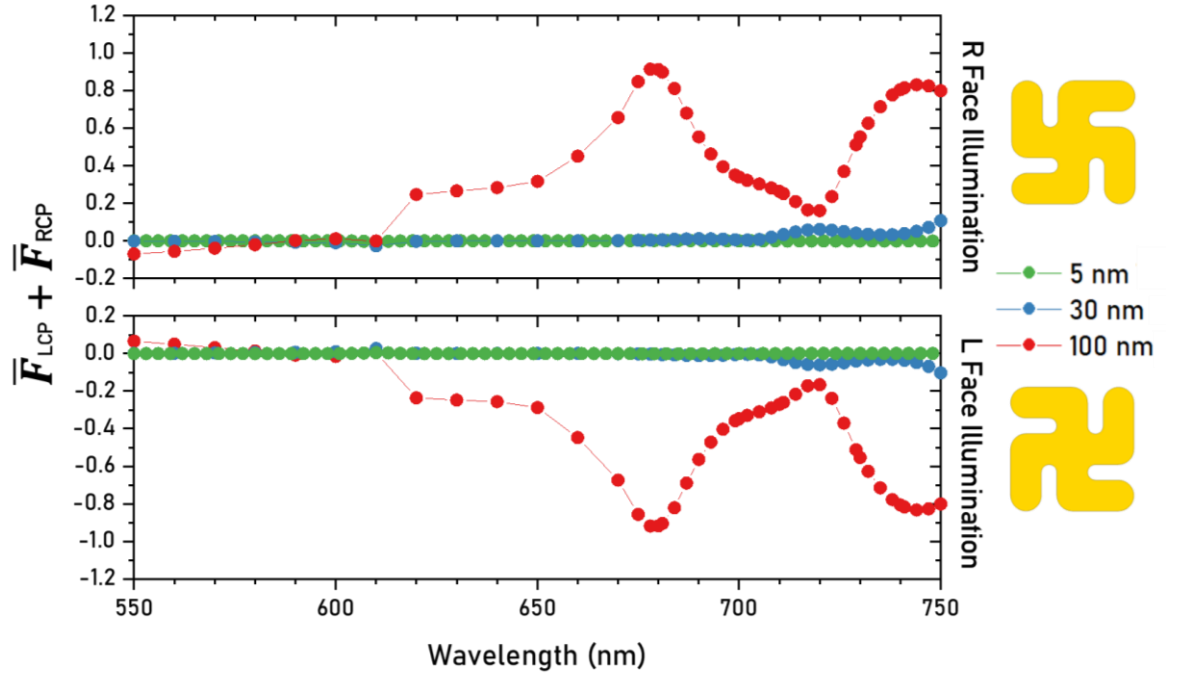


Figure 7.13: Sum of \bar{F} for LCP and RCP for R face illumination and L face illumination for the three gammadians in achiral media. For opposite face illuminations, the sum is equal in magnitude but opposite in sign.

The sum of LCP and RCP components for each structure for R face and L face illumination is shown in Figure 7.13. For opposite face illumination, the sum spectra are equal and opposite, like the CD spectra. The minima and maxima in the \bar{F} sum spectra do not correlate with resonance positions in the CD spectra.

Time-averaged optical chirality (\bar{C}) plots for each of the combinations at the wavelength of the maximum CD (Figure 7.14) have been calculated with

the integrated optical chirality values also included. For the thinnest structure, $h = 5$ nm, the sign of the optical chirality across the structure mostly matches that of the polarisation of the incident light. There are areas on the nanostructure where $\bar{C} > 1$ and so can be described as superchiral. The maximum value of $|\bar{C}|$ is approximately 6 on average, but there are areas where it falls below 1. Like the $h = 5$ nm case, for $h = 30$ nm the value of \bar{C} matches that of the incident light.

However, there are regions where the sign changes, most pronounced in the R/LCP and R/RCP combinations. The average maximum value of $|\bar{C}|$ for the $h = 30$ nm structures is ~ 5 . As with the \bar{F} plots, the most significant changes are to the $h = 100$ nm thick structures. The near fields have significant regions where the sign of \bar{C} is opposite to that of the incident CPL. The average maximum value of $|\bar{C}|$ is 8.

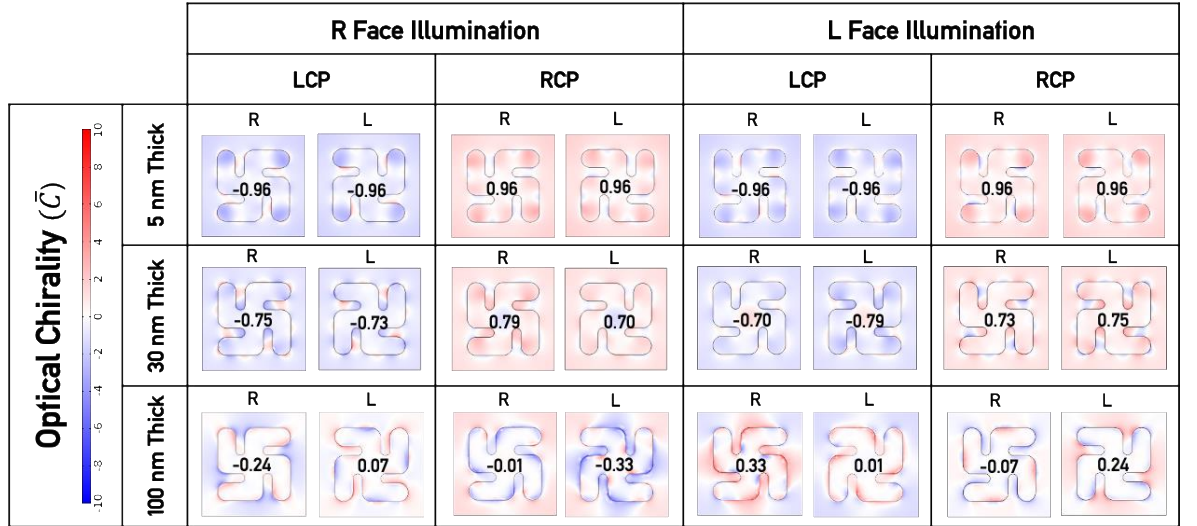


Figure 7.14: Optical chirality plots for the $h = 5, 30$ and 100 nm thick structures in achiral media. The integrated chirality value across the structure is shown in the centre of each plot.

It has been previously described how chirality is a conserved quantity [75], [79], [81], [106]. Thus, if there is a change observed to \bar{C} and \bar{F} , this must be offset by commensurate change in the chirality of the electron distributions of the chiral plasmonic nanostructure. This has been validated by generating instantaneous surface charge distributions of each of the nanostructures (Figure 7.15). The plots show surface charge density of both the planar faces of the gammadion nanostructure and a view of the side wall (see Figure 7.6 for side view position).

As with previous plots, configurations which are enantiomerically related are mirror symmetric. As would be expected, because of the increased dissipation of optical chirality the asymmetry of the charge distributions

increases with h . For the $h = 5$ nm structure, all four polarisations and light incidence combinations produce overall charge distributions on the L and R faces which are near identical. For the $h = 30$ nm case, the L and R faces display a 180° phase differences. The simulations thus indicate that the time-averaged charge distributions on the L and R faces will be very similar. For both of these thinner structures the side profile distributions are highly symmetrical about the horizontal mirror plane. If the symmetry of the gammadion nanostructure is considered in terms of the surface charge distribution then for the 5 and 30 nm case, the chiral perturbation is very small. Compare this with the 100 nm thick structure: L and R faces show distinct surface charge density distributions and side wall maps show breaking of the horizontal mirror plane.

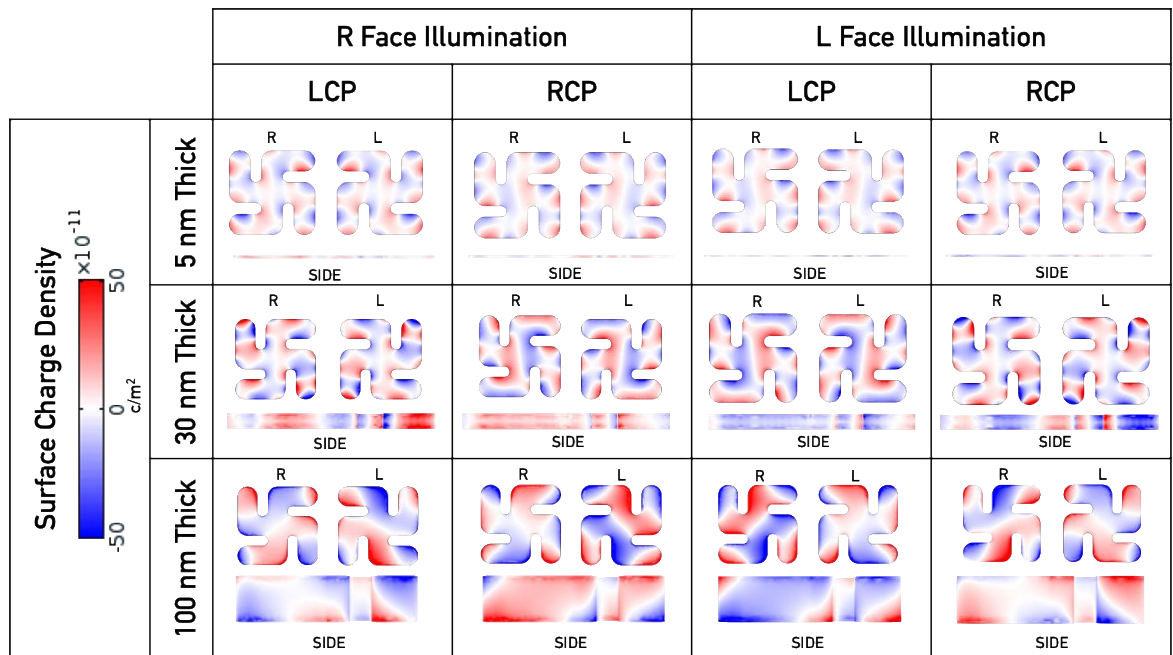


Figure 7.15: Surface charge density plots on the R and L faces of the structure and side views for the $h = 5, 30$ and 100 nm gammadions suspended in achiral media.

The simulation of \bar{C} , \bar{F} and surface charge density plots are consistent with the interconversion of optical and electronic chirality for the $h = 100$ nm thick structure. An increase in the dissipation of optical chirality results in a commensurate increase in chiral currents thus greater asymmetry in surface charge distributions.

Previously it has been proposed that optical chirality is dissipated through loss (by absorption) and at interfaces [79]. The h dependence of the optical chirality flux is inconsistent with a mechanism based on loss, as it does not scale with calculated absorption values. Similarly, if the interface mechanism was responsible for the observed effects, then it would be expected

that optical chirality flux would scale with the surface area of the gammadion: this is not observed.

This suggests the existence of a previously unconsidered mechanism of optical chirality dissipation which is consistent with the dependence on the nanostructure height, h . This model is referred to as an interference model as it occurs due to the interference of chiral near fields generated at the two planar faces of the gammadion nanostructures. In summary, the model assumes that these two oppositely handed faces are spatially separated sources of chiral near fields which can interfere both with each other and incident light. The result is that the optical chirality flux, $\bar{\mathbf{F}}$ is dependent upon the phase difference between the two sources and incident light.

Beginning with the expression for time average optical chirality flux, $\bar{\mathbf{F}}$, it is possible to then express \mathcal{E} and \mathcal{B} as the sum of fields generated by incident light and the oppositely handed faces of the structure:

$$\mathcal{E} = \mathcal{E}_I + \mathcal{E}_L e^{i\theta} + \mathcal{E}_R e^{i\varphi} \quad \text{Equation 7.5}$$

$$\mathcal{B} = \mathcal{B}_I + \mathcal{B}_L e^{i\theta} + \mathcal{B}_R e^{i\varphi} \quad \text{Equation 7.6}$$

where \mathcal{B}_I and \mathcal{E}_I are the fields of the incident light; \mathcal{B}_L , \mathcal{E}_L , \mathcal{B}_R and \mathcal{E}_R are the fields generated by the left and right handed faces and θ and φ are the relative phases of the fields at the left and right handed faces relative to the incident light. Substitution of **Equation 7.5** and **Equation 7.6** into **Equation 5.5**, the expression for time averaged optical chirality flux yields the following expression:

$$\begin{aligned} \bar{\mathbf{F}} = & \frac{1}{4} Re [(\mathcal{E}_I + \mathcal{E}_L e^{i\theta} \\ & + \mathcal{E}_R e^{i\varphi}) \times \nabla \times (\mathcal{B}_I^* + \mathcal{B}_L^* e^{-i\theta} + \mathcal{B}_R^* e^{-i\varphi}) \\ & - (\mathcal{B}_I + \mathcal{B}_L e^{i\theta} + \mathcal{B}_R e^{i\varphi}) \times \nabla \\ & \times (\mathcal{E}_I^* + \mathcal{E}_L^* e^{-i\theta} + \mathcal{E}_R^* e^{-i\varphi})] \end{aligned} \quad \text{Equation 7.7}$$

When expanded this gives:

$$\begin{aligned}
 \bar{F} &= \frac{1}{4} \text{Re} [\mathcal{E}_I \times (\nabla \times \mathcal{B}_I^*) + \mathcal{E}_I \times (\nabla \times \mathcal{B}_L^*) e^{-i\theta} \\
 &+ \mathcal{E}_I \times (\nabla \times \mathcal{B}_R^*) e^{-i\varphi} + \mathcal{E}_L \times (\nabla \times \mathcal{B}_I^*) e^{i\theta} \\
 &+ \mathcal{E}_L \times (\nabla \times \mathcal{B}_L^*) + \mathcal{E}_L \times (\nabla \times \mathcal{B}_R^*) e^{i(\theta-\varphi)} \\
 &+ \mathcal{E}_R \times (\nabla \times \mathcal{B}_I^*) e^{i\varphi} + \mathcal{E}_R \times (\nabla \times \mathcal{B}_L^*) e^{-i(\theta-\varphi)} \\
 &+ \mathcal{E}_R \times (\nabla \times \mathcal{B}_R^*) - \mathcal{B}_I \times (\nabla \times \mathcal{E}_I^*) \\
 &- \mathcal{B}_I \times (\nabla \times \mathcal{E}_L^*) e^{-i\theta} - \mathcal{B}_I \times (\nabla \times \mathcal{E}_R^*) e^{-i\varphi} \\
 &- \mathcal{B}_L \times (\nabla \times \mathcal{E}_I^*) e^{i\theta} - \mathcal{B}_L \times (\nabla \times \mathcal{E}_L^*) \\
 &- \mathcal{B}_L \times (\nabla \times \mathcal{E}_R^*) e^{i(\theta-\varphi)} - \mathcal{B}_R \times (\nabla \times \mathcal{E}_I^*) e^{i\varphi} \\
 &- \mathcal{B}_R \times (\nabla \times \mathcal{E}_L^*) e^{-i(\theta-\varphi)} - \mathcal{B}_R \times (\nabla \times \mathcal{E}_R^*)] \\
 &= \frac{1}{4} \text{Re} [\{\mathcal{E}_I \times (\nabla \times \mathcal{B}_I^*) - \mathcal{B}_I \times (\nabla \times \mathcal{E}_I^*)\} \\
 &+ \{\mathcal{E}_L \times (\nabla \times \mathcal{B}_L^*) - \mathcal{B}_L \times (\nabla \times \mathcal{E}_L^*)\} \\
 &+ \{\mathcal{E}_R \times (\nabla \times \mathcal{B}_R^*) - \mathcal{B}_R \times (\nabla \times \mathcal{E}_R^*)\} \\
 &+ \{\mathcal{E}_I \times (\nabla \times \mathcal{B}_L^*) e^{-i\theta} - \mathcal{B}_L \times (\nabla \times \mathcal{E}_I^*) e^{i\theta}\} \\
 &+ \{\mathcal{E}_I \times (\nabla \times \mathcal{B}_R^*) e^{-i\varphi} - \mathcal{B}_R \times (\nabla \times \mathcal{E}_I^*) e^{i\varphi}\} \\
 &+ \{\mathcal{E}_L \times (\nabla \times \mathcal{B}_I^*) e^{i\theta} - \mathcal{B}_I \times (\nabla \times \mathcal{E}_L^*) e^{-i\theta}\} \\
 &+ \{\mathcal{E}_R \times (\nabla \times \mathcal{B}_I^*) e^{i\varphi} - \mathcal{B}_I \times (\nabla \times \mathcal{E}_R^*) e^{-i\varphi}\} \\
 &+ \{\mathcal{E}_L \times (\nabla \times \mathcal{B}_R^*) e^{i(\theta-\varphi)} \\
 &- \mathcal{B}_R \times (\nabla \times \mathcal{E}_L^*) e^{-i(\theta-\varphi)}\} \\
 &+ \{\mathcal{E}_R \times (\nabla \times \mathcal{B}_L^*) e^{-i(\theta-\varphi)} \\
 &- \mathcal{B}_L \times (\nabla \times \mathcal{E}_R^*) e^{i(\theta-\varphi)}\}]
 \end{aligned} \tag{Equation 7.8}$$

The following expressions can be used to reduce the number of terms in the equations: $\mathcal{F}_{ij} = \mathcal{E}_i \times (\nabla \times \mathcal{B}_j^*) - \mathcal{B}_j \times (\nabla \times \mathcal{E}_i^*)$ and $\mathcal{G}_{ij} = \mathcal{E}_i \times (\nabla \times \mathcal{B}_j^*) + \mathcal{B}_j \times (\nabla \times \mathcal{E}_i^*)$. Thus, **Equation 7.8** can be written more succinctly as:

$$\begin{aligned}
 \bar{F} &= \frac{1}{4} \text{Re} [\mathcal{F}_{II} + \mathcal{F}_{LL} + \mathcal{F}_{RR} + (\mathcal{F}_{IL} + \\
 &\mathcal{F}_{LI}) \cos \theta - i(\mathcal{G}_{IL} - \mathcal{G}_{LI}) \sin \theta + (\mathcal{F}_{IR} + \\
 &\mathcal{F}_{RI}) \cos \varphi - i(\mathcal{G}_{IR} - \mathcal{G}_{RI}) \sin \varphi + (\mathcal{F}_{LR} + \\
 &\mathcal{F}_{RL}) \cos(\theta - \varphi) - i(\mathcal{G}_{LR} - \mathcal{G}_{RL}) \sin(\varphi - \theta)]
 \end{aligned} \tag{Equation 7.9}$$

Relationships $\mathcal{F}_{ji} = \mathcal{F}_{ij}^*$ and $\mathcal{G}_{ji} = \mathcal{G}_{ij}^*$ are valid in free space. Thus,

$$\begin{aligned}
 \bar{F} &= \frac{1}{4} \text{Re} [\mathcal{F}_{II} + \mathcal{F}_{LL} + \mathcal{F}_{RR} \\
 &+ 2\text{Re}(\mathcal{F}_{IL} \cos \theta + \mathcal{F}_{IR} \cos \varphi + \mathcal{F}_{LR} \cos(\varphi - \theta)) \\
 &+ 2\text{Im}(\mathcal{G}_{IL} \sin \theta + \mathcal{G}_{IR} \sin \varphi + \mathcal{G}_{LR} \sin(\varphi - \theta))]
 \end{aligned} \tag{Equation 7.10}$$

Collection of like terms in **Equation 7.10** and writing in terms of the optical chirality flux generated by each face of the nanostructure yields the following expression for the time averaged real part of optical chirality flux:

$$\begin{aligned} \bar{F} = & \frac{1}{4} Re(\mathcal{F}_{II} + \mathcal{F}_{LL} + \mathcal{F}_{RR}) + \frac{1}{2} Re(\mathcal{F}_{IL} \cos \theta \\ & + \mathcal{F}_{IR} \cos \varphi \\ & + \mathcal{F}_{LR} \cos(\varphi - \theta)) + \frac{1}{2} Im(\mathcal{G}_{IL} \sin \theta \\ & + \mathcal{G}_{IR} \sin \varphi + \mathcal{G}_{LR} \sin(\varphi - \theta)) \end{aligned} \quad \text{Equation 7.11}$$

Again, to reduce complexity the following expressions can be used: $\bar{F}_{ij} = \frac{1}{4} Re(\mathcal{F}_{ij})$ and $\bar{G}_{ij} = \frac{1}{4} Im(\mathcal{G}_{ij})$. Thus, **Equation 7.11** becomes:

$$\begin{aligned} \bar{F} = & (\bar{F}_{II} + \bar{F}_{LL} + \bar{F}_{RR}) \\ & + 2(\bar{F}_{IL} \cos \theta + \bar{F}_{IR} \cos \varphi \\ & + \bar{F}_{LR} \cos(\varphi - \theta)) \\ & + 2(\bar{G}_{IL} \sin \theta + \bar{G}_{IR} \sin \varphi \\ & + \bar{G}_{LR} \sin(\varphi - \theta)) \end{aligned} \quad \text{Equation 7.12}$$

Equation 7.12 is the critical expression of this model. In **Equation 7.12**, $\bar{F}_{II}, \bar{F}_{LL}, \bar{F}_{RR}$ are the time averaged optical chirality fluxes of the incident light, the left handed face in isolation and the right handed face in isolation respectively. The remaining terms account for interference between the incident light and the two sources. Crucially, the expression establishes the link between \bar{F} and phase. It suggests that optical chirality can be dissipated through an interference mechanism which involves relative changes in phase.

Up to this point \bar{F} has been considered only in generic terms, for any light polarisation and face incidence. It is possible to specify the optical chirality flux in terms of face of incidence, where L Inc and R Inc denote light incident on the left and right handed faces of the gammadion respectively. When surrounded by achiral material, ${}_{L\text{ Inc}(R\text{ Inc})}^{LCP} \bar{F}$ (optical chirality flux for LCP incident on the L(R) face of the gammadion, where L and R are interchangeable) and ${}_{R\text{ Inc}(L\text{ Inc})}^{RCP} \bar{F}$ (optical chirality flux for RCP incident upon the R(L) face of the gammadion, where R and L are interchangeable) are enantiomeric pairs: they have equal but opposite values. They can be related by the following expression:

$${}_{L\text{ Inc}(R\text{ Inc})}^{LCP} \bar{F} = - {}_{R\text{ Inc}(L\text{ Inc})}^{RCP} \bar{F} \quad \text{Equation 7.13}$$

From this expression it is possible to derive further enantiomeric pair relationships:

$${}_{L\text{ Inc}(R\text{ Inc})}^{LCP(RCP)} \theta = {}_{R\text{ Inc}(L\text{ Inc})}^{RCP(LCP)} \varphi \quad \text{Equation 7.14}$$

$$\text{LCP(RCP)}_{\text{R Inc(L Inc)}}\theta = \text{RCP(LCP)}_{\text{L Inc(R Inc)}}\varphi \quad \text{Equation 7.15}$$

$$\text{LCP(RCP)}_{\text{L Inc(R Inc)}}\bar{\mathbf{F}}_L = -\text{RCP(LCP)}_{\text{R Inc(L Inc)}}\bar{\mathbf{F}}_R \quad \text{Equation 7.16}$$

$$\text{LCP(RCP)}_{\text{R Inc(L Inc)}}\bar{\mathbf{F}}_L = -\text{RCP(LCP)}_{\text{L Inc(R Inc)}}\bar{\mathbf{F}}_R \quad \text{Equation 7.17}$$

$$\text{LCP}\bar{\mathbf{F}}_I = -\text{RCP}\bar{\mathbf{F}}_I \quad \text{Equation 7.18}$$

Equation 7.14 and **Equation 7.15** express the enantiomeric relationships for the interference terms which are introduced in **Equation 7.11**. For this simple interference model, the following relationship holds:

$$2\pi \frac{hn}{\lambda} = (\theta - \varphi) \quad \text{Equation 7.19}$$

where n is the refractive index of the surrounding medium, λ is the wavelength of light and h is the height of the nanostructure. **Equation 7.19** correlates the increase in the height of the nanostructure with an increase in the phase difference generated by its two faces.

In summary, it is proposed that this new model of optical chirality dissipation is dependent upon an interference mechanism. This mechanism is analogous to the case of energy flux where interference can suppress radiative emission, with material currents acting as a ‘reservoir’ of energy. In this case, instead of currents acting as a reservoir of energy, they instead act as a source of chirality. As h increases, so too do the values of $\theta - \varphi$ and θ or φ (depending upon the face of incidence).

The combination of **Equation 7.12** and **Equation 7.19** imply that an increase in h causes a commensurate change in optical chirality dissipation. The result of this is that there are higher levels of chiral material currents within the structure. Simply, LCP (RCP) is more strongly dissipated on a L(R) structure, which gives rise to the non-zero sum spectra shown in **Figure 7.13**.

7.3.2 Structures in chiral media

Up to this point, simulations have been performed by surrounding the structures with a non-absorbing achiral media. Subsequently, the structures were surrounded with an isotropic non-absorbing chiral medium as described in **Chapter 4.3**.

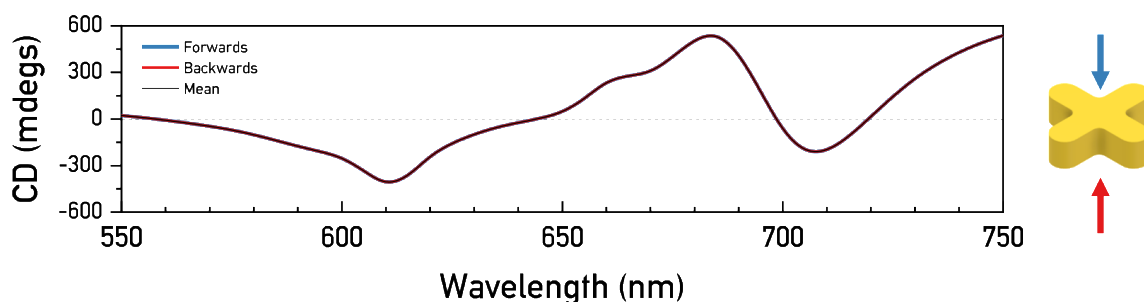


Figure 7.16: Simulated CD spectra for the cross surrounded by chiral media for light incident in the forwards and backwards direction.

First, the cross was surrounded in chiral media and CD calculations were repeated with light incident upon each planar face of the structure. These CD spectra are shown in **Figure 7.16** with the forwards direction shown in blue, backwards direction in red and their mean shown in black. The backwards and forwards direction CD signals are identical and can be described as reciprocal. This is intuitive as the cross structure is identical when viewed in these directions.

The wavelength position of the induced chiral plasmon in the simulation of the cross structures is qualitatively similar to chiral induction by molecular chiral layers in plasmonic crosses [107] and nano-islands [108]. In short, chiral induction describes the coupling between a localised surface plasmon from a nonchiral object with a chiral molecular layer which induces plasmonic chirality [107]. The size of the induced CD in the simulation is an order of magnitude larger than in the cross experiment described in the previous reference. This difference can be attributed to a number of factors including:

- (a) The cross in the experiment was not completely surrounded by the chiral dielectric.
- (b) The film in the experiment was thinner.
- (c) The experimental samples were fabricated in a ‘checkerboard’ pattern as previously described.

The same simulations were then performed with the gammadion nanostructures surrounded by chiral media. The observed effects of the chiral dielectric is dependent upon the thickness of the nanostructure (**Figure 7.17**). For the $h = 5$ nm gammadion structure, there is a background to due chiral induction which is comparable to the magnitude of the inherent CD of the nanostructure. This induced CD background has resonances at 615 and 670 nm: similar features are induced in the cross structure. When this background is

taken into account, there is minimal asymmetry in the inherent CD resonance positions.

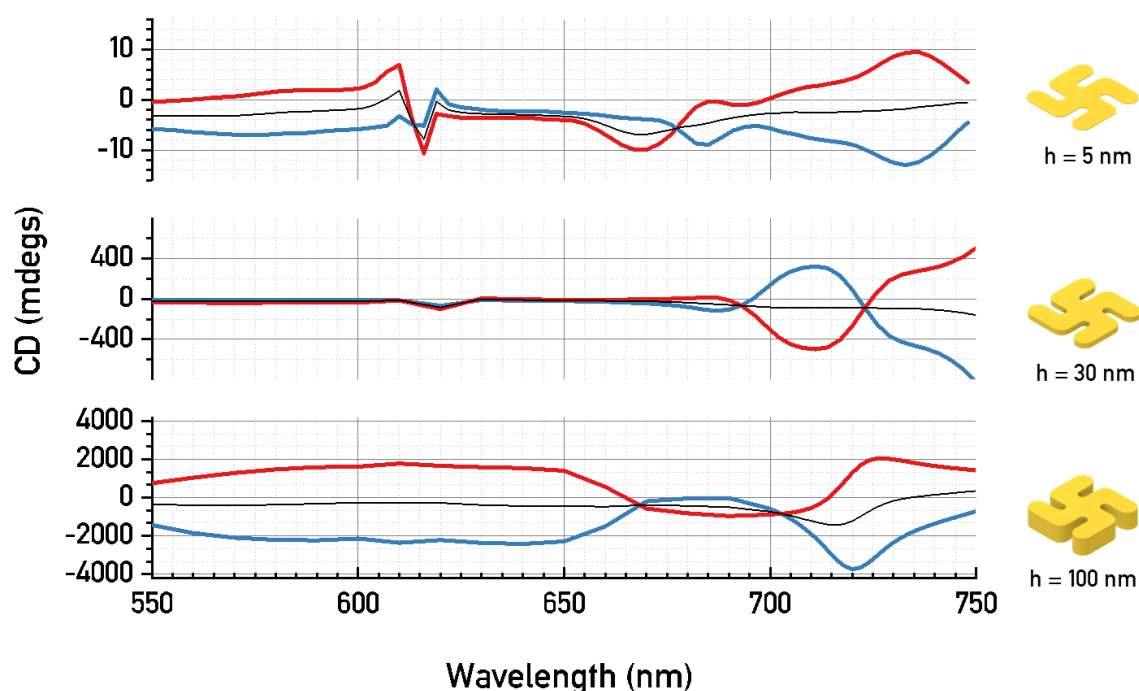


Figure 7.17: Simulated CD spectra for gammadions surrounded by chiral media of $h = 5$ (top panel), 30 (middle panel) and 100 nm (bottom panel). Blue lines are spectra for light incident upon the right-handed face (visible in the diagrams to the right of the spectra). Red lines are spectra for light incident upon left-handed faces of the structure. The mean of the two configurations is shown in black.

For the $h = 30$ and $h = 100$ nm thick structures, the background has less effect on the spectra because of the larger magnitude of the inherent CD resonances. For the $h = 30$ nm case, the presence of the chiral dielectric does not cause significant changes to the spectra. There are no significant changes in the inherent resonance positions. The greatest change occurs to the $h = 100$ nm thick structure. Asymmetric shifts of approximately 8 nm are observed in the intrinsic CD resonances of the structure, largest at around 720 nm. Qualitatively, this replicates previous observations of chiral molecular sensing [82], [109] although direct comparison is not applicable as previous experiments were conducted with the nanostructures on substrates rather than freely floating.

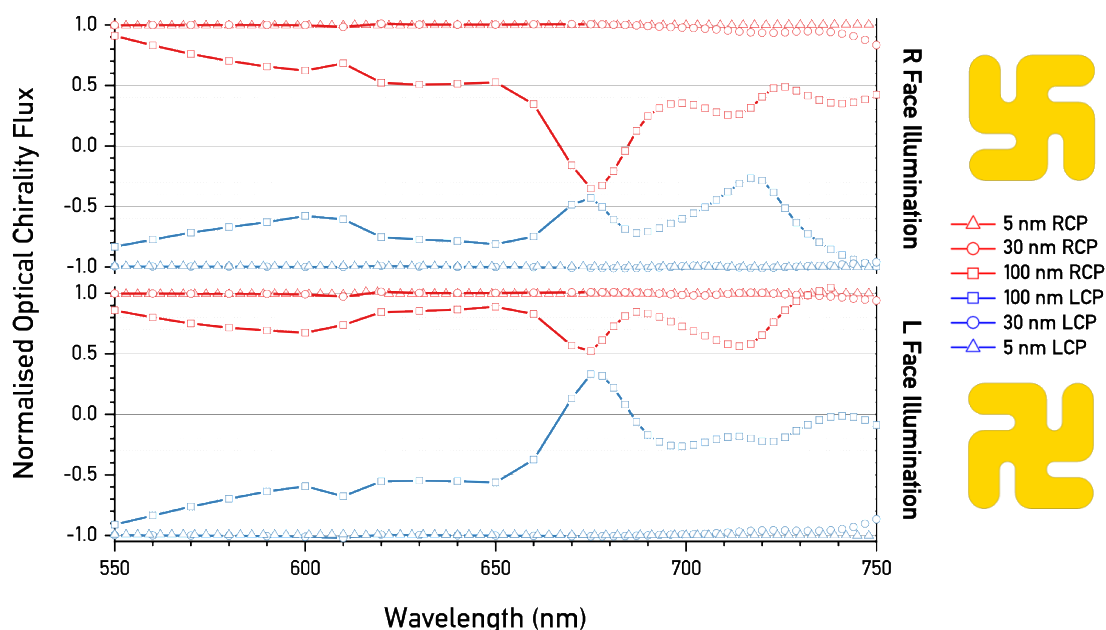


Figure 7.18: Normalised optical chirality flux plots for the nanostructures suspended in chiral media for $h = 5$ nm (triangles) 30 nm (circles) and 100 nm (squares) for R face illumination (top panel) and L face illumination (bottom panel) by RCP (red plots) and LCP (blue plots).

The \bar{F} spectra, as shown in **Figure 7.18** are similar to those derived from the structures immersed in achiral media, but with some key differences. For the $h = 5$ and 30 nm structures, the chiral dielectric induces a new feature at 610 nm, which coincides with the induced CD peak. This feature does not display mirror image behaviour between the enantiomeric pair combinations of face handedness and CPL. The presence of the chiral dielectric does not significantly affect the spectra in the rest of the wavelength range, with enantiomeric pairs displaying near mirror symmetry. The greatest change occurs to the $h = 100$ nm thick structure. There is complete breakdown between of the mirror symmetry between enantiomeric pair combinations. The chiral dielectric allows LCP to be more effectively dissipated whilst RCP is less effectively dissipated, compared to when the structures are immersed in achiral material.

As before, the sum of the LCP and RCP components of \bar{F} have been calculated and are shown in **Figure 7.19**. For a given structure, the LH and RH spectra are no longer symmetric with the 100 nm thick structure showing the largest asymmetry. Again, their resonance positions do not correlate with the CD positions. This indicates that the optical chirality flux spectra can serve as a sensor of optical chirality.

\bar{C} plots have been calculated at the maximum CD wavelength (**Figure 7.20**). These are like the plots generated in achiral media, with no significant changes in sign or distribution. Consider the average integrated \bar{C} values for

different light/face configurations. For LCP/R, \bar{C} values for the achiral and chiral dielectrics are -0.24 and 0.22 respectively. This decrease in the absolute value of optical chirality of the near field indicates enhanced dissipation. In the corresponding enantiomeric pair, RCP/L, the achiral and chiral values are 0.24 and 0.26 indicating a reduced level of dissipation.

The simulations of chiral dielectrics replicate two previously reported phenomena:

- (a) Molecular layer induced chiral induction in plasmonic nanoparticles.
- (b) Chiral molecular sensing with chiral plasmonic particles.

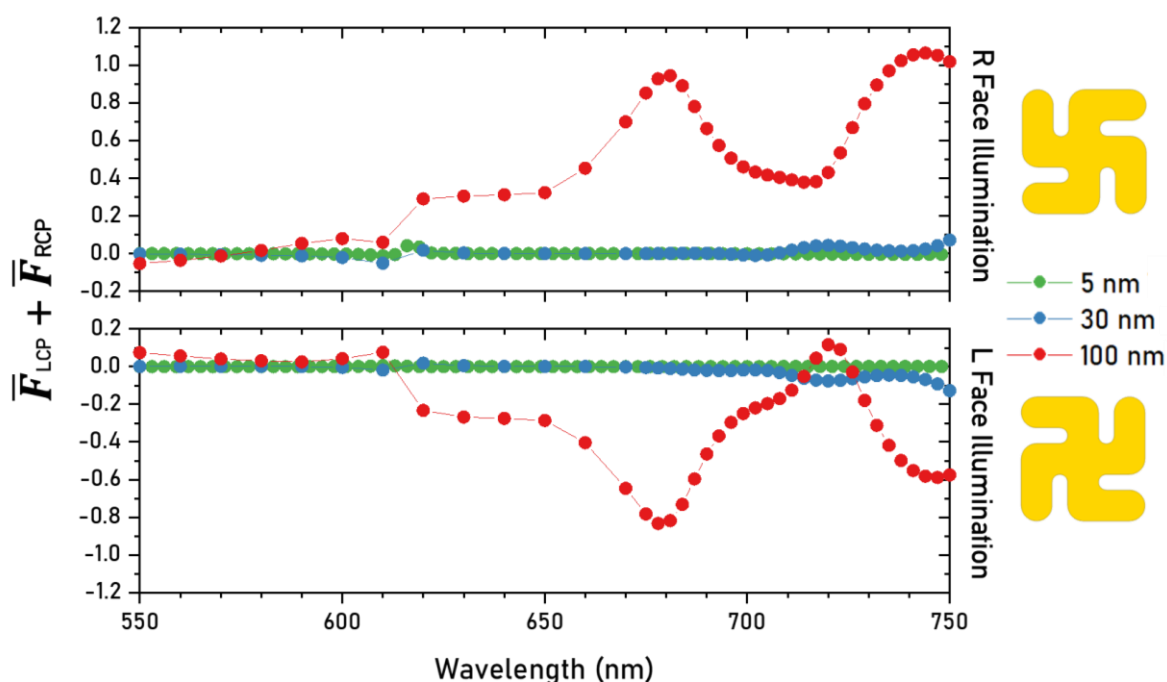


Figure 7.19: Sum of \bar{F} for LCP and RCP for R face illumination and L face illumination for the three gammadions in chiral media. For opposite face illuminations of the same structure, the spectra are no longer mirror images of one another.

One conclusion derived from the data presented is that the sensing capability in the circular dichroism spectra of the nanoparticles does not directly correlate with the maximum magnitude of \bar{C} . The thinner structure supports high levels of \bar{C} but this does not correspond to greater sensing capability. The sensing capability of the nanostructure both in the CD spectra and the summed \bar{F} spectra does appear to be correlated with h .

Consequently, a mechanism for enantiomeric sensing within the framework of an interference model of optical chirality dissipation is proposed. It is proposed that the phases θ and φ are asymmetrically changed by the presence of a chiral dielectric. Central to this assumption is that the presence of

a chiral dielectric breaks the symmetry of the system. Using notation previously introduced, this would mean that ${}_{L\text{ Inc}}^{LCP}\bar{\mathbf{F}}$ and ${}_{R\text{ Inc}}^{RCP}\bar{\mathbf{F}}$ are no longer enantiomeric pairs. Thus,

$${}_{L\text{ Inc}}^{LCP}\bar{\mathbf{F}} \neq -{}_{R\text{ Inc}}^{RCP}\bar{\mathbf{F}} \quad \text{Equation 7.20}$$

and consequently, the enantiomeric pair relationship shown in **Equation 7.13** - **Equation 7.17** no longer hold. **Equation 7.18** still holds if the surrounding dielectric is non-lossy.

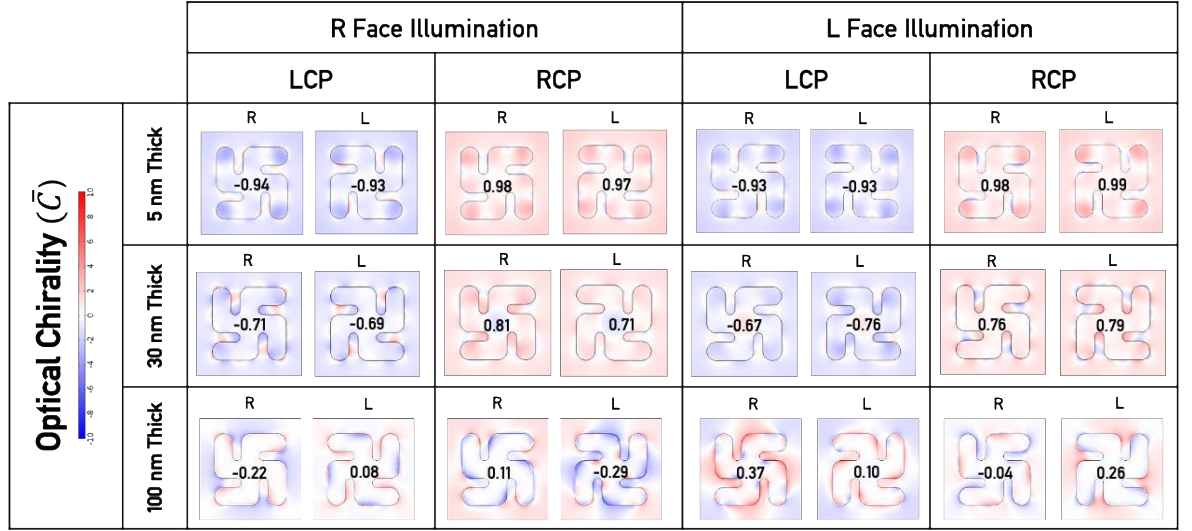


Figure 7.20: Optical chirality plots for the $h = 5, 30$ and 100 nm thick structures in chiral media. The integrated chirality value across the structure is shown in the centre of each plot.

The refractive index of a chiral material, (n_{chiral}) is given by the following equation:

$$n_{chiral} = n \pm \delta n \quad \text{Equation 7.21}$$

where n is the refractive index of an achiral or racemic mixture and the sign of δn is determined by the handedness of scattered light. **Equation 7.19** can be modified to include this expression:

$$2\pi \frac{h(n \pm \delta n)}{\lambda} = (\theta - \varphi) \quad \text{Equation 7.22}$$

From this expression it is clear that

$${}_{L\text{ Inc}}^{LCP}(\theta - \varphi) \neq {}_{R\text{ Inc}}^{RCP}(\theta - \varphi) \quad \text{Equation 7.23}$$

which in turn leads to the asymmetric behaviour expressed in the data in **Figure 7.18**, **Figure 7.19** and **Figure 7.20**.

The fundamental finding from this chapter is that the level of optical chirality which is radiated into the far field can be suppressed by interference. And so, interference which is supported by nanostructures can be considered a mechanism for the dissipation of optical chirality. It has been further demonstrated that this mechanism can be exploited for the detection of chiral material, analogous to previous findings in this area with regards to circular dichroism sensing [104], [110]. This characterisation offers a framework for the rational design of chiral nanostructures for sensing, with a suggestion that simply increasing the level of optical chirality should not be the sole condition for improving detection. The nanostructures should be able to support interference effects with asymmetry in the phase differences allowing for enantio-discrimination. The position of maxima and minima in the CD spectra and the summed \bar{F} spectra do not appear to be directly correlated. However, their magnitudes relative to h of the gammadion and levels of asymmetry are similar.

A more subtle implication of this work is that free floating nanostructures could be effective biosensors free floating in solution. The mean CD signal of the R and L face illumination when surrounded by chiral material is non-zero. This could be exploited as a useful tool for providing information on biological analytes in vivo. An obvious limitation to this is the consistent fabrication of complex free-floating nanoparticles.

Chapter 7 Key Findings

- Optical chirality can be dissipated by a nanostructure. The level of dissipation can be measured with the parameter optical chirality flux.
- The level of optical chirality dissipation correlates with the thickness of the nanostructure.
- Surrounding chiral material causes an asymmetry in the level of optical chirality dissipation, the level of which is thickness dependent.
- These observations are reconciled within a phase dependent model.

Part C

Active chiral metamaterials

Chapter 8

The flexoelectric effect for active chiral metamaterials

8.1 Introduction to active metamaterials

The development of advanced fabrication techniques has allowed for the creation of metamaterials where the size and morphology of the elements which comprise them can be controlled down to the nanometre. A limitation of ‘traditional’ fabrication techniques and materials is that once the elements have been constructed, they can no longer be altered, and neither can the interesting effects that they produce: they are fixed by the permanence of their geometry. It follows therefore that if the elements could be modified post-fabrication, then the effects that they produce could be controlled. This is the motivation behind the development of ‘active’ metamaterials whose size, shape or other properties can be controlled post-fabrication. The unique effects that they produce could be turned on or off or modulated by an external stimulus.

The potential applications of active metamaterials are far-reaching. Consider, for example an optical plasmonic biosensor whose resonances could effectively be tuned to the specific light-matter interaction frequency of the target molecule, allowing for an enhancement of the detection signal [111]. Or, as the components of integrated circuits: switches, modulators, and polarisers [17]. A plasmonic metamaterial whose resonances could be shifted could also form the basis of pixels for a display with very small dimensions. Perhaps the most crucial to this work is that at the nanoscale, small mechanical changes can produce very large effects related to the optical properties of materials.

As the world shifts towards a focus on smart engineered solutions, active metamaterials have the potential form the basis of these technologies [112]. Consider for example a smart windowpane, one which could reflect or transmit infrared light from sunlight to cool down or heat up a building as required [113]. All these applications are possible with active metamaterial. With these applications in mind, the field of active metamaterials has spawned creative and inventive approaches for device fabrication and control methods [17]. A few illustrative and interesting examples organised by their mechanism and strategy of control are set out in the next sections.

8.1.1 Chemically active metamaterials

As previously stated, the resonances of plasmonic nanoparticles are sensitive to the refractive index properties of the material which surrounds them. This property can be exploited for the development of active plasmonic

metamaterials whose mechanism is based on chemical changes to media which surround the nanostructures.

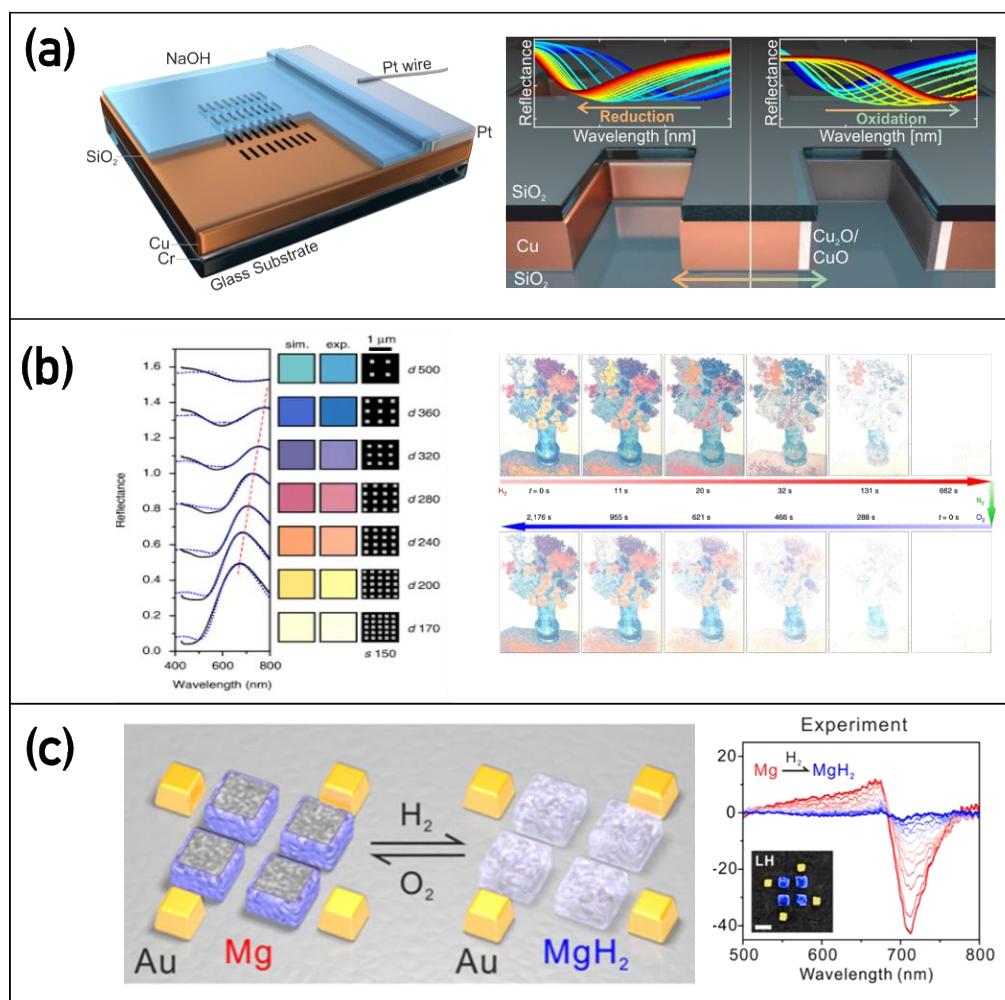


Figure 8.1: Chemical active metamaterial (a) Control of the reflectance spectrum by oxidation and reduction of copper in an array of inverse copper nano-antennas. Reproduced from [114]. (b) A dynamic plasmonic colour display. The colour of each 'pixel' is controlled by the spacing between gold nano-squares. The pixels are arranged into the shape of Vincent van Gogh's Flowers in a Blue Vase. Hydrogenation and dehydrogenation erases and restores the colour. Reproduced from [26]. (c) Four magnesium particles in a square arrangement are surrounded by four gold nanoparticles so that the arrangement is chiral. When hydrogenated from Mg to MgH_2 the central squares lose their plasmonic properties rendering the plasmonic element achiral. The CD spectrum of the metamaterial is 'quenched' by hydrogenation. Reproduced from [115].

Böhme and colleagues produced a metamaterial whose reflectance spectrum can be controlled by the oxidation of a copper layer incorporated into the device [114]. On a glass slide, they evaporate 30 nm of copper and 15 nm SiO_2 with an array of nano slits which penetrates both layers, **Figure 8.1 (a)**. The device is connected electrically via a 40 nm platinum edge with platinum

wire attached. The structure is immersed in sodium hydroxide (0.1 M) with a platinum counter electrode. When the copper is oxidised, it is covered in a layer of copper oxides (Cu_2O and CuO). The refractive index of the oxide layers is higher than the electrolyte solution, thus the wavelength position of the plasmons is shifted to the red. Additionally, because the exposed copper is converted into its oxide, the size of the nano slit has effectively increased. When the reaction is reversed and the copper is reduced, the position of the resonance shifts back to the blue. The shift is of approximately 210 nm in the visible to near-infrared range and is amongst the highest reported in the literature. The authors note that this configuration has possible applications for the development of plasmonic pixels or as a chemical sensor for carbon monoxide.

Duan and colleagues presented a dynamic plasmonic colour display which could be turned on and off via a hydrogenation/oxidation mechanism [26]. They fabricated arrays of magnesium nano-squares whose reflectance spectrum in the visible range was determined by the periodicity of the array, **Figure 8.1 (b)**. Thus, they constructed a colour image, in this case Vincent van Gogh's Flowers in a Blue Vase, by arranging the differently spaced nanostructures to correspond to the colours of the painting. The dynamic behaviour of the pixels is enabled by the hydrogenation of the magnesium to the dielectric MgH_2 . The loss of plasmonic elements flattens the reflectance spectrum of the nanoparticles. The different areas of the picture undergo vivid colour changes until the image is completely erased. The dehydrogenation of the magnesium by the introduction of oxygen causes the restoration of colour to the picture. As well as the obvious application as a dynamic display, the authors describe a mechanism for information encryption.

The same group utilised this magnesium hydrogenation mechanism to create a metamaterial whose chirality could effectively be turned on and off [115]. The elements of their metamaterial consist of four magnesium nanoparticles arranged in a square with four smaller gold nanoparticles on their outskirts arranged so that the overall structure of the element is a quasi-gammadion, as in **Figure 8.1 (c)**. This arrangement is chiral and gives a CD signal. When the magnesium is hydrogenated, it is converted to the dielectric MgH_2 and the plasmonic response of the central four squares is turned off. The remaining gold structures form a system which is not in itself chiral, and the CD spectrum is quenched. The authors outline possible applications for tuneable polarisers or, due to the sensitivity of magnesium to hydrogen, carbon dioxide and humidity, as a potential sensor.

These given examples illustrate how the properties of a material can be controlled by changing the surrounding media by chemical modification. All,

however, require the introduction of external reagents to enable the required reaction to occur. Furthermore, hydrogenation and dehydrogenation are slow processes, requiring optimisation with catalytic metals and choice of structure design. [16]. Their function may be more suitable in the converse arrangement, i.e. as sensors of chemical change, rather than as active materials.

8.1.2 Thermomechanical active metamaterials

The rationale behind thermomechanical control of metamaterials is simple in that most of the solid materials which constitute metamaterial elements will exhibit some change in their form when the temperature is changed. In most cases this will consist of an expansion of the material as the temperature is increased resulting in mechanical displacements.

Tao et al. constructed a terahertz metamaterial whose transmission properties were modulated by thermomechanical elements [116]. They constructed an array of free-standing split ring resonators which were connected to the substrate by cantilever legs, **Figure 8.2 (a)**. The substrate was made of SiN_x and the cantilever legs and split ring resonators were made of gold. As a result of the difference in thermal expansion coefficients between the two materials, an increase in temperature causes the split ring resonator to be lifted out of the plane of the substrate. The electromagnetic properties of the material are dramatically changed as a result. The authors note that although a thermally sensitive system is used in this case, it would be possible to substitute it for a resistive, piezoelectric or electrostatic actuation mechanism.

An active metamaterial developed by Ho et al [117] used a similar effect to Tao and colleagues, however they controlled the effect electrically. They constructed an array of interconnected aluminium Ω shapes which bent upwards from an Al_2O_3 coated substrate, **Figure 8.2 (b)**. An aluminium circle sat below the ring. Applying a potential difference causes resistive heating: the coefficients of thermal expansion of aluminium and its oxide are different which causes the structures to bend towards the substrate. As a result, the coupling between the disc and the ring changes which in turn affects the transmission spectrum. The device was able to return to its original state after cooling.

Yin and colleagues developed a thermomechanical material whose mechanism was not based on thermal expansion, but on the phase change of germanium antimony telluride, $\text{Ge}_3\text{Sb}_2\text{Te}_6$ (GST-362) [118]. They showed that they could control the CD spectrum of the device by surrounding a pair of plasmonic corner-stacked nanorods with the material, **Figure 8.2 (c)**. At room

temperature it is in its amorphous phase. Heating to 160 °C crystallises the material, causing an associated change in its refractive index. The position of the CD resonances of the system are sensitive to the refractive index of the material which surrounds the nanostructures, thus the change in phase causes a shift in the CD spectrum. The group were able to measure CD resonance shifts of 18% after heating the sample. They were further able to show changes in the sign of the CD resonance by employing another pair of stacked nanorods.

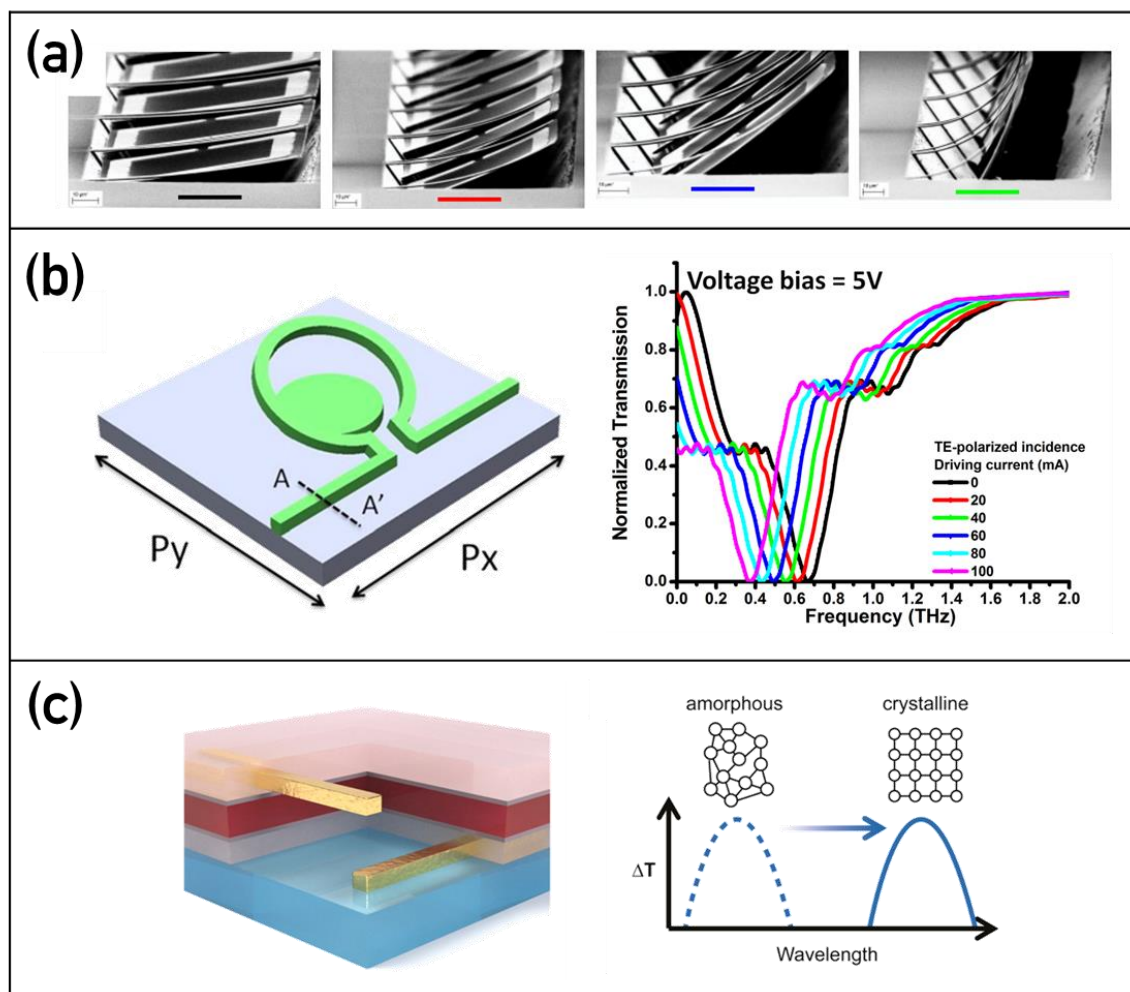


Figure 8.2 Thermomechanical active metamaterials. (a) An array of split ring resonators suspended by cantilever legs is constructed of two materials with different thermal expansion coefficients. Increasing the temperature causes the rings to be lifted from the plane of the substrate [116]. (b) The tilt angle of an omega ring is changed by a similar effect; however, the heating is induced by applying a potential difference. The transmission spectrum is modulated by changing the driving current [117]. Corner stacked nanorods are separated by a 50 nm layer of GST-326. The phase change from amorphous to crystalline causes a change in refractive index which red shifts the resonance. Reproduced from [118]..

Thermomechanical active metamaterials show a sensitivity to temperatures and exhibit large dynamic response; however, they have

fundamental weaknesses. Firstly, for those which are based on expansion, the response time is limited by the thermal conduction of the material: this is inherently slow. Secondly, the high temperatures required for a response are incompatible with polymer-based substrates which are key to reducing manufacturing costs.

8.1.3 Electromechanical active metamaterials

Electrical based actuation is the ideal mechanism for the integration of mechanical elements into modern systems. These devices combine fast response time, modulation of input signal and functionality across a wide range of frequencies.

Fabrication strategies for microelectromechanical systems (MEMS) are now fairly well established and there are many examples of such devices. Here, one illustrative example of a MEMS metamaterial is presented: an array of tuneable split ring resonators. In the initial state, the cantilever arm bends upwards from the substrate due to stress induced in the fabrication process: this is caused by different thermal expansion coefficients of a material bilayer which constitutes the arm. When a DC voltage is applied between the cantilever and the silicon substrate, the resulting electrostatic force pulls down the cantilever towards the substrate, as shown in **Figure 8.3 (a)**. At intermediate driving voltages, the position of the cantilever arm is determined by the balance of the electrostatic force and the cantilever restoring force. Thus, the device is tuneable depending upon the driving voltage applied. The authors show that changes to the transmission spectra of the array occur with the changes to the structure of the metamaterial element [119].

The interest of this work however is the reduction of the size elements of active materials to the nanoscale. This electro-opto-mechanical coupling can be mediated effectively by a plasmonic effect which dictates that the size of the elements must be on the nanometre scale. At these scales, electromagnetic forces between constituent elements become very large: consider for example how electrostatic forces square inversely with the square of charge separation distance. In opposition to this, elastic forces become much smaller. Thus, nanomechanical elements such as a cantilever can reach large displacements with the application of force in the micro to nano newton range [120]–[123]. The development of electrically controlled nanomechanical metamaterials is still in its infancy. Here, one of the few examples of a nanoelectromechanical metamaterial is given which well illustrates each of the properties discussed.

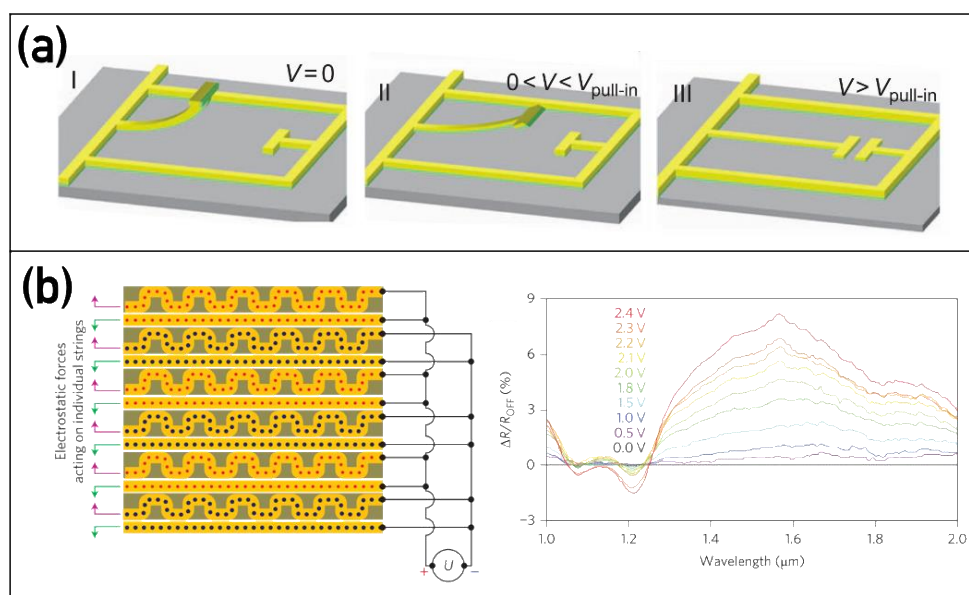


Figure 8.3 (a) An active split ring resonator. In its initial state a cantilever arm bends upwards. When an intermediate voltage is applied, the arm bends towards the substrate. When the electrostatic force overcomes the cantilever restoring force, the arm lies flat. Reproduced from [119]. (b) A ‘meander near the wire’ pattern fabricated on dielectric strings (shown in brown). The application of voltage creates an attractive electrostatic force between neighbouring patterns. Increasing the voltage reduces the gap with a commensurate effect observed in the reflectivity spectrum. Reproduced from [124].

Ou et al. constructed an active metamaterial which exploited the dominance of electrostatic forces at smaller scales: this size effect occurs because electrostatic forces are inversely proportional to distance. Their material consisted of a metal plasmonic ‘meander near the wire’ design manufactured on top of flexible dielectric strings, as shown in **Figure 8.3 (b)**. The application of a few volts (0 – 3 V in the measured cases) between neighbouring ‘wire’ and ‘meander’ patterns creates an electrostatic force of a few nanonewtons which is sufficient to move the structures closer together. The authors showed that the reflectance and reflectivity of the device could be modulated by up to 8% by changing the applied voltage. They note however that above 3 V, electrostatic attraction irreversibly overcomes the restoring force resulting in abrupt changes to the optical properties of the device [124]. Yamaguchi and colleagues developed an active plasmonic chip which operated on a similar principle albeit with a different metamaterial design. They were able to shift the wavelength of the material resonance by up to 60 nm in the visible spectrum [125].

8.1.4 Electromechanical coupling and the flexoelectric effect

The coupling between electric and mechanical properties exists across a wide range of artificial and natural materials. The ear is a simple example: it is essentially a device which converts the actuation of hair cell bundles caused by sound vibrations into electrical impulses which can be interpreted by the brain. Non-biological analogues have many applications as sensors, actuators and energy harvesters [126]. This work focuses on the electromechanical coupling phenomenon of flexoelectricity, but it is impossible to not first introduce the more well-known and well-studied mechanism of piezoelectricity. When piezoelectricity was first discovered, brothers Jacques and Pierre Curie wrote [127] that:

“The crystals that have one or more axes with dissimilar ends, i.e., the hemihedral [semi-symmetrical] crystals with oblique faces, possess a particular physical property of giving rise to two electric poles of opposite signs at the extremities of these axes when they undergo a change in temperature: This phenomenon is known as pyroelectricity. We have found a new method for developing polar electricity in these same crystals, which consists of subjecting them to variations in pressure along their hemihedral axes.”

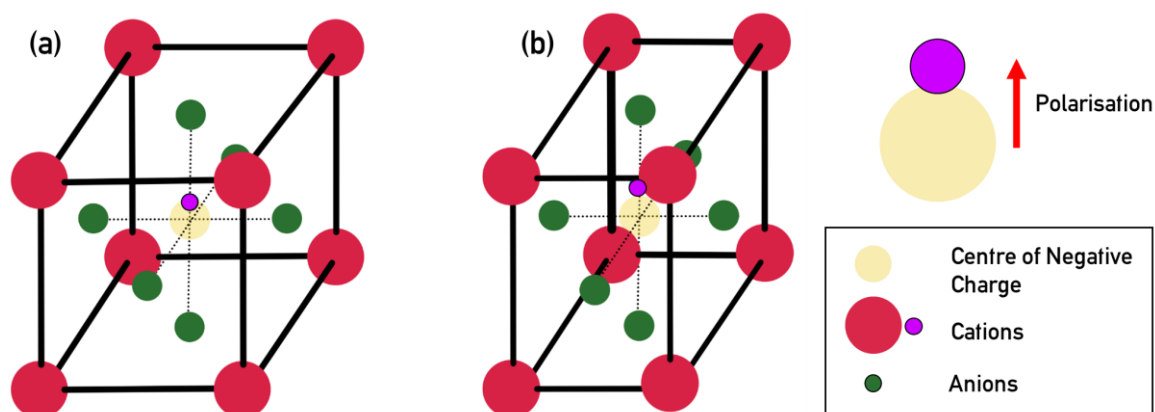


Figure 8.4: (a) A non-centrosymmetric crystal in its free state. (b) Under homogeneous distortion, the distance between the negative and positive charge centres changes, increasing polarisation.

Piezo comes from the Greek word meaning to press, with piezoelectricity describing the coupling between polarization and strain occurring in materials which lack inversion symmetry. Essentially piezoelectric materials can

accumulate charge in response to mechanical stress. It was not until a century after the Curie brothers made their announcement to the French Academy of Sciences that an avalanche of products which make use of piezoelectricity began to be produced. Piezoelectric materials are now present in technology for communications, industrial automation, medical diagnostics, defence and many other sectors [128].

For an intuitive description of piezoelectricity, consider a non-centrosymmetric crystal, as in **Figure 8.4 (a)**, whose positive and negative charge are not coincident, resulting in net polarisation. Under a homogeneous mechanical force in one direction, in this case a horizontal compression, **Figure 8.4 (b)** the position of charges is displaced, electric dipoles are induced and an electric field is produced. [128]–[130]. The converse effect also exists. If an electric field is applied to a piezoelectric material, then it will deform. Piezoelectricity can only exist in non-centrosymmetric materials: if the crystal were symmetric then a homogenous strain would not cause the breaking of crystal symmetry required for the generation of a net polarisation [131].

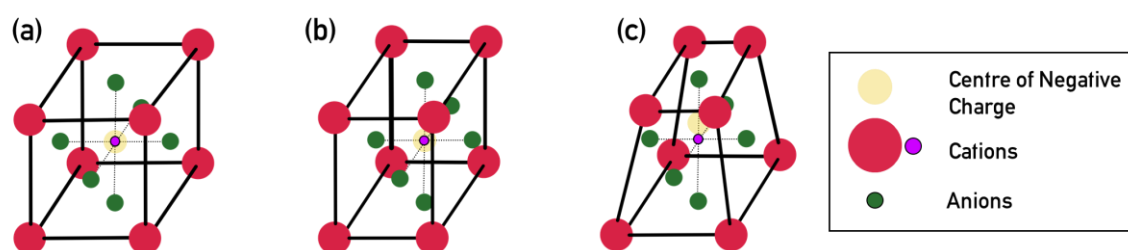


Figure 8.5: Schematic of the flexoelectric effect. (a) The free state of the crystal. (b) Under homogeneous deformation, the positive and negative charge centres are overlapping meaning there is no net polarisation. (c) Under inhomogeneous deformation, the centres of negative and positive charge are no longer coincident, thus polarisation is achieved.

The flexoelectric effect is the cousin of the piezoelectric effect and is the subject of this work. It occurs in dielectrics whereby when inhomogeneously deformed they become electrically polarised. An intuitive schematic of the flexoelectric in a centrosymmetric ionic crystal is shown in **Figure 8.5**. **Figure 8.5 (a)** depicts the free state of the crystal under no strain. Under a homogenous deformation, **Figure 8.5 (b)** there is no net polarisation as the negative and positive charge centres overlap. Under inhomogeneous deformation **Figure 8.5 (c)** the centres of positive and negative charge are no longer overlapping resulting in a net polarisation [129].

In a solid dielectric, the flexoelectric effect is mathematically described by the following expressions:

$$P_i = \mu_{ijkl} \frac{\partial \varepsilon_{jk}}{\partial x_l} \quad \text{Equation 8.1}$$

where,	P_i	flexoelectric polarisation
	μ_{ijkl}	flexoelectric coefficient
	ε_{jk}	elastic strain
	x_l	position coordinate.

The flexoelectric coefficient is analogous to the piezoelectric coefficient which mediates the piezoelectric effect. Both are tensors, but whilst the piezoelectric coefficient is third order (or third rank) the flexoelectric coefficient is fourth order (or fourth rank). The flexoelectric coefficient describes the coupling between polarisation (a first rank tensor) and strain gradient (a third rank tensor) [132]. The symmetry implication of this is that whilst piezoelectricity is only observed in non-centrosymmetric crystals, flexoelectricity is observed in all dielectrics. The flexoelectric coefficient contains 81 (3^4) components: the number of non-zero components are dependent upon the symmetry of the crystal in which the effect is observed. In a low symmetry triclinic crystal, this number can be as high as 54 making measurement of the flexoelectric components in these cases very complex [133]. In a cubic crystal, there are three independent non-zero components, μ_{1122} , μ_{1111} and μ_{1211} which are the transverse, longitudinal and shear components. These have been measured experimentally in cubic materials such as lead magnesium niobate, barium strontium titanate, lead zirconate titanate and barium titanate amongst others [132]–[134].

In this work, the interest is the thermodynamically equivalent but reverse process to the flexoelectric effect: the converse flexoelectric effect. It is described by the following expression:

$$T_{ij} = \mu_{ijkl} \frac{\partial E_k}{\partial x_l} \quad \text{Equation 8.2}$$

where	T_{ij}	mechanical stress (force per unit area)
	μ_{ijkl}	flexoelectric coefficient
	E_k	electric field
	x_l	position coordinate

Equation 8.2 describes how an applied field gradient can induce stress in a material [131], [132]. This induced stress can cause the distortion of flexoelectric materials: i.e. a change in their dimensions.

The flexoelectric effect is similar in mechanism to the piezoelectric effect, but whilst piezoelectricity is only possible in non-centrosymmetric crystals, flexoelectricity is observed in a range of materials and structures. Cellular membranes, viruses, liquid crystals and graphene nanomaterials, to name a few, have been shown to support the flexoelectric effect [132]. Whilst flexoelectricity broadens the selection of candidate materials for electromechanical coupling, there was little interest for many decades after it was first reported. This was primarily due to its small magnitude compared to piezoelectric effect. Interest was renewed due to two findings. The first was the discovery of giant flexoelectric coefficients in ferroelectric materials with high dielectric permittivity.

The second, which is important for this work, is that the flexoelectric effect exhibits a size effect. Consider two separated points, a_1 and a_2 within a shape which is subject to stress. The strain gradient will scale as $1/a_i$ where a_i is the distance between points a_1 and a_2 . Thus, if the size of the shape and its points is scaled down to the nanoscale, a_i becomes very small. It follows therefore that the strain gradients within the structure become very large. At the nanoscale these strain gradients can be enormous. [126]. In the converse effect, the reverse is also true: nanostructured materials can sustain very large electric field gradients [135]–[137].

In this work the ceramic lead zirconate titanate (PZT) has been chosen as the candidate flexoelectric material due to its moderate to large flexoelectric coefficient [126]. PZT is a ceramic with a chemical formula $\text{Pb}[\text{Zr}_x\text{Ti}_{1-x}]\text{O}_3$, where $0 < x < 1$. In its perovskite crystal structure, PZT exhibits a very strong piezoelectric effect, making it the most used piezo ceramic in industry. There is however a requirement that the PZT film is annealed by heating to temperatures between 650 – 850 °C. This high temperature processing renders the material incompatible with polymer-based platforms which are key to low-cost metamaterial production. Thus, taking advantage of the flexoelectric properties of PZT represents a new strategy for the fabrication of active metamaterials.

8.2 Device composition and fabrication

Fabrication of the flexoelectric device begins with the polycarbonate indented with the shuriken shapes as described in **Section 3.2 Shuriken structure fabrication**: the indentations in this case are 80 nm deep. After

cleaning, 20 nm of platinum is thermally evaporated onto the indented surface. Pt acts as the first electrode.

Following this, PZT is deposited onto the surface by pulsed laser deposition (PLD) with a thickness, d_{PZT} equal to either 50 or 150 nm. These values are chosen because they are significantly less than and greater than the indentation depth of the nanostructure respectively. PLD was performed using sintered PZT targets (Pi Kem Ltd., UK) in 50 mTorr pressure of oxygen. Deposition was conducted at room temperature directly onto the substrates in a Neocera Pioneer PLD vacuum system, employing a Coherent Compex Pro KrF excimer laser (248 nm, 20 ns pulses, 18 Hz, up to 200 mJ pulse energy). The target was rotated during deposition to minimise the transfer of particulates to the sample. Transmission electron microscopy and electron diffraction experiments confirm that the deposited films display no long-range order consistent with previous studies into PZT thin films, **Figure 8.6** [138]. Thus, the PZT film can be described as amorphous. After PZT deposition, a 70 nm thick Au film is thermally evaporated which acts as the second electrode. The film structure was then characterised by transmission electron microscopy by deposition a ~ 40 nm thick film directly onto an amorphous holey carbon film and imaged in a JEOL ARM CFEG instrument operated at 200kV. Lastly, 70 nm of gold is thermally evaporated onto the substrate.

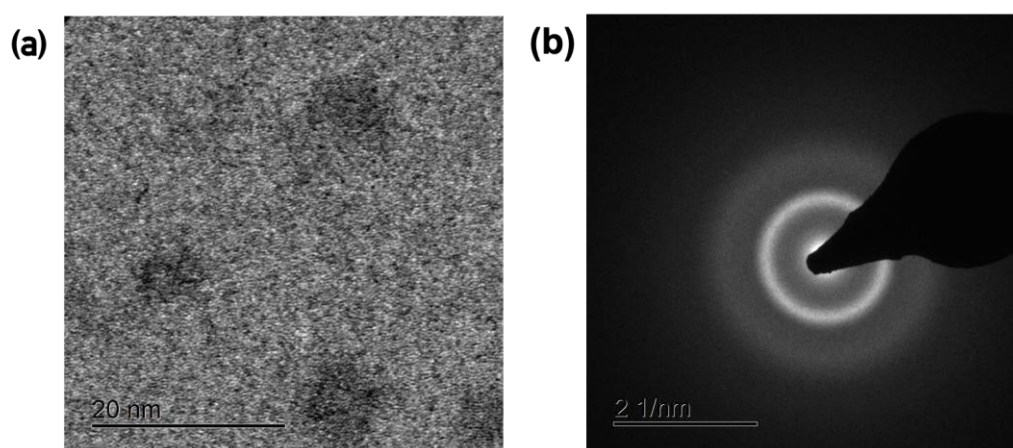


Figure 8.6: (a) Transmission electron microscopy image of the deposited PZT layer lacks the interference fringes which are characteristic of a crystalline material. (b) Electron diffraction pattern lacks sharp diffractive features.

A schematic diagram of the completed device with the thickness of each layer is shown in **Figure 8.7 (a)**. In this structure, the shuriken arms rotate counter-clockwise and so using a previously adopted convention the structure is described as being left-handed (LH). Where the shuriken arms rotate clockwise, the structures are described as right-handed (RH). The distribution of each material within the nanoindentation is shown in **Figure 8.7 (b)**.

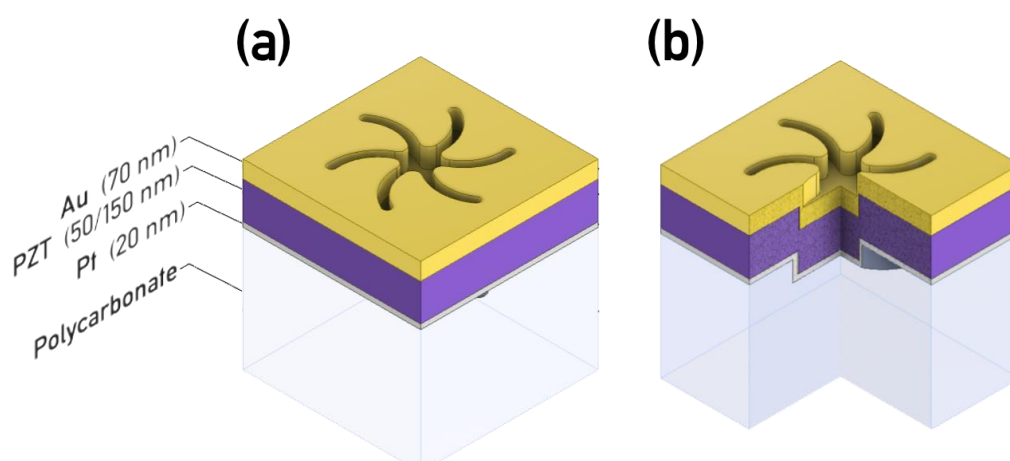


Figure 8.7: (a) Schematic diagram of a single nanoindentation with gold, PZT and platinum sandwich layer thicknesses identified. (b) A cross section view of the structure shows the distribution of each material.

8.3 Results

8.3.1 Spectroscopic measurements

In this work, the optical rotatory dispersion (ORD) and reflectance spectra of the structure is collected. As previously described, ORD spectroscopy measures the rotation of linearly polarised light as a function of wavelength. For oppositely handed nanostructures, the ORD spectra have a bisignate shape and are mirror images of one another. In this work, only the left-handed structure arrays are studied. It has previously been shown that the magnitude of the ORD spectrum can be modulated by changing the thickness of metal deposited onto the nanostructures [65]. Reflectance measures the amount of linearly polarised light reflected by the nanostructure relative to a gold film. As stated previously, Reflectance spectra are the same for oppositely handed nanostructures.

To ensure there are no large fluctuations in the optical response of the device when no external stimulus is applied, the ORD spectrum of the $d_{PZT} = 50$ nm is measured without the application of voltage, **Figure 8.8**. The peak-to-peak height of the ORD bisignate across the time increments measured is 16.70 degrees with a standard deviation of 0.16 degrees.

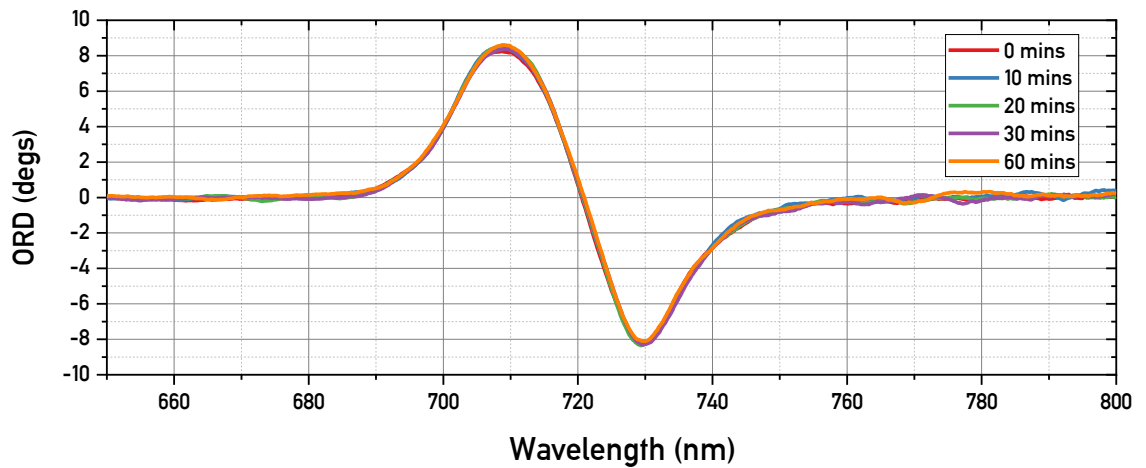


Figure 8.8: ORD spectrum of the $d_{PZT} = 50$ nm structure over 60 minutes without the application of voltage. It shows the stability of the device over time.

For both the $d_{PZT} = 50$ nm and 150 nm device, sequentially larger DC voltages in the range 0 -12 V were applied to the devices for a period of at least 1 hour with Au and Pt layers acting as positive and negative electrodes respectively. Both reflectance and ORD data were collected to monitor changes to optical properties induced by the applied voltage and if no change in optical spectra was observed within this period, the voltage was increased. However, if changes were observed the device was maintained at the voltage for a time period sufficient for spectra to stabilise and no further changes to occur: this is the threshold voltage of the device. After this point the device was maintained at 0 V and spectra collected to monitor any relaxation back towards the initial optical state of the device for periods of up to 3 hours. This cycle was the repeated approximately 15 hours later.

The active properties of the metafilms with $d_{PZT} = 150$ nm is studied first. For this device, the threshold voltage at which changes to the optical properties occurred was determined to be 12 V. The device underwent 8 cycles maintained at this threshold voltage for a time period until any changes to the ORD/reflectance spectra stabilised. The measured ORD and reflectance spectra for the device at its 1st, 4th and 8th cycle is given in **Figure 8.9**. When the device is maintained at the threshold value, there is a progressive decrease in the peak-to-peak height of the ORD bisignate. The size of the reduction increases with each cycle, with a 57% reduction observed at the 8th cycle. A similar trend is observed in the reflectance spectra however the magnitude of reduction is less, only approximately 4% at the 8th cycle.

The smaller reduction in reflectance compared to ORD can be interpreted within the framework of interactions between plasmonic elements of the

nanostructure and the incident light. Modes which arise in the structure are from a combination of electromagnetic coupling between elements of the nanostructure and because the wavelength of light and the dimensions of the nanostructures are comparable, between the incident light wave and nanostructures themselves. The chiroptical effects which arise, namely ORD, are dependent upon overlap of the electric and magnetic fields from these elements and these interactions are highly phase sensitive. As the reflectance is more dependent on the overall absorption properties from the resonant modes and chiroptical effects are highly susceptible to phase interactions, slight changes in geometry affect the phase more than the total resonance energy loss or scattering. Thus, the chiroptical response is more sensitive to slight changes in geometry than the reflectance spectra.

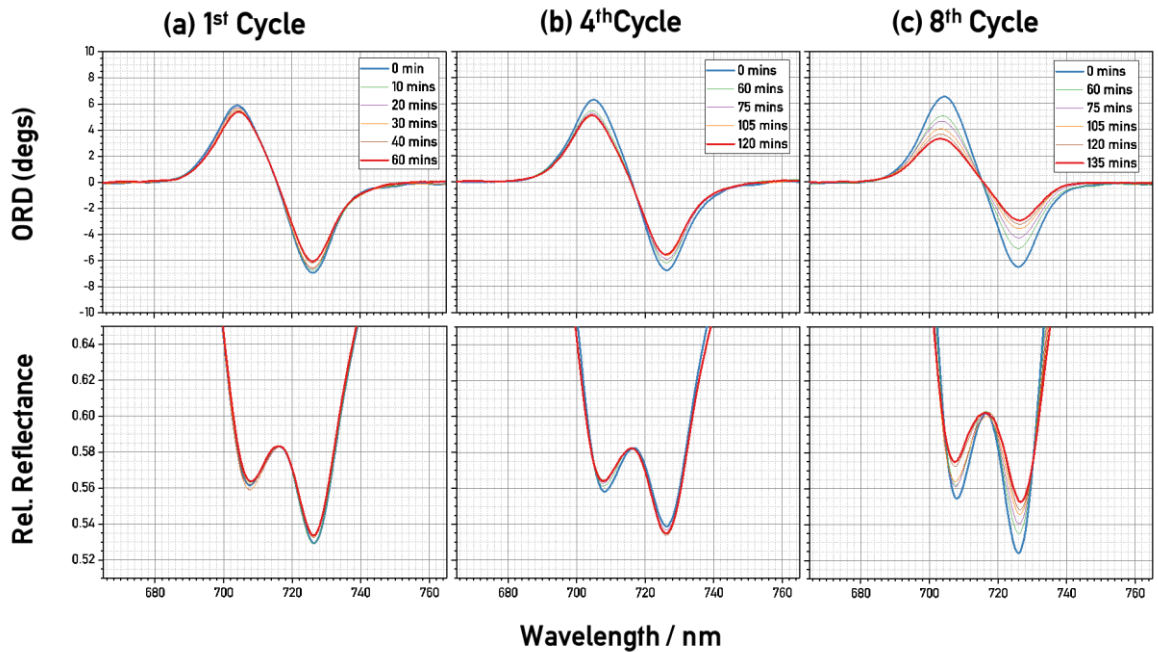


Figure 8.9: ORD (top panels) and reflectance (bottom panels) of sample $d_{PZT} = 150$ nm maintained at the threshold voltage for (a) one (b) four and (c) eight cycles. [Collected by Katie McKay].

To complete the cycle, the device was earthed, where the device returned to its initial state after a period of approximately 180 minutes, as shown in **Figure 8.10**. Promisingly, the effect is replicated across oppositely handed structures which are present on the same device, as shown in **Figure 8.11**. The left-handed (LH) and right-handed (RH) structures show a near-identical reduction in their ORD intensity which is expected as they are exposed to the same voltage cycle history. To determine whether there was good repeatability between separate devices, another $d_{PZT} = 150$ nm device was manufactured. It showed slightly lower threshold voltage of 10 V compared to the previously

discussed device. This difference can be attributed to slight differences in fabrication such as material surface area, thickness of materials deposited and the presence of defects caused by contamination. The ORD spectra were collected after the second voltage cycle.

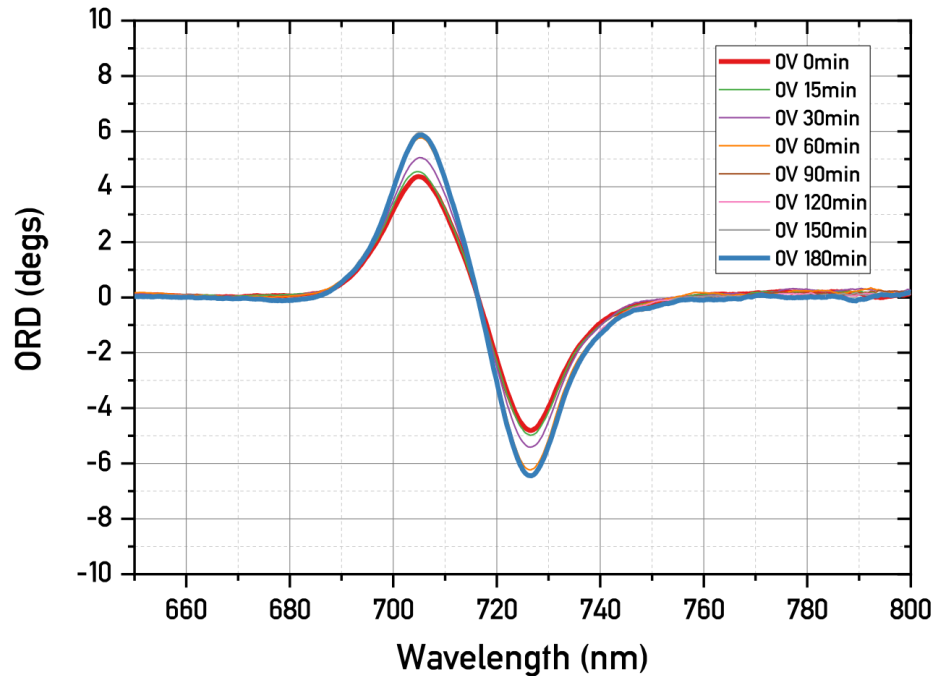


Figure 8.10: Relaxation of the $d_{\text{PZT}} = 150$ nm device after its 5th voltage cycle. After 180 minutes the ORD has returned to its original magnitude. [Collected by Katie McKay].

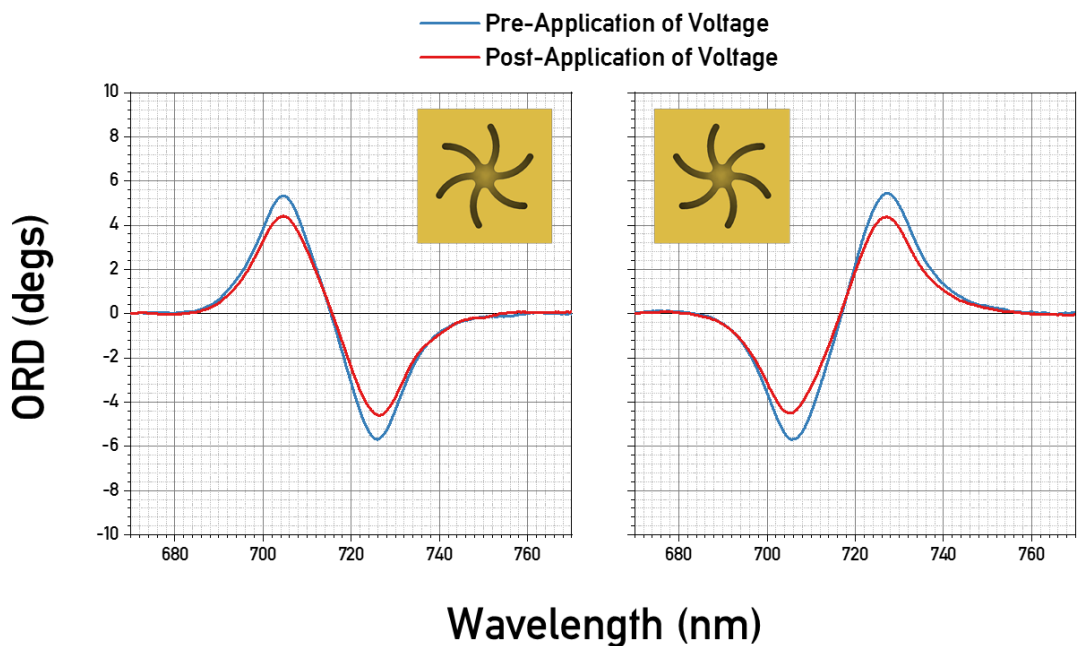


Figure 8.11: ORD spectra for LH (left panel) and RH (right panel) structures present on the same $d_{\text{PZT}} = 150$ nm device. They show a near-identical reduction in their ORD intensity.

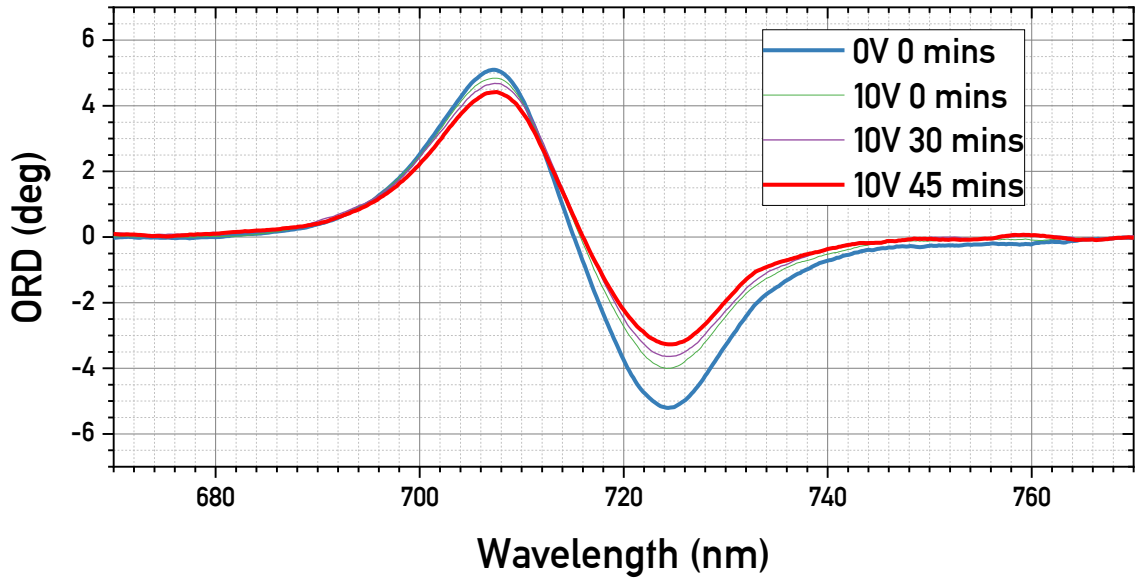


Figure 8.12: ORD spectra for a second $d_{PZT} = 150$ nm device. It shows a qualitatively similar reduction in ORD intensity after the application of voltage, albeit with a reduced threshold voltage.

For the $d_{PZT} = 50$ nm device, the threshold voltage was determined to be 18 V. There are reductions in magnitude of both the ORD and reflectance spectra as shown in **Figure 8.13 (a-b)**. The magnitude of the reduction is less than that of the $d_{PZT} = 150$ nm thick structure and, in contrast to the $d_{PZT} = 150$ nm structure, the changes are irreversible. SEM images of the $d_{PZT} = 50$ nm before and after the application of the voltage were collected and are presented in **Figure 8.13 (c-d)**. By purely visual inspection, the nanostructures show a significant narrowing of the shuriken arms and of the central circle diameter from which the arms emerge.

The nanostructure parameters have been calculating using the collected SEM images collected before and after the application of voltage. Using an image processing software, namely ImageJ, the following parameters of the shuriken arrays are measured: arm length, centre diameter, arm width, arm – arm length, structure diameter and arm area. 12-24 measurements are taken and averaged, with the standard deviation of this calculation also derived. All parameters show some difference between the pre- and post- application of voltage structures however, to determine which are statistically significant, we calculate the probability-value (p -value). For all parameters except the arm-arm distance the probability value is less than 0.002 indicating a high degree of significance. All values are presented in **Table 8.1** along with an SEM image with the measured parameters identified.

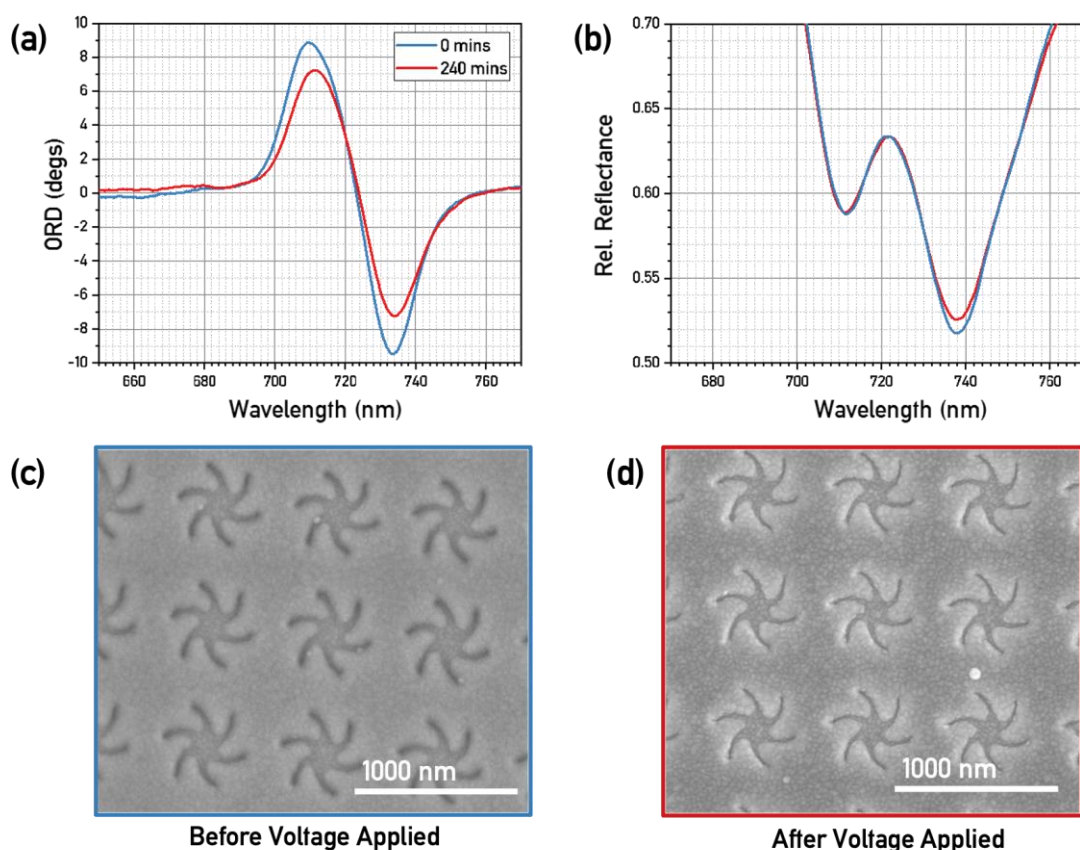
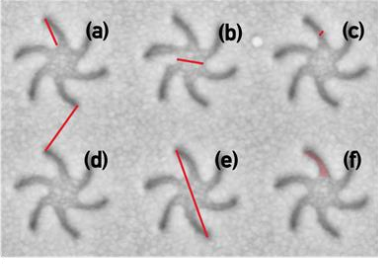


Figure 8.13: ORD (a) and reflectance (b) spectra for the $d_{PZT}=50$ nm device before voltage has been applied (blue) and after the application of a voltage (red). The reduction in ORD and reflectance magnitude is less than that for the $d_{PZT}=150$ nm device. SEM images have been collected pre- (c) and post- (d) application of voltage which show changes to the shuriken structures, most notably narrowing of the arms.

So, to this point a device has been presented which appears to be an active metamaterial: the ORD and reflectance spectrum of the device can be modulated by applying a voltage. The magnitude of the effect is dependent upon the thickness of the deposited dielectric, which crucially in the thinner case appears to be irreversible. The origin of this effect appears to be changes to the morphology of the nanostructures which comprise the metamaterial caused by the converse flexoelectric effect. Electromagnetic simulations of the device provide insight and serve the following two purposes:

1. To determine whether the device can support sufficiently large electric field gradients as to induce converse flexoelectric effects.
2. SEM changes can be distorted by aberration and charging effects and so the spectroscopic changes must be unambiguously linked to the changes observed in the micrographs.



	Before Voltage Applied		After Voltage Applied		p
	Mean value	σ	Mean Value	σ	
(a) Arm Length / nm	173.0	11.9	166.0	9.2	0.0012
(b) Centre Diameter / nm	184.0	11.5	169.0	15.1	0.0016
(c) Arm Width / nm	34.6	2.92	22.9	5.0	7.06×10^{-12}
(d) Arm – Arm / nm	314.0	12.6	309.0	10.2	0.445
(e) Structure Diameter / nm	521.0	7.4	505.0	6.2	9.16×10^{-5}
(f) Arm Area / nm ²	7840.0	878.0	5560.0	616.0	8.37×10^{-7}

Table 8.1: The geometric components of the $d_{PZT} = 50$ nm shuriken nanostructures have been parameterised before and after the application of voltage. The values are calculated from the mean of 12 – 24 measurements. The standard deviation of this calculation is shown alongside. Probability values (p) have been calculated and show that only the arm-arm distance shows a non-significant change.

8.3.2 Electric field simulations

Beginning with point one, models were developed of both the $d_{PZT} = 50$ nm and 150 nm devices, shown in **Figure 8.14**. In these models it is assumed that the PZT separates the gold and platinum completely. This assumption is based on the resistance between electrodes being >10 M Ω for all the devices studied, with < 0.1 μ A of current being drawn when the voltage was applied, suggesting no short-circuiting.

Subsequently, the electric field and the electric field gradients are calculated at four different positions in the modelling geometry, **Figure 8.15 (a-d)**. The positions of three horizontal slices through the modelling geometry are identified in **Figure 8.14**. The ‘Top’ surface is 5 nm below bulk gold. The ‘Base’ surface is 5 nm below the base of the shuriken. The ‘Side Walls’ surface is found halfway between the ‘Top’ and ‘Base’ surfaces. A fourth vertical slice, ‘Cut Slice’ is identified with a dashed line in **Figure 8.15(b)**.

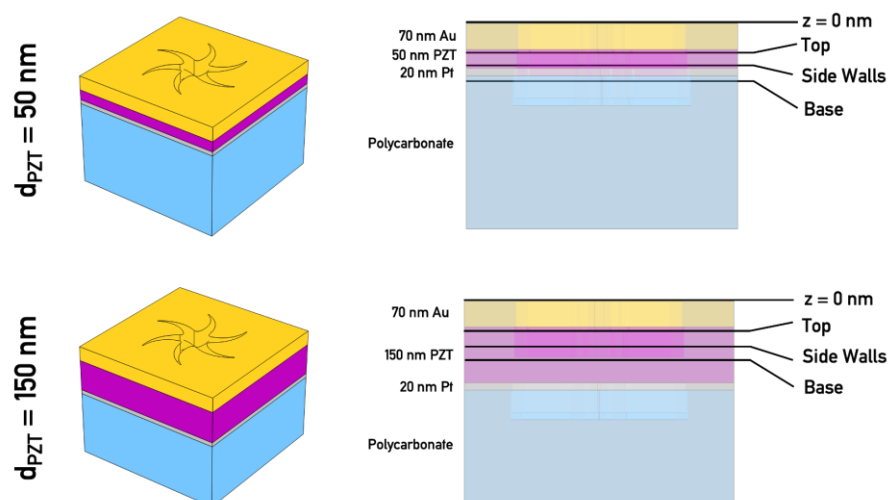


Figure 8.14: Electromagnetic models of the $d_{\text{PZT}} = 50 \text{ nm}$ and 150 nm devices were developed. The positions of the top, side walls and base positions are shown relative to the top of the gold surface which has been assigned here as $z = 0 \text{ nm}$.

The spatial distribution of electric field gradients supports the flexoelectric expansion of regions of the shuriken nanostructure which are consistent with the changes in physical structure observed by SEM. In the base plane, the electric field gradient distribution is spatially varying suggesting that any expansion of the base would be non-uniform. Both the thicker and thinner PZT devices support large gradients around the nanostructure arms.

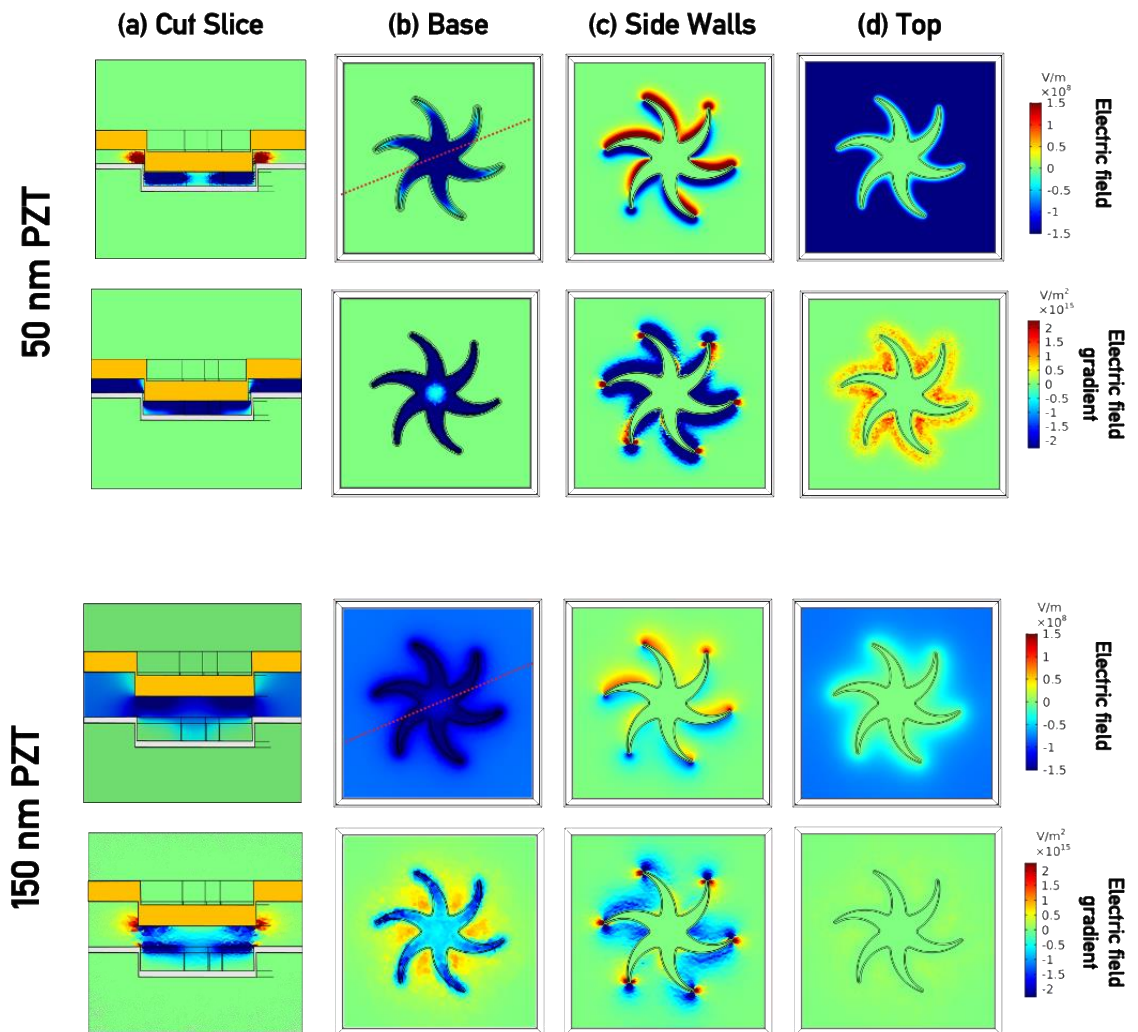


Figure 8.15: Electric field and electric field gradient plots of PZT material for the $d_{\text{PZT}} = 50$ nm (upper panels) and 150 nm (lower panels) devices. (a) Electric field and electric field gradients (both z-components) for a plane cutting the nanostructure at the point marked by the dashed line in (b). (b) Electric field and electric field gradient (z-component) at the base of the nanostructure. (c) Electric field and electric field gradient (y-component) surrounding the arms of the nanostructure, the slice is taken halfway between the top and bottom surfaces. (d) Electric field and electric field gradients (z-component) for the top surface of the PZT, 5 nm below the gold layer.

8.3.3 Spectroscopic simulations

Point two seeks to unambiguously link the observed spectroscopic effects to the geometric changes observed in the SEM images. In this model, a simplification is made to reduce the computational complexity: the PZT and platinum layers are omitted. This is valid given that the skin depth of gold at optical frequencies is much less than the thickness of metal deposited. For all the geometric models, the ORD spectrum is calculated using the far field x- and y- components.

The models used are designed in the computer aided design (CAD) software Inventor. The principal structure is shown in **Figure 8.16**. As the gold indentation depth (80 nm) is larger than the deposited gold thickness (70 nm) they have been joined with a 10 nm thick layer of gold. The two parameters changed in the models is the arm width and depth. The arm width is the width of the shuriken arm at its widest point. The depth is the distance of the nanostructure indentation.

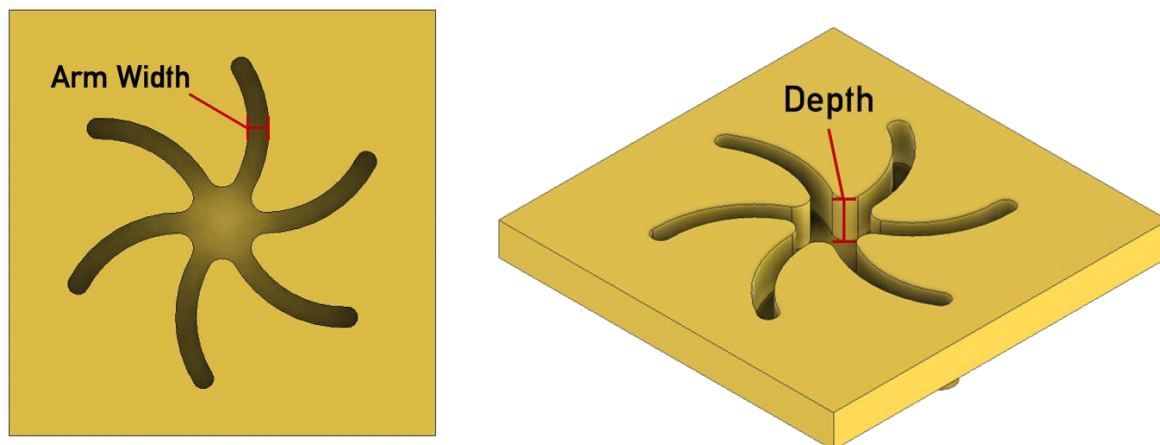


Figure 8.16: The two geometric parameters changed in the spectroscopic models are the arm width (left) and the indentation depth (right) of the nanostructure.

Using the collected SEM images, a model of the initial state of the dPZT = 50 nm is constructed. The arm width is 35 nm with an indentation depth of 80 nm. It shows the characteristic bisignate ORD spectrum, blue line **Figure 8.17 (a)**. From the SEM images, the reduction of the arm width is 12 nm after the voltage is applied to the sample. The ORD is calculated for a model for this reduction in arm width, with the indentation depth kept constant, the red line in **Figure 8.17 (a)**. The ORD in this case is nearly completely quenched to approximately 1 degree.

However, the electric field simulations suggest that the base of the nanostructure can support the strong electric field gradients required for a converse flexoelectric effect-based distortion. For this reason, the indentation depth is considered here as a varying parameter. Beginning with the dPZT = 50 nm post-application of voltage (where arm width and indentation depth are 23 and 80 nm respectively) the indentation depth is incrementally decreased. The resulting spectra are shown in **Figure 8.17 (b)**. As the depth decreases, the ORD becomes larger and its bisignate shape returns. The relation between the bisignate peak to peak height is shown in the inset.

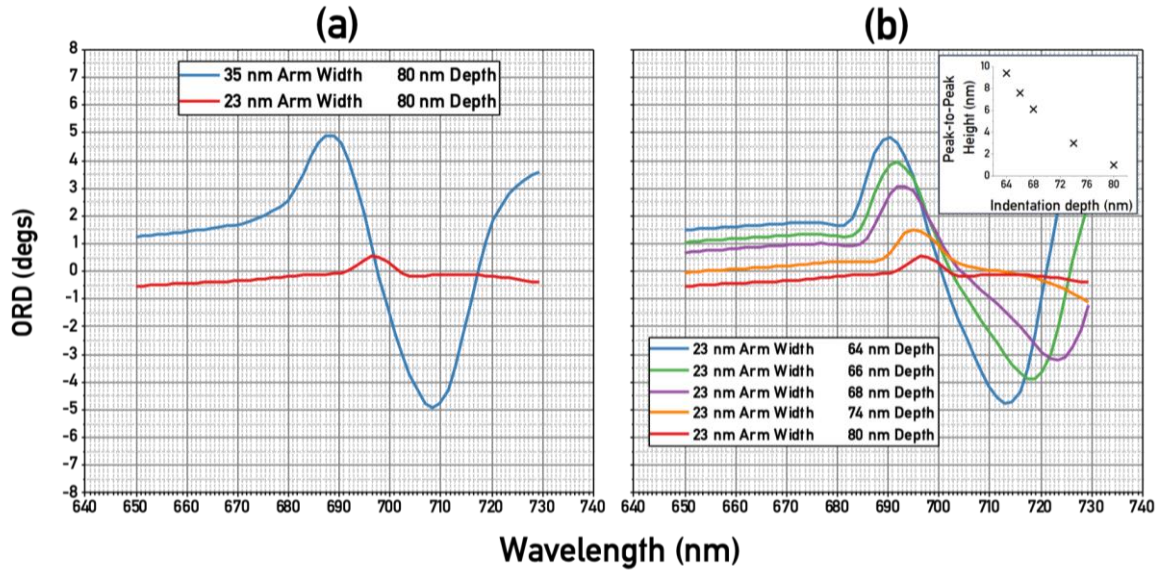


Figure 8.17: Simulated structures. (a) Reducing the arm width from 35 nm (blue line) to 23 nm (red line) nearly completely quenches the ORD signal. (b) ORD spectra for a 23 nm arm with shuriken with a progressively decreasing depth. As the depth decreases, the ORD bisignate peak to peak height decreases, as shown in the inset plot.

Thus, agreement between the experimental and simulated data can only be achieved if the decrease in the width of the arms is accompanied by a decrease in the depth (i.e. an expansion of the of the base of the structure). For the $d_{PZT} = 50$ nm case, the dimensions which correspond to a similar reduction in peak-to-peak height post-voltage were 23 and 66 nm for arm width and indentation depth respectively. For the $d_{PZT} = 150$ nm case, the arm width and indentation depth were reduced simultaneously until a reduction of ORD equal to that determined experimentally was determined. In this case this was 21 and 64 nm for arm width and indentation depth respectively.

Figure 8.18 is a summary of the calculated simulation data. **Figure 8.18 (a)** shows the simulation derived spectra for the shuriken structure pre-and post-application of voltage for the two structures. **Figure 8.18 (b)** contains the dimensional parameters of the models used in each of the simulations. What is clear from the simulation work is that very small changes to the shuriken geometry can result in substantial changes to the ORD spectra.

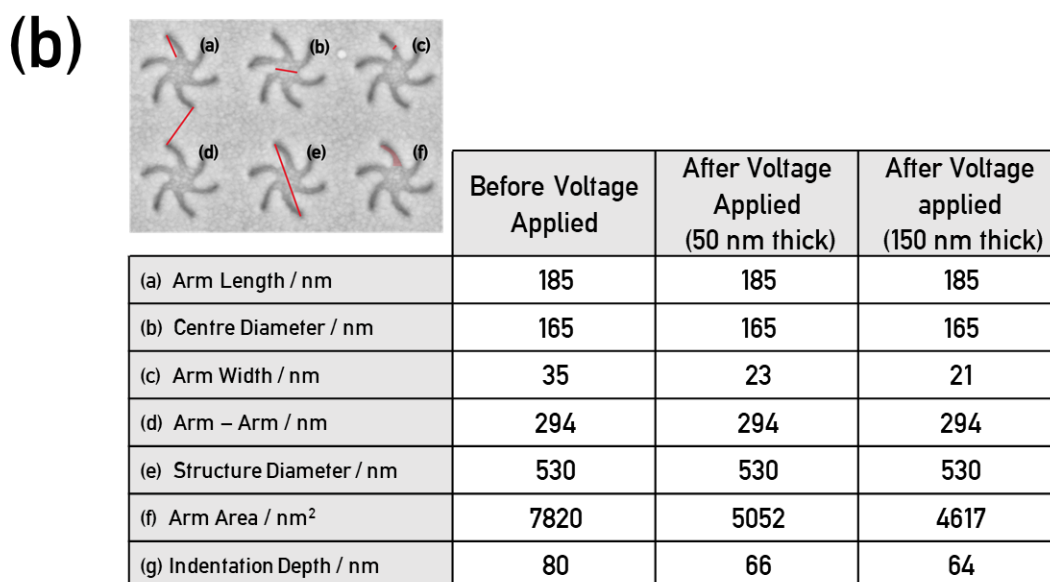
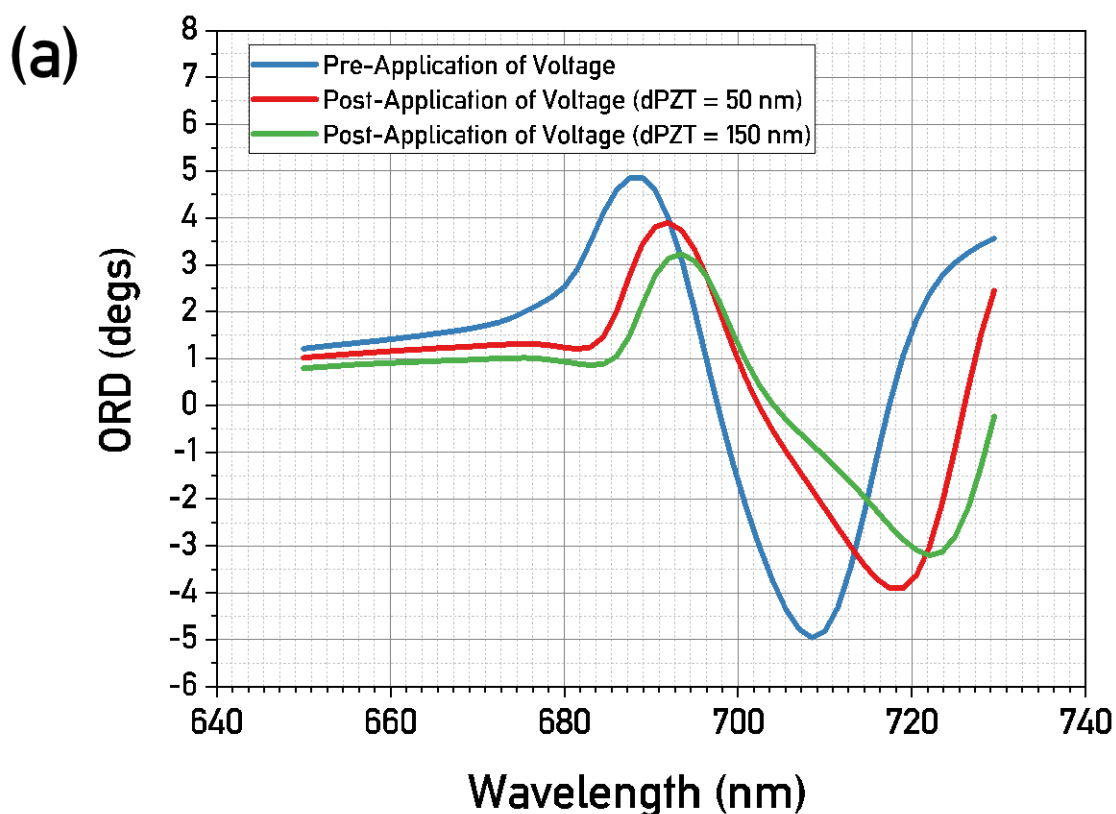


Figure 8.18: (a) Simulation-derived spectra for the shuriken structure pre- and post-application of voltage for the $d_{PZT} = 50$ nm and the $d_{PZT} = 150$ nm structures. The modelling parameters which define the shuriken structures modelled is shown in (b).

8.4 Discussion

The combined experimental and simulated data are consistent with the control of optical properties induced by structural changes to the nanostructures originating from a converse flexoelectric effect. The spectral simulations show that an expansion of both the base and the arms of the shuriken are required to reproduce the reduction in ORD spectra which is supported by the electric field simulations: they show that large electric field gradients exist at around the arms and the base of the shuriken. There are spatially varying gradients at the base of the nanostructure which suggests that the deformation there would be nonuniform. This is not accounted for in the spectroscopic simulations and accounts for the origin in small differences between the simulated and experimental spectra, such as the small wavelength shifts of the bisignate peaks.

A more quantitative interpretation of the electromechanical control of chiroptical properties requires an understanding of the stress-strain response of the Au film. The expression for the converse flexoelectric effect given in **Equation 8.2** can be simplified to:

$$T_{ij} = \mu \nabla E \quad \text{Equation 8.3}$$

where	T_{ij}	mechanical stress
	μ	flexoelectric constant
	∇E	electric field gradient.

Using the calculated electric field gradients and previous work on the flexoelectric constants of amorphous PZT, it is possible to estimate the order of mechanical stress generated in the device. A flexoelectric constant of $1 \times 10^{-6} \text{ C m}^{-1}$ is a reasonable estimate for amorphous PZT. As stated, this value is much higher than for conventional dielectric which are usually on an order of $\sim 10^{-10} \text{ C m}^{-1}$ [139]. From the electric simulations for the $d_{\text{PZT}} = 150 \text{ nm}$ device, the electric field gradients are on the order of $1 \times 10^{-16} \text{ V m}^{-2}$. Therefore, the mechanical stress experienced by the internal walls of the shuriken nanostructure is approximately 10^{10} N m^{-2} at 12 V.

For a 100 nm thick gold film, the Young's modulus (or modulus of elasticity) is $6 \times 10^{10} \text{ N m}^{-2}$ [140]–[142]. The deformation of the gold can be estimated using the following equation:

$$\Delta l = \frac{\sigma l_0}{E} \quad \text{Equation 8.4}$$

where,	Δl	change in length of material
	σ	stress in N m^{-2}
	l_0	initial length of material
	E	Young's modulus of material

For 20 nm – 70 nm thick gold, the change in length would be estimated to be 3.7 – 12 nm. This is on the order of the changes observed. Thus, the stresses produced by the converse flexoelectric effect in the underlying PZT would be sufficient to cause the deformations to the gold indentation which are suggested by the numerical modelling, collected SEMs and spectra.

The stress-strain curve for Au thin films display an initial linear elastic regime, followed by a plastic regime where greater deformations are induced for smaller stress increases [143] as shown in **Figure 8.19**. The threshold for changes to the optical spectra of the device can be understood within this framework. As the changes to the volume of the shuriken are on the order of 10s of percent, it is suggested that the changes take place within the plastic regime. Note that whilst freestanding gold would not return to its original shape under plastic deformation, the gold layer in this case is adhered to the underlying PZT: its relaxation can therefore restore the gold to its initial position. To a first approximation, the stress induced in the meta-film layers scales linearly with the voltage and any changes to the ORD spectrum will be proportional to the strain (the amount of deformation). Thus, it is expected that the applied voltage - ORD intensity changes will have the same form as the stress-strain curve of the composite film.

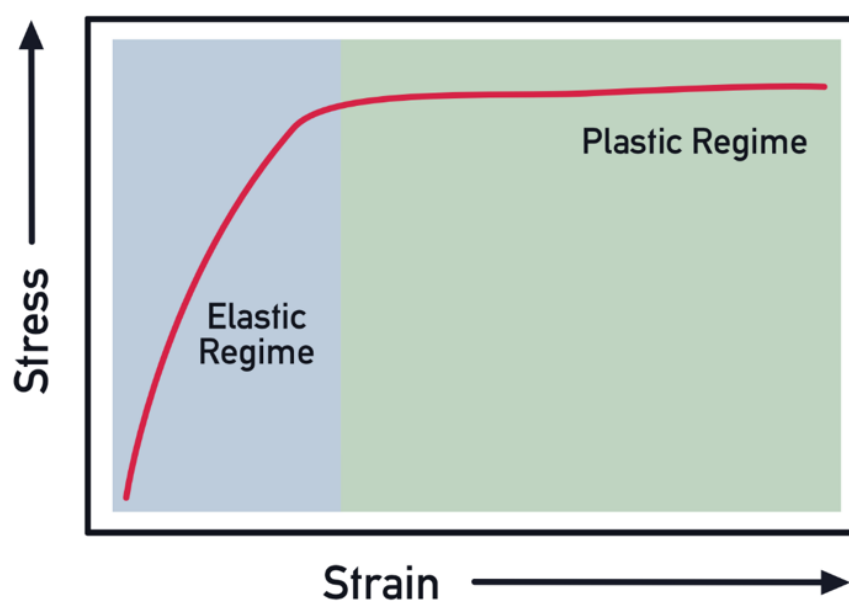


Figure 8.19: Stress strain curve for gold thin films.

It has been shown that after multiple deformation cycles the stress-strain behaviour of gold films changes. Previous work has shown that the stress-strain curve moves to the right with repeated deformations [141], [142] which indicates that it becomes progressively easier to deform the film. The origin of these effects are physical changes to the microstructure of the gold film and are consistent with the shortening of the timescale required for changes in the ORD spectrum to be observed as the number of voltage cycles progresses.

Lastly, the $d_{\text{PZT}} = 150$ nm and 50 nm structures exhibit different relaxation behaviours. In the $d_{\text{PZT}} = 50$ nm case the ORD signal does not relax to its original value, whereas the $d_{\text{PZT}} = 150$ nm device does. The fundamental difference between the two devices is that in the 50 nm case, the PZT layer is less than the indentation depth of the of the nanostructure (approximately 80nm). When this is the case, the bulk of the PZT on top of the substrate and that in the indentation hole do not directly overlap and are instead joined by a thinner layer of PZT which covers the shuriken sidewalls. The effect of this difference in geometric arrangement is not immediately clear. It is possible that deformations to the PZT are sufficiently large in the $d_{\text{PZT}} = 50$ nm case could fracture under the stress causing a freezing-in of the deformation. Manufacture of devices with progressively thicker PZT layers could aid understanding in this area.

This work is a proof-of-concept demonstration of a new paradigm of nano-electromechanical control: the use of the inverse flexoelectric effect to manipulate the form factor of a nanostructure and control its optical properties. The dynamic range presented here is greater than 4° , far better than previously reported work which showed a range of around 0.1° [144]. However, the performance of this prototype device has not been optimised and could be improved. For instance, the slow and history dependent response, likely associated with the mechanical properties of the PZT layer, could be mitigated against by using a more malleable flexoelectric polymer such as those based on polyvinylidene fluoride [145]. Also, a more substantial and reversible deformation may be possible if simpler 2-D chiral arrangement of closely coupled dot indentations were used instead of the complex shuriken design: this would also decrease variation in manufacturing between samples.

Active chiral metamaterials capable of modulating chiroptical properties have been previously demonstrated but these are often reliant upon complex multi-step fabrication techniques, or the introduction of external reagents [146], [147]: these mechanisms are more conducive toward chemical sensing. The concept of using flexoelectric materials to achieve nano-electromechanical control has unique benefits. Specifically, the concept is convergent with high

throughput polymer-based nanofabrication technologies such as injection moulding or nanoimprint lithography. Using an established platform of mass-produced prefabricated nanostructured polymer templates, active meta-devices can be created through the room temperature deposition of sandwich layers.

Chapter 8 Key Findings

- An active chiral metamaterial is fabricated which incorporates a flexoelectric layer, namely lead zirconate titanate.
- The geometry of the nanostructures is shown to be changed via a flexoelectric effect.
- Optical properties which are dependent upon the nanostructure geometry are shown to be controlled.
- The spectroscopic changes are linked to the geometric changes by numerical simulations.

Part D

Summary and outlook

Chapter 9

Summary and outlook

In summary, two applications of chiral metamaterials have been outlined in this work. The first is the application of chiral metamaterials for the sensing of biological materials. The effect of geometric and morphological defects on the chiroptical properties of the nanostructure were initially investigated. An obvious extension to this work would be to determine whether the surface roughening which leads to the generation of optical chirality ‘hotspots’ correlates with enhanced sensing of chiral material. This could be determined experimentally by increasing the surface roughness of the nanostructures by use of chemical agents such as tetrahydrofuran or potassium iodide [148]. Simulation of surfaces with randomly generated roughness would provide greater insight. The simulation structures derived directly from their atomic force micrographs has obvious potential for future work, but it requires refinement with regards to removal of artefacts.

With regards to the sensing mechanism introduced in Chapter 7, it would be informative to implement the direct modelling simulation strategy as idealised geometries are not truly representative of fabricated nanostructures. Experimental data to support this work would certainly be of interest, but the fabrication of free-floating nanostructures which can support such complex geometries are unlikely at the current time.

In **Chapter 8** a novel approach to active plasmonics is introduced. It has many benefits over methods which have already been described including integration with polymer-based substrates and ease of fabrication. There are some obvious improvements to be made with regards to the reproducibility of the observed effects which requires optimisation. The incorporation of different nanostructures or non-uniform changes to components of the nanostructure could also produce exciting effects.

Since starting this work, I have been fascinated by the creative approaches that researchers have taken with regards to the applications of plasmonics and metamaterials. I have cited many examples of those that find most interesting throughout this work. My hope is that I have, in a small way, contributed to this body of research with what I have described in this thesis and that anyone who comes across it in the future might think to themselves, “hmm, that’s interesting”.

References

- [1] L. D. Barron, “From Cosmic Chirality to Protein Structure: Lord Kelvin’s Legacy,” *Chirality*, vol. 24, no. 11, pp. 879–893, Nov. 2012, doi: 10.1002/chir.22017.
- [2] P. Fara, “Baron Kelvin of Largs: an economical engineer,” *Endeavour*. 2007, doi: 10.1016/j.endeavour.2007.10.002.
- [3] H. Gerlach, “Chirality: A Relational Geometric-Physical Property,” *Chirality*, vol. 25, no. 11, pp. 684–685, Nov. 2013, doi: 10.1002/chir.22216.
- [4] S. S. Oh and O. Hess, “Chiral metamaterials: enhancement and control of optical activity and circular dichroism,” *Nano Converg.*, vol. 2, no. 1, p. 24, 2015, doi: 10.1186/s40580-015-0058-2.
- [5] M. A. Schilthuizen Davison, M. Schilthuizen, and A. Davison, “The convoluted evolution of snail chirality,” *Naturwissenschaften*, vol. 92, no. 11, pp. 504–515, Nov. 2005, doi: 10.1007/s00114-05-0045-2.
- [6] R. S. Cahn, C. Ingold, and V. Prelog, “Specification of Molecular Chirality,” *Angew. Chemie Int. Ed. English*, vol. 5, no. 4, pp. 385–415, 1966, doi: 10.1002/anie.196603851.
- [7] G. Zhang and H. J. Sun, “Racemization in Reverse : Evidence that D-Amino Acid Toxicity on Earth Is Controlled by Bacteria with Racemases,” vol. 9, no. 3, pp. 1–6, 2014, doi: 10.1371/journal.pone.0092101.
- [8] D. G. Blackmond, “The origin of biological homochirality.,” *Cold Spring Harb. Perspect.*

- Biol.*, vol. 2, no. 5, pp. 1–17, 2010, doi: 10.1101/cshperspect.a002147.
- [9] J. C. Brookes, A. . Horsfield, and A. . Stoneham, “Odour character differences for enantiomers correlate with molecular flexibility,” *J. R. Soc. Interface*, vol. 6, no. 30, pp. 75–86, 2009, doi: 10.1098/rsif.2008.0165.
- [10] I. Čorić and B. List, “Asymmetric spiroacetalization catalysed by confined Brønsted acids,” *Nature*, vol. 483, no. 7389, pp. 315–319, 2012, doi: 10.1038/nature10932.
- [11] Y. Wei *et al.*, “An evidence for the chiral discrimination of naproxen enantiomers: A combined experimental and theoretical study,” *J. Phys. Chem. C*, vol. 115, no. 10, pp. 4033–4040, 2011, doi: 10.1021/jp108464r.
- [12] N. J. Halas, S. Lal, W. S. Chang, S. Link, and P. Nordlander, “Plasmons in strongly coupled metallic nanostructures,” *Chem. Rev.*, vol. 111, no. 6, pp. 3913–3961, 2011, doi: 10.1021/cr200061k.
- [13] S. A. Maier, *Plasmonics: Fundamentals and Applications*, vol. 53, no. 9. New York, NY: Springer US, 2007.
- [14] D. M. Lipkin, “Existence of a new conservation law in electromagnetic theory,” *J. Math. Phys.*, vol. 5, no. 5, pp. 696–700, May 1964, doi: 10.1063/1.1704165.
- [15] Y. Tang and A. E. Cohen, “Optical Chirality and Its Interaction with Matter,” *Phys. Rev. Lett.*, vol. 104, no. 16, p. 163901, Apr. 2010, doi: 10.1103/PhysRevLett.104.163901.
- [16] S. Xiao, T. Wang, T. Liu, C. Zhou, X. Jiang, and J. Zhang, “Active metamaterials and metadevices: A review,” *J. Phys. D. Appl. Phys.*, vol. 53, no. 50, 2020, doi: 10.1088/1361-6463/abaced.
- [17] N. Jiang, X. Zhuo, and J. Wang, “Active Plasmonics: Principles, Structures, and Applications,” *Chem. Rev.*, vol. 118, no. 6, pp. 3054–3099, 2018, doi: 10.1021/acs.chemrev.7b00252.
- [18] D. Fleisch, *A Student’s Guide to Maxwell’s Equations*, 1st ed. Cambridge: Cambridge University Press, 2008.
- [19] L. V. Poulikakos, “Chiral Light-Matter Interactions in the Near and Far Field,” ETH Zurich, 2018.
- [20] W. Zhang, “Optical Activity and Applications of Planar Chiral Metamaterials,” University of Southampton, 2006.
- [21] L. D. Barron, *Molecular Light Scattering and Optical Activity*, no. 1. Cambridge University Press, 2004.
- [22] S. M. Kelly, T. J. Jess, and N. C. Price, “How to study proteins by circular dichroism,” *Biochim. Biophys. Acta - Proteins Proteomics*, vol. 1751, no. 2, pp. 119–139, Aug. 2005, doi: 10.1016/j.bbapap.2005.06.005.
- [23] J. T. Collins, C. Kuppe, D. C. Hooper, C. Sibilía, M. Centini, and V. K. Valev, “Chirality and Chiroptical Effects in Metal Nanostructures: Fundamentals and Current Trends,” *Adv. Opt. Mater.*, vol. 5, no. 16, 2017, doi: 10.1002/adom.201700182.
- [24] D. M. Solís, J. M. Taboada, L. Landesa, J. L. Rodríguez, and F. Obelleiro, “Squeezing Maxwell’s equations into the nanoscale,” *Prog. Electromagn. Res.*, vol. 154, pp. 35–50, 2015, doi: 10.2528/PIER15110103.
- [25] D. P. O’Neal, L. R. Hirsch, N. J. Halas, J. D. Payne, and J. L. West, “Photo-thermal tumor ablation in mice using near infrared-absorbing nanoparticles,” *Cancer Lett.*, vol. 209, no. 2, pp. 171–176, 2004, doi: 10.1016/j.canlet.2004.02.004.
- [26] X. Duan, S. Kamin, and N. Liu, “Dynamic plasmonic colour display,” *Nat. Commun.*, vol. 8, pp. 1–9, 2017, doi: 10.1038/ncomms14606.
- [27] D. Zhang *et al.*, “Peptide functionalized nanoplasmonic sensor for explosive detection,” *Nano-Micro Lett.*, vol. 8, no. 1, pp. 36–43, 2016, doi: 10.1007/s40820-015-0059-z.

- [28] M. Rycenga *et al.*, “Controlling the synthesis and assembly of silver nanostructures for plasmonic applications,” *Chem. Rev.*, vol. 111, no. 6, pp. 3669–3712, 2011, doi: 10.1021/cr100275d.
- [29] W. Cai and V. Shalaev, *Optical Metamaterials*. Springer, 2010.
- [30] L. Novotny and B. Hecht, *Principles of Nano-Optics*, no. May. Cambridge: Cambridge University Press, 2012.
- [31] A. B. Khanikaev *et al.*, “Experimental demonstration of the microscopic origin of circular dichroism in two-dimensional metamaterials,” *Nat. Commun.*, vol. 7, no. May, pp. 1–8, 2016, doi: 10.1038/ncomms12045.
- [32] K. A. Willets and R. P. Van Duyne, “Localized Surface Plasmon Resonance Spectroscopy and Sensing,” *Annu. Rev. Phys. Chem.*, vol. 58, no. 1, pp. 267–297, 2007, doi: 10.1146/annurev.physchem.58.032806.104607.
- [33] Y. Li, *Plasmonic Optics: Theory and Applications*. SPIE, 2017.
- [34] M. Schäferling, *Chiral Nanophotonics: Chiral Optical Properties of Plasmonic Systems*, vol. 205. Cham: Springer International Publishing, 2017.
- [35] K. L. Kelly, E. Coronado, L. L. Zhao, and G. C. Schatz, “The Optical Properties of Metal Nanoparticles: The Influence of Size, Shape, and Dielectric Environment,” *J. Phys. Chem. B*, vol. 107, no. 3, pp. 668–677, Jan. 2003, doi: 10.1021/jp026731y.
- [36] S. Link and M. A. El-Sayed, “Shape and size dependence of radiative, non-radiative and photothermal properties of gold nanocrystals,” *Int. Rev. Phys. Chem.*, vol. 19, no. 3, pp. 409–453, 2000, doi: 10.1080/01442350050034180.
- [37] B. Khodashenas and H. R. Ghorbani, “Synthesis of silver nanoparticles with different shapes,” *Arab. J. Chem.*, vol. 12, no. 8, pp. 1823–1838, 2019, doi: 10.1016/j.arabjc.2014.12.014.
- [38] S. Barbosa *et al.*, “Tuning size and sensing properties in colloidal gold nanostars,” *Langmuir*, vol. 26, no. 18, pp. 14943–14950, 2010, doi: 10.1021/la102559e.
- [39] T. K. Sau and C. J. Murphy, “Room temperature, high-yield synthesis of multiple shapes of gold nanoparticles in aqueous solution,” *J. Am. Chem. Soc.*, vol. 126, no. 28, pp. 8648–8649, 2004, doi: 10.1021/ja047846d.
- [40] A. J. Haes and R. P. Van Duyne, “A nanoscale optical biosensor: Sensitivity and selectivity of an approach based on the localized surface plasmon resonance spectroscopy of triangular silver nanoparticles,” *J. Am. Chem. Soc.*, vol. 124, no. 35, pp. 10596–10604, 2002, doi: 10.1021/ja020393x.
- [41] W. P. Hall, J. Modica, J. Anker, Y. Lin, M. Mrksich, and R. P. Van Duyne, “A conformation- and ion-sensitive plasmonic biosensor,” *Nano Lett.*, vol. 11, no. 3, pp. 1098–1105, 2011, doi: 10.1021/nl103994w.
- [42] X. Zhang *et al.*, “Plasmon-Enhanced Catalysis: Distinguishing Thermal and Nonthermal Effects,” *Nano Lett.*, vol. 18, no. 3, pp. 1714–1723, 2018, doi: 10.1021/acs.nanolett.7b04776.
- [43] A. Nitzan and L. E. Brus, “Theoretical model for enhanced photochemistry on rough surfaces,” *J. Chem. Phys.*, vol. 75, no. 5, pp. 2205–2214, 1981, doi: 10.1063/1.442333.
- [44] E. C. Le Ru, E. Blackie, M. Meyer, and P. G. Etchegoint, “Surface enhanced Raman scattering enhancement factors: A comprehensive study,” *J. Phys. Chem. C*, vol. 111, no. 37, pp. 13794–13803, 2007, doi: 10.1021/jp0687908.
- [45] V. K. Valev, J. J. Baumberg, C. Sibilia, and T. Verbiest, “Chirality and chiroptical effects in plasmonic nanostructures: Fundamentals, recent progress, and outlook,” *Adv. Mater.*, vol. 25, no. 18, pp. 2517–2534, 2013, doi: 10.1002/adma.201205178.
- [46] M. Hentschel, M. Schäferling, T. Weiss, H. G. Kuball, N. Liu, and H. Giessen, “Three-dimensional chiral plasmonic oligomers,” *Opt. InfoBase Conf. Pap.*, 2012, doi: 10.1021/ol100000a001

- 10.1364/qels.2012.qth4f.1.
- [47] Z. Fan and A. O. Govorov, “Chiral nanocrystals: Plasmonic spectra and circular dichroism,” *Nano Lett.*, vol. 12, no. 6, pp. 3283–3289, 2012, doi: 10.1021/nl3013715.
- [48] O. Arteaga *et al.*, “Relation between 2D/3D chirality and the appearance of chiroptical effects in real nanostructures,” *Opt. Express*, vol. 24, no. 3, p. 2242, 2016, doi: 10.1364/OE.24.002242.
- [49] M. Kuwata-Gonokami *et al.*, “Giant optical activity in quasi-two-dimensional planar nanostructures,” *Phys. Rev. Lett.*, vol. 95, no. 22, pp. 1–4, 2005, doi: 10.1103/PhysRevLett.95.227401.
- [50] V. K. Valev, “Chiral Nanomaterials and Chiral Light,” *Opt. Photonics News*, vol. 27, no. 7, p. 34, 2016, doi: 10.1364/OPN.27.7.000034.
- [51] X. Yin, M. Schäferling, B. Metzger, and H. Giessen, “Interpreting chiral nanophotonic spectra: The plasmonic Born-Kuhn model,” *Nano Lett.*, vol. 13, no. 12, pp. 6238–6243, 2013, doi: 10.1021/nl403705k.
- [52] O. Arteaga, “Number of independent parameters in the Mueller matrix representation of homogeneous depolarizing media.,” *Opt. Lett.*, vol. 38, no. 7, pp. 1131–3, 2013, doi: 10.1364/OL.38.001131.
- [53] M. S. Davis, W. Zhu, J. K. Lee, H. J. Lezec, and A. Agrawal, “Microscopic origin of the chiroptical response of optical media,” *Sci. Adv.*, vol. 5, no. 10, 2019, doi: 10.1126/sciadv.aav8262.
- [54] M. Kafesaki, I. Tsiapa, N. Katsarakis, T. Koschny, C. M. Soukoulis, and E. N. Economou, “Left-handed metamaterials: The fishnet structure and its variations,” *Phys. Rev. B - Condens. Matter Mater. Phys.*, vol. 75, no. 23, 2007, doi: 10.1103/PhysRevB.75.235114.
- [55] B. Wood, “Metamaterials and invisibility,” *Comptes Rendus Phys.*, vol. 10, no. 5, pp. 379–390, 2009, doi: 10.1016/j.crhy.2009.01.002.
- [56] K. Yao and Y. Liu, “Plasmonic metamaterials,” *Nanotechnol. Rev.*, vol. 3, no. 2, pp. 177–210, 2014, doi: 10.1515/ntrev-2012-0071.
- [57] M. Esposito *et al.*, “Nanoscale 3D chiral plasmonic helices with circular dichroism at visible frequencies,” *ACS Photonics*, vol. 2, no. 1, pp. 105–114, 2015, doi: 10.1021/ph500318p.
- [58] Z. Wu and Y. Zheng, “Moiré Chiral Metamaterials,” *Adv. Opt. Mater.*, vol. 5, no. 16, pp. 1–9, 2017, doi: 10.1002/adom.201700034.
- [59] S. Zu, Y. Bao, and Z. Fang, “Planar plasmonic chiral nanostructures,” *Nanoscale*, vol. 8, no. 7, pp. 3900–3905, 2016, doi: 10.1039/C5NR09302C.
- [60] W. Whyte, *Cleanroom Technology*. 2001.
- [61] A. Sarangan, *Nanofabrication: Principles to Laboratory Practice*. CRC Press, 2016.
- [62] M. Stepanova and S. Dew, *Nanofabrication: Techniques and Principles*. New York: Springer, 2012.
- [63] F. Colas, D. Barchiesi, S. Kessentini, T. Toury, and M. L. D. La Chapelle, “Comparison of adhesion layers of gold on silicate glasses for SERS detection,” *J. Opt. (United Kingdom)*, vol. 17, no. 11, 2015, doi: 10.1088/2040-8978/17/11/114010.
- [64] J. M. Stormonth-Darling, R. H. Pedersen, C. How, and N. Gadegaard, “Injection moulding of ultra high aspect ratio nanostructures using coated polymer tooling,” *J. Micromechanics Microengineering*, vol. 24, no. 7, 2014, doi: 10.1088/0960-1317/24/7/075019.
- [65] A. S. Karimullah *et al.*, “Disposable Plasmonics: Plastic Templated Plasmonic Metamaterials with Tunable Chirality,” *Adv. Mater.*, vol. 27, no. 37, pp. 5610–5616, 2015, doi: 10.1002/adma.201501816.

- [66] B. Voigtländer, *Scanning Probe Microscopy*. Berlin, Heidelberg: Springer Berlin Heidelberg, 2015.
- [67] R. F. Egerton, *Physical principles of electron microscopy*, vol. 8, no. 12. 2005.
- [68] E. Collett, *Field Guide to Polarization*. SPIE, 2005.
- [69] B. M. A. Rahman and A. Agrawal, *Finite Element Modeling Methods for Photonics*. London: Artech House, 2013.
- [70] M. Okereke and S. Keates, *Finite Element Applications*. Cham: Springer Nature, 2018.
- [71] R. W. Pryor, *Multiphysics Modeling Using COMSOL. A First Principles Approach*. Sudbury: Jones and Bartlett Publishers, 2011.
- [72] W. Kuhn, “The physical significance of optical rotatory power,” *Trans. Faraday Soc.*, vol. 26, no. 3, pp. 293–308, 1930, doi: 10.1039/tf9302600293.
- [73] J. S. Choi and M. Cho, “Limitations of a superchiral field,” *Phys. Rev. A - At. Mol. Opt. Phys.*, vol. 86, no. 6, pp. 1–22, 2012, doi: 10.1103/PhysRevA.86.063834.
- [74] Y. Tang and A. E. Cohen, “Enhanced Enantioselectivity in Excitation of Chiral Molecules by Superchiral Light,” *Science (80-.)*, vol. 332, no. 6027, pp. 333–336, 2011, doi: 10.1126/science.1202817.
- [75] D. M. Lipkin, “Existence of a New Conservation Law in Electromagnetic Theory,” *J. Math. Phys.*, vol. 5, no. 5, pp. 696–700, May 1964, doi: 10.1063/1.1704165.
- [76] T. J. Davis and E. Hendry, “Superchiral electromagnetic fields created by surface plasmons in nonchiral metallic nanostructures,” *Phys. Rev. B - Condens. Matter Mater. Phys.*, vol. 87, no. 8, pp. 1–5, 2013, doi: 10.1103/PhysRevB.87.085405.
- [77] E. Hendry, R. V. Mikhaylovskiy, L. D. Barron, M. Kadodwala, and T. J. Davis, “Chiral electromagnetic fields generated by arrays of nanoslits,” *Nano Lett.*, vol. 12, no. 7, pp. 3640–3644, 2012, doi: 10.1021/nl3012787.
- [78] M. Schäferling, D. Dregely, M. Hentschel, and H. Giessen, “Tailoring Enhanced Optical Chirality: Design Principles for Chiral Plasmonic Nanostructures,” *Phys. Rev. X*, vol. 2, no. 3, p. 031010, Aug. 2012, doi: 10.1103/PhysRevX.2.031010.
- [79] L. V. Poulikakos *et al.*, “Optical Chirality Flux as a Useful Far-Field Probe of Chiral Near Fields,” *ACS Photonics*, vol. 3, no. 9, pp. 1619–1625, Sep. 2016, doi: 10.1021/acsp Photonics.6b00201.
- [80] F. Kempf, R. Mueller, E. Frey, J. M. Yeomans, and A. Doostmohammadi, “Active matter invasion,” ETH urich, 2019.
- [81] J. E. Vázquez-Lozano and A. Martínez, “Optical Chirality in Dispersive and Lossy Media,” *Phys. Rev. Lett.*, vol. 121, no. 4, p. 043901, Jul. 2018, doi: 10.1103/PhysRevLett.121.043901.
- [82] E. Hendry *et al.*, “Ultrasensitive detection and characterization of biomolecules using superchiral fields,” *Nat. Nanotechnol.*, vol. 5, no. 11, pp. 783–787, 2010, doi: 10.1038/nnano.2010.209.
- [83] R. Tullius *et al.*, “‘Superchiral’ Spectroscopy: Detection of Protein Higher Order Hierarchical Structure with Chiral Plasmonic Nanostructures,” *J. Am. Chem. Soc.*, vol. 137, no. 26, pp. 8380–8383, Jul. 2015, doi: 10.1021/jacs.5b04806.
- [84] T. Kakkar *et al.*, “Superchiral near fields detect virus structure,” *Light Sci. Appl.*, vol. 9, no. 1, pp. 1–10, 2020, doi: 10.1038/s41377-020-00433-1.
- [85] J. García-Guirado, M. Svedendahl, J. Puigdollers, and R. Quidant, “Enantiomer-Selective Molecular Sensing Using Racemic Nanoplasmonic Arrays,” *Nano Lett.*, vol. 18, no. 10, pp. 6279–6285, Oct. 2018, doi: 10.1021/acs.nanolett.8b02433.
- [86] G. W. Paterson, A. S. Karimullah, S. G. Smith, M. Kadodwala, and D. A. MacLaren, “Symmetry Reduction and Shape Effects in Concave Chiral Plasmonic Structures,” *J.*

- Phys. Chem. C*, vol. 122, no. 9, pp. 5049–5056, 2018, doi: 10.1021/acs.jpcc.7b12260.
- [87] J. M. Teulon *et al.*, “On the operational aspects of measuring nanoparticle sizes,” *Nanomaterials*, vol. 9, no. 1, 2019, doi: 10.3390/nano9010018.
- [88] Y. Gong, J. Xu, and R. C. Buchanan, “Surface roughness: A review of its measurement at micro-/nano-scale,” *Phys. Sci. Rev.*, vol. 3, no. 1, pp. 1–10, 2019, doi: 10.1515/psr-2017-0057.
- [89] P. B. Johnson and R. W. Christy, “Optical Constants of the Noble Metals,” *Phys. Rev. B*, vol. 6, no. 12, pp. 4370–4379, Dec. 1972, doi: 10.1103/PhysRevB.6.4370.
- [90] W. K. Phua, Y. L. Hor, E. S. P. Leong, Y. J. Liu, and E. H. Khoo, “Study of Circular Dichroism Modes Through Decomposition of Planar Nanostructures,” pp. 449–457, 2016, doi: 10.1007/s11468-015-0065-5.
- [91] C. Ciracì, F. Vidal-Codina, D. Yoo, J. Peraire, S. H. Oh, and D. R. Smith, “Impact of Surface Roughness in Nanogap Plasmonic Systems,” *ACS Photonics*, vol. 7, no. 4, pp. 908–913, 2020, doi: 10.1021/acsphotonics.0c00099.
- [92] H. Wei and H. Xu, “Hot spots in different metal nanostructures for plasmon-enhanced Raman spectroscopy,” *Nanoscale*, vol. 5, no. 22, pp. 10794–10805, 2013, doi: 10.1039/c3nr02924g.
- [93] S. L. Kleinman, R. R. Frontiera, A. I. Henry, J. A. Dieringer, and R. P. Van Duyne, “Creating, characterizing, and controlling chemistry with SERS hot spots,” *Phys. Chem. Chem. Phys.*, vol. 15, no. 1, pp. 21–36, 2013, doi: 10.1039/c2cp42598j.
- [94] M. Moskovits, “Surface roughness and the enhanced intensity of Raman scattering by molecules adsorbed on metals,” *J. Chem. Phys.*, vol. 69, no. 9, pp. 4159–4161, 1978, doi: 10.1063/1.437095.
- [95] E. H. Khoo, E. S. P. Leong, S. J. Wu, W. K. Phua, Y. L. Hor, and Y. J. Liu, “Effects of asymmetric nanostructures on the extinction difference properties of actin biomolecules and filaments,” *Sci. Rep.*, vol. 6, no. 1, p. 19658, Apr. 2016, doi: 10.1038/srep19658.
- [96] V. M. Shalaev and S. Kawata, “Nanophotonics with Surface Plasmons,” First Edit., Amsterdam: Elsevier, 2007, p. 341.
- [97] S. K. Ghosh, S. Nath, S. Kundu, K. Esumi, and T. Pal, “Solvent and ligand effects on the localized surface plasmon resonance (LSPR) of gold colloids,” *J. Phys. Chem. B*, vol. 108, no. 37, pp. 13963–13971, 2004, doi: 10.1021/jp047021q.
- [98] B. Koslowski *et al.*, “Oxidation of preferentially (1 1 1)-oriented Au films in an oxygen plasma investigated by scanning tunneling microscopy and photoelectron spectroscopy,” *Surf. Sci.*, vol. 475, no. 1–3, pp. 1–10, 2001, doi: 10.1016/S0039-6028(00)00986-9.
- [99] K. M. Cook and G. S. Ferguson, “Determination of the wavelength-dependent refractive index of a gold-oxide thin film,” *J. Phys. Chem. C*, vol. 115, no. 46, pp. 22976–22980, 2011, doi: 10.1021/jp207031s.
- [100] G. W. Kim and J. W. Ha, “Single-particle study: effects of oxygen plasma treatment on structural and spectral changes of anisotropic gold nanorods,” *Phys. Chem. Chem. Phys.*, vol. 22, no. 21, pp. 11767–11770, 2020, doi: 10.1039/d0cp00996b.
- [101] C. Kelly *et al.*, “Controlling Metamaterial Transparency with Superchiral Fields,” *ACS Photonics*, vol. 5, no. 2, pp. 535–543, Feb. 2018, doi: 10.1021/acsphotonics.7b01071.
- [102] A. O. Govorov and Z. Fan, “Theory of Chiral Plasmonic Nanostructures Comprising Metal Nanocrystals and Chiral Molecular Media,” *ChemPhysChem*, vol. 13, no. 10, pp. 2551–2560, Jul. 2012, doi: 10.1002/cphc.201100958.
- [103] C. Kelly *et al.*, “Chiral Plasmonic Fields Probe Structural Order of Biointerfaces,” *J. Am. Chem. Soc.*, vol. 140, no. 27, pp. 8509–8517, Jul. 2018, doi: 10.1021/jacs.8b03634.
- [104] C. Kelly *et al.*, “Controlling Metamaterial Transparency with Superchiral Fields,” pp. 1–8.

- [105] L. V. Poulikakos, J. A. Dionne, and A. García-Etxarri, “Optical helicity and optical chirality in free space and in the presence of matter,” *Symmetry (Basel)*, vol. 11, no. 9, pp. 1–16, 2019, doi: 10.3390/sym11091113.
- [106] T. G. Philbin, “Lipkin’s conservation law, Noether’s theorem, and the relation to optical helicity,” *Phys. Rev. A - At. Mol. Opt. Phys.*, vol. 87, no. 4, 2013, doi: 10.1103/PhysRevA.87.043843.
- [107] N. A. Abdulrahman *et al.*, “Induced Chirality through Electromagnetic Coupling between Chiral Molecular Layers and Plasmonic Nanostructures,” *Nano Lett.*, vol. 12, no. 2, pp. 977–983, Feb. 2012, doi: 10.1021/nl204055r.
- [108] B. M. Maoz *et al.*, “Amplification of Chiroptical Activity of Chiral Biomolecules by Surface Plasmons,” *Nano Lett.*, vol. 13, no. 3, pp. 1203–1209, Mar. 2013, doi: 10.1021/nl304638a.
- [109] Y. Zhao, A. N. Askarpour, L. Sun, J. Shi, X. Li, and A. Alù, “Chirality detection of enantiomers using twisted optical metamaterials,” *Nat. Commun.*, vol. 8, no. 1, p. 14180, Apr. 2017, doi: 10.1038/ncomms14180.
- [110] R. Tullius *et al.*, “Superchiral Plasmonic Phase Sensitivity for Fingerprinting of Protein Interface Structure,” *ACS Nano*, vol. 11, no. 12, pp. 12049–12056, 2017, doi: 10.1021/acsnano.7b04698.
- [111] X. Han, K. Liu, and C. Sun, “Plasmonics for biosensing,” *Materials (Basel)*, vol. 12, no. 9, 2019, doi: 10.3390/ma12091411.
- [112] M. Pishvar and R. L. Harne, “Foundations for Soft, Smart Matter by Active Mechanical Metamaterials,” *Adv. Sci.*, vol. 7, no. 18, pp. 1–17, 2020, doi: 10.1002/advs.202001384.
- [113] A. Llordés, G. Garcia, J. Gazquez, and D. J. Milliron, “Tunable near-infrared and visible-light transmittance in nanocrystal-in-glass composites,” *Nature*, vol. 500, no. 7462, pp. 323–326, 2013, doi: 10.1038/nature12398.
- [114] A. Böhme, F. Sterl, E. Kath, M. Ubl, V. Manninen, and H. Giessen, “Electrochemistry on Inverse Copper Nanoantennas: Active Plasmonic Devices with Extraordinarily Large Resonance Shift,” *ACS Photonics*, vol. 6, no. 8, pp. 1863–1868, 2019, doi: 10.1021/acsp Photonics.9b00716.
- [115] X. Duan, S. Kamin, F. Sterl, H. Giessen, and N. Liu, “Hydrogen-Regulated Chiral Nanoplasmonics,” *Nano Lett.*, vol. 16, no. 2, pp. 1462–1466, 2016, doi: 10.1021/acs.nanolett.5b05105.
- [116] H. Tao, A. C. Strikwerda, K. Fan, W. J. Padilla, X. Zhang, and R. D. Averitt, “Reconfigurable Terahertz Metamaterials,” *Phys. Rev. Lett.*, vol. 103, no. 14, p. 147401, Oct. 2009, doi: 10.1103/PhysRevLett.103.147401.
- [117] C. P. Ho, P. Pitchappa, Y. S. Lin, C. Y. Huang, P. Kropelnicki, and C. Lee, “Electrothermally actuated microelectromechanical systems based omega-ring terahertz metamaterial with polarization dependent characteristics,” *Appl. Phys. Lett.*, vol. 104, no. 16, 2014, doi: 10.1063/1.4871999.
- [118] X. Yin *et al.*, “Active Chiral Plasmonics,” *Nano Lett.*, vol. 15, no. 7, pp. 4255–4260, 2015, doi: 10.1021/nl5042325.
- [119] F. Ma, Y. S. Lin, X. Zhang, and C. Lee, “Tunable multiband terahertz metamaterials using a reconfigurable electric split-ring resonator array,” *Light Sci. Appl.*, vol. 3, no. December 2013, pp. 1–8, 2014, doi: 10.1038/lsa.2014.52.
- [120] K. L. Ekinici and M. L. Roukes, “Nanoelectromechanical systems,” *Rev. Sci. Instrum.*, vol. 76, no. 6, 2005, doi: 10.1063/1.1927327.
- [121] N. I. Zheludev and E. Plum, “Reconfigurable nanomechanical photonic metamaterials,” *Nat. Nanotechnol.*, vol. 11, no. 1, pp. 16–22, 2016, doi: 10.1038/nnano.2015.302.
- [122] H. G. Craighead, “Nanoelectromechanical Systems,” *Science (80-.)*, vol. 290, no. 5496, pp. 1532–1535, Nov. 2000, doi: 10.1126/science.290.5496.1532.

- [123] L. Midolo, A. Schliesser, and A. Fiore, “Nano-opto-electro-mechanical systems,” *Nat. Nanotechnol.*, vol. 13, no. 1, pp. 11–18, 2018, doi: 10.1038/s41565-017-0039-1.
- [124] J. Y. Ou, E. Plum, J. Zhang, and N. I. Zheludev, “An electromechanically reconfigurable plasmonic metamaterial operating in the near-infrared,” *Nat. Nanotechnol.*, vol. 8, no. 4, pp. 252–255, 2013, doi: 10.1038/nnano.2013.25.
- [125] K. Yamaguchi, M. Fujii, T. Okamoto, and M. Haraguchi, “Electrically driven plasmon chip: Active plasmon filter,” *Appl. Phys. Express*, vol. 7, no. 1, 2014, doi: 10.7567/APEX.7.012201.
- [126] L. L. Ma, W. J. Chen, and Y. Zheng, *Flexoelectric effect at the nanoscale*. 2019.
- [127] S. Katzir, *The Beginnings of Piezoelectrics - A Study in Mundane Physics*, vol. 67, no. 2. 2010.
- [128] W. Heywang, K. Lubitz, and W. Wersing, *Piezoelectricity*, vol. 114. Berlin, Heidelberg: Springer Berlin Heidelberg, 2008.
- [129] W. Huang, F.-G. Yuan, and X. Jiang, “Flexoelectric effect, materials, and structures,” in *Structural Health Monitoring (SHM) in Aerospace Structures*, Elsevier, 2016, pp. 119–148.
- [130] R. S. Dahiya and M. Valle, *Robotic tactile sensing: Technologies and system*, vol. 9789400705. 2014.
- [131] P. Zubko, G. Catalan, and A. K. Tagantsev, “Flexoelectric effect in solids,” *Annu. Rev. Mater. Res.*, vol. 43, pp. 387–421, 2013, doi: 10.1146/annurev-matsci-071312-121634.
- [132] T. D. Nguyen, S. Mao, Y. W. Yeh, P. K. Purohit, and M. C. McAlpine, “Nanoscale flexoelectricity,” *Adv. Mater.*, vol. 25, no. 7, pp. 946–974, 2013, doi: 10.1002/adma.201203852.
- [133] L. Shu, R. Liang, Z. Rao, L. Fei, S. Ke, and Y. Wang, “Flexoelectric materials and their related applications: A focused review,” *J. Adv. Ceram.*, vol. 8, no. 2, pp. 153–173, 2019, doi: 10.1007/s40145-018-0311-3.
- [134] S. Huang, L. Qi, W. Huang, L. Shu, S. Zhou, and X. Jiang, “Flexoelectricity in dielectrics: Materials, structures and characterizations,” *J. Adv. Dielectr.*, vol. 8, no. 2, pp. 1–11, 2018, doi: 10.1142/S2010135X18300025.
- [135] M. S. Majdoub, P. Sharma, and T. Cagin, “Enhanced size-dependent piezoelectricity and elasticity in nanostructures due to the flexoelectric effect,” *Phys. Rev. B - Condens. Matter Mater. Phys.*, vol. 77, no. 12, pp. 1–9, 2008, doi: 10.1103/PhysRevB.77.125424.
- [136] D. Lee *et al.*, “Giant Flexoelectric Effect in Ferroelectric Epitaxial Thin Films,” *Phys. Rev. Lett.*, vol. 107, no. 5, p. 057602, Jul. 2011, doi: 10.1103/PhysRevLett.107.057602.
- [137] A. Abdollahi, N. Domingo, I. Arias, and G. Catalan, “Converse flexoelectricity yields large piezoresponse force microscopy signals in non-piezoelectric materials,” *Nat. Commun.*, vol. 10, no. 1, pp. 1–6, 2019, doi: 10.1038/s41467-019-09266-y.
- [138] T. J. Zhu, L. Lu, and M. O. Lai, “Pulsed laser deposition of lead-zirconate-titanate thin films and multilayered heterostructures,” *Appl. Phys. A Mater. Sci. Process.*, vol. 81, no. 4, pp. 701–714, 2005, doi: 10.1007/s00339-005-3227-z.
- [139] W. Ma and L. E. Cross, “Flexoelectric effect in ceramic lead zirconate titanate,” *Appl. Phys. Lett.*, vol. 86, no. 7, pp. 1–3, 2005, doi: 10.1063/1.1868078.
- [140] A. S. Tran, T. H. Fang, and J. W. Hsiao, “Incipient plasticity and voids nucleation of nanocrystalline gold nanofilms using molecular dynamics simulation,” *Curr. Appl. Phys.*, vol. 19, no. 3, pp. 332–340, 2019, doi: 10.1016/j.cap.2018.12.015.
- [141] B. Merle and M. Göken, “Bulge fatigue testing of freestanding and supported gold films,” *J. Mater. Res.*, vol. 29, no. 2, pp. 267–276, 2014, doi: 10.1557/jmr.2013.373.
- [142] R. D. Emery and G. L. Povirk, “Tensile behavior of free-standing gold films. Part II. Fine-

-
- grained films,” *Acta Mater.*, vol. 51, no. 7, pp. 2079–2087, 2003, doi: 10.1016/S1359-6454(03)00007-7.
- [143] W. N. Sharpe *et al.*, “Tensile stress-strain curves of gold film,” *Am. Soc. Mech. Eng. Mater. Div. MD*, pp. 1–8, 2006.
- [144] S. P. Rodrigues *et al.*, “Intensity-dependent modulation of optically active signals in a chiral metamaterial,” *Nat. Publ. Gr.*, pp. 1–9, 2017, doi: <https://doi.org/10.1038/ncomms14602>.
- [145] J. Liu, Y. Zhou, X. Hu, and B. Chu, “Flexoelectric effect in PVDF-based copolymers and terpolymers,” *Appl. Phys. Lett.*, vol. 112, no. 23, 2018, doi: 10.1063/1.5028344.
- [146] Z. Wu, X. Chen, M. Wang, J. Dong, and Y. Zheng, “High-Performance Ultrathin Active Chiral Metamaterials,” *ACS Nano*, vol. 12, no. 5, pp. 5030–5041, 2018, doi: 10.1021/acsnano.8b02566.
- [147] Z. Wu, J. Li, X. Zhang, J. M. Redwing, and Y. Zheng, “Room-Temperature Active Modulation of Valley Dynamics in a Monolayer Semiconductor through Chiral Purcell Effects,” *Adv. Mater.*, vol. 31, no. 49, p. 1904132, Dec. 2019, doi: 10.1002/adma.201904132.
- [148] W. R. T. Barden, S. Singh, and P. Kruse, “Roughening of gold atomic steps induced by interaction with tetrahydrofuran,” *Langmuir*, vol. 24, no. 6, pp. 2452–2458, 2008, doi: 10.1021/la701757e.